Electronic and Magnetic Properties of Candidate Materials for Kitaev Physics Using a Combination of Density Functional Theory and Many-Body Methods

Dissertation
zur Erlangung des Doktorgrades
der Naturwissenschaften

vorgelegt beim Fachbereich Physik der
Goethe-Universität Frankfurt
in Frankfurt am Main

von
Ying Li

aus Shaanxi (China)

Frankfurt am Main (2016)

vom Fachbereich Physik der

Goethe Universität Frankfurt

als Dissertation angenommen.

Dekan: Prof. Dr. Owe Philipsen

Gutachter: Prof. Dr. Roser Valentí
Prof. Dr. Peter Kopietz

Datum der Disputation: 23 February 2017

To my parents...

Zusammenfassung

In den letzten Jahren hat die Suche nach einer Kitaev-Quantenspinflüssigkeit in realen Materialien für großes Interesse gesorgt. Solche Zustände beruhen auf starken, anisotropen magnetischen Wechselwirkungen, welche für eine Reihe von auf Ir und Ru basierenden Materialien vorgeschlagen wurden. Innerhalb dieser Arbeit wird sich auf zwei Hauptziele konzentriert. Diese sind zum Einen die Untersuchung der elektronischen und magnetischen Eigenschaften der für Kitaev-Physik möglichen Materialien Na_2IrO_3, α-Li_2IrO_3, α-RuCl3, γ-Li_2IrO_3 und $Ba_3YIr_2O_9$, in welchen sowohl Spin-Bahn-Kopplung als auch Korrelationseffekte eine wichtige Rolle spielen. Zum Anderen bildet die Entwicklung einer Methode für die mikroskopische Beschreibung von korrelierten Materialien, unter Kombination von Vielteilchen-Methoden mit Dichtefunktionaltheorie (DFT) einen wichtigen Bestandteil dieser Arbeit.

Eine Quantenspinflüssigkeit ist ein ungeordneter Spinzustand, in welchem die darin enthaltenen Spins stark korreliert sind, aber dennoch bis hin zu niedrigen Temperaturen fluktuieren. Es ist ein Superpositionszustand, in welchem die Spins gleichzeitig in viele verschiedene Richtungen zeigen, und welcher Anregungen mit fraktionalen Quantenzahlen möglich sind. In die Suche nach einem Quantenspinflüssigkeits-Zustand in einem realen Material sind seitdem große Anstrengungen eingegangen, insbesondere bei geometrisch frustrierten Antiferromagneten, wie es bei dem Kagome- oder dem Dreiecks-Gitter der Fall sein kann. In solch frustrierten Antiferromagneten können sich die Spins nicht spontan in ferromagnetische oder antiferromagnetische Zustände ordnen, dies führt selbst bei sehr tiefen Temperaturen zu einer Unordnung der Spins. Die dominanten Wechselwirkungen sind im Spinraum isotrop und werden durch den Heisenberg-Hamiltonian beschrieben. Da im Fall von isotroper Heisenberg-Wechselwirkung

aber nicht alle Wechselwirkungen gleichzeitig minimiert werden können, wird jede klassische Ordnungsstruktur destabilisiert. Vor einigen Jahren wurde ein weiterer Weg, ohne geometrische Frustration, zur Realisierung einer Spinflüssigkeit im Zuge von Kitaevs exakt lösbarem Honigwaben-Modell vorgeschlagen. Dieses Modell beinhaltet ausschließlich kurzreichweitige Korrelationen auf dem Honigwaben-Gitter. Im Gegensatz zum Heisenberg-Modell unterliegt dort jede Gitter-Bindung einer Ising-ähnlichen Wechselwirkung, welche von der Richtung der Bindung abhängig ist. Der Grundzustand ist dann eine Quantenspinflüssigkeit, mit entweder lückenlosen Anregungen, oder Majorana-Fermion-Anregungen, je nachdem welche relativen Wechselwirkungen vorliegen. Die exakte Lösung des Modells kann auf das Problem von Majorana-Fermion-Hüpfen im Hintergrund eines emergenten statischen Z_2 Eichfelds reduziert werden.

Nichtsdestotrotz bleibt es eine Herausforderung, Materialien zu finden, welche tatsächlich eine Kitaev-Spinflüssigkeit realisieren. Das fragliche System sollte von der Kitaev-Wechselwirkung dominiert werden, während andere Wechselwirkungen unterdrückt sind. Jackeli und Khaliullin [Phys.Rev.Lett 102, 017205 (2009)] schlugen eine Struktur mit 90° Bindungsgeometrie (an den Kanten verbundene Oktaeder aus schweren d^5 Metallen mit Winkeln nahe 90°) vor, welche auf natürliche Weise zu bindungsabhängigen Wechselwirkungen führen. Es gibt verschiedene Materialien, bei denen solche Wechselwirkungen auf dem Honigwaben-Gitter möglich sind, beispielsweise Na_2IrO_3, α-Li_2IrO_3 und α-$RuCl_3$, oder auf anderen dreidimensionalen Gittern β-Li_2IrO_3 und γ-Li_2IrO_3. Sie alle besitzen eine oktaedrische Struktur und sind Mott-Isolatoren. Allerdings haben diese Materialien magnetisch geordnete Grundzustände anstelle einer Spinflüssigkeit. Wie ein Kitaev-Zustand in einem realen System konstruiert werden könnte, ist eine der Fragen mit der sich diese Arbeit beschäftigt. Schließlich untersuchen wir ein System bei dem $Ir^{4.5+}$ eine $d^{4.5}$ Füllung besitzt, welches durch zweifach geschichtete Dreiecksgitter geformt wird und ein antiferromagnetischer Isolator ist. Die Details dieses Systems werden in den entsprechenden Kapiteln erörtert.

Vielteilchensysteme können mit Hilfe des sogenannten Hubbard-Modells beschrieben werden, dieses beinhaltet die kinetische Energie der Elektronen, welche zwischen den Atomrümpfen hüpfen, die Coulomb-Abstoßung der Elektronen U und die intra-atomare Hundskopplung J_H. Wenn die Elektro-

nengeschwindigkeit von der gleichen Größenordnung wie die Lichtgeschwindigkeit ist, dies ist bei schweren Atomen der Fall, dann ist es notwendig, relativistische Effekte in der Beschreibung der elektronischen Struktur zu berücksichtigen. Die Spin-Bahn-Wechselwirkung mischt "up" und "down" Spinzustände, so dass der totale Drehimpuls $j = l + s$ eine gute Quantenzahl wird, im Gegensatz zu l oder s. Man allgemein kann sagen, dass die Bedeutung von relativistischen Effekten in der Regel mit der Atomnummer zunimmt. Diese relativistischen Effekte wurden in schwach korrelierten Materialien, wie beispielsweise Halbleitern, bereits intensiv untersucht. In solchen Materialien verbindet die Spin-Bahn-Wechselwirkung die Bahndrehimpuls- mit den Spin-Freiheitsgraden, was zu Phänomenen wie dem anormalen Hall-Effekt, der Bildung von topologischen Isolatoren oder Spintronik-Physik führen kann.

Im Gegensatz zu schwach korrelierten Materialien, bei denen U klein ist, und im Gegensatz zu $3d$ Übergangsmetallen, bei denen Spin-Bahn-Effekte klein sind, sind in den untersuchten $4d$ Ru^{3+} und $5d$ Ir^{4+} Verbindungen die "on-site" Hubbard-Wechselwirkung U, die Hunds-Kopplung J_H, die Spin-Bahn-Kopplung λ, das Kristallfeld Δ und die kinetische Energie der Elektronen alle von derselben Größenordnung. Dies erschwert die Beschreibung ihrer Eigenschaften, da in der Regel keinerlei kleine Parameter vorhanden sind. Obwohl die Beschreibung dieser komplexen Materialien herausfordernd ist, bleibt zu bedenken, dass die Untersuchung von schweren $4d$ und $5d$ d-Block-Materialien erst seinen Anfang genommen hat. Dies impliziert aber, dass wir bisher über keinerlei Intuition bezüglich ihrer Eigenschaften verfügen. Daher ist es von Bedeutung, zunächst eine Vorstellung von ihrer elektronischen Struktur, ihren optischen Eigenschaften und ihren magnetischen Eigenschaften, beeinflusst von Korrelationen und Spin-Bahn-Kopplung, zu erlangen. Das niederenergetische t_{2g} Triplett in diesen Materialien ist aufgespalten in ein $j_{\text{eff}} = 1/2$ Doublet und ein $j_{\text{eff}} = 3/2$ Quartett. Im Fall von d^5 Füllung (fünf Elektronen in der äußeren d-Schale), sind di $j_{\text{eff}} = 3/2$ Zustände gefüllt und di $j_{\text{eff}} = 1/2$ werden von einem Elektron besetzt.

Diese Materialien wurden mit einer Reihe von Verfahren untersucht, welche in den entsprechenden Kapiteln zusammen gefasst werden. Dichtefunktionaltheorie (DFT) wird immer mehr verwendet um die Natur von existierenden Materialien zu beschreiben, um neue Materialien zu designen und um Verlässlichkeit und

Genauigkeit von anderen Theorien zu verifizieren. Allerdings funktioniert das nicht immer einwandfrei in Materialien mit stark korrelierten Wechselwirkungen. Hinzu kommt, dass Modelle, basierend auf Vielteilchen-Methoden, ebenso wichtig sind, um die Wechselwirkungen besser untersuchen zu können.

Im Fall der Honigwaben-Gitter-Materialien Na_2IrO_3, α-Li_2IrO_3 und α-$RuCl_3$ konnten wir eine Abhängigkeit der Qualität des Quasimolekular-Orbital-Bilds (QMO-Bilds) von den Hüpfamplituden, beeinflusst von den verschieden stark ausgeprägten trigonalen Verzerrungen, beobachten. Na_2IrO_3 besitzt die größte Verzerrung und in diesem Fall wird die nicht-relativistische Einteilchen-Elektronen-Struktur gut mit der QMO Basis beschrieben. Das QMO-Bild wird jedoch im $P3_112$ α-$RuCl_3$ zerstört, in welchem die nur kleinen Verzerrungen die Metall-Metall Hüpfamplituden verstärken. In α-Li_2IrO_3 und $C2/m$ α-$RuCl_3$ führt die mittlere Verzerrung zu signifikant gemischten QMOs.

Bezüglich der optischen Leitfähigkeit haben wir die zweidimensionalen Na_2IrO_3 und α-Li_2IrO_3, sowie das dreidimensionale γ-Li_2IrO_3 untersucht, wobei wir sowohl die relativistische DFT Methode inklusive Coulomb-Abstoßung, als auch exakte Diagonalisierung des gesamten wechselwirkenden Hamiltonians auf endlichen Clustern, mit Hüpfamplituden aus DFT-Rechnungen, verwendet haben. Beide Methoden reproduzieren sowohl den Haupt-Peak der "in-plane" Komponente der optischen Leitfähigkeit σ_c, als auch die experimentell beobachtete Lücke. Das isolierende Verhalten kann ebenfalls erklärt werden, indem Spin-Bahn-Kopplung und Coulomb-Abstoßung für die d^5 Füllung berücksichtigt werden. Unter Verwendung der Tatsache, dass die schmalen Bänder von Na_2IrO_3 sehr gut mit QMOs beschrieben werden können, haben wir gezeigt, dass die Stärke der verschiedenen Inter-Band-Beiträge zur optischen Leitfähigkeit gut mit Hilfe der Parität der quasimolekularen Orbitale beschrieben werden können, insbesondere die Unterdrückung der Gewichte in Übergängen gleicher Parität und die Verstärkung der Gewichte in Übergängen ungleicher Parität. Wir sind außerdem in der Lage, den Verlauf der optischen Leitfähigeit in α-Li_2IrO_3 vorauszusagen. Es scheint jedoch so, dass DFT den Beitrag des $j_{1/2} \rightarrow j_{1/2}$ Übergangs bei niedrigen Energien in σ_a und σ_b überschätzt.

Im Gegensatz dazu bestätigen die Ergebnisse der exakten Diagonalisierung (ED) die Modell-Parameter (U, J_H, λ) und legen die Vermutung nahe, dass hochenergetische Anregungen mit einem lokalisierten Bild in γ-Li_2IrO_3 gut erfasst werden können. Der Vergleich mit der Analyse der optischen Leitfähigkeit von Na_2IrO_3 zeigt, dass der Peak nahe 1,5 eV sowohl in Na_2IrO_3, als auch in γ-Li_2IrO_3 im Sinne von "*inter-site*" $j_{3/2} \rightarrow j_{1/2}$ Anregungen interpretiert werden können. Der Vergleich von $\sigma(\omega)$ für die verschiedenen Materialien legt nahe, dass das relative Spektralgewicht der Übergänge einen Einblick in die Größenordnungen der verschiedenen Hüpfamplituden, und damit der lokalen magnetischen Wechselwirkungen, gewähren kann.

Obwohl die Materialien, die mögliche Kandidaten für Kitaev-Physik darstellen, in den letzten Jahren intensiv untersucht wurden, ist kein Konsens bezüglich ihrer magnetischen Wechselwirkungen erreicht worden. Dies erschwert es erheblich, ihre Eigenschaften zu verstehen und heraus zu finden wie sie chemisch oder auf andere Weise verändert werden sollten. Um die gegenwärtigen Materialien im Phasendiagramm richtig einzuordnen und um zu wissen wie die Materialien modifiziert werden werden müssen, um ein Spinflüssigkeits-Verhalten zu erreichen, ist ein mikroskopisches Verständnis unbedingt notwendig. Im Zuge dessen haben wir unter anderem Störungstheorie zweiter Ordnung angewandt. Die Hüpfparameter wurden mit Hilfe der Projektormethode aus nicht-relativistischen DFT Rechnungen ermittelt. Auf diesen Hüpfparametern basierend, wird das Hubbard-Modell, unter Berücksichtigung von Spin-Bahn-Kopplung und Korrelationseffekten, konstruiert. Nach exakter Diagonalisierung des Hamiltonoperators ermitteln wir die Austausch-Wechselwirkungen und konstruieren ein mikroskopisches, effektives Modell, welches in der Lage ist, die experimentell ermittelten magnetischen Konfigurationen zu erklären. Der wichtige Beitrag dieser Arbeit zur wissenschaftlichen Gemeinschaft ist die Entwicklung einer Methode um Austauschparameter zu extrahieren, welche mit den bekannten experimentellen Details konsistent sind.

Alle in dieser Arbeit untersuchten Strukturen besitzen jedoch magnetisch geordnete Grundzustände anstelle einer Spinflüssigkeit. Kombiniert man die Heisenberg-Wechselwirkung mit der Kitaev-Wechselwirkung zum Heisenberg-Kitaev-Modell, und berücksichtigt zudem außerdiagonale Terme, sowie langreichweitige Wechselwirkungen, so entstehen reichhaltige Phasen. Die beobachtete Zickzack-Ordnung

in Na_2IrO_3 und α-$RuCl_3$ kann, unter Berücksichtigung von großer Heisenberg-Wechelwirkung zwischen dritten Nachbarn J_3, natürlich erklärt werden. Diese tritt als dominanter Term in Störungstheorie höherer Ordnung auf, daher wurde sie in den meisten bisherigen Studien vernachlässigt oder unterschätzt. Im Falle von α-Li_2IrO_3 lassen die berechneten Wechselwirkungen vermuten, dass eine große Bindungs-Anisotropie und signifikante Terme zwischen ersten, zweiten und dritten Nachbarn vorliegen. Wir haben insbesondere gezeigt, dass eine Kombination von Zweiter-Nachbar-Wechselwirkung die beobachtete Ordnung erklären kann. Die Komplexität der Wechselwirkungen könnte im Falle von den weniger symmetrischen β- und γ-Li_2IrO_3 sogar noch größer sein, da in diesen für bestimmte Nächste-Nachbar-Bindungen die Dzyaloshinskii-Moriya-Wechselwirkung erlaubt ist. Es bleibt zu bestimmen, welche Modelle effektiv zu den realen Materialien in Relation gebracht werden können, reine Nächste-Nachbar-Modelle scheinen jedoch unrealistisch zu sein.

Bedenkt man diese Beobachtungen, so erscheint die Realisierung einer Kitaev-Spinflüssigkeit als Grundzustand in d^5 Materialien als eine erhebliche synthetische Herausforderung. Aufgrund des hoch komplexen Phasendiagramms und der zahlreichen Möglichkeiten klassischer Entartung in dem erweiterten Wechselwirkungs-Bereich, ist es nichtsdestotrotz äußerst wahrscheinlich, dass diese Systeme andere exotische Phasen und Phasenübergange aufweisen.

Zusammenfassend kann man sagen, dass die untersuchten Materialien sowohl große Spin-Bahn-Kopplung als auch starke Korrelationseffekte besitzen, welche mit einer Kombination von DFT und Vielteilchen-Methoden untersucht werden können. Die Methode der exakten Diagonalisierung auf dem Honigwaben-Gitter ermöglicht eine genaueren Ermittlung der magnetischen Wechselwirkungen, welche auch auf weitere Systeme angewandt werden kann. Sie stellt ein mächtiges Mittel für Studien von magnetischen Systemen in stark korrelierten Systemen mit Spin-Bahn-Kopplung dar. Auf der Basis der in dieser Arbeit angewandten Berechnungen sind wir in der Lage die wichtigsten synthetischen Herausforderungen zur Realisierung eines Spinflüssigkeits-Zustands innerhalb der Kitaev Kandidaten zu identifizieren. Die verwendeten und entwickelten Methoden dieser Arbeit werden zweifelsohne bei künftigen Arbeiten zur Konstruktion von Kitaev-Spinflüssigkeiten in realen Materialien hilfreich sein.

Abstract

Great interest has emerged recently in the search for Kitaev spin liquid states in real materials. Such states rely on strongly anisotropic magnetic interactions, which have been suggested to exist in a number of candidate materials based on Ir and Ru. This thesis concentrates on two priority purposes. The first is the investigation of electronic and magnetic properties of candidate materials Na_2IrO_3, α-Li_2IrO_3, α-$RuCl_3$, γ-Li_2IrO_3, and $Ba_3YIr_2O_9$ for Kitaev physics where both spin-orbit coupling and correlation effects are important. The second is the method development for the microscopic description of correlated materials combining many-body methods and density functional theory (DFT).

A quantum spin liquid is a spin disordered state, in which the constituent spins are highly correlated but still fluctuate strongly down to low temperatures. It is a superposition state in which the spins simultaneously point in many different directions that support excitations with fractional quantum numbers. A great amount of effort has been made in the search for quantum spin liquid states in real materials, particularly in geometrically frustrated antiferromagnets such as kagome and triangular lattices. Recently, another way to realize the spin liquid without geometric frustration was suggested by Kitaev's exactly solvable honeycomb model. This model including only short range correlations on the honeycomb lattice. Different from the Heisenberg model, each bond has an Ising-like bond-directed interactions. The ground state is a quantum spin liquid, with either gapless or gapped Majorana fermion excitations, depending on the relative interaction. The exact solution can be reduced to the problem of Majorana fermions hopping in the background of an emergent static Z_2 gauge field.

However, to find materials to realize the Kitaev spin liquid is a challenge. The systems should be dominated by the Kitaev exchange while other interactions must be

suppressed. Jackeli and Khaliullin [Phys. Rev. Lett. 102, 017205 (2009)] suggested a structure of 90° bonding geometry (edge-sharing octahedra of heavy d^5 metals, with close to 90° bond angles), which can naturally generate bond-dependent interactions. There are several candidate materials to obtain such interactions on the honeycomb lattice Na_2IrO_3, α-Li_2IrO_3, α-$RuCl_3$ and other 3D lattices β-Li_2IrO_3 and γ-Li_2IrO_3. They all have octahedral structure and are Mott insulators. In these materials, the spin-orbit coupling, crystal field, band width, and Coulomb repulsion energy scales are all of similar order of magnitude. This makes the description of their properties difficult, since there are no relative small parameters. This difficulty is generally found in correlated $4d$ and $5d$ transition metal-based materials, which are now beginning to be explored in detail. *Ab initio*-based studies of such materials will help to build intuition about their electronic structure, optical properties, magnetic properties, and how these properties are affected by correlations and spin-orbit couplings.

The optical conductivity for Na_2IrO_3 and α-Li_2IrO_3 was calculated using density functional theory (DFT) and exact diagonalization of finite clusters. With the DFT method, we construct newly developed quasi-molecular orbitals for different materials and find sensitive dependences on the trigonal distortions. By making use of the parity of the quasi-molecular orbitals, optical conductivity intensities can be explained. We also analyze the excitation properties for the three dimensional material γ-Li_2IrO_3 to compare the similarities and differences.

While the Kitaev candidate materials have been intensively studied in the past years, there is no consensus about their magnetic interactions. This makes it difficult to understand their properties and to know how to change them chemically or by other means. In order to place the current materials in the phase diagram of interactions, and how the materials should be modified to reach a spin-liquid behavior, we need to get a microscopic understanding of the interactions. We have also considered second-order perturbation theory. The hopping parameters were calculated using the projector method from the non-relativistic DFT calculations. Based on these hopping parameters, Hubbard model is constructed including spin-orbit coupling and correlation effects. After exact diagonalization of the Hamiltonian, we extract the exchange interactions and construct the microscopic effective models which can explain the experimental magnetic configurations of these materials. The important contribution of this thesis to the community is the development of a method to extract exchange parameters that are consistent with the known experimental details.

Contents

Chapter 1

Introduction

This thesis is devoted to understanding the electronic and magnetic properties of a series of materials that have emerged as candidates for displaying spin-liquid behavior. In a quantum spin liquid state, spin are disordered and fluctuate strongly down to low temperatures. The spins are simultaneously point in many different directions and support fractional excitations [1–3]. It was first proposed as the ground state for antiferromagnetic spins on triangular lattice by Anderson [2]. The dominant interactions are the nearest neighbor interactions that are described by the Heisenberg Hamiltonian

$$H = J \sum_{\langle i,j \rangle} \hat{\mathbf{S}}_i \cdot \hat{\mathbf{S}}_j. \tag{1.1}$$

Two of the spins can be antiparallel but the third one cannot, leading to several orientations of spins. For isotropic Heisenberg magnetic interactions, not all interactions can be minimized simultaneously. This enhances the fluctuations and suppresses magnetic ordering. A quantum spin liquid state has been discovered in such geometrically frustrated antiferromagnets, for instance, organic Mott insulator with triangular lattice [4] and herbertsmithite with kagome lattice [5]. Recently, another way to realize the spin liquid without geometric frustration was suggested by Kitaev's exactly solvable honeycomb model [6]. In this model, the spin Hamiltonian is

$$H = \sum_{\gamma,\langle i,j \rangle} K_{ij}^{\gamma} \hat{\hat{S}}_i^{\gamma} \hat{\hat{S}}_j^{\gamma}, \tag{1.2}$$

where γ indicate the three different X, Y, Z bonds shown in Fig. 1.1. It's the model including only the short range correlations on the honeycomb lattice [6]. Different

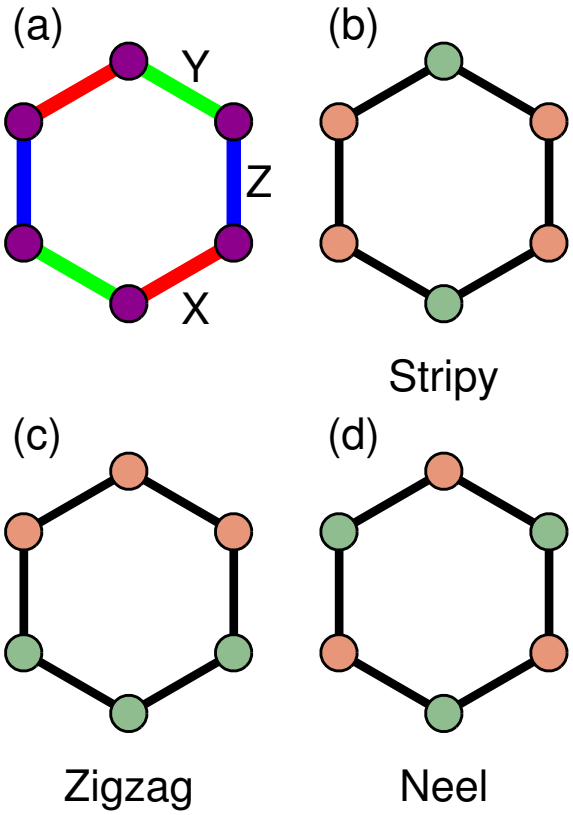

Figure 1.1: (a) Honeycomb lattice with three different bonds X, Y and Z. Different collinear magnetic configurations (b) Stripy, (c) Zigzag and (d) Neel. The orange (green) solid circles are the atoms with spin up (down).

from the Heisenberg model, the interactions between nearest neighbours are of XX, YY or ZZ type. The ground state is a quantum spin liquid, with either gapless or gapped Majorana fermion excitations, depending on the relative interaction. The exact solution can be reduced to the problem of Majorana fermions hopping in the background of an emergent static Z_2 gauge field [6].

However, to find materials to realize the Kitaev spin liquid is a challenge. The systems should be dominated by the Kitaev exchange while other interactions must be suppressed. Jackeli and Khaliullin [7] suggested a structure of 90° bonding geometry (edge-sharing octahedra of heavy d^5 metals, with close to 90° bond angles), which can naturally generate the bond-dependent interactions [8].

There are three candidate materials to obtain such interactions on the honeycomb lattice Na_2IrO_3, α-Li_2IrO_3, α-$RuCl_3$ and other 3D lattices β-Li_2IrO_3 [9, 10] and

γ-Li_2IrO_3 [11, 12]. They all have the octahedral structure shown in Fig. 1.2 (a) with a cage of O^{2-} in Na_2IrO_3, α-Li_2IrO_3, β-Li_2IrO_3, γ-Li_2IrO_3 or Cl^- in α-$RuCl_3$. As shown in Fig. 1.3, Ir in Na_2IrO_3, α-Li_2IrO_3 and Ru in α-$RuCl_3$ display such 2D honeycomb layers. The β-Li_2IrO_3 structure has zigzag chains linked in the **c** direction while γ-Li_2IrO_3 has Ir hexagonal chains which are connected along the **c** direction.

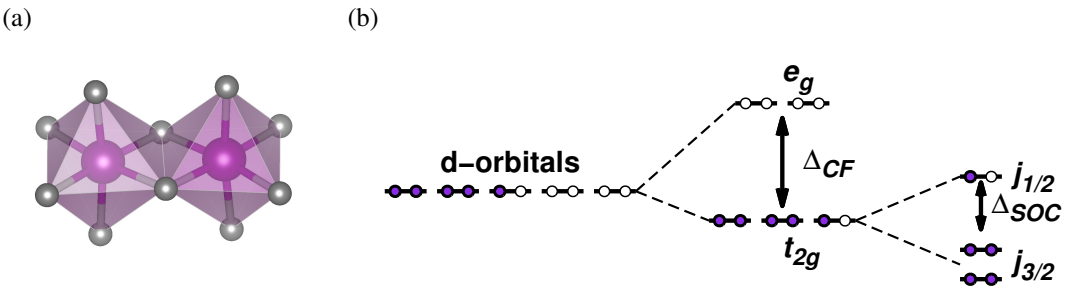

Figure 1.2: (a) IrO_6 octahedra. (b) Energy level diagram for the Ir^{4+} and Ru^{3+} honeycomb systems.

All the structures have magnetic ordered ground state instead of a spin liquid. How to engineer the Kitaev state in real systems is one of the questions we investigate in the thesis. Combining the Heisenberg interaction with Kitaev interaction into

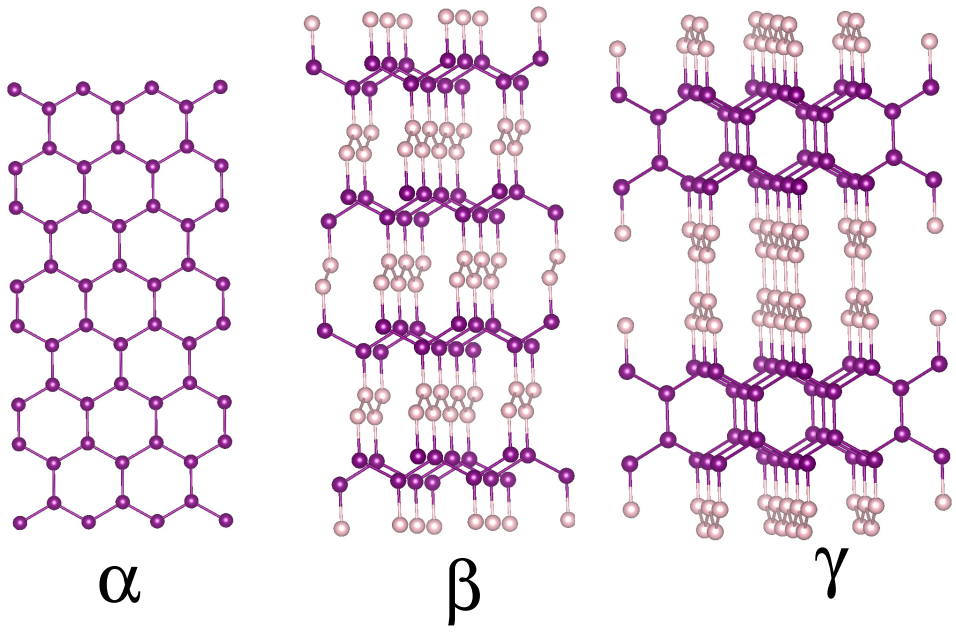

Figure 1.3: Structures of the honeycomb and 3D lattices.

the Heisenberg-Kitaev model, rich phases arise. Depending on the exchange parameters, the model can show collinear FM, Stripy, Zigzag, Neel order displayed in Fig. 1.1, noncollinear spin spiral, or spin liquid [13]. For the honeycomb structure, we show the magnetic zigzag order in Fig. 1.1. Na_2IrO_3 and α-$RuCl_3$ were found to have zigzag magnetic order by the neutron scattering and resonant x-ray experiments [14–19] while α-Li_2IrO_3 shows incommensurate spiral order [20]. Experimentally, it has been observed that Na_2IrO_3, α-Li_2IrO_3, α-$RuCl_3$ are insulators [21–25]. Their electronic structure can be described in terms of a relativistic basis [7, 26, 27] from a localized point of view or by using quasi-molecular orbitals (QMO) [18, 28–30] from the itinerant view. The 3D structure γ-Li_2IrO_3 also show spiral magnetic order, with wave vector 0.57 [12]. Finally, we investigate a system where $Ir^{4.5+}$ has a $d^{4.5}$ filling, which is formed by double layer triangular lattice and is an AFM insulator [31]. The details of these systems will be introduced in the corresponding chapters.

The many-body systems can be described by the Hubbard model

$$\begin{aligned}\hat{H} = &- \sum_{\substack{\langle i,j\rangle \\ m,m',\sigma}} (t_{ij}^{mm'} \hat{c}^{+}_{im\sigma}\hat{c}_{jm'\sigma} + h.c.) + \sum_{\substack{j,\sigma,\sigma' \\ m,m'}} \frac{U_{mm'}}{2}\hat{n}_{jm\sigma}\hat{n}_{jm'\sigma'}(1-\delta_{mm'}\delta_{\sigma\sigma'}) \\ &- \frac{J_H}{2}\sum_{\substack{j,\sigma,\sigma' \\ m,m'}} \hat{c}^{+}_{jm\sigma}\hat{c}_{jm\sigma'}\hat{c}^{+}_{jm'\sigma'}\hat{c}_{jm'\sigma}(1-\delta_{mm'}) \\ &+ \frac{J_H}{2}\sum_{\substack{j,\sigma,\sigma' \\ m,m'}} \hat{c}^{+}_{jm\sigma}\hat{c}^{+}_{jm\sigma'}\hat{c}_{jm'\sigma'}\hat{c}_{jm'\sigma}(1-\delta_{mm'})(1-\delta_{\sigma\sigma'}).\end{aligned} \tag{1.3}$$

where indices i and j represent the nearest neighbour lattice sites, and $i < j$. σ and σ' are spin index, while m and m' denote the different orbitals. The first term describes the hopping of the electrons from site to site with integrals $t_{ij}^{mm'}$. $U_{m,m'}$ denotes Coulomb repulsion of the electrons, the third term stands for the intra-atomic Hund's coupling exchange, and the last term denotes the pair hopping.

If the electron velocity is of the same order of magnitude as the velocity of light, we need to consider relativistic effects in the description of the electronic structure. The materials with strong relativistic effects are described by the Dirac Hamiltonian:

$$\hat{H} = c\alpha\hat{\mathbf{p}} + (\beta - 1)mc^2 + \hat{V}(\mathbf{r}), \tag{1.4}$$

where ,

$$\alpha = \begin{pmatrix} 0 & \sigma \\ \sigma & 0 \end{pmatrix}, \beta = \begin{pmatrix} I & 0 \\ 0 & -I \end{pmatrix}. \tag{1.5}$$

The eigenvectors Ψ are expressed as the large component Φ , and small component χ. The equation for the large component is given by:

$$[(1-\frac{\varepsilon-V}{2mc^2})\frac{p^2}{2m}+V]\,\Phi-\frac{\hbar^2}{4m^2c^2}(\nabla V\nabla\Phi)+\frac{\hbar^2}{4m^2c^2}(\sigma[\nabla V,\mathbf{p}]\Phi)=\varepsilon\Phi. \quad (1.6)$$

If the potential has the spherical symmetry, as in an isolated atom,

$$[\frac{\hat{p}^2}{2m}+V-\frac{p^2}{8m^3c^2}-\frac{\hbar^2}{4m^2c^2}\frac{dV}{dr}\frac{\partial}{\partial\mathbf{r}}+\frac{1}{2m^2c^2}\frac{1}{r}\frac{dV}{dr}(\mathbf{ls})]\Phi=\varepsilon\Phi. \quad (1.7)$$

The first and second term give the non relativistic Schrödinger equation. The third and fourth term correspond to the Darwin correction. The last term is the spin-orbit (SO) coupling, which couples the orbital and spin angular momentum of the electron. The SO interaction mixes up and down spin states, so that only the total angular momentum $j=l+s$ is a good quantum number rather than l or s. Writing $\lambda=\frac{1}{2m^2c^2}\frac{1}{r}\frac{dV}{dr}$ we obtain:

$$\hat{H}_{SO}=\lambda\mathbf{L}\cdot\mathbf{S}. \quad (1.8)$$

For a hydrogen-like atom (one electron), $V(r)=-\frac{1}{4\pi\varepsilon_0}\frac{Ze^2}{r}$,

$$\lambda=\frac{1}{2m^2c^2}\frac{1}{4\pi\varepsilon_0}\frac{Ze^2}{r^3}. \quad (1.9)$$

The average value of $\langle\frac{1}{r^3}\rangle$ is proportional to Z^3, thus $\lambda\propto Z^4$. Therefore the importance of relativistic effects tends to increase with the atomic number. These relativistic effects have been investigated in weakly correlated materials such as semiconductors. In these materials, the spin-orbit interaction links the orbital and spin degree of freedom, leading to such phenomena as anomalous Hall effect, topological insulators and the spintronic physics [32].

Different from weakly correlated materials where U is small and from $3d$ transition metals where SO effects are small, in the investigated $4d$ Ru^{3+} and $5d$ Ir^{4+} compounds, the on-site Hubbard interaction U, Hund's coupling J_H, SO interaction λ, crystal field Δ and electron kinetic energy are all of the same order of magnitude. This can make the material properties sensitive to the details. For the case of an octahedral crystal field, the d orbitals are split into t_{2g} triplet and e_g doublet shown in Fig. 1.2 (b). The low level t_{2g} triplet includes three orbitals d_{xy}, d_{xz}, and d_{yz}. The SO interaction between these three orbitals has similar behavior as in p_z, p_y, and p_x orbitals with l_{eff} = 1 and -λ [7]. The relativistic states include a $j_{\text{eff}}=1/2$ doublet with energy $E=+\lambda$ and a $j_{\text{eff}}=3/2$ quartet with energy $E=-\lambda/2$ displayed in

Figure 1.2 (b). The derivation of this result is in Appendix A; the relativistic states include $j_{\text{eff}} = 1/2$ doublet with energy $E = +\lambda$:

$$\begin{aligned}\left|\frac{1}{2},\frac{1}{2}\right\rangle &= \frac{1}{\sqrt{3}}\left(-|xy\uparrow\rangle - i|xz\downarrow\rangle - |yz\downarrow\rangle\right),\\ \left|\frac{1}{2},-\frac{1}{2}\right\rangle &= \frac{1}{\sqrt{3}}\left(|xy\downarrow\rangle + i|xz\uparrow\rangle - |yz\uparrow\rangle\right),\end{aligned} \tag{1.10}$$

and $j_{\text{eff}} = 3/2$ quartet with energy $E = -\lambda/2$:

$$\begin{aligned}\left|\frac{3}{2},\frac{3}{2}\right\rangle &= \frac{1}{\sqrt{2}}\left(-i|xz\uparrow\rangle - |yz\uparrow\rangle\right),\\ \left|\frac{3}{2},\frac{1}{2}\right\rangle &= \frac{1}{\sqrt{6}}\left(2|xy\uparrow\rangle - i|xz\downarrow\rangle - |yz\downarrow\rangle\right),\\ \left|\frac{3}{2},-\frac{1}{2}\right\rangle &= \frac{1}{\sqrt{6}}\left(2|xy\downarrow\rangle - i|xz\uparrow\rangle + |yz\uparrow\rangle\right),\\ \left|\frac{3}{2},-\frac{3}{2}\right\rangle &= \frac{1}{\sqrt{2}}\left(-i|xz\downarrow\rangle + |yz\downarrow\rangle\right).\end{aligned} \tag{1.11}$$

Where states are written in terms of $\left|J,m_j\right\rangle$. For the case of d^5 filling (five electrons in the outer d - shell), the $j_{\text{eff}} = 3/2$ states are filled and the $j_{\text{eff}} = 1/2$ is occupied by one electron.

These materials have been studied by a range of techniques which are summarized in the respective chapters. Density functional theory (DFT) is more and more widely used to explain the nature of the existing materials, to design new materials and to verify the reliability and accuracy of the theory. However it does not always work well in the materials with strong correlated interaction. On top of that, many-body methods based on models are also necessary to investigate the interactions better.

In short, in this thesis, combining DFT and many-body methods, we investigate the properties of Kitaev spin liquid candidates. The purpose of this thesis is to investigate the interplay between SO, Coulomb interaction and structural details on the electronic and magnetic properties. We try to answer the following questions in this thesis: i) How to understand insulating behavior despite heavy elements. ii) How close are these materials to the spin liquid? What are Heisenberg-Kitaev interactions? iii) How do we engineer the spin liquid? iv) How are the electronic and magnetic properties related? The structure of the thesis is as follows:

- We present Kitaev honeycomb model in **Chapter 2** and methods for electronic properties and magnetic properties in **Chapter 3** and **Chapter 4** respectively.

- Results of the optical conductivities are discussed in **Chapter 5** for Na_2IrO_3 and α-Li_2IrO_3 [33].

- In **Chapter 6**, we present the electronic properties and optical conductivity for the 3D structure γ-Li_2IrO_3 and compare it with the 2D results [34].

- The properties of α-$RuCl_3$ including the quasi-molecular orbital representation [18] and the electrostatic potential [35] are discussed in **Chapter 7**.

- We discuss the magnetic properties for Na_2IrO_3, α-Li_2IrO_3 and α-$RuCl_3$ in **Chapter 8** using the exact diagonalization method [36].

- In **Chapter 9**, we present analysis of the triangular lattice $Ba_3YIr_2O_9$ [37].

- In **Chapter 10**, we summarize the results and point out the possible directions of future research.

Chapter 2

Kitaev honeycomb model

The Kitaev model on the honeycomb lattice in the introduction can be written for X, Y, Z bonds:

$$\hat{H} = -\sum_{X-bonds} K_X \hat{\sigma}_i^x \hat{\sigma}_j^x - \sum_{Y-bonds} K_Y \hat{\sigma}_i^y \hat{\sigma}_j^y - \sum_{Z-bonds} K_Z \hat{\sigma}_i^z \hat{\sigma}_j^z, \tag{2.1}$$

where K_X, K_Y, and K_Z describe the interaction for X bonds, Y bonds, and Z bonds, respectively (see Fig. 2.1). $\hat{\sigma}^\gamma$ ($\gamma = x, y, z$) is the Pauli operator to describe spin $\hat{S}^\gamma = \frac{\hbar}{2}\hat{\sigma}^\gamma$, and

$$\hat{\sigma}^x\hat{\sigma}^y = 2i\hat{\sigma}^z,\ \hat{\sigma}^y\hat{\sigma}^z = 2i\hat{\sigma}^x,\ \hat{\sigma}^z\hat{\sigma}^x = 2i\hat{\sigma}^y. \tag{2.2}$$

This model can be exactly solved by rewriting the spin operators in terms of non-interacting Majorana fermions [6]. In this chapter, the Kitaev honeycomb lattice model will be explained in detail and we will derive the exact solution in terms of Majorana fermions. We will also show the gapped and gapless phases and discuss the spin-liquid behavior.

2.1 Conserved quantities

The first step to understand Kitaev's exact solution is to see that for each hexagon, the model has a conserved quantity. We label different hexagons with "p". In each

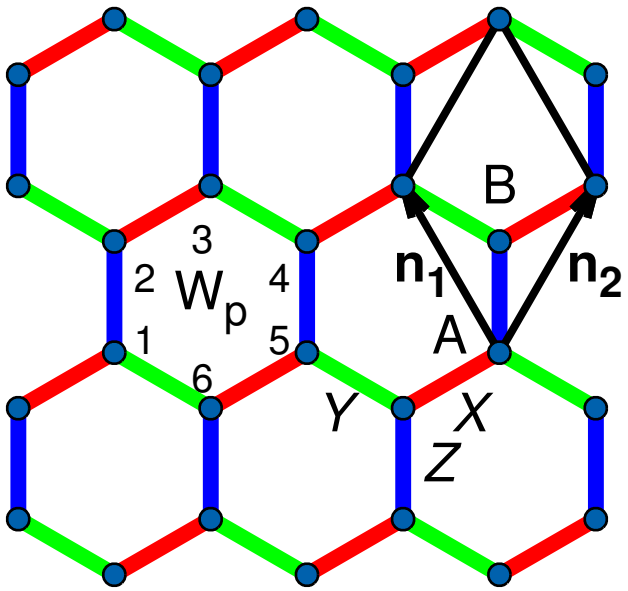

Figure 2.1: Three types of links (X, Y, Z) in honeycomb lattice. $\hat{W}_p$ is the flux operator for hexagon p. $\mathbf{n_1}$ and $\mathbf{n_2}$ are the vectors for the unit cell and A, B are the two sites in each unit cell.

hexagon p, the Z_2 flux operator is

$$\hat{W}_p = \hat{\sigma}_1^x \hat{\sigma}_2^y \hat{\sigma}_3^z \hat{\sigma}_4^x \hat{\sigma}_5^y \hat{\sigma}_6^z. \tag{2.3}$$

Flux free is defined as the eigenvalues w_p = 1 for $\hat{W}_p$, while w_p = -1 indicates a flux at hexagon p. The flux operators commute with the Hamitonian and also commute with each other:

$$[\hat{W}_p, \hat{W}_{p'}] = 0, \ [\hat{W}_p, \hat{H}] = 0. \tag{2.4}$$

The total Hilbert space can therefore be divided into sectors with eigenstates of $\hat{W}_p$. A convenient way is to represent this Hilbert space using Majorana fermions as suggested by Kitaev [6]. This simplifies the problem and makes an exact solution possible.

2.2 Majorana fermions

First, I will introduce the properties of Majorana fermions. The Majorana fermions are their own anti-particle $\hat{b}_\alpha^\dagger = \hat{b}_\alpha$ and have the following anticommutation rule

$$\{\hat{b}_\alpha, \hat{b}_\beta\} = 2\delta_{ij}. \tag{2.5}$$

Therefore the Majorana fermions square to a constant

$$\hat{b}_\alpha^2 = \hat{b}_\alpha \hat{b}_\alpha = \frac{1}{2}\{\hat{b}_\alpha, \hat{b}_\alpha\} = 1. \tag{2.6}$$

A single complex fermion can be built by two Majorana fermions

$$\hat{c}_j = \frac{1}{2}(\hat{b}_{j1} + i\hat{b}_{j2}),\ \hat{c}_j^\dagger = \frac{1}{2}(\hat{b}_{j1} - i\hat{b}_{j2}). \tag{2.7}$$

The Dirac fermions follow the anticommutation rule

$$\begin{aligned}\{\hat{c}_i, \hat{c}_j^\dagger\} &= \frac{1}{4}\{\hat{b}_{i1} + i\hat{b}_{i2}, \hat{b}_{j1} - i\hat{b}_{j2}\} \\ &= \frac{1}{4}(\{\hat{b}_{i1}, \hat{b}_{j1}\} + \{i\hat{b}_{i2}, \hat{b}_{j1}\} + \{\hat{b}_{i1}, -i\hat{b}_{j2}\} + \{i\hat{b}_{i2}, -i\hat{b}_{j2}\}) \\ &= \frac{1}{4}(2\delta_{ij} + 2\delta_{ij}) = \delta_{ij}.\end{aligned} \tag{2.8}$$

The Pauli operator $\hat{\sigma}^x$, $\hat{\sigma}^y$, and $\hat{\sigma}^z$ can be written by Majorana fermions. There are many different ways. One of these ways is proposed by Kitaev using the following representation:

$$\begin{aligned}\hat{\sigma}_j^x &= i\hat{b}_j\hat{b}_j^x, \\ \hat{\sigma}_j^y &= i\hat{b}_j\hat{b}_j^y, \\ \hat{\sigma}_j^z &= i\hat{b}_j\hat{b}_j^z, \\ \hat{b}_j\hat{b}_j^x\hat{b}_j^y\hat{b}_j^z &= 1.\end{aligned} \tag{2.9}$$

There are four Majorana fermions and satisfy the anticommutation relations

$$\{\hat{b}_i^\gamma, \hat{b}_j^{\gamma'}\} = 2\delta_{ij}\delta_{\gamma,\gamma'},\ \{\hat{b}_i, \hat{b}_j\} = 2\delta_{ij}. \tag{2.10}$$

Therefore for Pauli matrix:

$$\begin{aligned}[\hat{\sigma}_i^x, \hat{\sigma}_j^y] &= [i\hat{b}_i\hat{b}_i^x, i\hat{b}_j\hat{b}_j^y] \\ &= -(\hat{b}_i\hat{b}_i^x\hat{b}_j\hat{b}_j^y - \hat{b}_j\hat{b}_j^y\hat{b}_i\hat{b}_i^x) \\ &= \hat{b}_i\hat{b}_j\hat{b}_i^x\hat{b}_j^y - hatb_j\hat{b}_i\hat{b}_j^y\hat{b}_i^x \\ &= 2\delta_{ij}\hat{b}_i^x\hat{b}_j^y \\ &= 2i\sigma_j^z\delta_{ij}.\end{aligned} \tag{2.11}$$

Using the same methods, we can obtain

$$\begin{aligned}[\hat{\sigma}_i^y, \hat{\sigma}_j^z] &= 2i\sigma_j^x \delta_{ij}, \\ [\hat{\sigma}_i^z, \hat{\sigma}_j^x] &= 2i\sigma_j^y \delta_{ij}.\end{aligned} \tag{2.12}$$

2.3 Exact solution and phase diagram

In the Majorana fermions representation, the Kitaev Hamiltonian is

$$H = \frac{i}{4}\sum_{i,j} A_{ij}\hat{b}_i\hat{b}_j, \tag{2.13}$$

where

$$A_{ij} = 2K_{\gamma_{ij}}u_{ij}, \tag{2.14}$$

i, j are connected, and $u_{\langle ij\rangle_\gamma} = ib_i^a\hat{b}_j^a$. This Hamiltoinan includes the flux sector u_{ij} and the matter fermions $\hat{b}_i$. The flux operator $\hat{W}_p = u_{12}u_{23}u_{43}u_{45}u_{65}u_{61}$, and u_{ij} is also conserved. It can be shown that $w_p = 1$ represents the (flux free) ground state $|F_0\rangle$. One choice of u_{ij} that satisfies this condition is $u_{ij} = 1$. We use s, α to represent the i position, where s is the unit cell and α is a position type inside the cell to indicate A site or B site (see Fig. 2.1), while t, β correspond to j site. Using the Fourier transformation:

$$\begin{aligned}\widetilde{A}_{\alpha\beta}(\mathbf{q}) &= \sum_t e^{i\mathbf{q}\cdot\mathbf{r_t}}A_{0\alpha,t\beta}, \\ \hat{a}_{\mathbf{q},\alpha} &= \frac{1}{\sqrt{2N}}\sum_s e^{-i\mathbf{q}\cdot\mathbf{r_s}}\hat{b}_{s\alpha},\end{aligned} \tag{2.15}$$

the Hamiltonian is written as:

$$\hat{H} = \frac{1}{2}\sum_{\mathbf{q},\alpha,\beta} i\widetilde{A}_{\alpha\beta}(\mathbf{q})\hat{a}_{-\mathbf{q},\alpha}\hat{a}_{\mathbf{q},\beta}. \tag{2.16}$$

The Hamiltonian is expressed in two sublattices with the vectors for the unit cell $\mathbf{n_1}, \mathbf{n_2}$ shown in Fig. 2.1:

$$i\widetilde{A}(q) = \begin{pmatrix} 0 & if(\mathbf{q}) \\ -if(\mathbf{q})^* & 0 \end{pmatrix} \tag{2.17}$$

where

$$f(\mathbf{q}) = 2(K_X e^{i(\mathbf{q},\mathbf{n_1})} + K_Y e^{i(\mathbf{q},\mathbf{n_2})} + K_Z). \tag{2.18}$$

After diagonalized Eq. (2.17), two eigenstates are obtained:

$$\begin{aligned}\varepsilon_1(\mathbf{q}) &= |f(\mathbf{q})|, \quad \left|d_{1,\mathbf{q}}\right\rangle = \frac{1}{\sqrt{2}}|f(\mathbf{q})|\left|a_{-\mathbf{q},A}\right\rangle - if^*(\mathbf{q})\left|a_{\mathbf{q},B}\right\rangle, \\ \varepsilon_2(\mathbf{q}) &= -|f(\mathbf{q})|, \quad \left|d_{2,\mathbf{q}}\right\rangle = \frac{1}{\sqrt{2}}|f(\mathbf{q})|\left|a_{-\mathbf{q},A}\right\rangle + if^*(\mathbf{q})\left|a_{\mathbf{q},B}\right\rangle.\end{aligned} \tag{2.19}$$

Therefore, the Hamiltonian can be expressed as:

$$\hat{H} = \frac{1}{2}\sum_{\mathbf{q}}\{|f(\mathbf{q})|\,\hat{d}^\dagger_{1,\mathbf{q}}\hat{d}_{1,\mathbf{q}} - |f(\mathbf{q})|\,\hat{d}^\dagger_{2,\mathbf{q}}\hat{d}_{2,\mathbf{q}}\}, \tag{2.20}$$

where

$$\begin{aligned}\hat{d}^\dagger_{1,\mathbf{q}} &= \hat{a}_{-\mathbf{q},A} - if^*(\mathbf{q})\hat{a}_{\mathbf{q},B}, \\ \hat{d}_{1,\mathbf{q}} &= \hat{a}_{\mathbf{q},A} + if(\mathbf{q})\hat{a}_{-\mathbf{q},B}, \\ \hat{d}^\dagger_{2,\mathbf{q}} &= \hat{a}_{-\mathbf{q},A} + if^*(\mathbf{q})\hat{a}_{\mathbf{q},B}, \\ \hat{d}_{2,\mathbf{q}} &= \hat{a}_{\mathbf{q},A} - if(\mathbf{q})\hat{a}_{-\mathbf{q},B}.\end{aligned} \tag{2.21}$$

Since $\hat{d}^\dagger_{2,-\mathbf{q}} = \hat{d}_{1,\mathbf{q}}$, $\hat{d}_{2,-\mathbf{q}} = \hat{d}^\dagger_{1,\mathbf{q}}$ and $\{\hat{d}^\dagger_1, \hat{d}_1\} = 1$, the Hamiltonian becomes

$$\hat{H} = \sum_{\mathbf{q}}|f(\mathbf{q})|\,\{\hat{d}^\dagger_{1,\mathbf{q}}\hat{d}_{1,\mathbf{q}} - \frac{1}{2}\}. \tag{2.22}$$

The ground state $|S_0\rangle = |F_0\rangle\,|M_0\rangle$ is constructed by the flux ground state $|F_0\rangle$ and matter fermion ground state $|M_0\rangle$, which is a state without matter fermions $\hat{d}_1\,|M_0\rangle = 0$ with the energy $\varepsilon = -\sum_{\mathbf{q}}|f(\mathbf{q})|$. The excitation spectrum $\varepsilon(\mathbf{q}) = 2\,|f(\mathbf{q})|$ can be zero (gapless) or nonzero (gapped) depending on the values of K_X, K_Y, K_Z. The phases are displayed in a ternary plot in Fig. 2.2.

- The gapless B phase appears when $K_X < K_Y + K_Z$, $K_Y < K_X + K_Z$ and $K_Z < K_X + K_Y$. At $K_X = K_Y = K_Z$, the Majorana fermions have a Dirac spectrum.

- It is gapped for all other (K_X, K_Y, K_Z) values with A_x for $K_X > K_Y + K_Z$, A_y for $K_y > K_x + K_z$, and A_z for $K_z > K_x + K_y$.

The particles in the gapped A phase have Abelian statistics, which means under exchange of two particles, the wave function acquires +1 or -1. In contrast, Kitaev showed that in the presence of an external magnetic field, the B phase which is gapless capture a gap and obey non-Abelian statistics. These properties are important for topological quantum computation because of their stability against local perturbation that could lead to decoherence [6, 38].

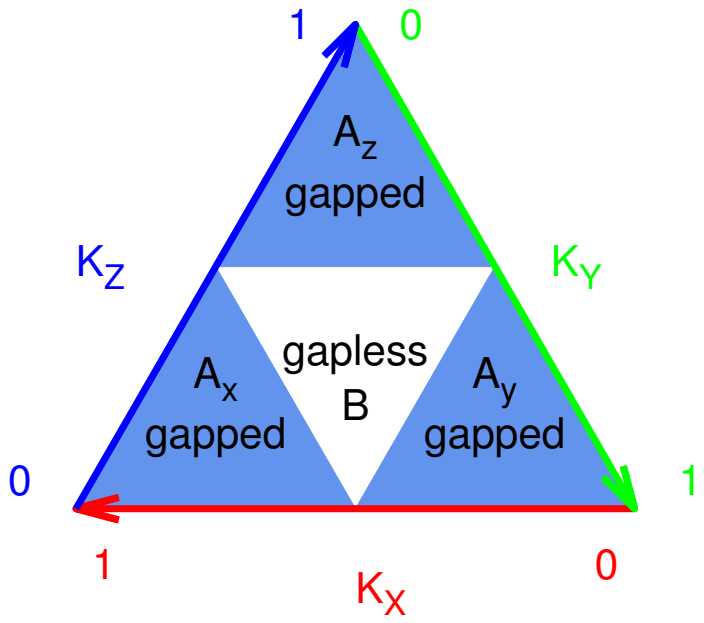

Figure 2.2: Phase diagram of the honeycomb Kitaev model [6].

2.4 Quantum spin liquid states

We already showed the exact solution of the lowest flux section, here we explain why the ground state is a quantum spin liquid (QSL). QSL is a state which does not show long range magnetic order even at low temperature. The important properties for Kitaev spin liquid is that it has fractionalization of the excitations and the spin correlations are short ranged even at zero temperature. The fractionalization of spins into Majorana fermions and static fluxes in the ground state denote the quantum spin liquid properties. Beyond the nearest neighbour, the spin correlation function is zero because of selection rules from the flux sector [39, 40].

Chapter 3

Methods for describing electronic properties

In this chapter, we will introduce different methods for the microscopic description of the electronic properties of materials including the electronic densities of states and optical response such as the dielectric function. The first method is density functional theory (DFT), which may be used to directly estimate properties, by including electronic correlations at a mean-field level. For materials where correlations are expected to have significant effects beyond this mean field level, DFT can also be used as a tool to parameterize alternative methods, such as diagonalization. This second method treats all correlations exactly, but is very computationally expensive, so its use is limited to small systems. We nevertheless show that this technique can be useful for insulators, where the important effects are local in nature.

DFT is one of the most successful method to describe the electronic properties. DFT uses the electron density $\rho(\mathbf{r})$ to describe the properties of the system. It is a "First-principles" or "*ab initio*" method since it doesn't depend on parametrization of a given model. One position dependent scalar function determines all the information in the many-body wave functions for the ground state.

The study of the optical properties of correlated materials is important both for fundamental research and industrial applications. It is one of the most general methods

to investigate the electronic structure, impurity levels, excitons, localized defects, lattice vibrations, and various magnetic excitations [41].

3.1 Density functional theory

The DFT theory description here follows Ref. [42].

3.1.1 Basic theory

Hohenberg and Kohn formulated the density functional theory as an exact theory of many-body systems [43]. Further, Kohn and Sham simplified the many-body equations to auxiliary independent particle equations, called Kohn-Sham equations [44]

$$\hat{H}_{\mathrm{KS}}\psi_i(\mathbf{r}) = \varepsilon_i\psi_i(\mathbf{r}), \tag{3.1}$$

with

$$\hat{H}_{\mathrm{KS}} = [-\frac{\hbar^2}{2m_e}\bigtriangledown^2 + \hat{V}_{\mathrm{eff}}(\mathbf{r})]. \tag{3.2}$$

The effective potential include:

$$\hat{V}_{\mathrm{eff}}(\mathbf{r}) = \hat{V}_{\mathrm{ext}}(\mathbf{r}) + \hat{V}_{\mathrm{H}}(\mathbf{r}) + \hat{V}_{\mathrm{xc}}(\mathbf{r}), \tag{3.3}$$

where $\hat{V}_{\mathrm{ext}}$ is the external potential, while $\hat{V}_H$ denote the Hartree potential, describing the Coulomb interaction between a single electron and the total electron density, and $\hat{V}_{\mathrm{xc}}$ is the exchange-correlation potential. The external Hartree (Coulomb) and exchange correlation potential is given by

$$\hat{V}_{\mathrm{H}}(\mathbf{r}) = \frac{e^2}{4\pi\varepsilon_0}\int d^3\mathbf{r}'\frac{\rho(\mathbf{r}')}{|\mathbf{r}-\mathbf{r}'|}, \tag{3.4}$$

$$\hat{V}_{\mathrm{xc}}(\mathbf{r}) = \frac{\delta E_{\mathrm{xc}}[\rho(\mathbf{r})]}{\delta\rho(\mathbf{r})}. \tag{3.5}$$

The exchange correlation potential includes all the exchange and correlation effects. In the local-density approximation (LDA), the exchange-correlation function has the form:

$$E_{\mathrm{xc}}^{LDA}[\rho] = \int \rho(\mathbf{r})\varepsilon_{\mathrm{xc}}(\rho)d\mathbf{r}, \tag{3.6}$$

where $\varepsilon_{\mathrm{xc}}$ is the exchange and correlation energy per particle in a uniform electron gas. Its exchange part has an analytical form while the correlation part is numerically calculated (*i.e.* quantum Monte Carlo [45] and subsequently parameterized in Ref. [46, 47]). Improvements for LDA are for instance including the non-local dependence of the exchange-correlation potential on electron densities, as it is the case for the generalized gradient approximation (GGA) [48–52]:

$$E_{\mathrm{xc}}^{GGA}[\rho] = \int \rho(\mathbf{r}) F(\rho, \nabla\rho) d\mathbf{r}. \tag{3.7}$$

In order to solve the equation, the potential is calculated from the electron density

$$\rho(\mathbf{r}) = \sum_{i}^{N_e} |\psi_i(r)|^2, \tag{3.8}$$

the electron wave functions are obtained by solving the Kohn-Sham equation. Thus, the Kohn-Sham equation can be solved by iteration, with self-consistency achieved when no further modification of ρ is made by successive updates, shown in Fig. 3.1.

So far, the above equation did not consider the electron spin. With spin, the spin polarized density functional theory can be defined, in which the exchange correlation functional $E_{\mathrm{xc}} = f(\rho, \sigma)$ is not only a function of electron density but also the magnetization density. If the magnetic structure is assumed to be collinear, the total energy is:

$$E = E[\rho(\mathbf{r}), m(\mathbf{r})] = E[\rho_{\uparrow}(\mathbf{r}), \rho_{\downarrow}(\mathbf{r})], \tag{3.9}$$

$$\rho(\mathbf{r}) = \rho_{\uparrow}(\mathbf{r}) + \rho_{\downarrow}(\mathbf{r}),\ m(\mathbf{r}) = \rho_{\uparrow}(\mathbf{r}) - \rho_{\downarrow}(\mathbf{r}). \tag{3.10}$$

Where σ labels the spin

$$\rho_{\sigma}(\mathbf{r}) = \sum_{occ} \psi_{i\sigma}^{*}(\mathbf{r}) \psi_{i\sigma}(\mathbf{r}), \tag{3.11}$$

and the spin polarized Kohn-Sham equation is

$$\hat{H}_{KS} \psi_{i\sigma}(\mathbf{r}) = \varepsilon_{\mathbf{i}\sigma} \psi_{\mathbf{i}\sigma}(\mathbf{r}). \tag{3.12}$$

The spin polarized Kohn-Sham equations are solved using the same method as the non spin polarized Kohn-Sham equations. In a solid with a periodic potential, the single electron wave-functions are Bloch wave-functions $\psi_{i\mathbf{k}}(\mathbf{r})$ with the periodic function $u_{i\mathbf{k}}(\mathbf{r})$ [53]

$$\psi_{i\mathbf{k}}(\mathbf{r}) = e^{i\mathbf{k}\cdot\mathbf{r}} u_{i\mathbf{k}}(\mathbf{r}). \tag{3.13}$$

We expand the function $\psi_{i\mathbf{k}}(\mathbf{r})$ in the basis $\phi_{n\mathbf{k}}(\mathbf{r})$ up to $n = P$ with the coefficient c_i^n,

$$\psi_{i\mathbf{k}}(\mathbf{r}) = \sum_n^P c_i^n \phi_{n\mathbf{k}}(\mathbf{r}). \tag{3.14}$$

In this basis, the Kohn-Sham equations in Eq. 3.1 for the solids become

$$HC = ESC, \tag{3.15}$$

where H is a matrix of $\hat{H}_{KS}$ in this basis, S denotes the overlap matrix of the basis, and C is the coefficient matrix

$$H = \begin{pmatrix} \langle\phi_{1\mathbf{k}}(\mathbf{r})|\hat{H}_{KS}|\phi_{1\mathbf{k}}(\mathbf{r})\rangle & \langle\phi_{1\mathbf{k}}(\mathbf{r})|\hat{H}_{KS}|\phi_{2\mathbf{k}}(\mathbf{r})\rangle & \cdots & \\ \langle\phi_{2\mathbf{k}}(\mathbf{r})|\hat{H}_{KS}|\phi_{1\mathbf{k}}(\mathbf{r})\rangle & \langle\phi_{2\mathbf{k}}(\mathbf{r})|\hat{H}_{KS}|\phi_{2\mathbf{k}}(\mathbf{r})\rangle & \cdots & \\ \vdots & \vdots & \ddots & \\ & & & \langle\phi_{P\mathbf{k}}(\mathbf{r})|\hat{H}_{KS}|\phi_{P\mathbf{k}}(\mathbf{r})\rangle \end{pmatrix}, \tag{3.16}$$

$$S = \begin{pmatrix} \langle\phi_{1\mathbf{k}}(\mathbf{r})|\phi_{1\mathbf{k}}(\mathbf{r})\rangle & \langle\phi_{1\mathbf{k}}(\mathbf{r})|\phi_{2\mathbf{k}}(\mathbf{r})\rangle & \cdots & \\ \langle\phi_{2\mathbf{k}}(\mathbf{r})|\phi_{1\mathbf{k}}(\mathbf{r})\rangle & \langle\phi_{2\mathbf{k}}(\mathbf{r})|\phi_{2\mathbf{k}}(\mathbf{r})\rangle & \cdots & \\ \vdots & \vdots & \ddots & \\ & & & \langle\phi_{P\mathbf{k}}(\mathbf{r})|\phi_{P\mathbf{k}}(\mathbf{r})\rangle \end{pmatrix}, \tag{3.17}$$

$$E = \varepsilon_i(\mathbf{k}), \quad C = \begin{pmatrix} c_i^1 \\ c_i^2 \\ \vdots \\ c_i^P \end{pmatrix}. \tag{3.18}$$

There are several basis sets used in different DFT codes for the solution of the Kohn-Sham equations. Plane waves are very simple but not able to describe strongly varying potentials. To overcome this problem, the projector augmented waves (PAW) [54] and localized orbitals are used. The basis we used in this thesis are the Augmented functions (APW) method and linearized augmented plane wave (LAPW) [55, 56], which treat the mixed basis sets as two parts: the non-overlapping atomic spheres and the interstitial region between the atomic spheres.

In the interstitial region, with the weakly varying potentials, the basis is expanded as a sum of plane waves with the reciprocal lattice vectors **G**, and wave vector **k** inside the first Brillouin zone:

$$\phi_{\mathbf{k}}^{\mathbf{G}}(\mathbf{r}) = \frac{1}{\sqrt{V}} e^{i(\mathbf{k}+\mathbf{G})\cdot\mathbf{r}}. \tag{3.19}$$

The atomic region where the potential is similar to a single atom, the APW basis employs

$$\phi_{\mathbf{k}}^{\mathbf{G}}(\mathbf{r}) = \sum_{l,m} \left[A_{l,m}^{\alpha,\mathbf{k}+\mathbf{G}} u_l^{\alpha}(r, E_{1,l}^{\alpha}) \right] Y_{l,m}(\theta,\varphi), \tag{3.20}$$

where $u_l^{\alpha}(r, E_{1,l}^{\alpha})$ is the solution of the radial Schrödinger equation for the energy $E_{1,l}^{\alpha}$ and the spherical potential inside the sphere. The coefficients $A_{lm}^{\alpha,\mathbf{k}+\mathbf{G}}$ are found by requiring that the basis functions in the atomic region matches each plane wave in the interstitial region. An improvement on this basis is to add a linearization term with the derivative $\dot{u}_l^{\alpha}(r, E_{1l}^{\alpha})$ to produce the LAPW basis

$$\phi_{\mathbf{k}}^{\mathbf{G}}(\mathbf{r}) = \sum_{l,m} \left[A_{l,m}^{\alpha,\mathbf{k}+\mathbf{G}} u_l^{\alpha}(r, E_{1,l}^{\alpha}) + B_{l,m}^{\alpha,\mathbf{k}+\mathbf{G}} \dot{u}_l^{\alpha}(r, E_{1,l}^{\alpha}) \right] Y_{l,m}(\theta,\varphi). \tag{3.21}$$

In the atomic sphere, the core states, not participating in the chemical bonding, are well treated. Local orbitals (LO) are added to the LAPW basis to treat semicore and valence states in one energy window:

$$\phi_{l,m}^{\alpha,LO}(\mathbf{r}) = \left[A_{l,m}^{\alpha,LO} u_l^{\alpha}(r, E_{1,l}^{\alpha}) + B_{l,m}^{\alpha,LO} \dot{u}_l^{\alpha}(r, E_{1,l}^{\alpha}) + C_{lm}^{\alpha,LO} u_l^{\alpha}(r, E_{2,l}^{\alpha}) \right] Y_{l,m}(\theta,\varphi). \tag{3.22}$$

The third term with the energy $E_{1,l}^{\alpha} \neq E_{2l}^{\alpha}$, represents the semicore states for the atom α with angular momentum quantum number l. The coefficients are obtained by considering the normalization and zero value and slope at the sphere boundary for $\phi_{lm,\alpha}^{LO}(\mathbf{r})$. A further improvement of APW is the APW+*lo* basis, which also has a linearization term:

$$\phi_{l,m}^{\alpha,lo}(\mathbf{r}) = \left[A_{l,m}^{\alpha,lo} u_l^{\alpha}(r, E_{1,l}^{\alpha}) + B_{l,m}^{\alpha,lo} \dot{u}_l^{\alpha}(r, E_{1,l}^{\alpha}) \right] Y_{l,m}(\theta,\varphi). \tag{3.23}$$

Different from the LAPW method, the coefficients $A_{l,m}^{\alpha,lo}$, $B_{l,m}^{\alpha,lo}$ do not depend on the **k** and **G** vector. Similar to LAPW+LO, APW+*lo* can also add an additional LO term at different energy to simultaneously investigate semicore and valence states:

$$\phi_{l,m}^{\alpha,LO}(\mathbf{r}) = \left[A_{l,m}^{\alpha,LO} u_l^{\alpha}(r, E_{1,l}^{\alpha}) + B_{l,m}^{\alpha,LO} \dot{u}_l^{\alpha}(r, E_{2,l}^{\alpha}) \right] Y_{l,m}(\theta,\varphi) \ . \tag{3.24}$$

In our calculation with the code WIEN2k [57], the LAPW or APW+*lo* basis is used for different atoms or different l values for the same atom. The APW+*lo* is used for the orbitals converging slowly or atoms with small sphere size. The $R_{mt}K_{max}$ ($\mathrm{RK_{max}}$) controls the convergence of the basis set with R_{mt} being the smallest atomic sphere radius, and $K_{\max}$ the magnitude of the largest **G** vector.

3.1.2 Extensions of DFT for spin-orbit coupling

The effects of spin-orbit coupling are important for the systems studied in this thesis. This section discusses the implementation of the SO interaction in DFT. For the interstitial region, the relativistic correction is not considered since the electron velocity is limited by the cut off in **k**-space $K_{\max}$. While for the atomic region, with the increase of the atomic number, the relativistic effects arise as described in Chapter 1:

$$\hat{H}_{SO} = \lambda \mathbf{L} \cdot \mathbf{S}. \tag{3.25}$$

An approximation used by various implementations of DFT (like WIEN2k, VASP, Elk *etc.*) to treat the spin-orbit coupling is the second variational method [58]. This method has two steps:

- First is to solve the non-relativistic spin up and spin down equation and obtain the eigenvalues and eigenfunctions separately, $\psi^{\uparrow}_{n\mathbf{k}}$, $E^{\uparrow}_{n\mathbf{k}}$, $\psi^{\downarrow}_{n\mathbf{k}}$, $E^{\downarrow}_{n\mathbf{k}}$.
- Within the above basis, the total Hamiltonian with spin-orbit coupling is calculated and diagonalized.

3.1.3 LDA+U

In addition to spin-orbit coupling, the on-site Coulomb interaction between two localized electrons is strong in the systems studied in this thesis. LDA can not capture this effect well. To overcome this problem, LDA is modified by adding an orbital-dependent correction (LDA+U) [59]. This method divides the electrons into two parts: the delocalized s and p electrons are described by one-electron potential (LDA), while the localized d or f electrons are described including the Coulomb $d-d$ interaction in a mean-field way (LDA+U). We use the Self-interaction corrected (SIC) method [60] in our calculations:

$$\begin{aligned} E =& E_{\mathrm{LDA}} - [UN(N-1)/2 - JN(N-2)/4] \\ &+ \frac{1}{2} \sum_{m,m',\sigma} U_{mm'} n_{m\sigma} n_{m'-\sigma} \\ &+ \frac{1}{2} \sum_{\substack{m,m',\sigma \\ m \neq m'}} (U_{mm'} - J_{mm'}) n_{m\sigma} n_{m'\sigma}, \end{aligned} \tag{3.26}$$

where N is the number of d electrons. The second term is the Coulomb energy of $d-d$ interactions as a function of N given by the LDA which is subtracted from the LDA energy. A Hubbard like term is then added to the total energy.

3.2 Extraction of hopping integrals from DFT

Following Ref. [29, 61], we first construct the projectors from the LAPW basis to Wannier basis, then extract the hopping parameters from the band structure and the projectors. In solids, the single particle wave functions can be described using Bloch states [53]:

$$\hat{H}\,|\psi^{\sigma}_{\mathbf{k}\nu}\rangle = \varepsilon^{\sigma}_{\mathbf{k}\nu}\,|\psi^{\sigma}_{\mathbf{k}\nu}\rangle\,. \tag{3.27}$$

The corresponding Wannier function is defined by

$$|w^{\sigma}_{\mathbf{R}\nu}\rangle = \frac{V}{(2\pi)^3}\int_{1.BZ} d\mathbf{k}\, e^{-i\mathbf{k}\cdot\mathbf{R}}\,|\psi^{\sigma}_{\mathbf{k}\nu}\rangle\,. \tag{3.28}$$

We choose the localized trial orbitals $\widetilde{\chi}$ and project the Bloch function on them [61]:

$$\left|\widetilde{\chi}^{\alpha,\sigma}_{\mathbf{k}m}\right\rangle = \sum_{\nu\in W}|\psi^{\sigma}_{\mathbf{k}\nu}\rangle\left\langle\psi^{\sigma}_{\mathbf{k}\nu}|\chi^{\alpha,\sigma}_{\mathbf{k}m}\right\rangle. \tag{3.29}$$

The bands ν are all in the energy window W

$$\widetilde{P}^{\alpha,\sigma}_{m\nu}(\mathbf{k}) = \left\langle\psi^{\sigma}_{\mathbf{k}\nu}|\chi^{\alpha,\sigma}_{\mathbf{k}m}\right\rangle. \tag{3.30}$$

The Wannier function is:

$$\left|w^{\alpha,\sigma}_{\mathbf{k}m}\right\rangle = \sum_{\nu\in W}|\psi^{\sigma}_{\mathbf{k}\nu}\rangle\sum_{n.\beta}\frac{\widetilde{P}^{\beta,\sigma}_{n\nu}(\mathbf{k})}{\sqrt{O(\mathbf{k},\sigma)^{\alpha\beta}_{mn}}}, \tag{3.31}$$

where $O(\mathbf{k})^{\alpha\beta}_{mn}$ is for orthonormalizing the basis

$$O(\mathbf{k},\sigma)^{\alpha\beta}_{mn} = \sum_{\nu\in W}\widetilde{P}^{*\alpha,\sigma}_{m\nu}(\mathbf{k})\widetilde{P}^{\beta,\sigma}_{\nu n}(\mathbf{k}). \tag{3.32}$$

Then, it is diagonalized[1], yielding eigenvalues O_i. $\frac{1}{\sqrt{O}}$ is constructed from the diagonal matrix D_{ij},

$$(D_{ij}) = (\frac{\delta_{ij}}{\sqrt{O_i}}), \tag{3.33}$$

[1] for each $(\mathbf{k},\sigma)$, so this dependency is dropped here.

using

$$\frac{1}{\sqrt{O}} = UDU^{\dagger}, \tag{3.34}$$

where U is the matrix of eigenvectors of O, and $U^{\dagger}$ is its Hermitian conjugate. The projector that maps the Bloch function to Wannier function is

$$P_{n\nu}^{\alpha,\sigma}(\mathbf{k}) = \sum_{n.\beta} \frac{\widetilde{P}_{n\nu}^{\beta,\sigma}(\mathbf{k})}{\sqrt{O(\mathbf{k},\sigma)_{mn}^{\alpha\beta}}}. \tag{3.35}$$

In WIEN2k, the Bloch state in LAPW/APW+lo (+LO) basis in the atomic part is:

$$\begin{aligned}\psi_{\mathbf{k},\nu}^{\sigma}(\mathbf{r}) = &\sum_{l,m}[A_{l,m}^{\nu,\alpha}(\mathbf{k})u_l^{\alpha,\sigma}(\mathbf{r},E_{1,l}^{\alpha}) + B_{l,m}^{\nu,\alpha}(\mathbf{k})\dot{u}_l^{\alpha,\sigma}(\mathbf{r},E_{1,l}^{\alpha}) \\ &+ C_{lm}^{\nu,\alpha}(\mathbf{k})u_l^{\alpha,\sigma}(\mathbf{r},E_{2,l}^{\alpha})]Y_{l,m}(\theta,\varphi).\end{aligned} \tag{3.36}$$

We choose the localized trial orbitals

$$|\chi_m^{\alpha,\sigma}\rangle = \left|u_l^{\alpha,\sigma}(E_{1,l}^{\alpha})Y_{lm}\right\rangle. \tag{3.37}$$

The projectors are

$$\begin{aligned}\widetilde{P}_{m\nu}^{\alpha,\sigma}(\mathbf{k}) = &\left\langle \psi_{\mathbf{k}\nu}|u_l^{\alpha,\sigma}(E_{1l}^{\alpha})Y_{lm}\right\rangle \\ = &A_{lm}^{\nu,\alpha}(\mathbf{k},\sigma) + C_{lm}^{\nu,\alpha}(\mathbf{k},\sigma)\widetilde{O}(\mathbf{k})_{lm,l'm'},\end{aligned} \tag{3.38}$$

with

$$\left\langle u_l^{\alpha,\sigma}(E_{1,l}^{\alpha})Y_{l,m}|u_l^{\alpha,\sigma}(E_{1,l'}^{\alpha})Y_{l,'m'}\right\rangle = \delta_{ll',mm',\alpha\alpha'}, \tag{3.39}$$

$$\left\langle u_l^{\alpha,\sigma}(E_{1,l}^{\alpha})Y_{l,m}|\dot{u}_l^{\alpha',\sigma}(E_{1,l'}^{\alpha})Y_{l,'m'}\right\rangle = 0, \tag{3.40}$$

$$\left\langle u_l^{\alpha,\sigma}(E_{1,l}^{\alpha})Y_{l,m}|u_l^{\alpha,\sigma}(E_{2,l'}^{\alpha})Y_{l,'m'}\right\rangle = \widetilde{O}(\mathbf{k})_{lm,l'm'}. \tag{3.41}$$

The projectors $\tilde{P}_{m\nu}^{\alpha,\sigma}(\mathbf{k})$ are obtained in terms of quantum numbers m (*e.g.*, $m = -2,-1,0,1,2$ for $l=2$) in the global cartesian coordinates. After transforming the projectors $\tilde{P}_{m\nu}^{\alpha,\sigma}(\mathbf{k})$ to the irreducible representation orbitals by the transformation matrix R and rotating the direction to the local coordinates with the matrix S, we can obtain the projectors from the Bloch basis to the local orbital Wannier basis ($d_{3z^2-r^2}$, $d_{x^2-y^2}$, d_{xy}, d_{xz}, d_{yz})

$$\tilde{P'}_{m\nu}^{\alpha,\sigma}(\mathbf{k}) = \sum_{m'} U_{mm'}\tilde{P}_{m'\nu}^{\alpha,\sigma}(\mathbf{k}), \tag{3.42}$$

where the unitary transformation $U_{mm'}$ is

$$U_{mm'} = \sum_{p} S_{mp}R_{pm'}. \tag{3.43}$$

For instance, for d-orbitals,

$$S = \begin{pmatrix} 0 & 0 & 1 & 0 & 0 \\ \frac{1}{\sqrt{2}} & 0 & 0 & 0 & \frac{1}{\sqrt{2}} \\ \frac{i}{\sqrt{2}} & 0 & 0 & 0 & -\frac{i}{\sqrt{2}} \\ 0 & \frac{1}{\sqrt{2}} & 0 & -\frac{1}{\sqrt{2}} & 0 \\ 0 & \frac{i}{\sqrt{2}} & 0 & \frac{i}{\sqrt{2}} & 0 \end{pmatrix}. \tag{3.44}$$

With the constructed projectors and the eigenvalues, we can determine the TB model parameters, including the hopping integrals t_{ij} and onsite energies μ_i. The Wannier functions are obtained from the projector and the Bloch function with the translational vector $\mathbf{R}$

$$\begin{aligned} w_m^{\alpha,\sigma}(\mathbf{r}-\mathbf{R}) &= \sum_{\mathbf{k}} e^{-i\mathbf{k}\cdot\mathbf{R}} \sum_{\nu\in W} P_{m\nu}^{\alpha,\sigma}(\mathbf{k})\, \phi_{\mathbf{k}\nu}^{\sigma}(\mathbf{r}), \\ &= \sum_{\mathbf{k}} e^{-i\mathbf{k}\cdot\mathbf{R}}\, w_{\mathbf{k}m}^{\alpha,\sigma}(\mathbf{r}). \end{aligned}$$

The energy window W is set to be the energy window including the bands ν considered in the systems. The method can only be used for the number of bands equal to the number of correlated orbitals $N_\nu = N_M$. The kinetic energy matrix operator $\hat{T}$ is diagonal in the basis of $\phi_{\mathbf{k}\nu}^{\sigma}(\mathbf{r})$

$$\begin{aligned} &\begin{pmatrix} \phi_{\mathbf{k},1}^{\sigma *}(\mathbf{r}) & \phi_{\mathbf{k},2}^{\sigma *}(\mathbf{r}) & \cdots & \phi_{\mathbf{k},N_\nu}^{\sigma *}(\mathbf{r}) \end{pmatrix} \hat{T} \begin{pmatrix} \phi_{\mathbf{k},1}^{\sigma}(\mathbf{r}) \\ \phi_{\mathbf{k},2}^{\sigma}(\mathbf{r}) \\ \vdots \\ \phi_{\mathbf{k},N_\nu}^{\sigma}(\mathbf{r}) \end{pmatrix} \\ &= \begin{pmatrix} \varepsilon_1^{\sigma}(\mathbf{k}) & 0 & \cdots & 0 \\ 0 & \varepsilon_2^{\sigma}(\mathbf{k}) & \cdots & 0 \\ \vdots & \vdots & \ddots & \\ 0 & 0 & & \varepsilon_{N_\nu}^{\sigma}(\mathbf{k}) \end{pmatrix}, \end{aligned} \tag{3.45}$$

with the transformation:

$$w_{m\mathbf{k}}^{\alpha,\sigma}(\mathbf{r}) = \sum_{\nu\in W} P_{m\nu}^{\alpha,\sigma}(\mathbf{k})\, \phi_{\mathbf{k}\nu}^{\sigma}(\mathbf{r}), \tag{3.46}$$

$$\begin{aligned}
&\begin{pmatrix} w^{\sigma *}_{\mathbf{k},1}(\mathbf{r}) & w^{\sigma *}_{\mathbf{k},2}(\mathbf{r}) & \cdots & w^{\sigma *}_{\mathbf{k},N_M}(\mathbf{r}) \end{pmatrix} \hat{T} \begin{pmatrix} w^{\sigma}_{\mathbf{k},1}(\mathbf{r}) \\ w^{\sigma}_{\mathbf{k},2}(\mathbf{r}) \\ \vdots \\ w^{\sigma}_{\mathbf{k},N_M}(\mathbf{r}) \end{pmatrix} \\
&= \hat{P}^{\sigma\dagger}(\mathbf{k}) \begin{pmatrix} \varepsilon^{\sigma}_1(\mathbf{k}) & 0 & \cdots & 0 \\ 0 & \varepsilon^{\sigma}_2(\mathbf{k}) & \cdots & 0 \\ \vdots & \vdots & \ddots & \\ 0 & 0 & & \varepsilon^{\sigma}_{N_v}(\mathbf{k}) \end{pmatrix} \hat{P}^{\sigma}(\mathbf{k}),
\end{aligned} \tag{3.47}$$

where

$$\hat{P}^{\sigma}(\mathbf{k}) = \begin{pmatrix} P^{\sigma}_{1,1}(\mathbf{k}) & P^{\sigma}_{1,2}(\mathbf{k}) & \cdots & \\ P^{\sigma}_{2,1}(\mathbf{k}) & P^{\sigma}_{2,2}(\mathbf{k}) & \cdots & \\ \vdots & \vdots & \ddots & \\ & & & P^{\sigma}_{N_M,N_v}(\mathbf{k}) \end{pmatrix}. \tag{3.48}$$

After this transformation, we have the overlap matrix

$$\begin{pmatrix} \langle w^{\sigma}_{\mathbf{k},1}|\hat{T}|w^{\sigma}_{\mathbf{k},1}\rangle & \langle w^{\sigma}_{\mathbf{k},1}|\hat{T}|w^{\sigma}_{\mathbf{k},2}\rangle & \cdots & \\ \langle w^{\sigma}_{\mathbf{k},2}|\hat{T}|w^{\sigma}_{\mathbf{k},1}\rangle & \langle w^{\sigma}_{\mathbf{k},2}|\hat{T}|w^{\sigma}_{\mathbf{k},2}\rangle & \cdots & \\ \vdots & \vdots & \ddots & \\ & & & \langle w^{\sigma}_{\mathbf{k},N_M}|\hat{T}|w^{\sigma}_{\mathbf{k},N_M}\rangle \end{pmatrix} \tag{3.49}$$

as a function of $\mathbf{k}$. By Fourier transforming $\langle w^{\sigma}_{\mathbf{k},M}|\hat{T}|w^{\sigma}_{\mathbf{k},M'}\rangle$, one obtains the hopping integrals t_{ij} and onsite energies μ_i as

$$t_{i-\mathbf{r}_i,j-\mathbf{r}_j} = \frac{1}{N_{\mathbf{k}}} \sum_{\mathbf{k}} \langle w^{\sigma}_{\mathbf{k},M_i}|\hat{T}|w^{\sigma}_{\mathbf{k},M_j}\rangle e^{-i\mathbf{k}\cdot(\mathbf{r}_j-\mathbf{r}_i)}, \tag{3.50}$$

$$\mu_i = \frac{1}{N_{\mathbf{k}}} \sum_{\mathbf{k}} \langle w^{\sigma}_{\mathbf{k},M_i}|\hat{T}|w^{\sigma}_{\mathbf{k},M_i}\rangle. \tag{3.51}$$

3.3 Theory of optical conductivity

In the optical experiment, observables like reflectivity, transmission, absorption are measured. From these measurements, the dielectric function $\varepsilon(\omega)$ and optical conductivity $\sigma(\omega)$ are obtained and can be related to the band structure. This section details how to calculate such observables from *ab initio* methods.

3.3.1 Fundamental relations for optical phenomena

The electromagnetic field is described by the Maxwell's equations [41]:

$$\begin{aligned} \nabla \times \mathbf{H} - \frac{1}{c}\frac{\partial \mathbf{D}}{\partial t} &= \frac{4\pi}{c}\mathbf{j}, \\ \nabla \times \mathbf{E} + \frac{1}{c}\frac{\partial \mathbf{B}}{\partial t} &= 0, \\ \nabla \cdot \mathbf{D} &= 0, \\ \nabla \cdot \mathbf{B} &= 0. \end{aligned} \tag{3.52}$$

Here the charge density is zero, $\mathbf{j}$ is the current density, $\mathbf{E},\mathbf{D}$ describe the electric field, $\mathbf{H},\mathbf{B}$ is corresponding to the magnetic field. The first two equations relate the electric field and the magnetic field. Since in the linear materials

$$\mathbf{D} = \varepsilon \mathbf{E}, \tag{3.53}$$

$$\mathbf{j} = \sigma \mathbf{E}, \tag{3.54}$$

$$\mathbf{B} = \mu \mathbf{H}, \tag{3.55}$$

we have

$$\nabla^2 \mathbf{E} = \frac{\varepsilon\mu}{c^2}\frac{\partial^2 \mathbf{E}}{\partial t^2} + \frac{4\pi\sigma\mu}{c^2}\frac{\partial \mathbf{E}}{\partial t}. \tag{3.56}$$

With the form of the solution:

$$\mathbf{E} = \mathbf{E}_0 e^{i(\mathbf{K}\cdot\mathbf{r} - \omega t)}, \tag{3.57}$$

we obtain

$$\mathbf{E}(\mathbf{r},t) = \mathbf{E}_0 e^{-i\omega t} e^{i\frac{\omega \mathbf{r}}{c}\sqrt{\varepsilon\mu}\sqrt{1+\frac{4\pi i\sigma}{\varepsilon\omega}}}. \tag{3.58}$$

We write

$$\mathbf{E}(\mathbf{r},t) = \mathbf{E}_0 e^{-i\omega t} e^{i\frac{\omega \mathbf{r}}{c}\sqrt{\varepsilon_{\text{complex}}\mu}}, \tag{3.59}$$

where

$$\begin{aligned} \varepsilon_{\text{complex}} &= \varepsilon + \frac{4\pi i\sigma}{\omega} \\ &= \frac{4\pi i}{\omega}\left(\frac{\varepsilon\omega}{4\pi i} + \sigma\right). \end{aligned} \tag{3.60}$$

We define the complex conductivity as

$$\sigma_{\text{complex}} = \frac{\varepsilon\omega}{4\pi i} + \sigma, \tag{3.61}$$

and therefore deduce the relation of the complex dielectric function and complex conductivity

$$\varepsilon_{\text{complex}} = \frac{4\pi i}{\omega}\sigma_{\text{complex}}. \tag{3.62}$$

We divide $\sqrt{\varepsilon_{\text{complex}}\mu}$ as the real part $\widetilde{n}(\omega)$ and imaginary part $i\widetilde{k}(\omega)$, and therefore the wavefunction become

$$\mathbf{E}(\mathbf{r},t) = \mathbf{E}_0 e^{-i\omega t} e^{i\frac{\omega \mathbf{r}}{c}\widetilde{n}(\omega)} e^{-\frac{\omega \mathbf{r}}{c}\widetilde{k}(\omega)}. \tag{3.63}$$

The amplitude of the wavefunction exponentially decays in the material over a distance, the optical skin depth $\frac{c}{\omega\widetilde{k}(\omega)}$,which means the intensity of the electric field, $|\mathbf{E}(\mathbf{r},t)|^2$, decrease to 1/e of its value in a distance $\frac{c}{2\omega\widetilde{k}(\omega)}$, connecting to the absorption coefficient by

$$\frac{1}{\alpha_{abs}} = \frac{c}{2\omega\widetilde{k}(\omega)}. \tag{3.64}$$

As we know, light is a transverse wave, thus there are two possible orthogonal directions for $\mathbf{E}$ in the plane normal to the propagation direction. The optical properties, taking optical conductivity as example in cubic materials has the same value in the three transverse directions, while anisotropic media may have different values in the three polarization directions.

For the measurements of the optical properties, the wave inside the solid for the one-dimensional system is:

$$E_x = E_0 e^{-i\omega t} e^{i\frac{\omega z}{c}\widetilde{n}(\omega)} e^{-\frac{\omega z}{c}\widetilde{k}(\omega)}. \tag{3.65}$$

In free space, the electric field including the incident and reflected waves:

$$E_x = E_1 e^{-i\omega t} e^{i\frac{\omega z}{c}} + E_2 e^{-i\omega t} e^{-i\frac{\omega z}{c}}. \tag{3.66}$$

The continuity of the E_x requires

$$E_0 = E_1 + E_2. \tag{3.67}$$

Because of

$$\frac{\partial E_x}{\partial z} = \frac{i\mu\omega}{c} H_y, \tag{3.68}$$

$\frac{\partial E_x}{\partial z}$ also continue at the surface, resulting in

$$E_0(\widetilde{n}(\omega) + i\widetilde{k}(\omega)) = E_1 - E_2. \tag{3.69}$$

The reflection coefficient r and the normal incident reflectivity R are

$$r = \frac{E_2}{E_1} = \frac{1-\widetilde{n}(\omega)-i\widetilde{k}(\omega)}{1+\widetilde{n}(\omega)+i\widetilde{k}(\omega)}, \tag{3.70}$$

$$\begin{aligned} R &= \left|\frac{E_2}{E_1}\right|^2 = \left|\frac{1-\widetilde{n}(\omega)-i\widetilde{k}(\omega)}{1+\widetilde{n}(\omega)+i\widetilde{k}(\omega)}\right|^2 \\ &= \frac{(1-\widetilde{n}(\omega))^2+\widetilde{k}(\omega)^2}{(1+\widetilde{n}(\omega))^2+\widetilde{k}(\omega)^2}. \end{aligned} \tag{3.71}$$

From experiment, the reflectivity can be measured, and the real and imaginary parts of the function are connected by the Kramers-Kronig relation:

$$\mathrm{Re}[\varepsilon(\omega)] - 1 = \frac{2}{\pi}\mathcal{P}\int_0^\infty \frac{\omega' \,\mathrm{Im}[\varepsilon(\omega')]}{\omega'^2-\omega^2} d\omega', \tag{3.72}$$

$$\mathrm{Im}[\varepsilon(\omega)] = -\frac{2}{\pi}\mathcal{P}\int_0^\infty \frac{\omega' \,\mathrm{Re}[\varepsilon(\omega')]}{\omega'^2-\omega^2} d\omega', \tag{3.73}$$

by

$$\mathrm{Re}[\varepsilon(\omega)] = \widetilde{n}^2 - \widetilde{k}^2, \tag{3.74}$$

$$\mathrm{Im}[\varepsilon(\omega)] = 2\widetilde{n}\widetilde{k}. \tag{3.75}$$

The optical constants $\widetilde{n}(\omega)$, $\widetilde{k}(\omega)$ are obtained from the experiment, and therefore the dielectric function and optical conductivity can be given. In the real materials, there are two contributions from different band processes. One is the intraband transitions of the electrons in the conducting materials. Another is the interband transitions of an electron from an occupied valence states below the Fermi level to an unoccupied conduction states in the higher band. The materials we will investigate are insulators, and hence we only consider the contribution of the interband process. This process is a quantum mechanical process and should be considered using the corresponding concepts.

3.3.2 Interband transitions

The optical conductivity for an anisotropic material is defined by:

$$j_\mu(\mathbf{q},\omega) = \sum_\nu \sigma_{\mu\nu}(\mathbf{q},\omega) E_\nu(\mathbf{q},\omega), \tag{3.76}$$

where μ , ν indicate cartesian direction, $\mathbf{q}$, ω denote the wave vector and energy of the photon, respectively. Since photons have a linear dispersion relation $\varepsilon_{\mu\nu}(\mathbf{q})$ =

$c\mathbf{q}$, typical transition energies in solids correspond to very small photon momenta $\mathbf{q}$. Thus we assume the transition is in the long-wavelength limit $\mathbf{q} \to 0$. That means an absorption emission of photons may cause electrons to transition at the same $\mathbf{k}$ point, that is a direct transition. The system can be described by the Hamiltonian

$$\begin{aligned}\hat{H} =& \frac{(\mathbf{p} - \frac{e}{c}\mathbf{A})^2}{2m} + V(\mathbf{r}) \\ =& \frac{\mathbf{p}^2}{2m} + V(\mathbf{r}) - \frac{e}{2mc}(\mathbf{A}\cdot\mathbf{p} + \mathbf{p}\cdot\mathbf{A}) + \frac{e^2A^2}{2mc^2} \\ =& \hat{H}_0 + \hat{H}',\end{aligned} \tag{3.77}$$

where $\hat{H}_0$ is the one-electron Hamiltonian without optical fields, and $\hat{H}'$ is the optical field terms

$$\hat{H}_0 = \frac{\mathbf{p}^2}{2m} + V(\mathbf{r}), \tag{3.78}$$

$$\hat{H}' = -\frac{e}{2mc}(\mathbf{A}\cdot\mathbf{p} + \mathbf{p}\cdot\mathbf{A}) + \frac{e^2A^2}{2mc^2}. \tag{3.79}$$

With $\hat{\mathbf{p}} = \frac{m}{e}\hat{J}$ and the μ direction electric field, the perturbation can be expressed as [62]:

$$\begin{aligned}\hat{H}' =& -\frac{1}{c}\int d^3\mathbf{r}\,\hat{j}_\mu(\mathbf{r})A_\mu(\mathbf{r},t) \\ =& \frac{i}{\omega}\int d^3\mathbf{r}\,\hat{j}_\mu(\mathbf{r})E_\mu(\mathbf{r},t).\end{aligned} \tag{3.80}$$

The current is:

$$J_\mu(\mathbf{r},t) = \frac{e}{V}\sum_{i=1}^{N_e}\left\langle \hat{v}_{i\mu}\right\rangle, \tag{3.81}$$

where V is the volume, $\hat{v}_i$ is the velocity for particle i.

$$\hat{v}_i = \nabla_{p_i}\hat{H} = \frac{1}{m}\sum_{i=1}^{N_e}(\hat{p}_i - \frac{e}{c}A(r_i,t)), \tag{3.82}$$

$$J_\mu(r,t) = \frac{e}{mV}\sum_{i=1}^{N_e}\left\langle \hat{p}_{i\mu}\right\rangle + i\frac{n_0e^2}{m\omega}E_\mu(r,t), \tag{3.83}$$

here n_0 is the particle density. We label the second term as $J_\mu^{(1)}(r,t)$, which is proportional to the electric field. The first term is labelled as $J_\mu^{(2)}(r,t)$. At zero temperature, in Heisenberg representation,

$$J_\mu^{(2)}(\mathbf{r},t) = \left\langle \psi \left| e^{i(\hat{H}_0+\hat{H}')t}\,\hat{j}_\mu(r)e^{-i(\hat{H}_0+\hat{H}')t} \right| \psi \right\rangle, \tag{3.84}$$

where $|\psi\rangle$ is the Schrödinger wave function at t = 0 for the Hamiltonian $\hat{H}_0 + \hat{H}'$

and $|\psi_0\rangle$ is the function for $\hat{H}_0$. The relation is

$$|\psi\rangle = \tilde{T} e^{-i\int_{-\infty}^{0} dt' \hat{H}'(t')} |\psi_0\rangle, \tag{3.85}$$

where $\tilde{T}$ is the time ordering operator. Then we assume

$$U(t) = \tilde{T} e^{-i\int_{0}^{t} dt' \hat{H}'(t')}, \tag{3.86}$$

and transform the operator into the interaction representation

$$\hat{H}'(t) = e^{i\hat{H}_0 t} \hat{H}' e^{-i\hat{H}_0 t}, \tag{3.87}$$

$$\hat{j}_\mu(\mathbf{r},t) = e^{i\hat{H}_0 t} j_\mu(\mathbf{r}) e^{-i\hat{H}_0 t}, \tag{3.88}$$

$$J_\mu^{(2)}(\mathbf{r},t) = \left\langle \psi_0 \left| S^+(t,-\infty) \hat{j}_\mu(\mathbf{r},t) S(t,-\infty) \right| \psi_0 \right\rangle, \tag{3.89}$$

here

$$S(t,-\infty) = \tilde{T} e^{-i\int_{-\infty}^{t} dt' \hat{H}'(t')}. \tag{3.90}$$

For linear response, we only keep up to first order of $\hat{H}'(t')$

$$S(t,-\infty) = T e^{-i\int_{-\infty}^{t} dt' \hat{H}'(t')} = 1 - i\int_{-\infty}^{t} dt' \hat{H}'(t') + O(\hat{H}')^2, \tag{3.91}$$

$$J_\mu^{(2)}(\mathbf{r},t) = \left\langle \psi_0 \left| \hat{j}_\mu(\mathbf{r},t) - i\int_{-\infty}^{t} dt' [\hat{j}_\mu(\mathbf{r},t), \hat{H}'(t')] \right| \psi_0 \right\rangle. \tag{3.92}$$

Without electric field, there is no current, thus

$$\left\langle \psi_0 \left| \hat{j}_\mu(\mathbf{r},t) \right| \psi_0 \right\rangle = 0, \tag{3.93}$$

$$J_\mu^{(2)} = -i \left\langle \psi_0 \left| \int_{-\infty}^{t} dt' [\hat{j}_\mu(\mathbf{r},t), \hat{H}'(t')] \right| \psi_0 \right\rangle, \tag{3.94}$$

$$\hat{H}' = \frac{i}{\omega} \int d^3\mathbf{r} \hat{j}_\nu(\mathbf{r}) E_\nu(\mathbf{r},t), \tag{3.95}$$

$$J_\mu^{(2)} = \frac{1}{\omega V} E_\nu(\mathbf{r},t) e^{-iq\cdot\mathbf{r}} \int_{-\infty}^{t} dt' e^{i\omega(t-t')} \left\langle \psi_0 \left| [\hat{j}_\mu(\mathbf{r},t), \hat{j}_\nu(\mathbf{q},t')] \right| \psi_0 \right\rangle. \tag{3.96}$$

Comparing it to Eq. 3.76 and averaging over the space variable $\mathbf{r}$ we obtain the Kubo formula:

$$\sigma_{\mu\nu}(\omega) = \frac{1}{\omega V} \int_0^\infty dt e^{i\omega t} \left\langle \psi_0 \left| [\hat{j}_\mu(t), \hat{j}_\nu(0)] \right| \psi_0 \right\rangle + i\frac{n_0 e^2}{m\omega} \delta_{\mu\nu}. \tag{3.97}$$

We took E_n, E_m as eigenvalues and $|n\rangle$, $|m\rangle$ as the corresponding eigenstates.

$$\begin{aligned} \left\langle \hat{j}_\mu(t) \hat{j}_\nu(0) \right\rangle &= \frac{1}{\mathrm{Tr} e^{-\beta H}} \mathrm{Tr} e^{-\beta H} \hat{j}_\mu(t) \hat{j}_\nu(0) \\ &= \frac{1}{\mathrm{Tr} e^{-\beta H}} \sum_n \left\langle n | e^{-\beta H} \hat{j}_\mu(t) \hat{j}_\nu(0) | n \right\rangle \\ &= \frac{1}{\mathrm{Tr} e^{-\beta H}} \sum_{nm} \langle n | \hat{j}_\mu | m \rangle \langle m | \hat{j}_\nu | n \rangle e^{-\beta E_n} e^{-\frac{i}{\hbar}(E_n - E_m)t} \end{aligned} \tag{3.98}$$

The definition of the delta function is

$$\delta(\omega) = \frac{1}{2\pi}\int_{-\infty}^{\infty} dt e^{-i\omega t}. \tag{3.99}$$

In the spectral representation, the real part of the optical conductivity is

$$\begin{aligned}\mathrm{Re}\sigma_{\mu\nu}(\omega) =& \frac{\pi(1-e^{-\omega/(k_BT)})}{\omega V \sum_{n'} e^{-E_{n'}\omega/(k_BT)}} \\ & \sum_{nm} e^{-E_n/(k_BT)} \left\langle n \left| \hat{j}_\mu \right| m \right\rangle \left\langle m \left| \hat{j}_\nu \right| n \right\rangle \delta(\omega + E_n - E_m).\end{aligned} \tag{3.100}$$

The current operator is [63]

$$\hat{j}_\mu = \frac{ie}{\hbar} \sum_{i<j,\mu,\nu} (\hat{c}^\dagger_{i\mu}\hat{c}_{j\nu} - \hat{c}^\dagger_{j\nu}\hat{c}_{i\mu}) t^{\mu,\nu}_{i,j} \mathbf{r}^\mu_{ij}, \tag{3.101}$$

where μ and ν denote orbitals, $t^{\mu,\nu}_{i,j}$ label the corresponding hopping parameters and $\mathbf{r}^\mu_{ij}$ indicate the μ component of the vector from site j to site i.

3.3.3 Optical conductivity in LAPW

In the LAPW basis, we calculate the eigenvalues and eigenvectors in k space, and obtain the imaginary part of the interband contribution to the dielectric function given by [64, 65] in the zero temperature as:

$$\begin{aligned}\mathrm{Im}\,\varepsilon_{\mu\nu}(\omega) \propto \frac{1}{\omega^2}\sum_{c,v}\int d\mathbf{k} \langle c_\mathbf{k}|\hat{p}^\mu|v_\mathbf{k}\rangle \langle v_\mathbf{k}|\hat{p}^\nu|c_\mathbf{k}\rangle \\ \times \delta(\varepsilon_{c_\mathbf{k}} - \varepsilon_{v_\mathbf{k}} - \omega).\end{aligned} \tag{3.102}$$

Here, μ and ν indicate directional components, $\hat{p}$ is the momentum operator, and ω corresponds to the energy of the photon. $c_\mathbf{k}$ denotes a state in the conduction band with the energy $\varepsilon_{c_\mathbf{k}}$ and $v_\mathbf{k}$ is a state in the valence band with the energy $\varepsilon_{v_\mathbf{k}}$. By absorbing photon energy, the electrons transit from $v_\mathbf{k}$ to $c_\mathbf{k}$. The real part of the dielectric function can be evaluated from the imaginary part using the Kramers-Kronig relation. In this work we focus on the analysis of the real part of the optical conductivity

$$\mathrm{Re}\,\sigma_{\mu\nu}(\omega) = \frac{\omega}{4\pi}\mathrm{Im}\,\varepsilon_{\mu\nu}(\omega). \tag{3.103}$$

In what follows we will describe how to calculate the momentum matrix element in the LAPW basis. We already described the LAPW basis in section 3.1. The

matrix elements are also analyzed in two parts: the muffin-tin spheres and interstitial region:

$$\left\langle n'\mathbf{k}\left|\hat{p}\right|n\mathbf{k}\right\rangle = \sum_{\mu}\left\langle n'\mathbf{k}\left|\hat{p}\right|n\mathbf{k}\right\rangle_{MT_\mu} + \left\langle n'\mathbf{k}\left|p\right|nk\right\rangle_{I}. \tag{3.104}$$

The function

$$\psi_{n\mathbf{k}}(\mathbf{r}) = \sum_{\mathbf{G}} C_{n\mathbf{k}}(\mathbf{G})\phi_{\mathbf{k}+\mathbf{G}}(\mathbf{r}), \tag{3.105}$$

G indicate the reciprocal lattice vector. In the interstitial region,

$$\phi_{\mathbf{k}+\mathbf{G}}(\mathbf{r}) = \frac{1}{\sqrt{\Omega_c}} e^{i(\mathbf{k}+\mathbf{G})\mathbf{r}}, \tag{3.106}$$

while in the atomic region,

$$\phi_{\mathbf{k}+\mathbf{G}}(S_\alpha+\mathbf{r}) = \sum_{lm}[A^{\alpha}_{lm}(\mathbf{k}+\mathbf{G})u^{\alpha}_{l}(\mathbf{r},E_l) + B^{\alpha}_{lm}(\mathbf{k}+\mathbf{G})\dot{u}^{\alpha}_{l}(\mathbf{r},E_l)]Y_{l,m}, \tag{3.107}$$

For the atomic part, LAPW use spherical harmonics to do the calculation, thus we can only calculate the combination of $\partial_x \pm i\partial_y$ and ∂_z:

$$\begin{aligned}
\Phi^{x+iy}_{\mathbf{k}+\mathbf{G}',\mathbf{k}+\mathbf{G}} &\equiv \left\langle \Phi_{\mathbf{k}+\mathbf{G}'}(S_\alpha+\mathbf{r})\left|\partial_x + i\partial_y\right|\Phi_{\mathbf{k}+\mathbf{G}}(S_\alpha+\mathbf{r})\right\rangle, \\
\Phi^{x-iy}_{\mathbf{k}+\mathbf{G}',\mathbf{k}+\mathbf{G}} &\equiv \left\langle \Phi_{\mathbf{k}+\mathbf{G}'}(S_\alpha+\mathbf{r})\left|\partial_x - i\partial_y\right|\Phi_{\mathbf{k}+\mathbf{G}}(S_\alpha+\mathbf{r})\right\rangle, \\
\Phi^{z}_{\mathbf{k}+\mathbf{G}',\mathbf{k}+\mathbf{G}} &\equiv \left\langle \Phi_{\mathbf{k}+\mathbf{G}'}(S_\alpha+\mathbf{r})\left|\partial_z\right|\Phi_{\mathbf{k}+\mathbf{G}}(S_\alpha+\mathbf{r})\right\rangle.
\end{aligned} \tag{3.108}$$

In spherical coordinates:

$$\begin{aligned}
\partial_x \pm i\partial_y &= \sin\theta e^{\pm i\phi}\frac{\partial}{\partial r} + \frac{1}{r}e^{\pm i\phi}(\cos\theta\frac{\partial}{\partial\theta} \pm \frac{i}{\sin\theta}\frac{\partial}{\partial\phi}), \\
\partial_z &= \cos\theta\frac{\partial}{\partial r} - \frac{1}{r}\sin\theta\frac{\partial}{\partial\theta}.
\end{aligned} \tag{3.109}$$

After evaluating the matrix element of the above operator in the basis, we obtain:

$$\begin{aligned}
\left\langle n'\mathbf{k}\left|\partial_x\right|n\mathbf{k}\right\rangle_{MT_\mu} &= \frac{1}{2}\sum_{\mathbf{G}',\mathbf{G}} C^{*}_{n'\mathbf{k}}(\mathbf{G}')({}^{\mu}\Phi^{x+iy}_{\mathbf{k}+\mathbf{G}',\mathbf{k}+\mathbf{G}} + {}^{\mu}\Phi^{x-iy}_{\mathbf{k}+\mathbf{G}',\mathbf{k}+\mathbf{G}})C_{n\mathbf{k}}(\mathbf{G}), \\
\left\langle n'\mathbf{k}\left|\partial_y\right|n\mathbf{k}\right\rangle_{MT_\mu} &= \frac{1}{2i}\sum_{\mathbf{G}',\mathbf{G}} C^{*}_{n'\mathbf{k}}(\mathbf{G}')({}^{\mu}\Phi^{x+iy}_{\mathbf{k}+\mathbf{G}',\mathbf{k}+\mathbf{G}} - {}^{\mu}\Phi^{x-iy}_{\mathbf{k}+\mathbf{G}',\mathbf{k}+\mathbf{G}})C_{n\mathbf{k}}(\mathbf{G}), \\
\left\langle n'\mathbf{k}\left|\partial_z\right|n\mathbf{k}\right\rangle_{MT_\mu} &= \sum_{\mathbf{G}',\mathbf{G}} C^{*}_{n'\mathbf{k}}(\mathbf{G}')^{\mu}\Phi^{z}_{\mathbf{k}+\mathbf{G}',\mathbf{k}+\mathbf{G}}C_{n\mathbf{k}}(\mathbf{G}).
\end{aligned} \tag{3.110}$$

and in the interstitial region,

$$\left\langle n'\mathbf{k}\left|\nabla\right|n\mathbf{k}\right\rangle_{I} = \frac{1}{\Omega_c}\sum_{\mathbf{G}',\mathbf{G}}(\mathbf{k}+\mathbf{G})C^{*}_{n'\mathbf{k}}(\mathbf{G}')C_{n\mathbf{k}}(\mathbf{G})\int_{I} e^{i(\mathbf{G}'-\mathbf{G}\cdot\mathbf{r})}d\mathbf{r}. \tag{3.111}$$

3.3.4 Optical conductivity from exact diagonalization method

Hubbard model for finite cluster was written and diagonalized. Then the eigenstates were transformed to relativistic basis to construct states n and m in Eq. (3.101). Finally, real part of the optical conductivity for finite clusters can be calculated using Eq. (3.100).

3.4 Summary

In summary, in this chapter, an overview of describing the electronic properties were given. We started from the density functional theory and discussed the extensions of it when including spin-orbit coupling with second-variational method and Coulomb repulsion using the mean-field approach. All procedures are summarized in Figure 3.1, showing the DFT cycle.

This method is typically applicable for describing the electronic properties of weakly correlated materials, and magnetic insulators deep in the ordered state. However, DFT neglects some aspects of dynamical correlations, which can be important for describing correlated materials. Therefore, one may gain further insight by exactly diagonalizing small clusters using model Hubbard Hamiltonians. In order to parameterize such models, we described how to estimate hopping integrals from the projectors projecting the eigenstates of DFT calculations from the LAPW basis to the Wannier basis.

Finally, we introduced the fundamental relations for optical phenomena and the spectral representation formula of optical conductivity for interband transitions in the linear response theory. The calculation details in the LAPW basis were also discussed. For simplification, we will use $\sigma(\omega)$ to represent the real part of the optical conductivity in this thesis.

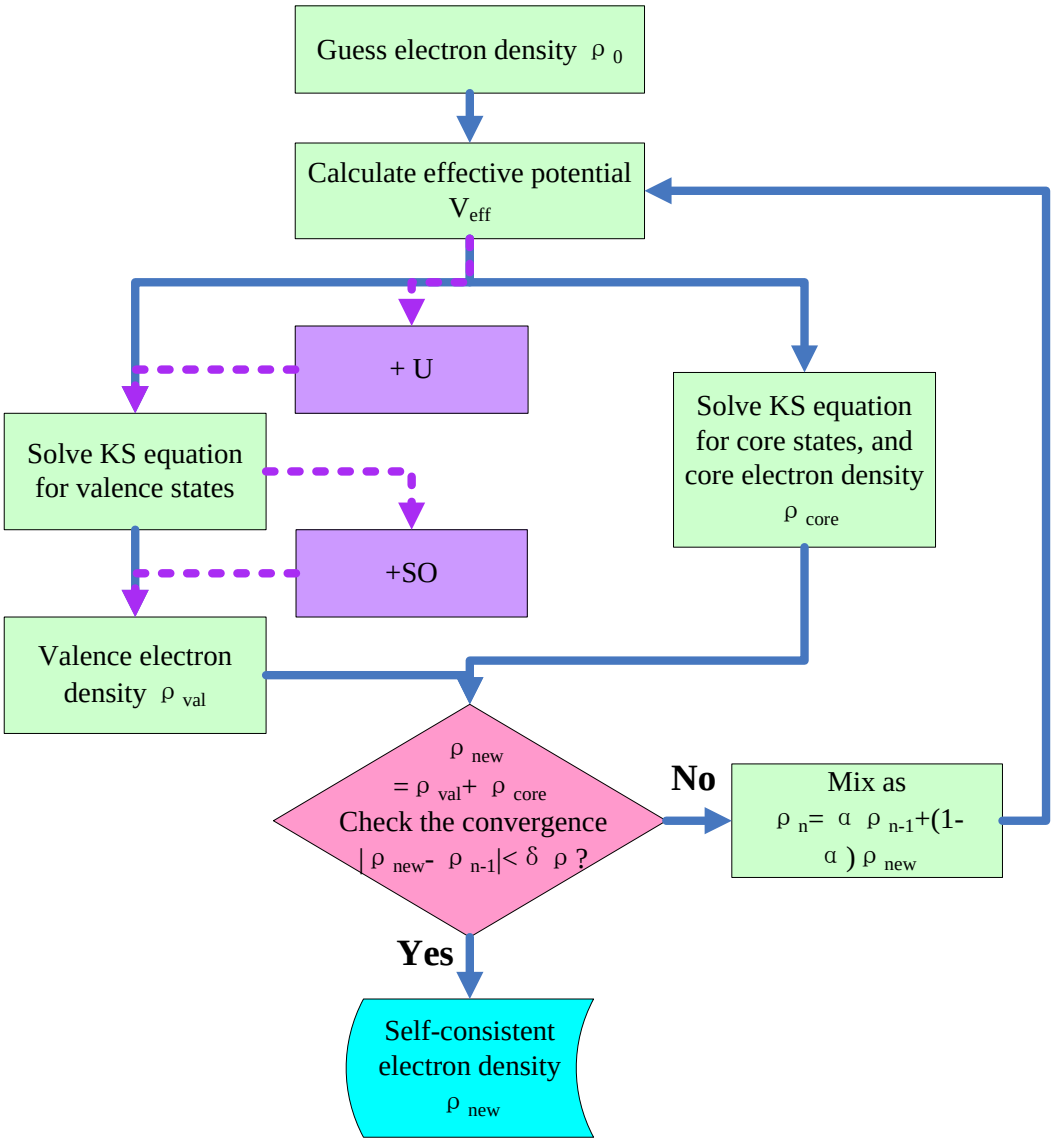

Figure 3.1: DFT cycle.

Chapter 4

Methods for magnetic properties

In this chapter, we will introduce the perturbative and nonperturbative to construct the effective spin models. In particular, we focus on magnetic interactions between local $J = 1/2$ magnetic moments in the presence of strong spin-orbit coupling, which is relevant for the materials Na_2IrO_3, α-Li_2IrO_3, α-$RuCl_3$ that are the focus of this thesis. We will therefore start by introducing the relativistic local basis to describe such strongly spin-orbitally coupled moments. Then the effective magnetic Hamiltonians from second order perturbation theory expressions exact in U, J_H, and λ will be discussed. Further, we introduce nonperturbative exact diagonalization (ED) techniques to estimate higher order corrections and long range interactions up to third neighbors. These methods are relevant to Chapter 8.

4.1 Effective magnetic Hamiltonians from perturbation theory

4.1.1 From the single-band Hubbard model to Heisenberg model

We first demonstrate how to derive magnetic interactions for the simple case of a one-band model without spin-orbit coupling. The one-band Hubbard Hamiltonian

can be written as:

$$\hat{H} = -t \sum_{\langle i\, j\rangle\sigma} (\hat{c}^{+}_{i\sigma}\hat{c}_{j\sigma} + h.c.) + U \sum_{i} \hat{n}_{i\uparrow}\hat{n}_{i\downarrow}, \tag{4.1}$$

where the first term is the kinetic term and the second term is the Coulomb interaction of the electrons with opposite spin on the same site. Indices i and j represent lattice sites, while σ is the spin index. The operator $\hat{c}^{+}_{i\sigma}(\hat{c}_{i\sigma})$ creates (destroys) an electron of spin σ on site i. The operator $\hat{n}_{i\sigma}$ is defined by

$$\hat{n}_{i\sigma} = \hat{c}^{+}_{i\sigma}\hat{c}_{i\sigma}, \tag{4.2}$$

and counts the number of electrons of spin σ on site i. In the limit $U \gg t$, $\sum_{\sigma} \langle n_{i\sigma}\rangle \sim 1$, there is approximately one electron at each site. In this case, we may divide the Hamiltonian into

$$\hat{H} = \hat{H}_0 + \hat{H}_1, \tag{4.3}$$

where the unperturbed Hamiltonian $\hat{H}_0$ is given by

$$\hat{H}_0 = U \sum_{i} \hat{n}_{i\uparrow}\hat{n}_{i\downarrow}, \tag{4.4}$$

and the perturbation is

$$\hat{H}_1 = -t \sum_{\langle i\, j\rangle\sigma} (\hat{c}^{+}_{i\sigma}\hat{c}_{j\sigma} + h.c.). \tag{4.5}$$

The effective Hamiltonian to second order in H_1 is

$$\hat{H}_{\text{eff}} = -\hat{P}\frac{\hat{H}_1(1-\hat{P})\hat{H}_1}{\hat{H}_0 - E^{(0)}}\hat{P}, \tag{4.6}$$

where the operator $\hat{P}$ projects on the ground state manifold

$$|\alpha_1\sigma_1, \cdots, \alpha_N\sigma_N\rangle\,. \tag{4.7}$$

$$\begin{aligned}\hat{H}_{\text{eff}} &= -t^2 \sum_{\langle i\, j\rangle} \hat{P}\frac{(\hat{c}^{+}_{i\uparrow}\hat{c}_{j\uparrow} + \hat{c}^{+}_{i\downarrow}\hat{c}_{j\downarrow})(1-\hat{P})(\hat{c}^{+}_{j\uparrow}\hat{c}_{i\uparrow} + \hat{c}^{+}_{j\downarrow}\hat{c}_{i\downarrow})}{E^{(0)}_{p} - E^{(0)}_{0}}\hat{P} \\ &= \frac{2t^2}{U} \sum_{\langle i\, j\rangle\sigma} (\hat{c}^{+}_{i\sigma}\hat{c}_{i\sigma}\hat{c}^{+}_{j-\sigma}\hat{c}_{j-\sigma} - \hat{c}^{+}_{i\sigma}\hat{c}_{i-\sigma}\hat{c}^{+}_{j-\sigma}\hat{c}_{j\sigma}).\end{aligned} \tag{4.8}$$

The spin operators $\hat{\mathbf{S}}_{\mathbf{i}}$ have three components $\hat{S}^{x}_{i}, \hat{S}^{y}_{i}, \hat{S}^{z}_{i}$. The relations between the spin operator and creation and annihilation operator are given by

$$\begin{aligned}\hat{S}^{z}_{i} &= \frac{1}{2}(\hat{c}^{+}_{i\uparrow}\hat{c}_{i\uparrow} - \hat{c}^{+}_{i\downarrow}\hat{c}_{i\downarrow}) \\ \hat{S}^{+}_{i} &= \hat{S}^{x}_{i} + i\hat{S}^{y}_{i} = \hat{c}^{+}_{i\uparrow}\hat{c}_{i\downarrow} \\ \hat{S}^{-}_{i} &= \hat{S}^{x}_{i} - i\hat{S}^{y}_{i} = \hat{c}^{+}_{i\downarrow}\hat{c}_{i\uparrow}.\end{aligned} \tag{4.9}$$

With these relations, $\hat{H}_{\text{eff}}$ becomes

$$\begin{aligned}\hat{H}_{\text{eff}} &= \frac{2t^2}{U}\sum_{\langle i\ j\rangle}(\frac{1}{2} - 2\hat{S}_i^z\hat{S}_j^z - \hat{S}_i^+\hat{S}_j^- - \hat{S}_i^-\hat{S}_j^+) \\ &= -\frac{2t^2}{U}\sum_{\langle i\ j\rangle}(2\hat{\mathbf{S}}_\mathbf{i}\cdot\hat{\mathbf{S}}_\mathbf{j} - \frac{1}{2}).\end{aligned} \tag{4.10}$$

This final effective Hamiltonian is the Heisenberg interaction.

4.1.2 From the multi-band Hubbard model to the Heisenberg - Kitaev model

We follow the derivation from Ref. [7], which was the first to point out the possibility of realizing Kitaev interactions in edge-sharing d^5 materials with strong spin orbit coupling. This derivation is presented for historical purpose, as it yields expressions that are only approximate, exact results up to $\mathcal{O}(t^2)$ are given in the next section, following our derivation. The model considered is a three-orbital variant of the Hubbard model with the intra-atomic exchange taken into account. We write the Hamiltonian for the t_{2g} electrons in the form of Eq. 1.3. The second order perturbation theory is used to derive the effective Hamiltonian. The unperturbed Hamiltonian $\hat{H}_0$ is chosen to be

$$\begin{aligned}\hat{H}_0 = &\sum_{\substack{j,\sigma,\sigma'\\ m,m'}}\frac{U_{mm'}}{2}\hat{n}_{jm\sigma}\hat{n}_{jm'\sigma'}(1-\delta_{mm'}\delta_{\sigma\sigma'}) - \frac{J_H}{2}\sum_{\substack{j,\sigma,\sigma'\\ m,m'}}\hat{c}^+_{jm\sigma}\hat{c}_{jm\sigma'}\hat{c}^+_{jm'\sigma'}\hat{c}_{jm'\sigma}(1-\delta_{mm'}) \\ &+ \frac{J_H}{2}\sum_{\substack{j,\sigma,\sigma'\\ m,m'}}\hat{c}^+_{jm\sigma}\hat{c}^+_{jm\sigma'}\hat{c}_{jm'\sigma'}\hat{c}_{jm'\sigma}(1-\delta_{mm'})(1-\delta_{\sigma\sigma'}),\end{aligned} \tag{4.11}$$

and the perturbation is

$$\hat{H}_1 = -\sum_{\substack{\langle i,j\rangle\\ m,m',\sigma}}(t_{ij}^{mm'}\hat{c}^+_{im\sigma}\hat{c}_{jm'\sigma} + h.c.). \tag{4.12}$$

We use $U_{mm} = U$, and $U_{mm'} = U - 2J_H$ $(m \neq m')$ to diagonalize the above Hamiltonian and obtain the eigenvalues and eigenvectors:

$$\begin{aligned}
-3J_H + U: \quad & |yz\uparrow xz\uparrow\rangle,\ |yz\downarrow xz\downarrow\rangle,\ |xy\uparrow yz\uparrow\rangle, \\
& |xy\downarrow yz\downarrow\rangle, |xz\uparrow xy\uparrow\rangle, |xz\downarrow xy\downarrow\rangle, \\
& |yz\uparrow xz\downarrow\rangle + |xz\uparrow yz\downarrow\rangle, |xy\uparrow yz\downarrow\rangle + |yz\uparrow xy\downarrow\rangle, \\
& |xz\uparrow xy\downarrow\rangle + |xy\uparrow xz\downarrow\rangle; \\
-J_H + U: \quad & -|yz\uparrow xz\downarrow\rangle + |xz\uparrow yz\downarrow\rangle, -|xy\uparrow yz\downarrow\rangle + |yz\uparrow xy\downarrow\rangle, \\
& -|xz\uparrow xy\downarrow\rangle + |xy\uparrow xz\downarrow\rangle, \\
& |xy\uparrow\downarrow\rangle - |yz\uparrow\downarrow\rangle, |xz\uparrow\downarrow\rangle - |yz\uparrow\downarrow\rangle; \\
2J_H + U: \quad & |yz\uparrow\downarrow\rangle + |xz\uparrow\downarrow\rangle + |xy\uparrow\downarrow\rangle.
\end{aligned} \tag{4.13}$$

In the second order perturbation theory,

$$\hat{H}_{\text{eff}} = -\hat{P}\hat{H}_1 \frac{1-\hat{P}}{\hat{H}_0 - E_0}\hat{H}_1\hat{P}, \tag{4.14}$$

The effective interaction is written as

$$\begin{aligned}
\hat{H}_{\text{eff}} &= -\hat{P} \sum_{\substack{\langle i,j\rangle \\ m,m',\sigma}} (t_{ij}^{mm'} \hat{c}^{+}_{im\sigma}\hat{c}_{jm'\sigma} + h.c.) \frac{(1-\hat{P})}{\hat{H}_0 - E_0} \sum_{\substack{\langle i,j\rangle \\ m,m',\sigma}} (t_{ij}^{mm'} \hat{c}^{+}_{im\sigma}\hat{c}_{jm'\sigma} + h.c.)\hat{P} \\
&= \sum_{\langle i,j\rangle} \hat{H}_{\text{eff}}^{<i,j>},
\end{aligned} \tag{4.15}$$

where

$$\hat{H}_{\text{eff}}^{<i,j>} = -\hat{P} \sum_{\substack{m_1,m_2, \\ m_3,m_4, \\ \sigma,\eta}} (t_{ij}^{m_1m_2} \hat{c}^{+}_{im_1\sigma}\hat{c}_{jm_2\sigma} + h.c.) \frac{(1-\hat{P})}{\hat{H}_0 - E_0} (t_{ij}^{m_3m_4} \hat{c}^{+}_{jm_3\eta}\hat{c}_{im_4\eta} + h.c.)\hat{P}. \tag{4.16}$$

We consider two kinds of bonding geometries shown in Fig. 4.1. For z direction of the 180° bond structure (see Fig. 4.1 (a)), the hopping parameter $t_{ij}^{yz,yz} = t_{ij}^{xz,xz} = t$, $t_{ij}^{yz,xz} = t_{ij}^{yz,xy} = t_{ij}^{xz,xy} = 0, t^{xy,xy} = 0$. Substituting the hopping parameter, we obtain

$$\hat{H}_{\text{eff}}^{<i,j>(z)} = -t^2 \hat{P}_{ij} \sum_{m,m',\sigma,\eta} (\hat{c}^{+}_{im\sigma}\hat{c}_{jm\sigma} + h.c.) \frac{(1-\hat{P})_{ij}}{\hat{H}_0 - E_0} (\hat{c}^{+}_{jm'\eta}\hat{c}_{im'\eta} + h.c.)\hat{P}_{ij} \tag{4.17}$$

with $m, m' = d_{xz}, d_{yz}$. We introduce

$$\begin{aligned}
& \hat{c}^{+}_{im\uparrow}\hat{c}_{im'\uparrow} \to (\hat{c}^{+}_{im}\hat{c}_{im'})(\frac{1}{2} + \hat{S}^z_i),\ \ \hat{c}^{+}_{im\downarrow}\hat{c}_{im'\downarrow} \to (\hat{c}^{+}_{im}\hat{c}_{im'})(\frac{1}{2} - \hat{S}^z_i), \\
& \hat{c}^{+}_{im\uparrow}\hat{c}_{im'\downarrow} \to (\hat{c}^{+}_{im}\hat{c}_{im'})\hat{S}^{+}_i,\ \hat{c}^{+}_{im\downarrow}\hat{c}_{im'\uparrow} \to (\hat{c}^{+}_{im}\hat{c}_{im'})\hat{S}^{-}_i,
\end{aligned} \tag{4.18}$$

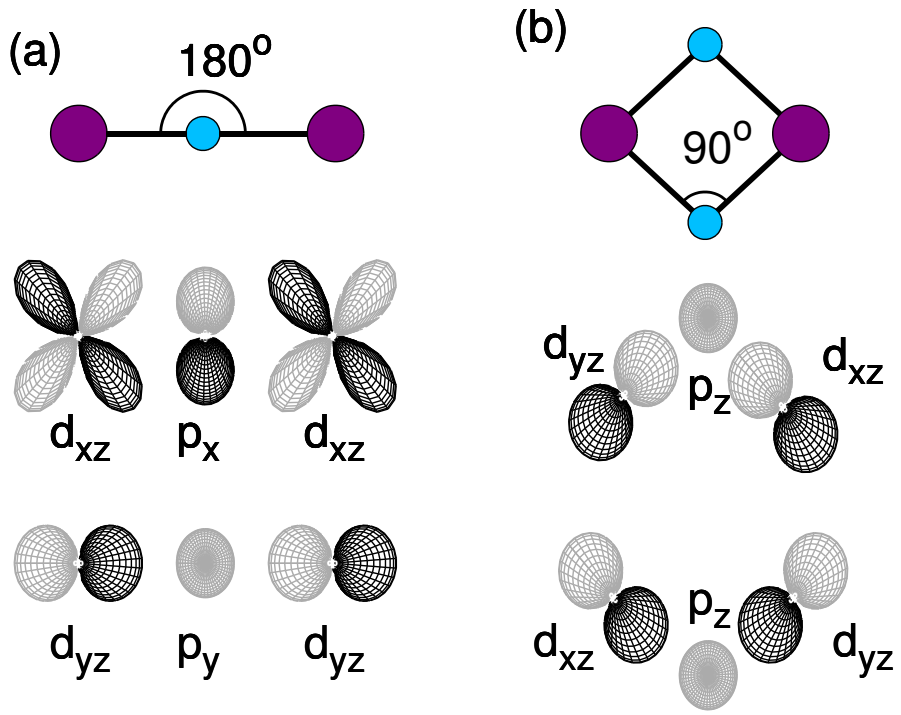

Figure 4.1: Two possible geometries of bond with corresponding orbitals active along these bonds. The large (small) circles are the transition metal (ligand) ions. (a) A 180°-bond and (b) a 90°-bond.

which is similar as the notation defined by Kugel and Khomskii in Ref. [66]. For 180° bond structure along z direction, the effective Hamiltonian is then:

$$
\begin{aligned}
H_{\text{eff}}^{(z)} =& \frac{2t^2}{U-3J_H}(\hat{\mathbf{S}}_\mathbf{i}\cdot\hat{\mathbf{S}}_\mathbf{j}+\frac{3}{4})[\hat{n}_{i,yz}\hat{n}_{j,yz}+\hat{n}_{i,xz}\hat{n}_{j,xz}+\hat{c}^+_{i,yz}\hat{c}_{i,xz}\hat{c}^+_{j,xz}\hat{c}_{j,yz}+\hat{c}^+_{i,xz}\hat{c}_{i,yz}\hat{c}^+_{j,yz}\hat{c}_{j,xz} \\
& -\frac{1}{2}(\hat{n}_{i,yz}+\hat{n}_{i,xz})-\frac{1}{2}(\hat{n}_{j,yz}+\hat{n}_{j,xz})]+\frac{2t^2}{U-J_H}(\hat{\mathbf{S}}_\mathbf{i}\cdot\hat{\mathbf{S}}_\mathbf{j}-\frac{1}{4}) \\
& [\hat{n}_{i,yz}\hat{n}_{j,yz}+\hat{n}_{i,xz}\hat{n}_{j,xz}+\hat{c}^+_{i,yz}\hat{c}_{i,xz}\hat{c}^+_{j,xz}\hat{c}_{j,yz}+\hat{c}^+_{i,xz}\hat{c}_{i,yz}\hat{c}^+_{j,yz}\hat{c}_{j,xz} \\
& +\frac{1}{2}(\hat{n}_{i,yz}+\hat{n}_{i,xz})+\frac{1}{2}(\hat{n}_{j,yz}+\hat{n}_{j,xz})] \\
& (\frac{2t^2}{U+2J_H}-\frac{2t^2}{U-J_H})(\hat{\mathbf{S}}_\mathbf{i}\cdot\hat{\mathbf{S}}_\mathbf{j}-\frac{1}{4})\frac{2}{3} \\
& (\hat{n}_{i,yz}\hat{n}_{j,yz}+\hat{n}_{i,xz}\hat{n}_{j,xz}+\hat{c}^+_{i,yz}\hat{c}_{i,xz}\hat{c}^+_{j,yz}\hat{c}_{j,xz}+\hat{c}^+_{i,xz}\hat{c}_{i,yz}\hat{c}^+_{j,xz}\hat{c}_{j,yz}).
\end{aligned}
\tag{4.19}
$$

We introduce

$$\begin{aligned} \hat{n}_i^{(z)} &= \hat{n}_{i,yz} + \hat{n}_{i,xz}, \\ \hat{c}_{i,yz}^{+}\hat{c}_{i,yz} \to \frac{1}{2}\hat{n}_i^{(z)} + \hat{\tau}_i^{(z)z}, &\quad \hat{c}_{i,xz}^{+}\hat{c}_{i,xz} \to \frac{1}{2}\hat{n}_i^{(z)} - \hat{\tau}_i^{(z)z}, \\ \hat{c}_{i,yz}^{+}\hat{c}_{i,xz} \to \hat{\tau}_i^{(z)+}, &\quad \hat{c}_{i,xz}^{+}\hat{c}_{i,yz} \to \hat{\tau}_i^{(z)-}, \end{aligned} \tag{4.20}$$

$$\begin{aligned} \hat{A}_{ij}^{(z)} &= \hat{n}_{i,yz}\hat{n}_{j,yz} + \hat{n}_{i,xz}\hat{n}_{j,xz} + \hat{c}_{i,yz}^{+}\hat{c}_{i,xz}\hat{c}_{j,xz}^{+}\hat{c}_{j,yz} + \hat{c}_{i,xz}^{+}\hat{c}_{i,yz}\hat{c}_{j,yz}^{+}\hat{c}_{j,xz} \\ &= 2\hat{\tau}_i^{(z)} \cdot \hat{\tau}_j^{(z)} + \frac{1}{2}\hat{n}_i^{(z)}\hat{n}_j^{(z)}, \end{aligned} \tag{4.21}$$

and

$$\begin{aligned} \hat{B}_{ij}^{(z)} &= \hat{n}_{i,yz}\hat{n}_{j,yz} + \hat{n}_{i,xz}\hat{n}_{j,xz} + \hat{c}_{i,yz}^{+}\hat{c}_{i,xz}\hat{c}_{j,yz}^{+}\hat{c}_{j,xz} + \hat{c}_{i,xz}^{+}\hat{c}_{i,yz}\hat{c}_{j,xz}^{+}\hat{c}_{j,yz} \\ &= 2\hat{\tau}_i^{(z)} \otimes \hat{\tau}_j^{(z)} + \frac{1}{2}\hat{n}_i^{(z)}\hat{n}_j^{(z)}. \end{aligned} \tag{4.22}$$

The Hamiltonian for x and y direction is gained by changing x, y and z. Finally, we get the effective Hamiltonian for the γ direction of the 180°-bond structure:

$$\begin{aligned} \hat{H}_{\text{eff}}^{(\gamma)} =& \frac{2t^2}{U-3J_H}(\hat{\mathbf{S}}_\mathbf{i} \cdot \hat{\mathbf{S}}_\mathbf{j} + \frac{3}{4})(\hat{A}_{ij}^{(\gamma)} - \frac{1}{2}\hat{n}_i^{(\gamma)} - \frac{1}{2}\hat{n}_j^{(\gamma)}) \\ &+ \frac{2t^2}{U-J_H}(\hat{\mathbf{S}}_\mathbf{i} \cdot \hat{\mathbf{S}}_\mathbf{j} - \frac{1}{4})(\hat{A}_{ij}^{(\gamma)} + \frac{1}{2}\hat{n}_i^{(\gamma)} + \frac{1}{2}\hat{n}_j^{(\gamma)}) \\ &(\frac{2t^2}{U+2J_H} - \frac{2t^2}{U-J_H})(\hat{\mathbf{S}}_\mathbf{i} \cdot \hat{\mathbf{S}}_\mathbf{j} - \frac{1}{4})\frac{2}{3}\hat{B}_{ij}^{(\gamma)}. \end{aligned} \tag{4.23}$$

The results coincide with those of Ref. [8]. If $J_H << U$,

$$\begin{aligned} \hat{H}_{\text{eff}}^{(\gamma)} =& \frac{2t^2}{U}(1-3\frac{J_H}{U})(\hat{\mathbf{S}}_\mathbf{i} \cdot \hat{\mathbf{S}}_\mathbf{j} + \frac{3}{4})(2\hat{\tau}_i^{(\gamma)} \cdot \hat{\tau}_j^{(\gamma)} + \frac{1}{2}\hat{n}_i^{(\gamma)}\hat{n}_j^{(\gamma)} - \frac{1}{2}\hat{n}_i^{(\gamma)} - \frac{1}{2}\hat{n}_j^{(\gamma)}) \\ &+ \frac{2t^2}{U}(1-\frac{J_H}{U})(\hat{\mathbf{S}}_\mathbf{i} \cdot \hat{\mathbf{S}}_\mathbf{j} - \frac{1}{4})(2\hat{\tau}_i^{(\gamma)} \cdot \hat{\tau}_j^{(\gamma)} + \frac{1}{2}\hat{n}_i^{(\gamma)}\hat{n}_j^{(\gamma)} + \frac{1}{2}\hat{n}_i^{(\gamma)} + \frac{1}{2}\hat{n}_j^{(\gamma)}) \\ &+ \frac{4t^2}{U}\frac{J_H}{U}(\hat{\mathbf{S}}_\mathbf{i} \cdot \hat{\mathbf{S}}_\mathbf{j} - \frac{1}{4})(2\hat{\tau}_i^{(\gamma)} \otimes \hat{\tau}_j^{(\gamma)} + \frac{1}{2}\hat{n}_i^{(\gamma)}\hat{n}_j^{(\gamma)}). \end{aligned} \tag{4.24}$$

The super-exchange (SE) Hamiltonian can be expressed as

$$\begin{aligned} \hat{H}_{ij}^{(\gamma)} =& \frac{2t^2}{U}[(\frac{3}{4}r_1 - \frac{1}{4}r_2)\hat{A}_{ij}^{(\gamma)} + (r_1+r_2)\hat{\mathbf{S}}_\mathbf{i} \cdot \hat{\mathbf{S}}_\mathbf{j}\hat{A}_{ij}^{(\gamma)} - \frac{1}{6}(r_3-r_2)\hat{B}_{ij}^{(\gamma)} \\ &+ \frac{2}{3}(r_3-r_2)\hat{\mathbf{S}}_\mathbf{i} \cdot \hat{\mathbf{S}}_\mathbf{j}\hat{B}_{ij}^{(\gamma)} - (\frac{3}{4}r_1 + \frac{1}{4}r_2)(\frac{1}{2}\hat{n}_i^{(\gamma)} + \frac{1}{2}\hat{n}_j^{(\gamma)}) \\ &+ (r_2-r_1)\hat{\mathbf{S}}_\mathbf{i} \cdot \hat{\mathbf{S}}_\mathbf{j}(\frac{1}{2}\hat{n}_i^{(\gamma)} + \frac{1}{2}\hat{n}_j^{(\gamma)})], \end{aligned} \tag{4.25}$$

where $r_1 = U/(U-3J_H), r_2 = U/(U-J_H)$, and $r_3 = U/(U+2J_H)$. The SE Hamiltonian in z direction is

$$\begin{aligned}\hat{H}_{ij}^{(z)} = \frac{2t^2}{U}[(\frac{3}{4}r_1 - \frac{1}{4}r_2)\hat{A}_{ij}^{(z)} + (r_1+r_2)\hat{\mathbf{S}}_\mathbf{i}\cdot\hat{\mathbf{S}}_\mathbf{j}\hat{A}_{ij}^{(z)} - \frac{1}{6}(r_3-r_2)\hat{B}_{ij}^{(z)} \\ + \frac{2}{3}(r_3-r_2)\hat{\mathbf{S}}_\mathbf{i}\cdot\hat{\mathbf{S}}_\mathbf{j}\hat{B}_{ij}^{(z)} - \frac{1}{2}(\frac{3}{4}r_1 + \frac{1}{4}r_2)(\hat{n}_i^{(z)} + \hat{n}_j^{(z)}) \\ + \frac{1}{2}(r_2-r_1)\hat{\mathbf{S}}_\mathbf{i}\cdot\hat{\mathbf{S}}_\mathbf{j}(\hat{n}_i^{(z)} + \hat{n}_j^{(z)})],\end{aligned} \tag{4.26}$$

where

$$\begin{aligned}\hat{A}_{ij}^{(z)} &= \hat{n}_{i,yz}\hat{n}_{j,yz} + \hat{n}_{i,xz}\hat{n}_{j,xz} + \hat{c}_{i,yz}^+\hat{c}_{i,xz}\hat{c}_{j,xz}^+\hat{c}_{j,yz} + \hat{c}_{i,xz}^+\hat{c}_{i,yz}\hat{c}_{j,yz}^+\hat{c}_{j,xz} \\ \hat{B}_{ij}^{(z)} &= \hat{n}_{i,yz}\hat{n}_{j,yz} + \hat{n}_{i,xz}\hat{n}_{j,xz} + \hat{c}_{i,yz}^+\hat{c}_{i,xz}\hat{c}_{j,yz}^+\hat{c}_{j,xz} + \hat{c}_{i,xz}^+\hat{c}_{i,yz}\hat{c}_{j,xz}^+\hat{c}_{j,yz} \\ \hat{n}_i^{(z)} &= \hat{n}_{i,yz} + \hat{n}_{i,xz}.\end{aligned} \tag{4.27}$$

In order to account for SO interaction, we project every term of $\hat{H}_{ij}^{(z)}$ into the relativistic basis. The $\hat{A}_{ij}^{(z)}$ term in the relativistic basis is then:

$$\begin{aligned}\hat{A}_{ij}^{(z)} &= \frac{4}{9}[\hat{\tilde{c}}_{i\uparrow}^+\hat{\tilde{c}}_{i\uparrow}\hat{\tilde{c}}_{j\uparrow}^+\hat{\tilde{c}}_{j\uparrow} + \hat{\tilde{c}}_{i\downarrow}^+\hat{\tilde{c}}_{i\downarrow}\hat{\tilde{c}}_{j\downarrow}^+\hat{\tilde{c}}_{j\downarrow}] \\ &= \frac{2}{9} + \frac{8}{9}\hat{\tilde{S}}_i^z\hat{\tilde{S}}_j^z.\end{aligned} \tag{4.28}$$

Analogously we find

$$\hat{\mathbf{S}}_\mathbf{i}\cdot\hat{\mathbf{S}}_\mathbf{j}\hat{A}_{ij}^{(z)} = \frac{4}{9}\hat{\tilde{\mathbf{S}}}_i\cdot\hat{\tilde{\mathbf{S}}}_j - \frac{2}{9}\hat{\tilde{S}}_i^z\hat{\tilde{S}}_j^z + \frac{1}{18}, \tag{4.29}$$

$$\hat{B}_{ij}^{(z)} = \frac{2}{9} - \frac{8}{9}\hat{\tilde{S}}_i^z\hat{\tilde{S}}_j^z, \tag{4.30}$$

$$\hat{\mathbf{S}}_\mathbf{i}\cdot\hat{\mathbf{S}}_\mathbf{j}\hat{B}_{ij}^{(z)} = \frac{4}{9}\hat{\tilde{\mathbf{S}}}_i\cdot\hat{\tilde{\mathbf{S}}}_j - \frac{2}{9}\hat{\tilde{S}}_i^z\hat{\tilde{S}}_j^z - \frac{1}{18}, \tag{4.31}$$

$$(\hat{n}_i^{(z)} + \hat{n}_j^{(z)}) = \frac{4}{3}, \tag{4.32}$$

$$\hat{\mathbf{S}}_\mathbf{i}\cdot\hat{\mathbf{S}}_\mathbf{j}(\hat{n}_i^{(z)} + \hat{n}_j^{(z)}) = \frac{4}{9}\hat{\tilde{S}}_i^z\hat{\tilde{S}}_j^z. \tag{4.33}$$

We use $\hat{\mathbf{S}}$ to indicate the Pseudospin $\hat{\tilde{\mathbf{S}}}$, the effective Hamiltonian becomes

$$\begin{aligned}\hat{H}_{ij}^{(z)} =& \frac{4t^2}{U}\frac{4}{9} \\ & [(\frac{3r_1+r_2+2r_3}{6})\hat{\mathbf{S}}_i\cdot\hat{\mathbf{S}}_j + \frac{(r_1-r_2)}{4}\hat{S}_i^z\hat{S}_j^z] \\ & + \frac{t^2}{27U}(-15r_1 - 5r_2 - 4r_3),\end{aligned} \tag{4.34}$$

$$\hat{H}_{ij}^{(z)} = \frac{4t^2}{U}\frac{4}{9}[(\frac{3r_1+r_2+2r_3}{6})\hat{\mathbf{S}}_i\cdot\hat{\mathbf{S}}_j + \frac{(r_1-r_2)}{4}\hat{S}_i^z\hat{S}_j^z]. \tag{4.35}$$

For x and y direction, we use the same method and obtain the same formula. From the above result, the effective Hamiltonian for Pseudospins is:

$$\hat{H}_{ij}^{(\gamma)} = J_1\hat{\mathbf{S}}_i\cdot\hat{\mathbf{S}}_j + K_1\hat{S}_i^{\gamma}\hat{S}_j^{\gamma}, \tag{4.36}$$

with

$$J_1 = \frac{4t^2}{U}\frac{4}{9}(\frac{3r_1+r_2+2r_3}{6}), \tag{4.37}$$

$$K_1 = \frac{4t^2}{U}\frac{4}{9}\frac{(r_1-r_2)}{4}. \tag{4.38}$$

These results agree well with the findings of Khaliullin *et al*. [7]. When $J_H << U, r_1 = 1/(1-3\frac{J_H}{U}) = 1-3\frac{J_H}{U}, r_2 = 1/(1-\frac{J_H}{U}) = 1-\frac{J_H}{U}, r_3 = 1/(1+2\frac{J_H}{U}) = 1+2\frac{J_H}{U}$

$$J_1 = \frac{4t^2}{U}\frac{4}{9}(1-\frac{J_H}{U}), \tag{4.39}$$

$$K_1 = -\frac{4t^2}{U}\frac{2}{9}\frac{J_H}{U}. \tag{4.40}$$

If we do not consider the Hund's coupling,

$$J_1 = \frac{4t^2}{U}\frac{4}{9}, \tag{4.41}$$

$$K_1 = 0. \tag{4.42}$$

The model reduces to the Heisenberg Hamiltonian.

For Z bond (in xy plane) of the 90^0 bond structure (see Fig. 4.1 (b)), the hopping parameter $t_{ij}^{yz,yz} = t_{ij}^{xz,xz} = t^{xy,xy} = t_{ij}^{yz,xy} = t_{ij}^{xz,xy} = 0$, $t_{ij}^{yz,xz} = t$. The exchange couplings [7].

$$J_1 \sim 0,\ K_1 \sim -\frac{8}{3}\frac{t^2}{U}\frac{J_H}{U}. \tag{4.43}$$

When including other hoppings, the effective spin model may contain the Heisenberg term, Kitaev term and other off diagonal terms [67].

4.1.3 Exact perturbation method

The summary of this section appeared in the supplemental section of Ref. [36]. Here, we present the details of derivation. The above analytical expressions are

based on the projection of the $\lambda = 0$ Hamiltonian for the t_{2g} orbitals onto the relativistic $j_{\text{eff}} = 1/2$ basis. This is only valid in the limit $U \gg \lambda \gg t$ which is not generally satisfied in real materials. An improvement are the expressions using the second order perturbation theory in the limit $U \gg t$ and otherwise the exact expressions to all orders of J_H, U, λ in the absence of crystal field splitting ($\Delta_n = 0$) [36]. We first transform the Hamiltonian into a basis that exact diagonalizes spin-orbit coupling at the single electron level, and then the spin Hamiltonians in this basis are computed.

The Hamiltonian is divided into $H = H_0 + H_1$ where H_1 contains all hopping terms, and $H_0 = H_{SO} + H_U$. In the limit $U/t \to \infty$ and $\lambda > 0$. The effective Hamiltonian in the second order is

$$H_{\text{eff}}(\omega) = \sum_{i,j} \hat{P}\hat{\mathbf{c}}_i^\dagger \mathbf{T}_{ij} \hat{\mathbf{c}}_j (1-\hat{P})(\omega - \hat{H}_0)^{-1}(1-\hat{P})\hat{\mathbf{c}}_j^\dagger \mathbf{T}_{ji} \hat{\mathbf{c}}_i \hat{P}. \tag{4.44}$$

In the low order within perturbation theory, we take $\omega =< H_0 >$, which is the energy of the ground state. For convenience, this perturbation is performed in the relativistic basis labeled $|j, m_j\rangle$:

$$\hat{\mathbf{c}}_i = \begin{pmatrix} \hat{\mathbf{c}}_{i,\frac{1}{2}} \\ \hat{\mathbf{c}}_{i,\frac{3}{2}} \end{pmatrix}, \tag{4.45}$$

where

$$\hat{\mathbf{c}}_{i,\frac{1}{2}} = \begin{pmatrix} \hat{c}_{i,|\frac{1}{2},\frac{1}{2}\rangle} \\ \hat{c}_{i,|\frac{1}{2},-\frac{1}{2}\rangle} \end{pmatrix} \ , \ \hat{\mathbf{c}}_{i,\frac{3}{2}} = \begin{pmatrix} \hat{c}_{i,|\frac{3}{2},\frac{1}{2}\rangle} \\ \hat{c}_{i,|\frac{3}{2},-\frac{1}{2}\rangle} \\ \hat{c}_{i,|\frac{3}{2},\frac{3}{2}\rangle} \\ \hat{c}_{i,|\frac{3}{2},-\frac{3}{2}\rangle} \end{pmatrix}. \tag{4.46}$$

The hopping matrix $\mathbf{T}_{ij}$ is expressed as

$$\mathbf{T}_{ij} = \begin{pmatrix} \Theta_{ij}^{\frac{1}{2}\frac{1}{2}} & \Theta_{ij}^{\frac{1}{2}\frac{3}{2}} \\ \Theta_{ij}^{\frac{3}{2}\frac{1}{2}} & \Theta_{ij}^{\frac{3}{2}\frac{3}{2}} \end{pmatrix}, \tag{4.47}$$

where

$$\Theta_{ij}^{\frac{1}{2}\frac{1}{2}} = t_{ij}^{\frac{1}{2}\frac{1}{2}} \mathbb{I}_{2\times 2} + i\boldsymbol{\lambda}_{ij}^{\frac{1}{2}\frac{1}{2}} \cdot \boldsymbol{\sigma}, \tag{4.48}$$

$$\begin{aligned} \Theta_{ij}^{\frac{1}{2}\frac{3}{2}} =& (t_{ij}^{\frac{1}{2}\frac{3}{2},a} \mathbb{I}_{2\times 2} + i\boldsymbol{\lambda}_{ij}^{\frac{1}{2}\frac{3}{2},a} \cdot \boldsymbol{\sigma}) \begin{pmatrix} 1 & 0 & 0 & 0 \\ 0 & 1 & 0 & 0 \end{pmatrix} \\ &+ (t_{ij}^{\frac{1}{2}\frac{3}{2},b} \mathbb{I}_{2\times 2} + i\boldsymbol{\lambda}_{ij}^{\frac{1}{2}\frac{3}{2},b} \cdot \boldsymbol{\sigma}) \begin{pmatrix} 0 & 0 & 1 & 0 \\ 0 & 0 & 0 & 1 \end{pmatrix}. \end{aligned} \tag{4.49}$$

The hopping parameters from the kinetic term and the spin-orbit term are

$$\begin{aligned} t_{ij}^{\frac{1}{2}\frac{1}{2}} &= \frac{1}{3}(t_{i,j}^{xy,xy}+t_{i,j}^{xz,xz}+t_{i,j}^{yz,yz}), \\ \lambda_{ij}^{\frac{1}{2}} &= \frac{1}{3}(t_{ij}^{xy,xz}-t_{ij}^{xz,xy},t_{ij}^{xy,yz}-t_{ij}^{yz,xy},t_{ij}^{yz,xz}-t_{ij}^{xz,yz}), \end{aligned} \tag{4.50}$$

$$\begin{aligned} t_{ij}^{\frac{1}{2}\frac{3}{2},a} &= \frac{1}{3\sqrt{2}}(2t_{i,j}^{xy,xy}-t_{i,j}^{xz,xz}-t_{i,j}^{yz,yz}), \\ \lambda_{ij}^{\frac{1}{2}\frac{3}{2},a} &= \frac{1}{3\sqrt{2}}(-t_{ij}^{xy,xz}-2t_{ij}^{xz,xy},2t_{ij}^{xy,yz}+t_{ij}^{yz,xy},-t_{ij}^{yz,xz}+t_{ij}^{xz,yz}), \end{aligned} \tag{4.51}$$

$$\begin{aligned} t_{ij}^{\frac{1}{2}\frac{3}{2},b} &= \frac{1}{\sqrt{6}}t_{i,j}^{yz,xy}, \\ \lambda_{ij}^{\frac{1}{2}\frac{2}{3},b} &= \frac{1}{\sqrt{6}}(-t_{ij}^{xy,xz}-t_{ij}^{xz,xy},t_{ij}^{yz,yz}-t_{ij}^{xz,xz},t_{ij}^{xy,xz}). \end{aligned} \tag{4.52}$$

For Z bond, we use $t_{ij}^{yz,yz}=t_{ij}^{xz,xz}\equiv t_1$, $t_{ij}^{yz,xz}=t_{ij}^{xz,yz}\equiv t_2$, $t_{ij}^{xy,xy}\equiv t_3$, and $t_{ij}^{xy,xz}=t_{ij}^{xz,xy}=t_{ij}^{xy,yz}=t_{ij}^{yz,xy}\equiv 0$ which gives:

$$\begin{aligned} \Theta_{ij}^{\frac{1}{2},\frac{1}{2}} &= \frac{1}{3}(2t_1+t_3)\mathbb{I}_{2\times 2}, \\ \Theta_{ij}^{\frac{1}{2},\frac{3}{2}} &= \frac{\sqrt{2}}{3}(t_3-t_1)\begin{pmatrix} 1 & 0 \\ 0 & 1 \\ 0 & 0 \\ 0 & 0 \end{pmatrix} - i\sqrt{\frac{2}{3}}t_2\begin{pmatrix} 0 & 0 \\ 0 & 0 \\ 0 & 1 \\ 1 & 0 \end{pmatrix}. \end{aligned} \tag{4.53}$$

Without the crystal field splitting, the projection operator in the low energy space is

$$\hat{P}=\prod_i \hat{\mathbf{c}}_{i,\frac{1}{2}}^{\dagger}\hat{\mathbf{c}}_{i,\frac{1}{2}}. \tag{4.54}$$

The magnetic spin operators are written in the $j_{1/2}$ basis

$$\hat{\mathbf{S}}_i=\frac{1}{2}\hat{\mathbf{c}}_{i,\frac{1}{2}}^{\dagger}\hat{\sigma}\hat{\mathbf{c}}_{i,\frac{1}{2}}. \tag{4.55}$$

where σ is the Pauli vector:

$$\hat{\sigma}_x=\begin{pmatrix} 0 & 1 \\ 1 & 0 \end{pmatrix}, \hat{\sigma}_y=\begin{pmatrix} 0 & -i \\ i & 0 \end{pmatrix}, \hat{\sigma}_z=\begin{pmatrix} 1 & 0 \\ 0 & -1 \end{pmatrix}. \tag{4.56}$$

The effective Hamitonian is

$$\begin{aligned} \hat{H}_{\text{eff}}=\sum_{ij}\mathbb{A}\,\hat{\mathbf{S}}_j\cdot\left(\mathbf{c}_{i,\frac{1}{2}}^{\dagger}\Theta_{ij}^{\frac{1}{2}\frac{1}{2}}\sigma\Theta_{ji}^{\frac{1}{2}\frac{1}{2}}\mathbf{c}_{i,\frac{1}{2}}\right) \\ +\mathbb{B}\hat{\mathbf{S}}_j\cdot\left(\mathbf{c}_{i,\frac{1}{2}}^{\dagger}\Theta_{ij}^{\frac{1}{2}\frac{3}{2}}\tau\Theta_{ji}^{\frac{3}{2}\frac{1}{2}}\mathbf{c}_{i,\frac{1}{2}}\right)+(i\leftrightarrow j). \end{aligned} \tag{4.57}$$

The final effective Hamiltonian is

$$\hat{H}_{\text{spin}} = \sum_{\langle ij \rangle} J_{ij}\, \hat{\mathbf{S}}_i \cdot \hat{\mathbf{S}}_j + \mathbf{D}_{ij} \cdot \hat{\mathbf{S}}_i \times \hat{\mathbf{S}}_j + \hat{\mathbf{S}}_i \cdot \Gamma_{ij} \cdot \hat{\mathbf{S}}_j, \tag{4.58}$$

where $\mathbf{D}_{ij}$ is the Dzyalloshinskii-Moriya (DM) vector, which is zero when $t^{m,m'} = t^{m',m}$. Other exchange paramters are [36]:

$$\begin{aligned}
J &= \frac{4\mathbb{A}}{9}(2t_1+t_3)^2 - \frac{8\mathbb{B}}{9}\left\{9t_4^2 + 2(t_1-t_3)^2\right\} \\
K &= \frac{8\mathbb{B}}{3}\left\{(t_1-t_3)^2 + 3t_4^2 - 3t_2^2\right\} \\
\Gamma &= \frac{8\mathbb{B}}{3}\left\{3t_4^2 + 2t_2(t_1-t_3)\right\} \\
\Gamma' &= \frac{8\mathbb{B}}{3}\left\{t_4(3t_2+t_3-t_1)\right\},
\end{aligned} \tag{4.59}$$

where

$$\begin{aligned}
\mathbb{A} &= -\frac{1}{3}\left\{\frac{J_H + 3(U+3\lambda)}{6J_H^2 - U(U+3\lambda) + J_H(U+4\lambda)}\right\}, \\
\mathbb{B} &= \frac{4}{3}\left\{\frac{(3J_H - U - 3\lambda)}{(6J_H - 2U - 3\lambda)}\eta\right\}, \\
\mathbb{C} &= \frac{6}{8}\left\{\frac{1}{2U - 6J_H + 3\lambda} + \frac{5}{9}\frac{(3U - 7J_H - 9\lambda)}{J_H}\eta\right\}, \\
\eta &= \frac{J_H}{6J_H^2 - J_H(8U+17\lambda) + (2U+3\lambda)(U+3\lambda)}.
\end{aligned} \tag{4.60}$$

In the limit of $J_H \ll \lambda$ and $J_H \ll U$, it is the formula in Ref. [68]:

$$\begin{aligned}
J &= \frac{4}{27}\frac{(2t_1+t_3)^2(4J_H+3U)}{U^2} - \frac{16J_H(t_1-t_3)^2}{(2U+3\lambda)^2}, \\
K &= \frac{32J_H}{9}\frac{(t_1-t_3)^2 - 3t_2^2}{(2U+3\lambda)^2}, \\
\Gamma &= \frac{64J_H}{9}\frac{t_2(t_1-t_3)}{(2U+3\lambda)^2}.
\end{aligned} \tag{4.61}$$

When $t_1 = t_3 = 0$, $\lambda = 0$, it is similar as Eq. (4.43).

4.2 Effective model from exact diagonalization

4.2.1 General form

In order to improve on the determination of parameters, we have also performed exact diagonalization of finite clusters and we will compare both procedures further below. The clusters used in the exact diagonalization to obtain the exchange param-

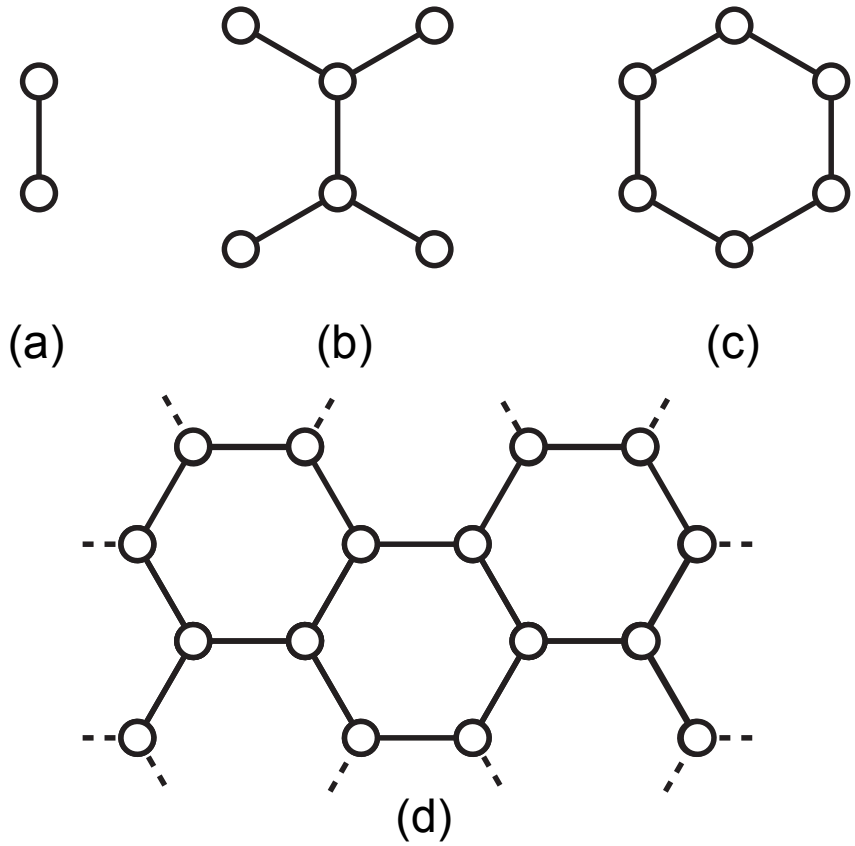

Figure 4.2: Clusters employed in exact diagonalization studies for the extraction of magnetic parameters: (a) two-site cluster, (b) "bridge" cluster, and (c) "hexagon" cluster. The 16-site cluster (d) has been used for ED studies of the resulting magnetic models.

eters are shown in Fig. 4.2 (a), (b), and (c). (a) is the two-site cluster, (b) include the center bond of X_1, Y_1, or Z_1 bond. (c) can account for second and third nearest neighbors. We diagonalize the total Hamiltonian to obtain the eigenvalues E_n and eigenstates $\{|n\rangle\}$. For N site clusters, we only use the lowest $N_l = 2^N$ energy and

project the corresponding eigenstates on the low energy subspace (pure j_{eff} = 1/2)

$$|n'\rangle = \sum_{n_l}^{N_l} |n_l\rangle\langle n_l|n\rangle \equiv \mathbf{R}|n\rangle \quad , \quad n,n' = 1 \ldots N_l. \tag{4.62}$$

The lower Hilbert space is not the complete set of states and therefore not orthonormal. We use the intermediate basis in terms of overlap matrix to define a total unitary transformation

$$\mathbf{U} = \mathbf{R}\mathbf{S}^{-1/2} \quad , \quad \mathbf{S}_{mn} = \langle m'|n'\rangle. \tag{4.63}$$

And finally, we write the effective Hamiltonian in the spin subspace as:

$$\hat{H}_{\text{spin}} = \mathbf{U}^{\dagger} \left(\sum_{n}^{N_l} E_n |n\rangle\langle n| \right) \mathbf{U}. \tag{4.64}$$

From it, we can obtain the exchange parameters. When spin-orbit coupling is important, the j_{eff} =1/2 is the pseudo-spin as discussed in [67, 69–71]. The effective spin Hamiltonian is expressed as:

$$\hat{H}_{\text{spin}} = \sum_{\langle ij \rangle} \hat{\mathbf{S}}_i \cdot \mathbf{J}_{ij} \cdot \hat{\mathbf{S}}_j + \hat{O}(\mathbf{S}^4), \tag{4.65}$$

where $\langle ij \rangle$ is the sum over all pairs of sites up to third nearest neighbors. The interactions can also be expressed as:

$$\hat{H}_{\text{spin}} = \sum_{\langle ij \rangle} J_{ij}\, \hat{\mathbf{S}}_i \cdot \hat{\mathbf{S}}_j + \hat{\mathbf{S}}_i \cdot \Gamma_{ij} \cdot \hat{\mathbf{S}}_j + \mathbf{D}_{ij} \cdot \hat{\mathbf{S}}_i \times \hat{\mathbf{S}}_j, \tag{4.66}$$

where the first term is the Heisenberg interaction, while the second term is the pseudo-dipolar interaction which include the Kitaev term, and the last term is the Dzyaloshinskii-Moriya (DM) couplings. The first and second terms are symmetric and the last term is antisymmetric. The parameters are:

$$\mathbf{J}_{ij,s} = \begin{pmatrix} J_{ij} + \Gamma_{ij}^{aa} & \Gamma_{ij}^{ab} & \Gamma_{ij}^{ac} \\ \Gamma_{ij}^{ab} & J_{ij} + \Gamma_{ij}^{bb} & \Gamma_{1}^{bc} \\ \Gamma_{1}^{ac} & \Gamma_{1}^{bc} & J_{ij} + \Gamma_{ij}^{cc} \end{pmatrix}, \tag{4.67}$$

$$\mathbf{J}_{ij,a} = \begin{pmatrix} 0 & D_{ij}^{c} & -D_{ij}^{b} \\ -D_{ij}^{c} & 0 & D_{ij}^{a} \\ D_{ij}^{b} & -D_{ij}^{a} & 0 \end{pmatrix}. \tag{4.68}$$

For the symmetric part, there are three different bonds (X_n, Y_n, Z_n). The formulas are given by:

$$\mathbf{J}_{n,s}^{Z} = \begin{pmatrix} J_1^z & \Gamma_n^z & \Gamma_n'^z \\ \Gamma_n^z & J_n^z & \Gamma_n'^z \\ \Gamma_n'^z & \Gamma_n'^z & J_n^z + K_n^z \end{pmatrix}, \tag{4.69}$$

$$\mathbf{J}^X_{n,s} = \begin{pmatrix} J_1^{xy}+K_1^{xy} & \Gamma_1'^{xy}+\zeta_1 & \Gamma_1'^{xy}-\zeta_1 \\ \Gamma_1'^{xy}+\zeta_1 & J_1^{xy}+\xi_1 & \Gamma_1^{xy} \\ \Gamma_1'^{xy}-\zeta_1 & \Gamma_1^{xy} & J_1^{xy}-\xi_1 \end{pmatrix}, \tag{4.70}$$

$$\mathbf{J}^Y_{n,s} = \begin{pmatrix} J_1^{xy}+\xi_1 & \Gamma_1'^{xy}+\zeta_1 & \Gamma_1^{xy} \\ \Gamma_1'^{xy}+\zeta_1 & J_1^{xy}+K_1^{xy} & \Gamma_1'^{xy}-\zeta_1 \\ \Gamma_1^{xy} & \Gamma_1'^{xy}-\zeta_1 & J_1^{xy}-\xi_1 \end{pmatrix}, \tag{4.71}$$

with the convention introduced in Ref. [67, 72].

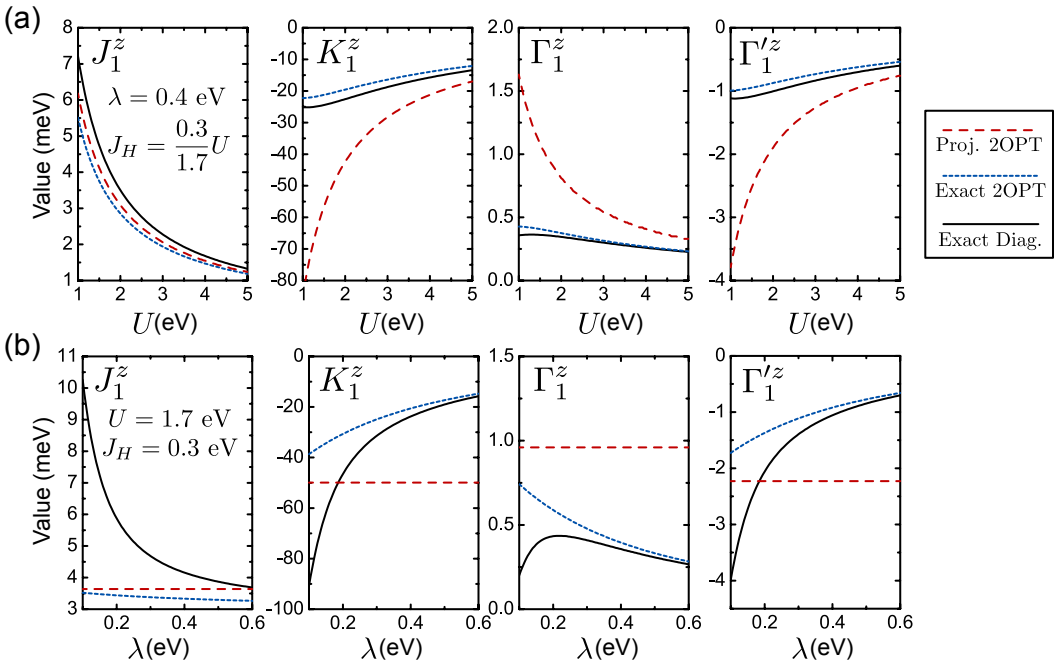

Figure 4.3: Nearest neighbour interactions for the Z_1-bond in Na_2IrO_3 in the absence of crystal-field splitting, employing hopping parameters described in Chapter 8. The results of 2-site exact diagonalization (black solid line) are compared with approximate projective expressions (red dashed line, Ref. [67]) and second order perturbation theory exact in λ, U, J_H (blue dotted line). (a) U-dependence, with constant J_H/U ratio of $0.3/1.7$, and $\lambda = 0.4$ eV. (b) λ-dependence, with $J_H = 0.3$ eV, and $U = 1.7$ eV.

4.2.2 Comparison to exact second order perturbation

For the exact perturbation formula in Eq. 4.59, at $\mathcal{O}(t^2)$, magnetic interactions result from a combination of i) "*intra*band" terms ($\propto \mathbb{A} > 0$) arising from virtual hopping

of holes between $j_{\text{eff}} = 1/2$ states, and ii) "*inter*band" terms ($\propto \mathbb{B} > 0$) arising from hopping between $j_{\text{eff}} = 1/2$ and lower-lying $j_{\text{eff}} = 3/2$ states. Both processes contribute to the isotropic exchange J_1, but with opposite sign, while the anisotropic terms arise only from interband processes ($\propto \mathbb{B}$). The values of these constants can be estimated for the real materials; for $5d$ Ir^{4+} ions (as in A_2IrO_3, A = Na, Li), we take $U = 1.7$, $J_H = 0.3$, and $\lambda = 0.4$ eV, suggesting:

$$\mathbb{A}_{5d} \sim 0.9 \text{ eV}^{-1} \quad , \quad \mathbb{B}_{5d} \sim 0.04 \text{ eV}^{-1}, \tag{4.72}$$

while for $4d$ Ru^{3+} ions (as in α-$RuCl_3$), we take $U = 3.0$, $J_H = 0.6$, and $\lambda = 0.15$ eV, suggesting:

$$\mathbb{A}_{4d} \sim 0.6 \text{ eV}^{-1} \quad , \quad \mathbb{B}_{4d} \sim 0.05 \text{ eV}^{-1}. \tag{4.73}$$

The second order expressions may be compared with the results of exact diagonalization (ED) of the full Hamiltonian on two sites (for $\Delta_n = 0$). In the latter case, the interaction parameters J_1^z, K_1^z, etc. for Z_1 bond were extracted via projection of the exact low-energy states onto the $j_{\text{eff}} = 1/2$ states. We show in Fig. 4.3 the dependence of the interactions on λ and U for Hamiltonian parameters suitable for the Z_1-bond of Na_2IrO_3. For the λ-dependence plots, $U = 1.7, J_H = 0.3$ eV are fixed, while U-dependence is considered with fixed $\lambda = 0.4$ eV and J_H/U ratio. One can see that the exact second order expressions (4.59) agree with the ED results over a wide range of U-values, and break down only in the weak λ limit. Interestingly, large λ tends to suppress the anisotropic terms, due to enhancement of the gap between the $j_{\text{eff}} = 1/2$ and $j_{\text{eff}} = 3/2$ states. The close agreement between the perturbative and ED results validates both approaches. In contrast, the projective expressions of Ref. [67] seem to overestimate the magnitude of the anisotropic terms over a large region of parameters, and fail to capture any λ-dependence by construction.

In real materials, $\mathbb{A} \gg \mathbb{B}$, so that the anisotropic interactions typically represent subleading terms. For materials close to the Kitaev limit ($K_1 \gg J_1$), the leading term J_1 must therefore be suppressed to an order of magnitude below its natural scale [7], which opens the possibility that other subleading interactions such as second and third neighbour terms may also be relevant. These are considered in the next section.

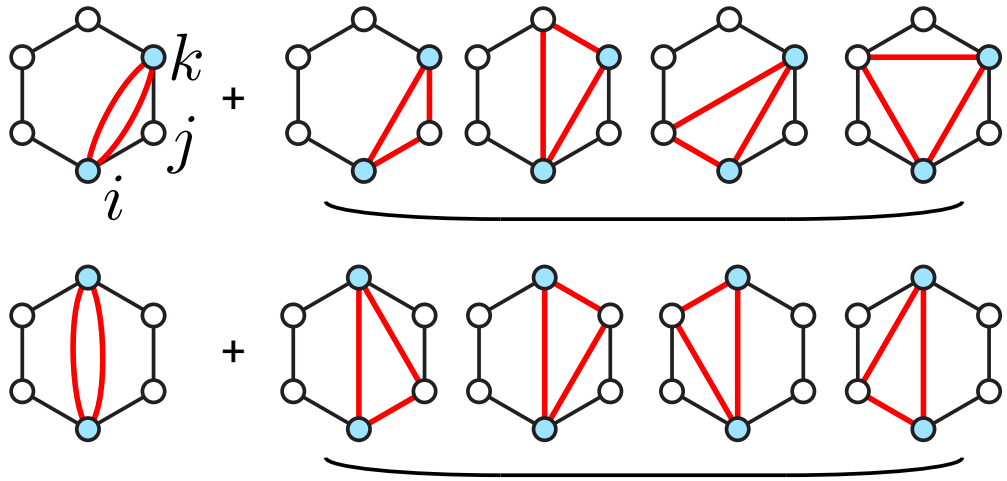

Figure 4.4: Hopping paths associated with contributions $\mathcal{O}(t^2)$ and $\mathcal{O}(t^3)$ to the long-range second neighbour (top) and third neighbour (bottom) interactions. The many higher order corrections to these terms must be included to produce accurate estimates.

4.2.3 Long-range interactions

Various previous works have considered long-range terms for the honeycomb materials, either for interpretation of experimental data[15, 73–76], or from an *ab-initio* perspective[25, 27, 69, 70]. In the latter reports, such interactions where estimated only at the level of second order perturbation theory in the direct second or third neighbour hopping. Here we consider the validity of this approach. For second neighbour interactions, we consider three adjacent sites i, j, k. The lowest order contributions to the second neighbour interactions arise from direct hopping associated with virtual hopping processes such as $i \to k \to i$:

$$J_2^{(2)} \sim \frac{|\mathbf{T}_{ik}\mathbf{T}_{ki}|}{U_{\text{eff}}} \tag{4.74}$$

where $U_{\text{eff}}(U, J_H, \lambda) \sim \mathbb{A}^{-1} \sim 1.0 - 1.5$ eV gives the rough energy cost for double occupancy of a given site. Such contributions have been previously considered in the literature. As shown in Fig. 4.4, several virtual hopping paths contribute to $\mathcal{O}(t^3)$ terms, the largest of which provides:

$$J_2^{(3)} \sim \frac{|\mathbf{T}_{ij}\mathbf{T}_{jk}\mathbf{T}_{ki}|}{U_{\text{eff}}^2} \tag{4.75}$$

This corresponds to the three site ring exchange $i \to j \to k \to i$ process. Strong convergence of the perturbation expansion would require $J_2^{(2)} \gg J_2^{(3)}$. However,

for conservative estimates of $U_{\text{eff}} \sim 1$ eV, and $|\mathbf{T}_{ij}/|\mathbf{T}_{ik}| \sim 10$, the second order $J_2^{(2)}$ and third order $J_2^{(3)}$ contributions can be of similar magnitude. On this basis, we conclude that perturbation theory for the long-range interactions may not be strongly convergent, questioning the reliability of previous estimates. This finding is consistent with previous suggestions that long-range interactions on the scale of $n = 2,3$ would emerge naturally from a semi-itinerant picture of the holes within the hexagonal plaquettes [28, 29]. In order to bridge these two perspectives, we have applied nonperturbative exact diagonalization methods to the real materials in Chapter 8, which allow for accurate estimation of all terms up to third neighbour. We have also considered 4-spin and 6-spin ring-exchange interactions that similarly emerge at high orders in perturbation theory, but we find them to be negligible in calculations below, implying sufficient convergence at third order.

4.3 Comparison to experiment

On the basis of the above calculations to extract the parameters (perturbation or small clusters), we therefore suggest the minimal model for each material and construct the spin model of larger clusters (sixteen-site in Fig. 4.2 (d)) with ED method or classical method to calculated the phase diagram. Phase boundaries were identified from extrema of $\partial^2 E/(\partial J_n)^2$ in the ED model, where E is the ground state energy. Then the orientations of the ordered moments were calculated by using all the parameters in a classical simulation. We further estimate the Weiss constant given a particular orientation of the magnetic field $\hat{h}(\theta,\phi)$ via:

$$\Theta(\theta,\phi) = -\frac{S(S+1)}{3k_b}\sum_j \hat{h}\cdot\mathbf{J}_{ij}\cdot\hat{h}, \tag{4.76}$$

where $\hat{h}(\theta,\phi)$ is the magnetic field. The summation is for all the nearest neighbors of site i. The isotropic Weiss constant is estimated by the average value:

$$\Theta_{iso} \sim \int \Theta(\theta,\phi)\sin\theta\, d\theta\, d\phi \tag{4.77}$$

$$\sim -\frac{1}{4k_b}\left(3J_1+6J_2+3J_3+K_1+2K_2\right), \tag{4.78}$$

which is independent of all off-diagonal Γ_1, Γ_1' terms.

4.4 Summary

In this chapter, a general overview of methods for magnetic properties was presented.

The relativistic effects are important in the Kitaev spin-liquid candidate materials. With the relativistic basis, we constructing the effective spin Hamiltonian. Two methods were outlined. One is the second-order perturbation theory which was already studied by various investigations. However, previous treatments were not exact in λ, U, J_H. A revised perturbation theory calculation was therefore introduced.

The second method introduced was exact diagonalization in finite clusters. In this method, we treated all interactions up to third neighbors on equal footing and therefore allow estimation of all parameters. This method therefore provides us with a numerical tool to investigate the significant long-range coupling including high order perturbation, which is neglected in the second-order perturbation theory.

Finally, we introduced parameters obtained by the small cluster to construct the spin Hamiltonian of the larger cluster to calculate the magnetic phase and Curie-Weiss constant to compared with experimental observations.

Chapter 5

Analysis of the electronic properties and optical conductivity for A_2IrO_3 from first principles

Ying Li, Kateryna Foyevtsova, Harald O. Jeschke, Roser Valentí
Phys. Rev. B **91**, 161101 (R) (2015) [33]

With the aim of unveiling the origin of different behavior in Na_2IrO_3 and α-Li_2IrO_3, in this chapter, we compute the optical conductivity in Na_2IrO_3 with density functional theory calculations using the method described in Chapter 3 and analyze the multi-peaks by the parity of the underlying quasi molecular orbital (QMO) description. We also predict the optical conductivity for α-Li_2IrO_3 and compare the similarities and differences with α-Li_2IrO_3.

5.1 Properties of Na_2IrO_3 and α-Li_2IrO_3

Na_2IrO_3 and α-Li_2IrO_3 crystallize in the monoclinic space group $C2/m$ shown in Fig. 5.1 [15, 22]. The IrO_6 octahedra discussed in Chapter 1 share the edges and form honeycomb layers within the *ab*-plane. The experimental structures have the following distortions: (i) orthorhombic distortions along the preferred axis, leading to different Ir-Ir bond lengths, and (ii) trigonal distortion compressing the IrO_6 octahedra along the direction perpendicular to the honeycomb plane that leads to a

departure from 90° Ir-O-Ir angles. Na and Li ions occupy interlayer positions as well as the centers of Ir hexagons in the layer. The α-Li_2IrO_3 structure is known from powder x-ray diffraction [22] and from a careful DFT structure prediction using a spin-polarized GGA+SO+U exchange correlation functional [77]. These two structures differ slightly.

Na_2IrO_3 was found to have zigzag magnetic order below $T_N = 14$ K by neutron scattering and resonant x-ray experiments [14–16]. In the zigzag magnetic structure, the spins are ferromagnetic (FM) along the zigzag chain, and antiferromagnetic (AFM) between different chains shown in Figure 5.5. The material has a large Weiss constant Θ_{iso} ∼-116 K, while the anisotropy $\chi_{ab} < \chi_c$ suggests bond-anisotropy or off-diagonal terms [78]. Recently, the moments' direction were found to be ordered at 45° with **a** axis in the **ac** plane [79]. This order was obtained by Heisenberg-Kitaev models with more terms [69, 80, 81], which we will discuss in Chapter 8. The sec-

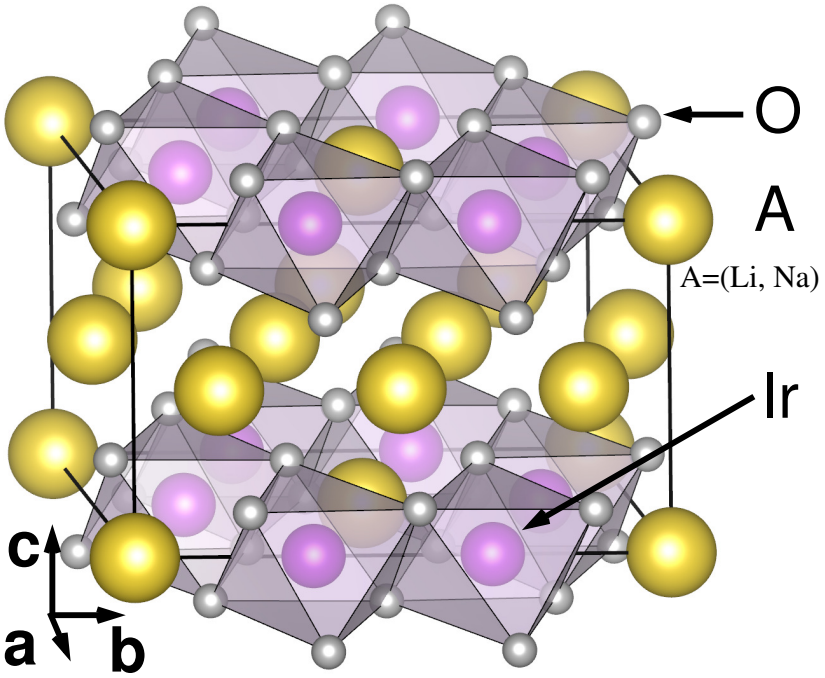

Figure 5.1: A_2IrO_3 crystal structure.

ond material of interest, α-Li_2IrO_3 also order magnetically with $T_N = 15$ K, but with a smaller Curie-Weiss temperature of CW ∼ 33 K [75]. The magnetic order was recently shown to be an incommensurate phase with $\mathbf{q}||a$, and $|\mathbf{q}| = q \sim 0.3$ in the first Brillouin zone given by the x-ray and neutron experiments [20]. The spiral phase has been discussed in terms of three different models [67, 69, 72, 74, 80, 82, 83].

Photoemission and optical conductivity measurements [21] for Na_2IrO_3 indicate that it is an insulator with an optical gap of 340 meV. The gap of α-Li_2IrO_3 has been reported to be of the same order of magnitude as in Na_2IrO_3 [22] or a little bit smaller [23]. The different properties through the series $(Na_{1-x}Li_x)_2IrO_3$ were investigated in Ref. [77, 84]. Manni *et al.* [77] find that with $x \leq 0.25$ the system forms uniform solid solutions and otherwise the system shows a miscibility gap and phase separates. In contrast, Cao *et al.* [84] find a homogeneous phase at $x \sim 0.7$ with a disappearance of long range magnetic order.

From Chapter 1 we know that these materials are candidates to realize the bond-dependent anisotropic Heisenberg-Kitaev model [7, 26, 67, 69, 70, 74, 81]. The electronic structure can be interpreted in terms of the localized $j_{\text{eff}} = 1/2$ and $j_{\text{eff}} = 3/2$ relativistic orbitals. Alternatively, from an itinerant point of view, the electronic structure can also be described in terms of the quasi-molecular orbitals (QMO) [28, 29] explained in the next section. Further, since the contributing energy scales in these systems are of the same order of magnitude, both the localized description of relativistic basis and itinerant description of QMO may be equally compatible [29].

The optical conductivity $\sigma(\omega)$ measurements for Na_2IrO_3 [21, 85] show that there is a broad peak around 1.5 eV [21] (1.66 eV in Ref. [85]) and smaller peaks around 0.52 eV, 0.72 eV, 1.32 eV, 1.98 eV [85]. These properties have been suggested to be dominated by j_{eff}= 3/2 and j_{eff}= 1/2 transitions [85, 86].

5.2 Electronic structures and optical conductivity for Na_2IrO_3

5.2.1 Quasi-molecular orbitals

In Na_2IrO_3, for each bond, only the O-assisted hopping between unlike orbitals (t_{1O}) are large. There are three kinds of bonds in this system: for X bond, there are only hoppings between d_{xy} and d_{xz}; d_{xy} and d_{yz} for Y bond, and d_{xz} and d_{yz} for Z bond. As shown in Fig. 5.2 (a), one electron on one Ir site d_{xy} can only hop to the neighboring state d_{yz} along Y bond with a magnitude of t_{1O}. From there, the electron can hop further to d_{xz} through the Z bond. At each site, only the electron

on one special orbital can hop along a particular bond. After hopping six times from the original site, the electron comes back to the position where it started. Therefore, each electron is localized in one hexagon with Ir1(d_{xy})-Ir2(d_{xz})-Ir3(d_{yz})-Ir4(d_{xy})-Ir5(d_{xz})-Ir6(d_{yz}), which can be called a quasi-molecular orbital (QMO). Each Ir contribute to three different QMOs with three t_{2g} orbitals. Six QMOs on a hexagon form six levels: highest A_{1g} and lowest B_{1u} singlet, and E_{2u}, E_{1g} doublets.

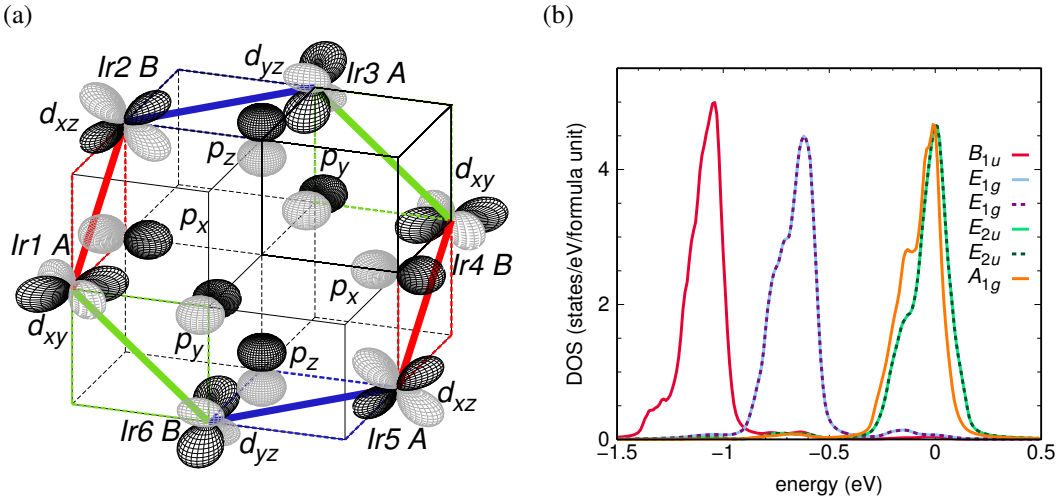

Figure 5.2: (a) Most relevant O-assisted hopping paths in Na_2IrO_3 structure which form the quasi-molecular orbitals. Ir-Ir bonds are shown in different colors: Z bonds by blue lines, Y bonds by green, and X bonds by red ones. (b) Density of states of Na_2IrO_3 projected onto the six quasi-molecular orbitals for a nonrelativistic calculation [29].

Based on the above discussions, the QMO can be constructed from the t_{2g} orbitals. There are two sublattices in each primitive unitcell A and B. For the QMOs $Q = A_{1g}, E_{2u}, E_{1g}, B_{1u}, E_{1g}, E_{2u}$ and t_{2g} orbitals $M = d^A_{xy}, d^A_{xz}, d^A_{yz}, d^B_{xy}, d^B_{xz}, d^B_{yz}$, the relation of this two basis is

$$Q = U_{Q,M} T_M M, \tag{5.1}$$

with

$$U_{Q,M} = \begin{pmatrix} 1 & 1 & 1 & 1 & 1 & 1 \\ 1 & \omega^4 & \omega^2 & -1 & \omega & \omega^5 \\ 1 & \omega^2 & \omega^4 & 1 & \omega^2 & \omega^4 \\ 1 & 1 & 1 & -1 & -1 & -1 \\ 1 & \omega^4 & \omega^2 & 1 & \omega^4 & \omega^2 \\ 1 & \omega^2 & \omega^4 & -1 & \omega^5 & \omega \end{pmatrix}, \tag{5.2}$$

here T_M are the Bloch factors transforming the A, B sites to the corresponding unit cell for the six-site hexagon. After multiplying the projectors from bands to t_{2g} orbitals, the projectors to the QMOs from the bands can be obtained:

$$P_{Q\nu}(\mathbf{k}) = \sum_M U_{Q,M} T_M(\mathbf{k}) P_{M\nu}(\mathbf{k}). \tag{5.3}$$

The density of states is calculated within DFT and also through local Green's functions. The Green's function is obtained from the KS eigenvalues as:

$$G_{\nu,\nu'}(\mathbf{k},\omega) = [\omega - (E_{\nu,\nu'} - E_F) + i\eta]^{-1}. \tag{5.4}$$

With the Green's function and projectors $P^{\alpha(s)}_{m\nu}$ projecting the states from the band ν to the QMOs m, we calculated the local orbital Green's function:

$$G_{mm'}(\omega) = \sum_{\mathbf{k}}^{1BZ} \sum_{\nu,\nu'} P^{\alpha(s)}_{m\nu}(\mathbf{k}) G_{\nu,\nu'}(\mathbf{k},\omega) P^{\alpha(s)}_{\nu'm'}(\mathbf{k}). \tag{5.5}$$

Finally, the density of states for QMO m can be obtained using the the local Green's function:

$$D_m(\omega) = -\frac{1}{\pi} \mathrm{Im} G_{mm}(\omega). \tag{5.6}$$

The density of states projected to QMOs for Na_2IrO_3 are shown in Fig. 5.2 (b) [28]. In principle, when we sum up the QMO density, we should obtain the same DOS as directly calculated from DFT. In DFT, usually one uses the tetrahedron method to calculate the DOS. With QMOs, we directly add up the contribution from each $\mathbf{k}$ point, thus we need more $\mathbf{k}$ points to reproduce the DFT's DOS using the tetrahedron method. We consider Na_2IrO_3 as the example to compare the differences. We show the DOS with different number of $\mathbf{k}$ points N_k in Fig. 5.3 calculated within (a) the tetrahedron and (b) Green's function. The result shows that with 8000 $\mathbf{k}$ points, we can almost obtain the shape. However, in order to reproduce the tetrahedron result, we also need to be careful about the energy step δE and parameter η in the Green's function. We choose δE = 10 meV and show the DOS with different η values in Fig. 5.4 (a). With the decrease of η, the nonzero DOS around -1 and -0.5 eV decreases to the result obtained from the tetrahedron method in the DFT calculation 0. Thus, we choose η = 0.1 meV. With such small η, the DOS curve is not smooth, we therefore broaden and display the DOS from QMO and tetrahedron in Fig. 5.4 (b). With these settings, the QMO and DFT DOS are almost the same.

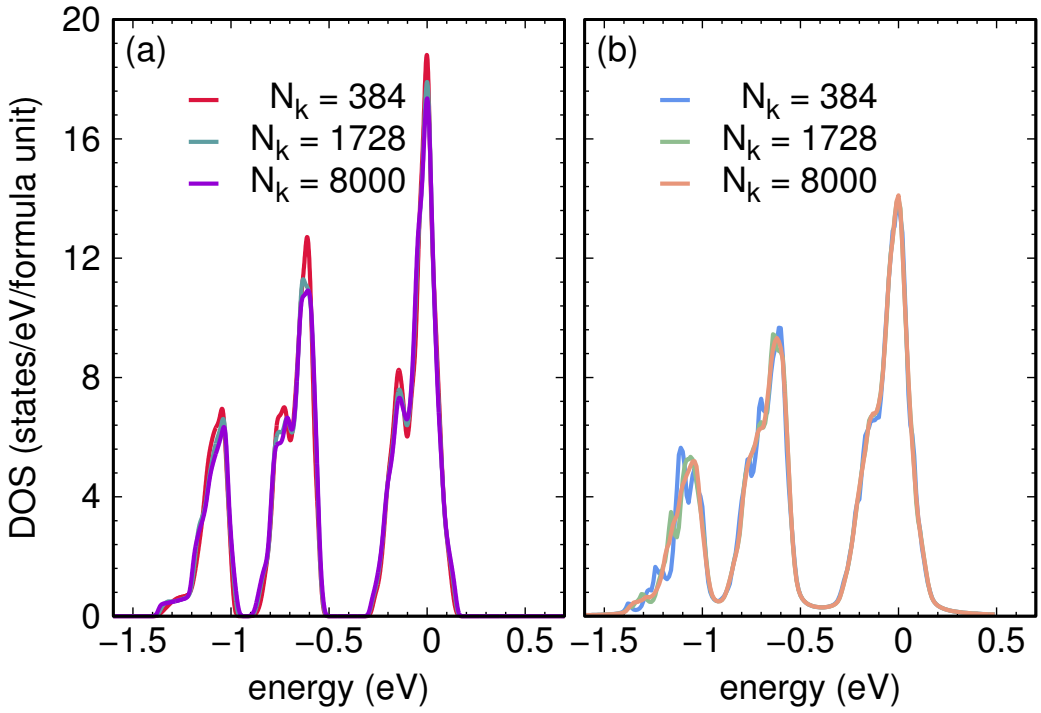

Figure 5.3: Density of states with different number of **k** points using (a) tetrahedron and (b) Green's function method.

5.2.2 Electronic structures with GGA+SO+U

The DFT calculations were performed using the LAPW basis with the GGA exchange-correlation functional in WIEN2k. The energy cut off for the basis RK_{max} was chosen to be 8. We used 450 **k** points in the first Brillouin zone (FBZ) for the self-consistency cycle and 1568 **k** points for the density of states and optical conductivity. Both magnetism and U_{eff} as implemented in GGA+U [60] were required to reproduce the experimentally observed optical gap. Spin-orbit coupling was considered with the second variational approximation (GGA+SO+U). For the zigzag antiferromagnetic (AFM) structure of Na_2IrO_3 (see Fig. 5.5) with the magnetization parallel to the **a** direction [14] we performed GGA+SO+U ($U = 3$ eV, $J_H = 0.6$ eV, $U_{\text{eff}} = U - J_H = 2.4$ eV) calculations[1]. Figure 5.6 shows the band structures and density of states (DOS) of Na_2IrO_3 with GGA, GGA+SO and GGA+SO+U for the

[1]Please note that the U value used in density functional theory calculations depends on how the U term is implemented in the calculation. For example, FPLO (full potential local orbital code) can reproduce the experimental gap of 340 meV with $U = 1.1$ eV and $J = 0.5$ eV while WIEN2k needs $U_{\text{eff}} = 2.4$ eV.

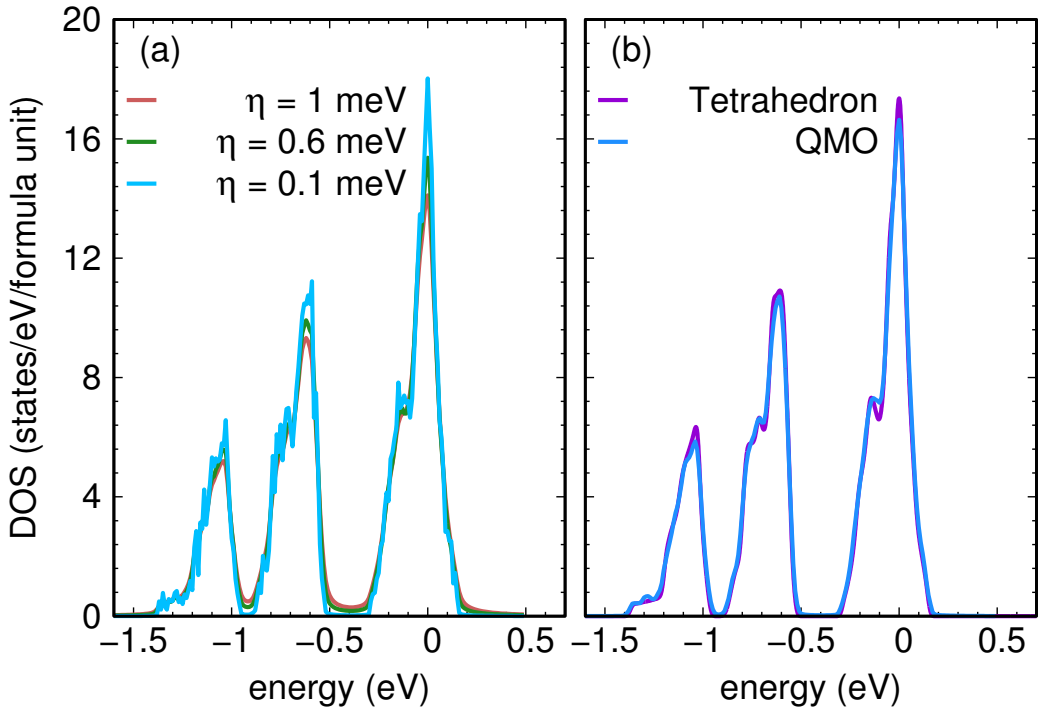

Figure 5.4: Density of states using Green's function (QMO) method (a) with different η values and (b) compared with tetrahedron result.

zigzag magnetic configuration. There are four Iridium in each unit cell, thus there are twelve t_{2g} bands for GGA. With spin-orbit coupling, the bands are split and a suppression of the DOS at E_F is clearly visible. This suppression is enhanced and opened to a 341 meV gap with GGA+SO+U, which is consistent with the experimental results [21].

5.2.3 Optical conductivity

Using the methods described in Chapter 3, we calculated the optical conductivity in LAPW with 1568 **k** points in the FBZ from the eigenstates of the GGA+SO+U calculations within the zigzag magnetic configurations. Because of the monoclinic symmetry, the optical conductivity tensor has four independent elements σ_{xx}, σ_{yy}, σ_{zz}, σ_{xy}:

$$\begin{pmatrix} J_x \\ J_y \\ J_z \end{pmatrix} = \begin{pmatrix} \sigma_{xx} & \sigma_{xy} & 0 \\ \sigma_{xy} & \sigma_{yy} & 0 \\ 0 & 0 & \sigma_{zz} \end{pmatrix} \begin{pmatrix} E_x \\ E_y \\ E_z \end{pmatrix}. \tag{5.7}$$

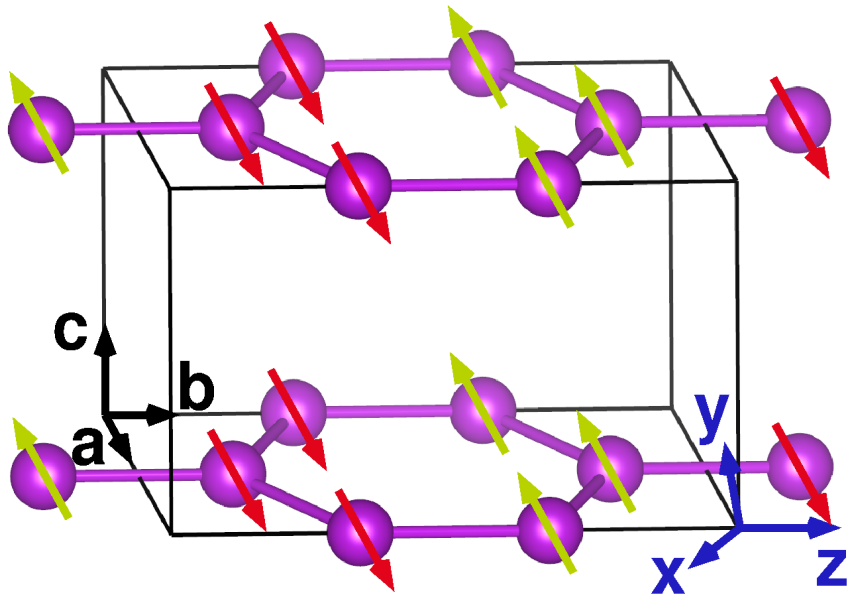

Figure 5.5: Ir honeycomb layers of Na_2IrO_3. The black axis **a**, **b**, and **c** are the vectors of the unit cell, while the dark blue axes **x**, **y**, **z** are the Cartesian axes. The red and green arrows show the zigzag AFM phase.

Where **x**, **y**, and **z** are the cartesian coordinates, as displayed in Fig. 5.5. **z** takes the **b** direction, which is in the Ir hexagonal plane, while **x** and **y** lie in the *ac* plane. Spin-orbit coupling also introduces tiny non-zero σ_{xz} and σ_{yz} components. We show, in Fig. 5.7 (a), the four optical conductivity tensor elements of Na_2IrO_3 in the t_{2g} region. All the components are different, which means the optical conductivity is anisotropic and depends on the direction. Only the component σ_{zz} is in the Ir hexagonal plane. We therefore compare σ_{zz} with the experimental results [21, 85] and a theory calculation using four-site iridium cluster by Kim *et al.* [86]. Both our DFT calculations and the cluster calculations [86] reproduce the experimental dominant peak at $\omega = 1.5$ eV.

5.2.4 Broadening

In order to compare with the experimental data, a Lorentzian broadening procedure was used in the calculations. We use different values of the Lorentzian broadening γ and show the corresponding optical conductivity σ_{zz} in Fig. 5.8. We choose $\gamma =$ 0.1 eV as the broadening for all the components.

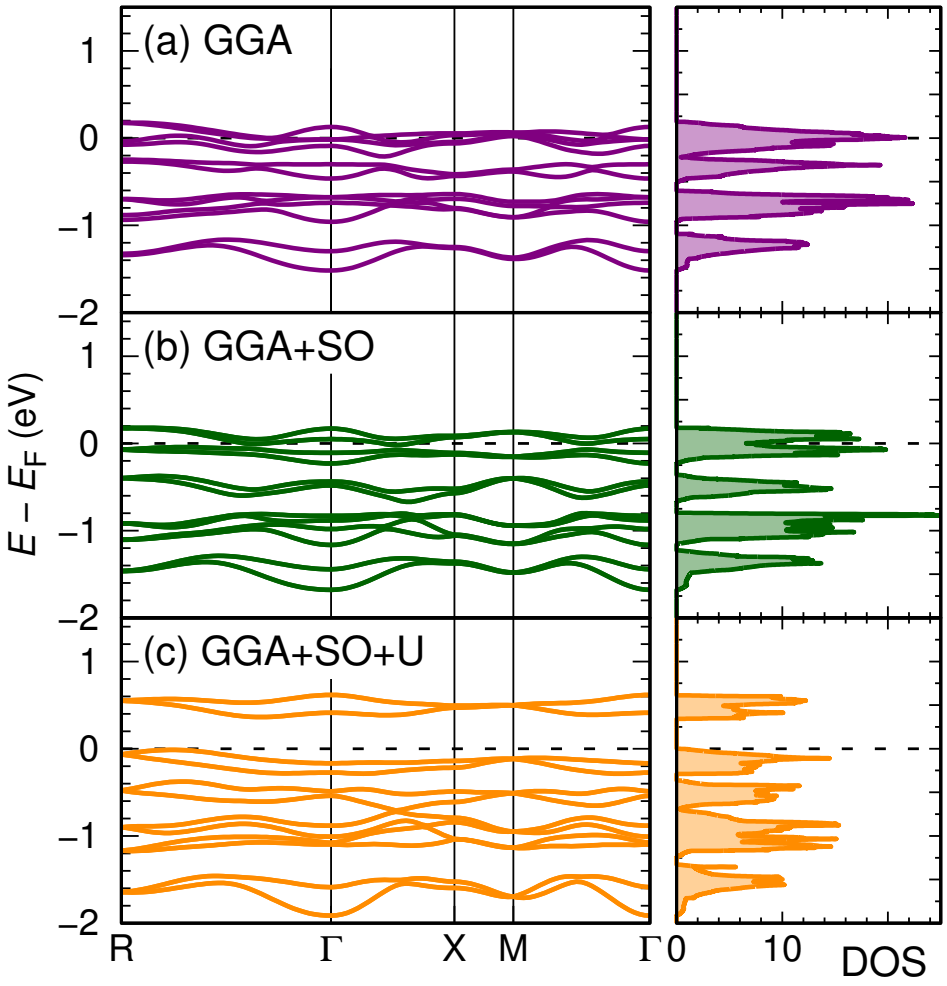

Figure 5.6: Ir 5*d* t_{2g} DOS and band structures for Na_2IrO_3 in zigzag magnetic order, obtained with (a) GGA, (b) GGA+SO, and (c) GGA+SO+U (U = 3 eV, J_H = 0.6 eV, U_{eff} = U-J_H = 2.4 eV).

5.2.5 Different $d-d$ transitions

The dominant peak was suggested to be due to the j_{eff}= 3/2 and j_{eff}= 1/2 transitions [85, 86] from the localized view. From the itinerant point of view, with the aim of disentangling the origin of the various peaks of the optical conductivity in Fig. 5.7, we show in Fig 5.9 the different interband processes. For that purpose, we label in Fig. 5.9 (a) the valence states v_s as a, b, c, d and the conduction states c_s as e. Note that the states denoted by c include twice the number of bands compared to the rest of the states. We identify four peaks in $\sigma(\omega)$ (Fig. 5.9 (b)); peaks A, B, C, D correspond to the transitions from a, b, c, d to e states, respectively. The analysis of

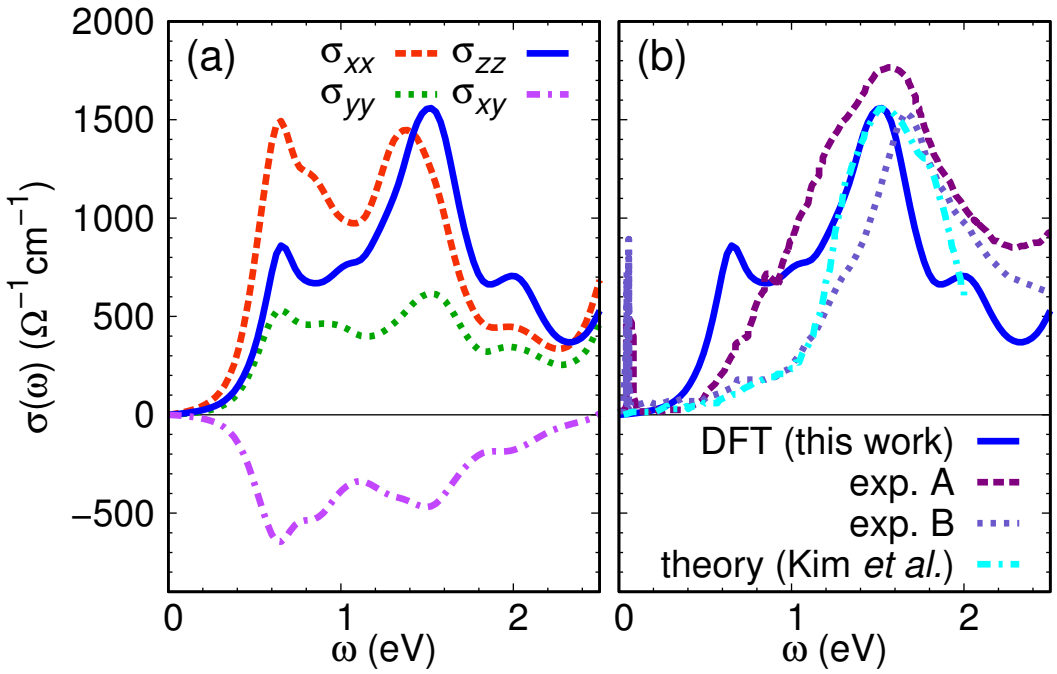

Figure 5.7: (a) Optical conductivity tensor components σ_{xx}, σ_{yy}, σ_{zz}, σ_{xy} and (b) DFT σ_{zz} for Na_2IrO_3 compared with experiment A [21], B [85] and theory data [86].

the electronic structure in terms of quasi-molecular orbitals [28, 29] predicts a clear odd/even parity related to the symmetry of the quasi-molecular orbitals, i.e., odd B_{1u}, even E_{1g}, odd E_{2u} and even A_{1g}. Even though the zigzag magnetic order used for the calculations mixes states of different parities, we find in our analysis of the magnetic quasi-molecular orbitals that the dominating parity contribution to a given state matches the parity of this state's counterpart in the paramagnetic phase. This, in particular, allows us to compare our spin-polarized calculations with the measurements performed above the magnetic transition temperature. In the GGA+SO+U calculations we find that the states a, b, c, d, and e are predominantly of even, odd, even, odd, and odd parity, respectively. Since c contains twice the number of bands, we have an equal number of (predominantly) even and odd states, as expected for a parity conserving system; note that in the presence of spin-orbit coupling the states from the upper triad cannot be identified in terms of quasimolecular orbitals, however, we can still discern the dominant parity. Since the dielectric tensor matrix elements involved in the optical interband transitions are of the form $\langle v_s|\mathbf{E}\cdot\mathbf{r}|c_s\rangle$, with $\mathbf{E}\cdot\mathbf{r}$ being an odd parity operator, clearly, transitions between states of the same parity will be strongly suppressed whereas transitions between states of different parity will dominate. This is reflected in the large peak at 1.5 eV (peak C)

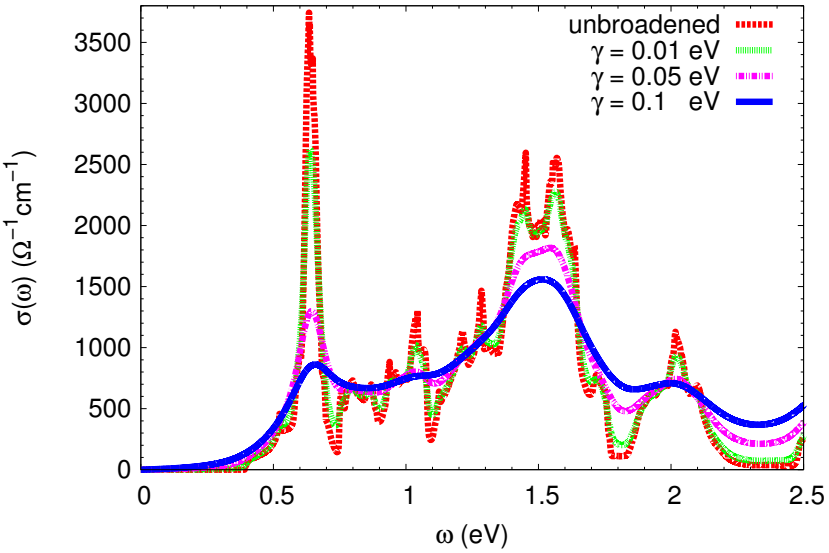

Figure 5.8: Optical conductivity for Na_2IrO_3 without and with different broadenings $\gamma = 0.01$, 0.05, and 0.1 eV.

that corresponds to a predominantly even to odd parity transition, followed by peak A (predominantly even to odd), while peaks B and D are of transitions between predominantly equal (odd) parity states and are strongly suppressed. The optical conductivity is therefore an important measure of the underlying molecular-orbital structure in Na_2IrO_3. Before dealing with α-Li_2IrO_3, we would like to discuss the possible origin of the experimentally observed suppressed intensity of the peak centered at A with respect to the calculations. Possible sources of discrepancy could be (i) the fact that the optical conductivity was measured in the ab plane and σ tensor components other than σ_{zz} could influence the results. However, we estimated this contribution by averaging over the nonzero tensor components and found the effect to be very small. Another source of discrepancy may be (ii) effects not accounted for in the present DFT calculations, such as high-order contributions not included in linear response theory or vertex correction in Kubo formula or correlation effects, which will be addressed further below in the Chapter 6.

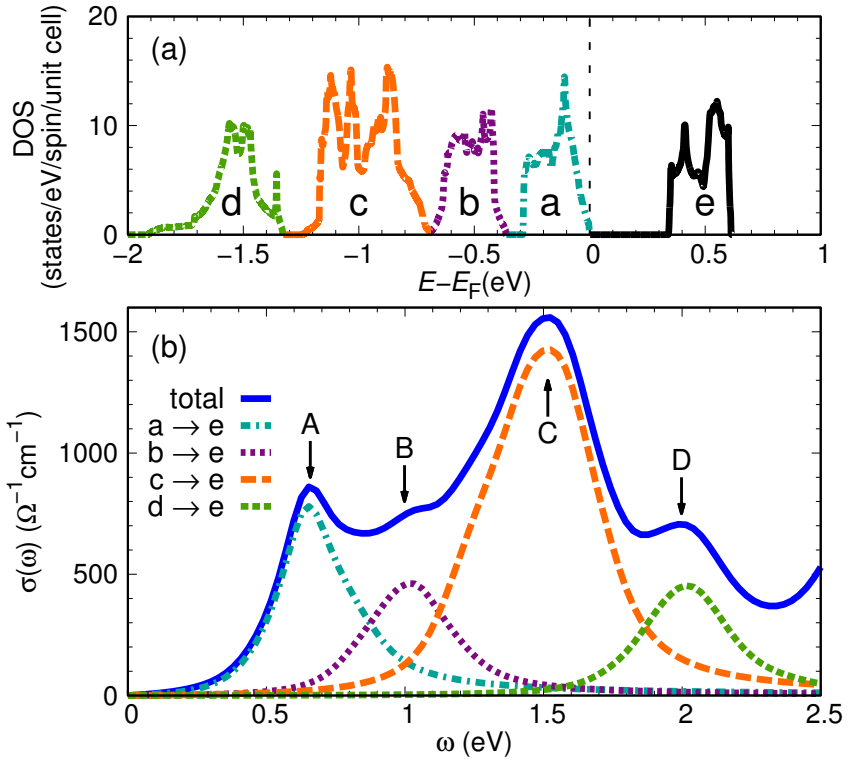

Figure 5.9: GGA+SO+U density of states (a) and contributions from different *d*-*d* transitions (b). The a, b, c, d, e label the 5 states.

5.3 Electronic structures and optical conductivity for α-Li_2IrO_3

5.3.1 Electronic structure

We project the nonmagnetic GGA density of states to the quasi-molecular orbitals in Fig. 5.10 for α-Li_2IrO_3. The QMO picture for this system is still valid, but shows significant QMO mixing, similar to Li_2RhO_3 [87]. As with Na_2IrO_3, for the experimental structure, the gap of 318 meV is opened with the inclusion of the magnetism as well as $U_{\text{eff}} = 2.4$ eV, while for theoretical structure which has less distortion, a gap of 307 meV is opened with $U_{\text{eff}} = 2.0$ eV. We present the electronic structure with GGA, GGA+SO, and GGA+SO+U for the experimental structure in Figure 5.11 (left) and for the relaxed structure in Figure 5.11 (right). The Zigzag GGA+SO calculations for the theoretical structure converges to the nonmagnetic phase and the DOS is suppressed at E_F, similar as Na_2IrO_3.

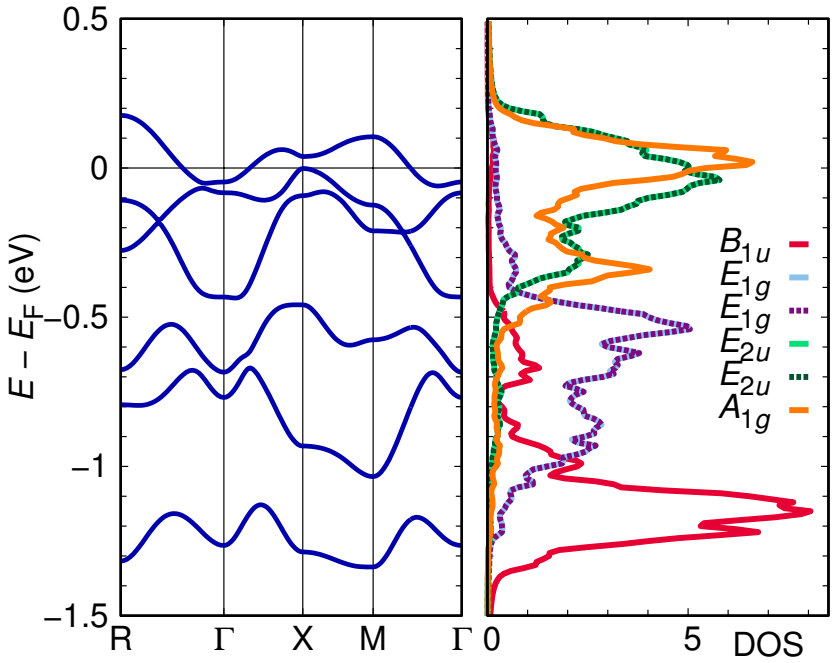

Figure 5.10: Nonrelativistic nonmagnetic band structure and density of states of the theoretically predicted α-Li_2IrO_3 structure, projected onto quasi-molecular orbitals.

5.3.2 Optical conductivity

Using the same method as Na_2IrO_3, we compare the optical conductivities of Na_2IrO_3 and α-Li_2IrO_3 in Fig. 5.12. The energy integral of the optical conductivity in both cases is proportional to the effective number density of electrons. While the dominant peak in the Na_2IrO_3 optical conductivity is at 1.5 eV, we find it at 1.17 eV for the experimental structure and at 1.33 eV for the theoretical structure of α-Li_2IrO_3 . Also, we observe an increase of the optical conductivity weight between 0.66 and 1.48 eV with respect to Na_2IrO_3.

5.3.3 Different $d-d$ transitions

We display different $d-d$ transitions in Fig. 5.13. In order to analyze this behavior, we project the nonmagnetic GGA electronic structure of α-Li_2IrO_3 onto the quasimolecular-orbital basis (see Fig. 5.10). We observe that the separation of the density of states into isolated narrow bands of unique quasimolecular-orbital characters is much less clean than in Na_2IrO_3 and resembles the case of Li_2RhO_3 [87].

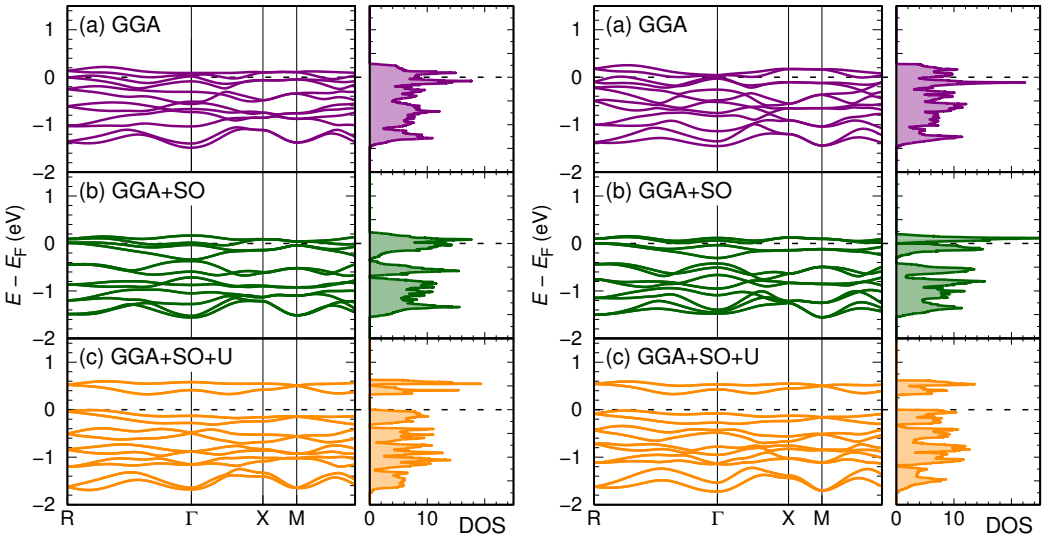

Figure 5.11: Ir $5d$ t_{2g} density of states and band structures for experimental α-Li_2IrO_3 structure in zigzag magnetic order (left) and for the theoretical α-Li_2IrO_3 structure in zigzag magnetic order (right), obtained with (a) GGA, (b) GGA+SO, and (c) GGA+SO+U.

In α-Li_2IrO_3, there is overlapping between B_{1u} and E_{1g} states and between E_{1g} and A_{1g}/E_{2u} states, as shown in Fig. 5.10. This strong mixing of character, which remains in the magnetic calculations, explains why the B peak in α-Li_2IrO_3 is much stronger than in Na_2IrO_3; the suppressed odd to odd transition in Na_2IrO_3 evolves into a mixture of enhanced and suppressed transitions in α-Li_2IrO_3.

5.4 Summary

In this chapter, we have investigated the electronic structure and optical conductivity in Na_2IrO_3 and α-Li_2IrO_3 by performing magnetic GGA+SO+U calculations. Magnetism and a nonzero U were necessary in order to reproduce the experimental insulating gap in both systems. Using the fact that the narrow bands of Na_2IrO_3 are well described in terms of quasi-molecular orbitals, we showed that the strength of the various interband contributions to the optical conductivity can be well described in terms of the parity of the quasi-molecular orbitals, namely, weight suppression in like-parity transitions and weight enhancement in unlike-parity transitions.

We also predict the shape of the optical conductivity for α-Li_2IrO_3. Contrary to

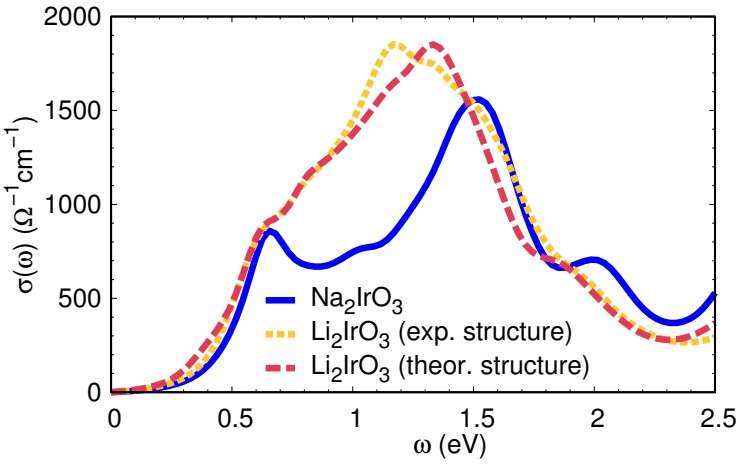

Figure 5.12: Comparison of the optical conductivity σ_{zz} between Na_2IrO_3 (experimental structure) and α-Li_2IrO_3 (experimental and theoretically predicted structure).

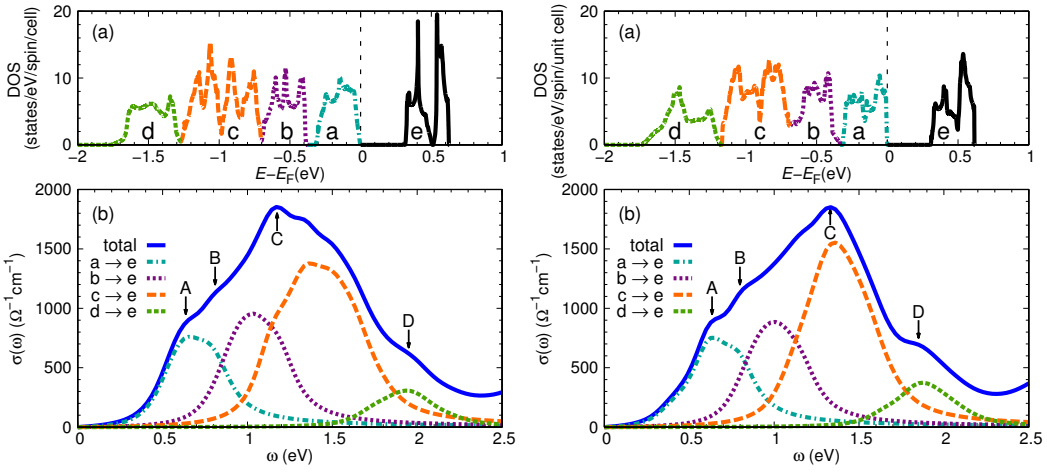

Figure 5.13: Density of states (a) and contributions from different *d-d* transitions (b) for the experimental α-Li_2IrO_3 structure (left) and for the theoretical α-Li_2IrO_3 structure (right). The a, b, c, d, e label the 5 states.

Na_2IrO_3, in α-Li_2IrO_3 the quasi-molecular orbitals strongly overlap and parities mix. This explains the relative weight differences in the optical conductivity between α-Li_2IrO_3 and Na_2IrO_3. We would like to emphasize that all the above DFT calculations have been performed with the inclusion of spin-orbit effects, and, strictly speaking, neither the t_{2g} (or the linear combination of t_{2g} states forming quasimolecular orbitals) nor spin are well-defined entities. Nevertheless, we have shown that the main features observed in optical conductivity are related to the underlying symmetries of the molecular-orbital basis, which is a manifestation of the fact that spin-orbit coupling is not the only determining interaction in these materials. We show the optical conductivity of these materials from a localized picture in Section 6.3 of the following chapter.

Chapter 6

Electronic excitations in γ-Li_2IrO_3

Ying Li, Stephen M. Winter, Harald O. Jeschke, Roser Valentí
Phys. Rev. B **95**, 045129 (2017) [34]

In the previous chapter, we have discussed the two-dimensional (2D) honeycomb lattice. In this chapter, we focus on the stripy-honeycomb γ-Li_2IrO_3. In order to gain microscopic insight on the electronic properties of γ-Li_2IrO_3 in comparison to its 2D counterparts, we present results on its electronic structure and optical conductivity within density functional theory (DFT) and the exact diagonalization (ED) method. In these 3D systems, the QMO picture is not valid because of the absence of well defined hexagon loops. For this reason, the $j_{1/2} \rightarrow j_{1/2}$ and $j_{1/2} \rightarrow j_{3/2}$ transitions are used to identify the main peaks. We also employ ED to study the 2D materials, and compare the results to those of γ-Li_2IrO_3.

6.1 Properties of γ-Li_2IrO_3

The γ-Li_2IrO_3 structure [11, 12], shown in Fig. 6.1 (a), has two Ir hexagonal chains in the directions of $\mathbf{a} \pm \mathbf{b}$, which are connected along the **c**-direction. Like α-Li_2IrO_3, Ir has an octahedral local environment with O. In figure 6.1 (b), we show the structure for γ-Li_2IrO_3 system with different bond definitions. The cartesian coordinates x, y, z for the orbitals are displayed in Fig. 6.1 (b). We define the two hexagonal chains as hexagonal A and hexagonal B. In A, the corresponding bonds are X_A, Y_A and Z_A while for B are X_B, Y_B, Z_B. An additional Z_C bond links the two

Table 6.1: Nearest neighbour distances (in Å) and Ir-O-Ir angles for the different bond types, determined in the experimental γ-Li_2IrO_3 structure (see Fig. 6.1 (b) for bond notation).

γ-Li_2IrO_3	X_A, Y_A	Y_B, X_B	Z_A, Z_B	Z_C
Ir-Ir distance	2.976		2.982	2.96
Ir-O1 distance	1.99,2.14		2.10	1.97
Ir-O2 distance	2.01,2.01		2.10	1.97
Ir-O1-Ir angle	92.00°		90.37°	97.40°
Ir-O2-Ir angle	95.52°		90.37°	97.40°

hexagons. There are two nonequivalent Ir atoms in each unit cell: Z_A and Z_B links the Ir(1) atoms while Z_C link Ir(2) atoms. Details of the crystal structure are given in Table. 6.1.

Similar with α-Li_2IrO_3, it also shows the spiral magnetic order, with wave vector 0.57 along the orthorhombic **a** axis [12]. In order to obtain this spin spiral states, the Kitaev interactions has been suggested to be dominant over the Heisenberg terms [12, 74, 83, 88–90]. The projection of the magnetic structure on the **ac** plane is the zigzag chain in the **a** direction. Since we cannot employ a non-collinear magnetic structure in the DFT calculations, we approximate the magnetic configuration with the zigzag state shown in Fig. 6.1 (c).

For the optical conductivity, the measurements for γ-Li_2IrO_3 [91] show the anisotropy for **a** and **b** direction and they both have a broad peak around 1.5 eV. Compared with Na_2IrO_3, the magnitude of $\sigma(\omega)$ in γ-Li_2IrO_3 is decreased, which has been attributed to the inherently 3D versus 2D structure rather than the replacement of Na by Li. However, a clear understanding of this behavior is still missing.

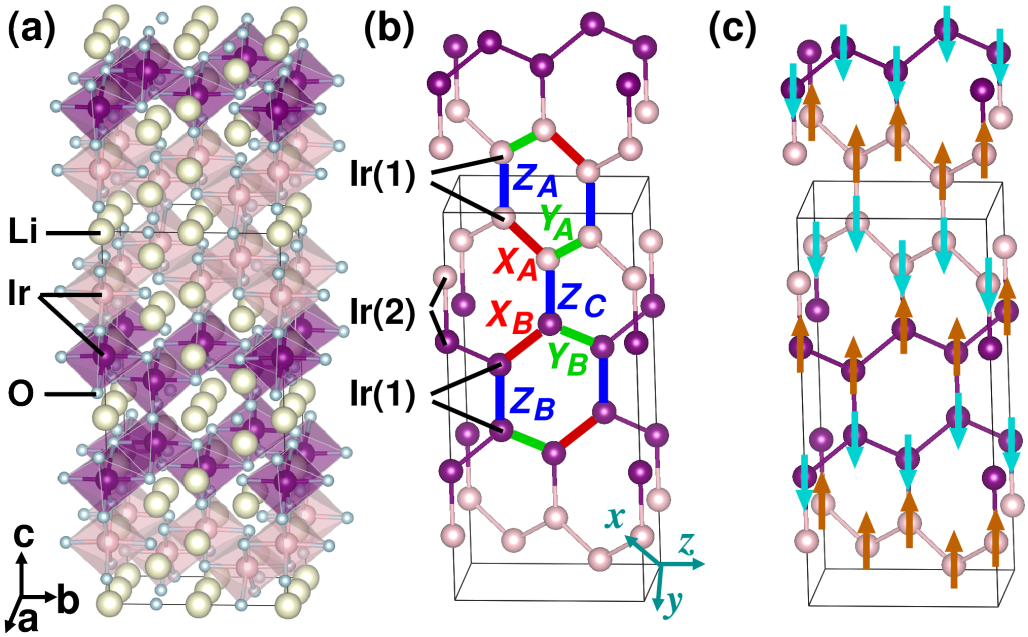

Figure 6.1: (a) Crystal structure of stripyhoneycomb γ-Li_2IrO_3 [11, 12]. Honeycomb rows alternating in orientation along **c**. The black axis **a**, **b**, and **c** are the vectors of the unit cell. (b) Crystal structure showing only Ir atoms. The red, green and blue bonds show the seven different types of bonds X_A, X_B, Y_A, Y_B, Z_A, Z_B, Z_C. x, y, z are the cartesian coordinates for the d orbitals. (c) The zigzag magnetic configurations used in our GGA+SO+U calculations.

6.2 Electronic properties of γ-Li_2IrO_3

6.2.1 Density functional theory calculations

We performed linearized augmented plane-wave (LAPW) calculations with the generalized gradient approximation (GGA) [51]. We chose the basis-size controlling parameter RK_{max} = 8 and a mesh of 432 **k** points in the first Brillouin zone (FBZ) of the primitive unit cell. Relativistic effects were taken into account within the second variational approximation. The hopping parameters between Ir 5d orbitals in γ-Li_2IrO_3 were computed via the Wannier function projection method and optical conductivity calculations with DFT described in Chapter 3. The density of states and optical properties were computed with 10 $\times$ 10 $\times$ 10 **k** points in the full Brillouin zone while the hopping parameters were evaluated using 12 $\times$ 12 $\times$ 12 **k** points. The non-relativistic GGA density of states (DOS) for γ-Li_2IrO_3 is displayed

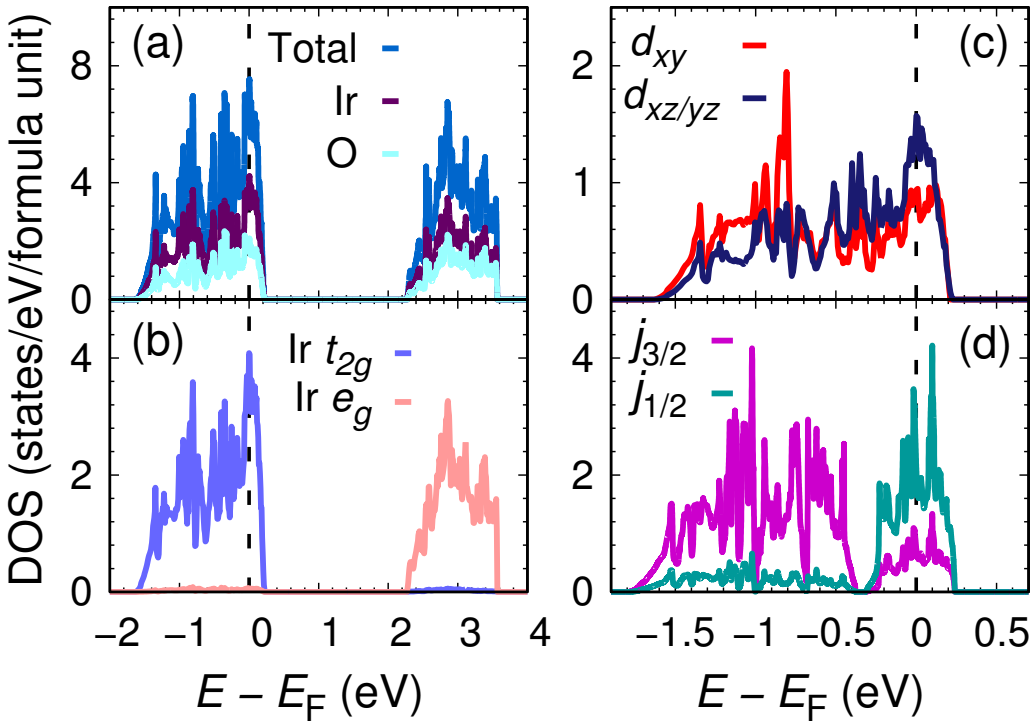

Figure 6.2: Density of states (DOS) for γ-Li_2IrO_3 in nonmagnetic configuration obtained with GGA (a-c) and GGA+SO (d).

in Fig. 6.2 (a) - (c). The Iridium 5d states are split into e_g (2.2 eV to 3.6 eV) and t_{2g} (-1.6 eV to 0.2 eV) states (Fig. 6.2 (b)) due to the octahedral crystal field of IrO_6 with the Fermi level lying within the t_{2g} manifold. The t_{2g} band is further slightly split into lower d_{xy} and higher d_{xz}, d_{yz} (Fig. 6.2 (c)), arising from an additional weak trigonal field. The band structures are shown in Fig. 6.3 (a). There are 24 bands in each unit cell, arising from the 3 t_{2g} bands of the 8 Ir.

By using the projection method described in Chapter 3, we obtained the hopping parameters from the GGA bandstructure. Table 6.2 displays the crystal field splitting compared with Na_2IrO_3. Full hopping integral tables are given in Appendix A. The t_{2g} crystal fields Δ_1, Δ_2 denote the on-site hopping between d_{xz} and d_{yz} orbitals, and between d_{xy} and $d_{yz/xz}$ orbitals, respectively (Table 6.2). Δ_3 is the on-site energy of d_{xy} minus that of $d_{yz/xz}$ [36]. Δ_3 is -213.5 meV for Ir(1) and -110.9 meV for Ir(2) (see Fig. 6.1), which is much larger in magnitude than in Na_2IrO_3 (-27.2 meV) [36]. This means that in the 3D γ-Li_2IrO_3 structure, the t_{2g} crystal field is of the same order of magnitude as the spin-orbit coupling λ and this likely has significant effects on the local magnetic interactions.

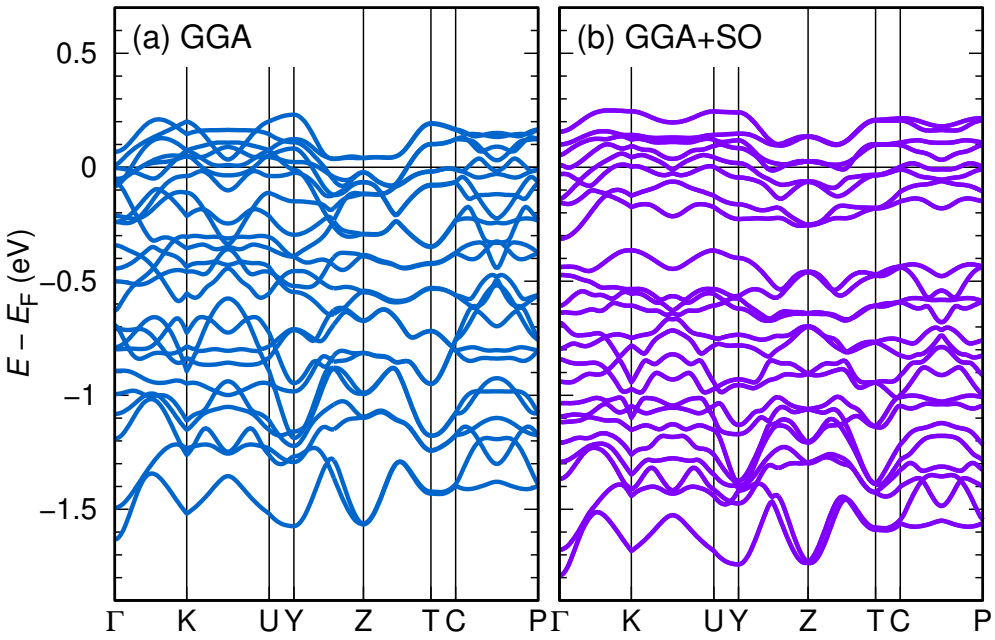

Figure 6.3: Ir $5d$ t_{2g} Band structures for γ-Li_2IrO_3 in nonmagnetic configuration, obtained with (a) GGA, (b) GGA+SO.

Table 6.3 shows the nearest neighbour hopping parameters where $t_{1\|}$, t_{1O} and $t_{1\sigma}$ are defined as in Ref. [29] while t_1, t_2, and t_3 are given in Ref. [36, 67] (see Fig. 8.7). There are three significant differences in the nearest neighbour hoppings of the 3D γ-Li_2IrO_3 (see Table 6.3) when compared with α-Li_2IrO_3:

- the direct metal-metal hopping $t_{1\sigma}$ ($d_{xy} \rightarrow d_{xy}$) along the Z_A and Z_B bonds (Fig. 6.1 (b)) is larger than the oxygen-assisted hopping t_{1O} ($d_{xz} \rightarrow d_{yz}$, $d_{yz} \rightarrow d_{xz}$) due to the nearly 90° Ir-O-Ir angle (Table 6.1),

- the t_{1O} in the X_A (Y_A), X_B (Y_B) bonds have opposite signs, as a result of different local environments. The negative value corresponds to type 1 bonds in Fig. 6.4, while the positive values are type 2 bonds.

- Finally, the absence of inversion symmetry for the majority of nearest neighbour bonds allows for some asymmetry in the t_{1O} hopping, e.g. for the X_A bond, $d_{xy} \rightarrow d_{xz}$ and $d_{xz} \rightarrow d_{xy}$ hoppings are unequal. For this reason, a finite Dzyaloshinskii-Moriya (DM) interaction is both allowed and expected to ap-

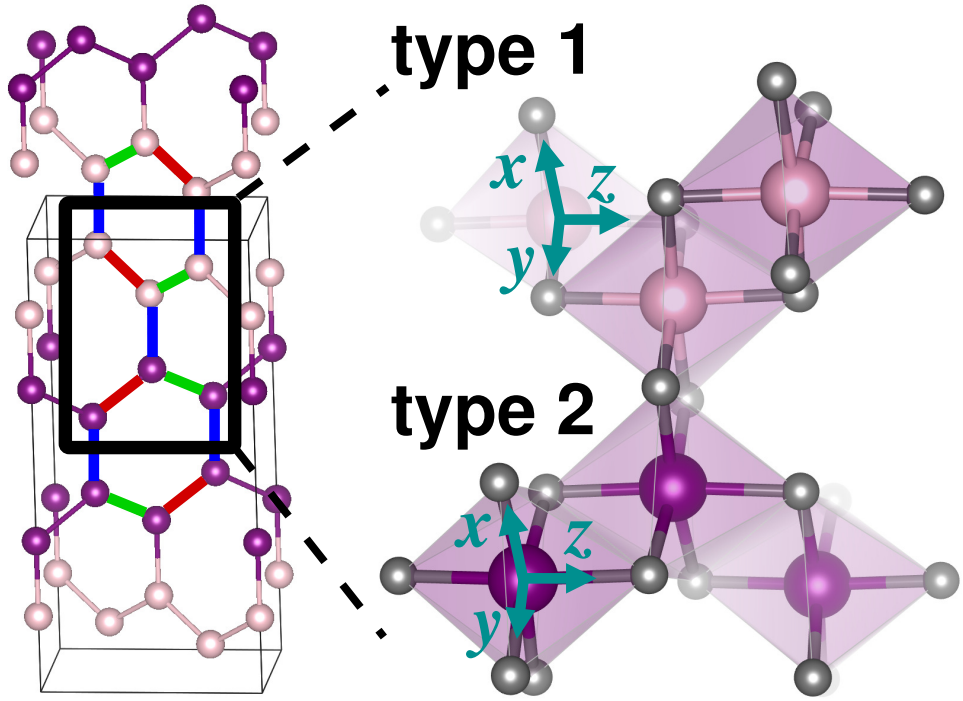

Figure 6.4: Local octahedral environment of type 1 and type 2 in γ-Li_2IrO_3.

Table 6.2: Crystal field splitting compared with Na_2IrO_3. The t_{2g} crystal fields Δ_1, Δ_2 denote, respectively, the onsite hopping between d_{xz} and d_{yz} orbitals, d_{xy} and $d_{yz/xz}$ orbitals. Δ_3 is the on-site energy of d_{xy} minus $d_{yz/xz}$ [36].

Crystal field	Na_2IrO_3 [36]	γ-Li_2IrO_3 Ir(1)	Ir(2)
Δ_1	-22.9	-24.4	-29.9
$\lvert\Delta_2\rvert$	27.6	4.2	37.4
Δ_3	-27.2	-213.5	-110.9

pear for the majority of first-neighbour bonds: X_A, X_B, Y_A, Y_B, and Z_C. This result is in contrast with α-Li_2IrO_3, for which a weaker DM interaction only exists for the second nearest neighbour bonds [36]. Since these antisymmetric interactions are likely to strongly stabilize the observed incommensurate magnetic order [12], one may question the completeness of previous interaction models for γ-Li_2IrO_3 including only symmetric exchange interactions [83, 88].

The full table of the onsite and nearest neighbour hopping parameters are shown in

Table 6.3: Nearest neighbour hopping integrals in meV between Ir t_{2g} orbitals for the experimental γ-Li_2IrO_3 structure (see Fig. 6.1 (b) for bond notation). The labels $t_{1\|}$, t_{1O} and $t_{1\sigma}$ are the same as in Ref. [29], and the notations t_1, t_2 and t_3 are given in Ref. [36, 67].

γ-Li_2IrO_3	X_A, Y_A	Y_B, X_B	Z_A, Z_B	Z_C
$t_{1\|}$ (t_1)	91.4	91.4	91.8	77.4
	69.2	69.2	91.8	77.4
t_{1O} (t_2)	-262.5	262.5	132.8	294.1
	-240.5	240.5	132.8	294.1
$t_{1\sigma}$ (t_3)	-168.3	-168.3	-319.7	-17.1

Table 6.4 and Table 6.5. Unlike the 2D Na_2IrO_3 and α-Li_2IrO_3, the 3D γ-Li_2IrO_3 does not allow a clear description of the DFT electronic structure in terms of QMOs. As in the $P3_112$ structure of α-$RuCl_3$ [18], the oxygen assisted hopping t_{1O}, which is crucial for the formation of the QMOs, is smaller than $t_{1\sigma}$ [18, 29]. In addition, since not all local Ir $5d$ orbitals can be attributed to a single hexagon, the QMO basis is incomplete. We therefore choose to work with the j_{eff} basis. Fig. 6.2 (d) shows the projection of the GGA+SO DOS onto the j_{eff} basis. At the Fermi level, the DOS is dominantly $j_{\text{eff}} = 1/2$ with a small contribution from $j_{\text{eff}} = 3/2$.

Inclusion of U within the GGA+SO+U approach in the zigzag magnetic configuration (Fig. 6.1(c)) opens a gap of 242 meV (Fig. 6.5) which is smaller than the experimentally measured value of 0.5 eV [91]. We note that the size of the gap is influenced by the choice of U. We however decided here to use the same U parameter as for previous calculations for Na_2IrO_3 and α-Li_2IrO_3 [33] in order to allow a better comparison further below. The magnetic moment converged to 0.58 μ_B for Ir(1) and 0.44 μ_B for Ir(2).

6.2.2 Exact diagonalization of finite clusters

While the GGA+SO+U calculations are able to describe many significant aspects of the electronic structure of γ-Li_2IrO_3 they do not fully capture effects originat-

Table 6.4: Hopping parameters for the on-site terms (meV). A is for hexagon including X_A, Y_A, Z_A bonds while B is for hexagon including X_B, Y_B, Z_B.

0	Ir(1) $xy \rightarrow xy$	-592.6
	Ir(1) $xz \rightarrow xz$	-379.1
	Ir(1) $yz \rightarrow yz$	-379.1
	Ir(2) $xy \rightarrow xy$	-651.3
	Ir(2) $xz \rightarrow xz$	-540.4
	Ir(2) $yz \rightarrow yz$	-540.4
Ir(1)		
	$xy \rightarrow xz$	4.2 (A), -4.2 (B)
	$xy \rightarrow yz$	4.2 (A), -4.2 (B)
	$xz \rightarrow yz$	-24.4
Ir(2)		
	$xy \rightarrow xz$	37.4 (A), -37.4 (B)
	$xy \rightarrow yz$	37.4 (A), -37.4 (B)
	$xz \rightarrow yz$	-29.9

Table 6.5: Nearest neighbor tight-binding hopping matrix elements (meV) for $\gamma - Li_2IrO_3$.

$\gamma - Li_2IrO_3$	X_A	X_B	Y_A	Y_B	Z_A	Z_B	Z_C
$xy \rightarrow xy$	91.4	91.4	91.4	91.4	-319.7	-319.7	-17.1
$xz \rightarrow xz$	69.2	69.2	-168.3	-168.3	91.8	91.8	77.4
$yz \rightarrow yz$	-168.3	-168.3	69.2	69.2	91.8	91.8	77.4
$xy \rightarrow xz$	-262.5	262.5	4.2	-4.2	63.9	-63.9	-18.7
$xz \rightarrow xy$	-240.5	240.6	76.5	-76.5	63.9	-63.9	18.7
$xy \rightarrow yz$	4.2	-4.2	-262.5	262.5	63.9	-63.9	-18.7
$yz \rightarrow xy$	76.5	-76.5	-240.5	240.6	63.9	-63.9	18.7
$xz \rightarrow yz$	-60.2	-60.2	-10.6	-10.6	132.8	132.8	294.1
$yz \rightarrow xz$	-10.6	-10.6	-60.2	-60.2	132.8	132.8	294.1

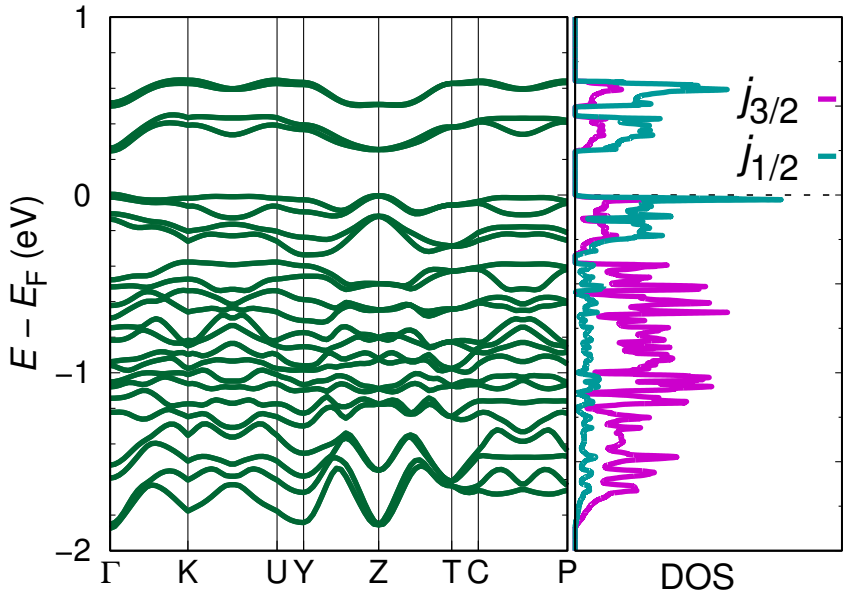

Figure 6.5: Ir 5*d* t_{2g} DOS and band structures for γ-Li_2IrO_3 in zigzag magnetic order, obtained with GGA+SO+U (U_{eff} = U-J_H = 2.4 eV).

ing from correlations beyond GGA+SO+U, which are expected to be relevant when analyzing electronic excitations. Therefore, we consider here a complementary approach to DFT, namely exact diagonalization of the fully interacting Hamiltonian on finite clusters [86] described in Chapter 3 and compare with DFT results. There are four symmetry inequivalent clusters constructed from bonds (X_A, Y_A, Z_A), (X_B, Y_B, Z_B), (X_A, Y_A, Z_C), and (X_B, Y_B, Z_C). The results presented correspond to an average over these four clusters.

In each four-site cluster, we consider states with a total of four holes in the t_{2g} orbitals; each Ir site contains six relativistic orbitals including two $j_{\text{eff}} = 1/2$ and four $j_{\text{eff}} = 3/2$ levels. As in Ref. [86], the states of the cluster can be divided into several subspaces based on the occupancy of the various orbitals and sites.

- States with site occupancy $d^5 - d^5 - d^5 - d^5$ are included in subspaces $\mathcal{S}_1 - \mathcal{S}_3$,
- states with site occupancy $d^4 - d^6 - d^5 - d^5$ belong to $\mathcal{S}_4 - \mathcal{S}_7$,
- $\mathcal{S}_8$ contains all higher excitations.

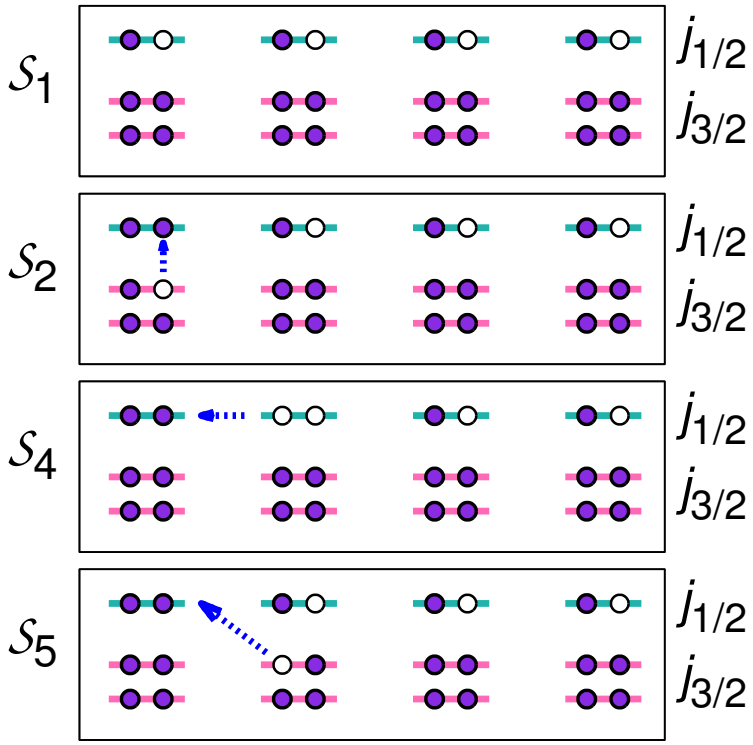

Figure 6.6: Schematic diagrams of cluster for the ground state $\mathcal{S}_1$ and one particle excitation $\mathcal{S}_2$, $\mathcal{S}_4$, and $\mathcal{S}_5$. The solid circles are the electrons while the empty circles indicate the hole. $\mathcal{S}_1$ are all the states with $(j_{3/2})^4(j_{1/2})^1$, $\mathcal{S}_2$ are the states with from $\mathcal{S}_1$, promotion of an electron $j_{3/2} \to j_{1/2}$ on the same site. $\mathcal{S}_4$ are the states from $\mathcal{S}_1$, promotion of an electron $j_{1/2} \to j_{1/2}$ to another site, and $\mathcal{S}_5$ are the states with promotion of an electron $j_{3/2} \to j_{1/2}$.

We show the diagrams of cluster for the ground state $\mathcal{S}_1$ and one particle excitation $\mathcal{S}_2$, $\mathcal{S}_4$, and $\mathcal{S}_5$ in Fig. 6.6.

- Subspace $\mathcal{S}_1$ contains all states with $(j_{3/2})^4(j_{1/2})^1$ occupancy at every site, and form a significant contribution to the ground state and low-lying magnon-like spin excitations.

- From these configurations, promotion of an electron via *onsite* $j_{3/2} \to j_{1/2}$ generates $\mathcal{S}_2$, containing all states with a single spin-orbital exciton; the characteristic excitation energy is given by $\Delta E_2 \sim 3\lambda/2 \sim 0.6$ eV. States with

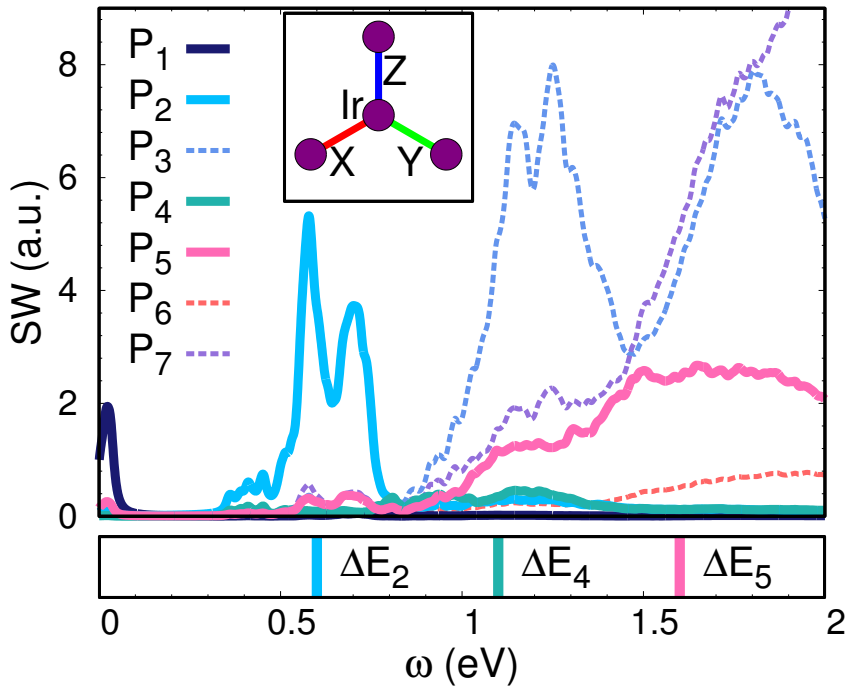

Figure 6.7: The investigated four-site cluster (inset) and spectral weight (SW) of projected excitations spectra for γ-Li_2IrO_3. P_1 is for all states with with $(j_{3/2})^4(j_{1/2})^1$ ($\mathcal{S}_1$), P_2 and P_3 are for the states with exciton on one site ($\mathcal{S}_2$) and exciton on more ($\mathcal{S}_3$), respectively. P_4 is for the states from $\mathcal{S}_1$, promotion of an electron $j_{1/2} \rightarrow j_{1/2}$ to another site ($\mathcal{S}_4$), and P_5 is for states with promotion of an electron $j_{3/2} \rightarrow j_{1/2}$ ($\mathcal{S}_5$). P_6 is for states contain two-particle excited states for which the d^4 site contains occupancies $(j_{3/2})^2(j_{1/2})^2$ ($\mathcal{S}_6$), while P_7 are for all other excitations with occupancy of $d^4 - d^6 - d^5 - d^5$ ($\mathcal{S}_7$). $\Delta E_2 \sim 0.6$ eV, $\Delta E_4 \sim 1.1$ eV, $\Delta E_5 \sim 1.6$ eV are the excitation energy for P_2, P_4 and P_5 respectively.

multiple excitons are grouped into $\mathcal{S}_3$, and represent n-particle excitations from the ground state, with energies $\Delta E_3 \sim 3n\lambda/2 \sim 1.2, 1.8, \ldots$ eV.

- Starting from $\mathcal{S}_1$, promotion of an electron via *intersite* $j_{1/2} \rightarrow j_{1/2}$ yields $\mathcal{S}_4$, with characteristic energy $\Delta E_4 \sim \mathbb{A}^{-1}$, where $\mathbb{A}$ is in Eq. (4.60). Taking $U = 1.7$ eV, $J_H = 0.3$ eV, and $\lambda = 0.4$ eV suggests $\Delta E_4 \sim 1.1$ eV.

- Starting from $\mathcal{S}_1$, promotion of an electron via *intersite* $j_{3/2} \rightarrow j_{1/2}$ yields $\mathcal{S}_5$, with characteristic energy $\Delta E_5 \sim \mathbb{C}^{-1} \sim 1.6$ eV, where $\mathbb{C}$ is in Eq. (4.60).

- Subspace $\mathcal{S}_6$ contains two-particle excited states for which the d^4 site contains

occupancies $(j_{3/2})^2(j_{1/2})^2$, while subspace $\mathcal{S}_7$ contains all other excitations with occupancy of $d^4 - d^6 - d^5 - d^5$.

Single particle excitations most relevant for the optical conductivity are contained in $\mathcal{S}_1$, $\mathcal{S}_4$, $\mathcal{S}_5$. We project the cluster eigenstates ϕ_m on different subspaces:

$$\Gamma_i^m = \sum_{s \in \mathcal{S}_i} |\langle \phi_m | s \rangle|^2 , \tag{6.1}$$

and take the spectral weight (SW) of the projected excitation spectra P_i [92]:

$$P_i(\omega) = \sum_m \Gamma_i^m \delta(\omega - E_m) . \tag{6.2}$$

P_1 to P_7 are shown in Fig. 6.7. As expected, the ground state and low-lying magnon-like spin excitations ($\omega \sim 0$ eV) have the dominant $\mathcal{S}_1$ character (large P_1), while intersite hopping weakly mixes in some $\mathcal{S}_2$, $\mathcal{S}_4$, $\mathcal{S}_5$ character. Indeed, *intersite* $j_{3/2} \rightarrow j_{1/2}$ mixing as in $\mathcal{S}_5$ is the origin of the anisotropic Kitaev exchange couplings in the localized picture.

Centered at $\omega = \Delta E_2 \sim 0.6$ eV are the single exciton-like states, with dominant $\mathcal{S}_2$ character, but weakly mixing with the single-particle $\mathcal{S}_4$ and $\mathcal{S}_5$ and multi-particle $\mathcal{S}_6$ and $\mathcal{S}_7$ excitations via intersite hopping. As expected, excitations with dominant $\mathcal{S}_4$ character (i.e. $j_{1/2} \rightarrow j_{1/2}$) are centered around $\omega = \Delta E_4 \sim 1.1$ eV, and excitations with dominant $\mathcal{S}_5$ character (i.e. $j_{3/2} \rightarrow j_{1/2}$) are centered around $\omega = \Delta E_5 \sim 1.6$ eV. The widths of these bands are approximately 1 eV and 2 eV, respectively. It is worth noting that the total spectral weight $\int P_i \, d\omega$ is much larger for $\mathcal{S}_5$ than $\mathcal{S}_4$, such that $j_{3/2} \rightarrow j_{1/2}$ excitations dominate the projected excitation spectra. Similar results were obtained in Ref. [86] in the analysis of the excitation spectrum of Na_2IrO_3. The real part of the optical conductivity is calculated using Eq. (3.100) in Chapter 3.

Note that the expression of the optical conductivity considered in DFT is defined at zero temperature and in k space while in ED we consider the definition in real space and at finite temperature $k_B T$ = 30 meV (room temperature). We observe that the finite temperature modifies the zero temperature results only slightly. The optical conductivity is normalized by the sum-rule that the energy integral of the optical conductivity in both ED and DFT methods is proportional to the effective density of electrons.

For γ-Li_2IrO_3, the orthorhombic symmetry of the space group allows the optical

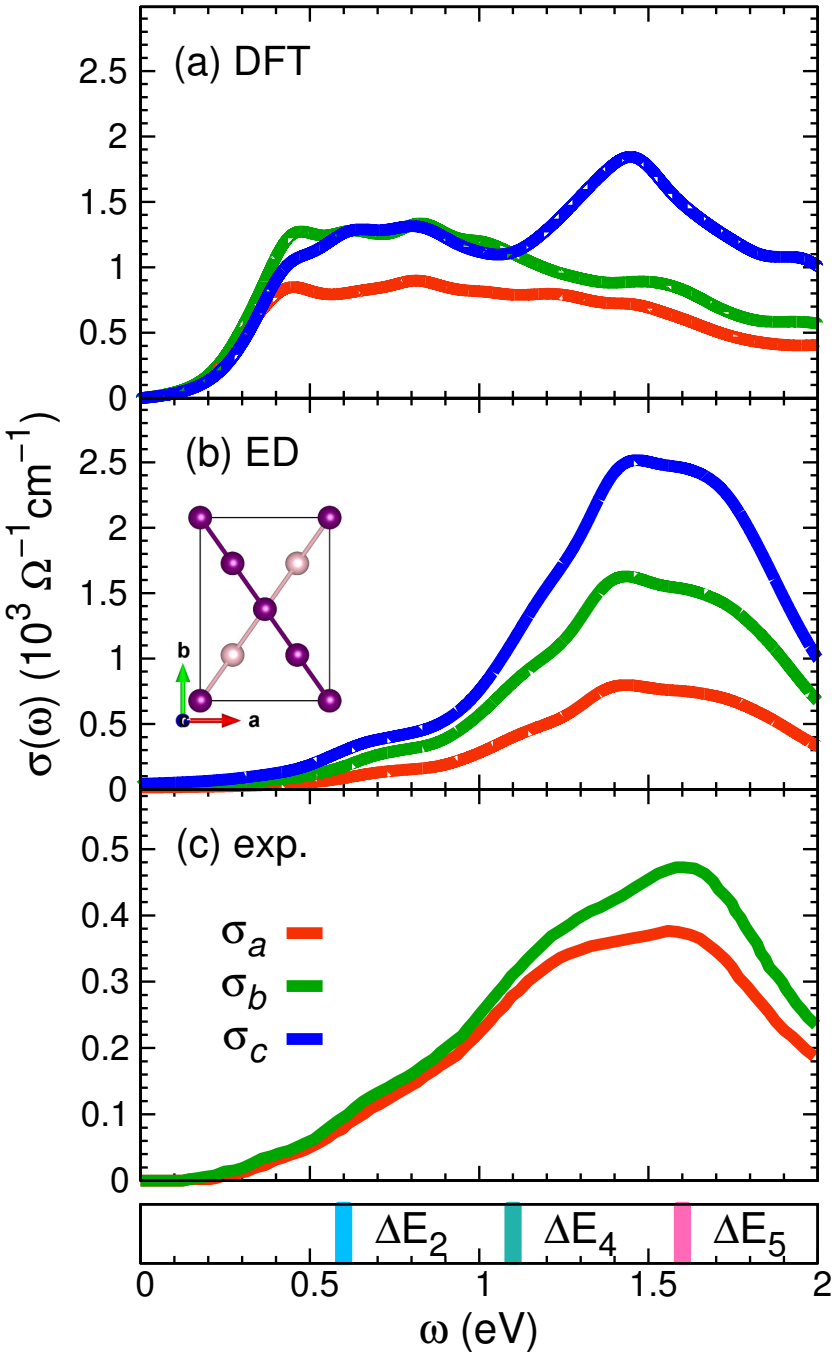

Figure 6.8: Optical conductivity components for γ-Li_2IrO_3 in (a) DFT, (b) ED method and (c) Experiment [91]. $\Delta E_2 \sim 0.6$ eV, $\Delta E_4 \sim 1.1$ eV, $\Delta E_5 \sim 1.6$ eV are the excitation energy for P_2, P_4 and P_5 respectively. The inset of (b) is the crystal structure projected in **ab** plane.

conductivity tensor to be defined in terms of the three independent components σ_a, σ_b, σ_c (σ_a= $\sigma_{x'x'}$, σ_b= $\sigma_{y'y'}$, σ_c= $\sigma_{z'z'}$):

$$\begin{pmatrix} J_a \\ J_b \\ J_c \end{pmatrix} = \begin{pmatrix} \sigma_a & 0 & 0 \\ 0 & \sigma_b & 0 \\ 0 & 0 & \sigma_c \end{pmatrix} \begin{pmatrix} E_a \\ E_b \\ E_c \end{pmatrix}. \tag{6.3}$$

In Fig. 6.8, we compare the DFT (GGA+U+SO), ED and experimental optical conductivity tensor components for γ-Li_2IrO_3 in the low-frequency region. Both DFT and ED capture correctly the anisotropy $\sigma_a < \sigma_b$, which is due to the structural orientation of the planes shown in the inset of Fig. 6.8 (b). In Eq. 3.101, for the same $\mathbf{r}_{ij}$, the b component $\mathbf{r}_{ij}^{y'}$ (contributing to σ_b) is larger than the a component $\mathbf{r}_{ij}^{x'}$ (contributing to σ_a), and therefore $\sigma_b > \sigma_a$. While ED calculations show a dominant peak around $\omega = 1.5$ eV for all polarizations, the DFT results suggest also significant spectral weight at lower frequencies, particularly within the **ab** plane, which doesn't seem to agree with the experimental results. The origin of this anomalous spectral weight can be found in Fig. 6.9. For the DFT calculations, we show the decomposition of $\sigma(\omega)$ into intraband $j_{1/2} \rightarrow j_{1/2}$ and interband $j_{3/2} \rightarrow j_{1/2}$ excitations, while for the ED calculations, we plot the projection of $\sigma(\omega)$ onto $\mathcal{S}_5 \rightarrow \mathcal{S}_2$, $\mathcal{S}_1 \rightarrow \mathcal{S}_4$ (i.e. $j_{1/2} \rightarrow j_{1/2}$), and $\mathcal{S}_1 \rightarrow \mathcal{S}_5$ (i.e. $j_{3/2} \rightarrow j_{1/2}$) excitations. Both methods suggest that the peak around 1.5 eV is dominated by interband $j_{3/2} \rightarrow j_{1/2}$ contributions. However, the DFT calculations don't have a proper partition of the $j_{1/2} \rightarrow j_{1/2}$ transitions into magnon-like ($\omega \sim 0$) and charge-transfer ($\omega \sim \mathbb{A}^{-1}$) excitations, resulting in a dramatic overestimation of the $j_{1/2} \rightarrow j_{1/2}$ spectral weight in the mid-energy region ~ 0.5 eV.

6.3 Comparison to Na_2IrO_3 and α-Li_2IrO_3

In the previous chapter, we analyzed the excitation spectrum of the 2D honeycomb systems in terms of the QMO basis and we showed that the parity of the quasi-molecular orbitals is largely responsible for the strength of the optical transitions in these systems. Here we investigate the excitation spectrum via ED calculations. Despite differences in crystal architecture, the experimental optical conductivity of γ-Li_2IrO_3, Na_2IrO_3 and α-Li_2IrO_3 share a very similar profile that we will ana-

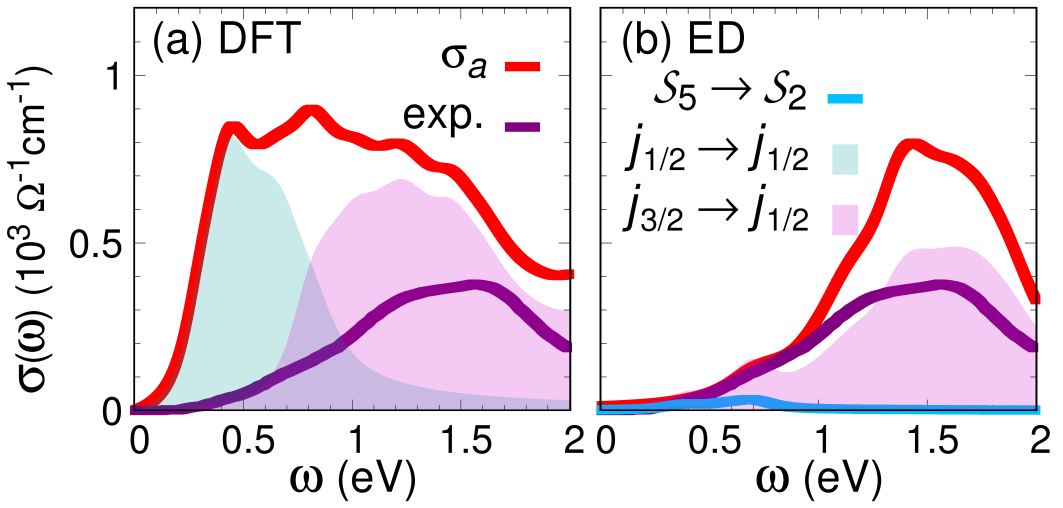

Figure 6.9: (a) Optical conductivity component σ_a for γ-Li_2IrO_3 and different $d-d$ transitions in relativistic basis using (a) DFT method and (b) ED method compared with experiment [91].

lyze in what follows. As stated in the previous section, $\sigma(\omega)$ should therefore be dominated by intersite $j_{3/2} \rightarrow j_{1/2}$ excitations, at $\omega \sim \mathbb{C}^{-1} \sim 1.6$ eV, as observed. The soft shoulder observed at lower energies results from a combination of low spectral weight from intersite $j_{1/2} \rightarrow j_{1/2}$ excitations centered at $\omega \sim \mathbb{A}^{-1} \sim 1.1$ eV, and weak mixing with optically forbidden local $j_{3/2} \rightarrow j_{1/2}$ excitons near $\omega \sim$ 0.6 eV. These assignments are consistent with the fitting of $\sigma(\omega)$ in Ref. [85] for Na_2IrO_3, which suggested peaks in the vicinity of 0.72, 1.32, and 1.66 eV. However, the "band gap" reported to be 0.32 eV may be significantly contaminated by low-lying excitonic states, and may therefore not represent the natural charge gap of the material.

There are two noticeable differences between the optical conductivity of Na_2IrO_3 and γ-Li_2IrO_3 observed experimentally. The first one is that $\sigma(\omega)$ tends to have smaller values for the latter material due to geometric considerations mentioned above. For the 2D structure, the experimental polarization is exactly within the honeycomb plane, maximizing $\sigma(\omega)$, while for the 3D structure, light is polarized along **a** and **b**, capturing both in-plane and out-of-plane components.

In Fig. 6.10 we display the DFT and ED results for the in-plane σ_c component for Na_2IrO_3, α-Li_2IrO_3 (which was labeled as σ_{zz} in Ref. [33]) and γ-Li_2IrO_3. For α-Li_2IrO_3, we employed the recently obtained single-crystal structure[93]. Both

calculations give a stronger main peak in α-Li_2IrO_3 and γ-Li_2IrO_3 than Na_2IrO_3 for σ_c. Further, both DFT and ED calculations show an enhanced spectral weight at lower energies in γ-Li_2IrO_3 with respect to Na_2IrO_3, which has also been observed experimentally. A possible origin of this enhancement can be seen by writing the hopping integrals in the relativistic basis for the Z bond:

$$t_{ij}(j_{1/2} \rightarrow j_{1/2}) \propto (2t_1 + t_3), \tag{6.4}$$

$$t_{ij}(j_{3/2}; m_{\pm 1/2} \rightarrow j_{1/2}) \propto (t_3 - t_1), \tag{6.5}$$

$$t_{ij}(j_{3/2}; m_{\pm 3/2} \rightarrow j_{1/2}) \propto t_2. \tag{6.6}$$

For materials dominated by oxygen-assisted hopping such as Na_2IrO_3, $t_2 \gg t_1, t_3$ means that hopping is dominated by $t_{ij}(j_{3/2}; m_{\pm 3/2} \rightarrow j_{1/2})$, suggesting negligible spectral weight for $j_{1/2} \rightarrow j_{1/2}$ excitations in $\sigma(\omega)$. In contrast, for significant t_1, t_3, additional spectral weight may appear in the mid-energy region due to enhanced $t_{ij}(j_{1/2} \rightarrow j_{1/2})$. The Kitaev limit of the magnetic interactions will therefore be most closely approached, at the level of nearest neighbour interactions, by materials with the lowest spectral weight near $\omega \sim 1.1$ eV. This identifies Na_2IrO_3 as the closest material from all three investigated here, in agreement with Ref. [36]. The origin of the peaks for Na_2IrO_3 in the relativistic basis are shown in Fig. 6.11 for both calculations.

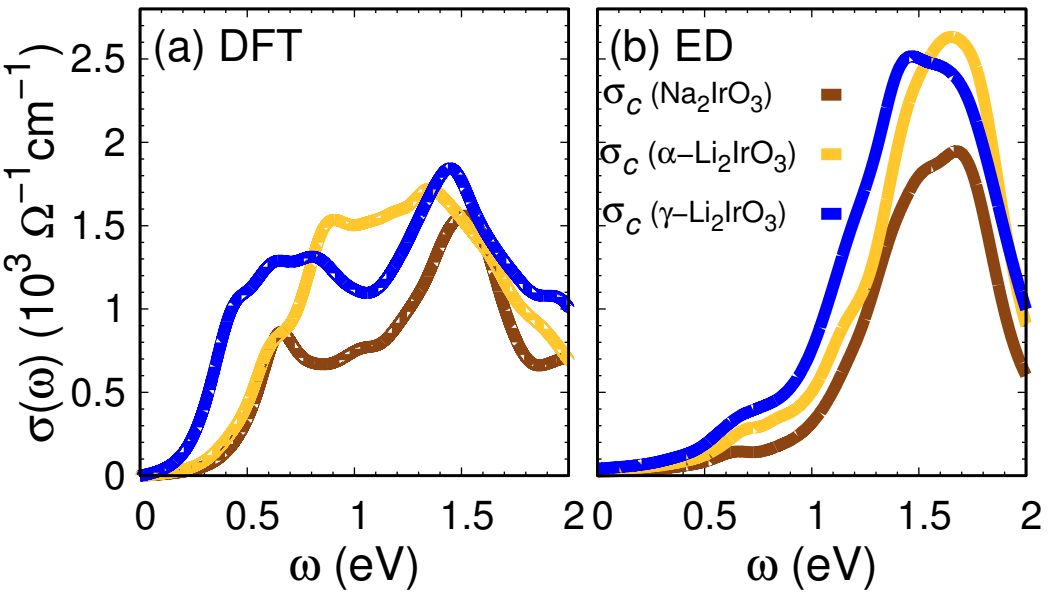

Figure 6.10: Optical conductivity σ_c for Na_2IrO_3, α-Li_2IrO_3, and γ-Li_2IrO_3 using (a) DFT and (b) ED method. σ_c of Na_2IrO_3 and α-Li_2IrO_3 corresponds to the σ_{zz} component in Ref. [33].

6.4 Summary

In summary, we have investigated the electronic structure, hopping parameters and optical excitation spectrum of the three-dimensional γ-Li_2IrO_3. Due to the lower symmetry of the local Ir-O-Ir environment, the hopping integrals display significant deviations from the ideal case, suggesting e.g. large metal-metal hoppings and departures from inversion symmetric values. This situation likely leads to highly complex magnetic interactions in this system.

We computed the optical conductivity by two methods; (i) relativistic DFT calculations within GGA+SO+U and (ii) exact diagonalization of the full interacting Hamiltonian on finite clusters where the hopping integrals were obtained from DFT. Both methods reproduce the main peak of the in-plane component of the optical conductivity σ_c. However, GGA+SO+U seems to overestimate the contribution of the $j_{1/2} \rightarrow j_{1/2}$ transition at low energies in σ_a and σ_b. The ED results, in contrast, validate the model parameters (U, J_H, λ) and suggest that the high-lying excitations seem to be well captured within a localized picure in γ-Li_2IrO_3. The comparison with the optical conductivity analysis of Na_2IrO_3 shows that the peak near 1.5 eV

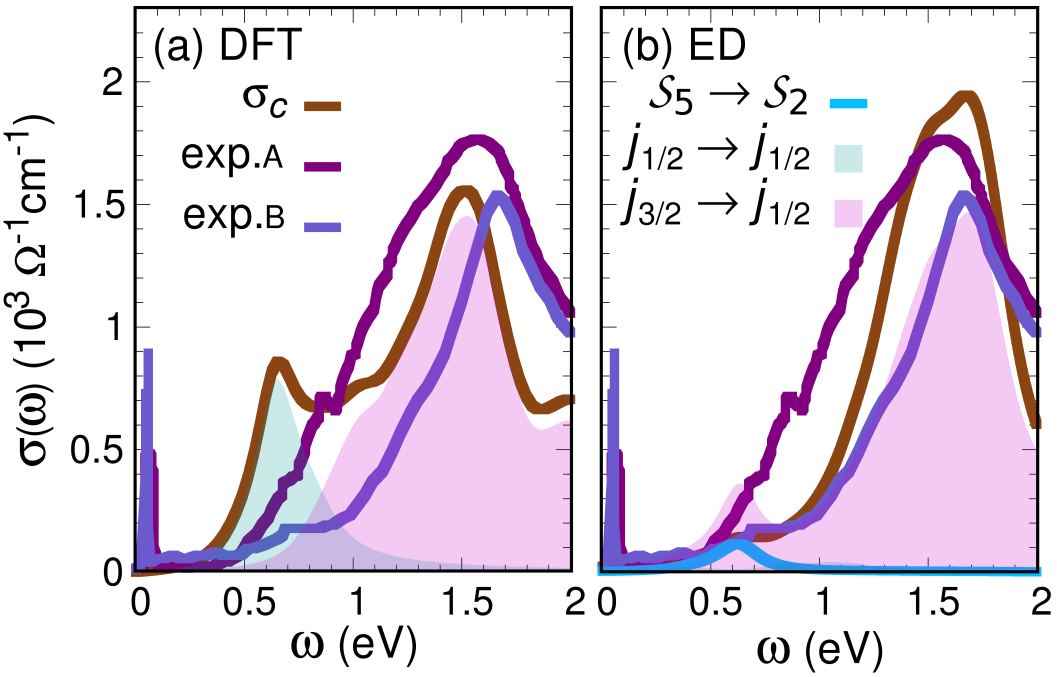

Figure 6.11: Optical conductivity component σ_c for Na_2IrO_3 and different $d-d$ transitions in relativistic basis using (a) DFT and (b) ED method compared with experiment A in Ref. [21] and B in Ref. [85]. σ_c of Na_2IrO_3 for DFT corresponds to the σ_{zz} component in Ref. [33].

in both Na_2IrO_3 and γ-Li_2IrO_3 can be identified in terms of *intersite* $j_{3/2} \rightarrow j_{1/2}$ excitations. The comparison of $\sigma(\omega)$ for the various materials suggests that the relative spectral weight of the transitions may provide insight into the magnitudes of various hopping integrals, and therefore the local magnetic interactions.

Chapter 7

Electronic properties of α-$RuCl_3$

R. D. Johnson, S. Williams, A. A. Haghighirad, J. Singleton, V. Zapf,
P. Manuel, I. I. Mazin, **Y. Li** , H. O. Jeschke, R. Valentí, R. Coldea
Phys. Rev. B **92**, 235119 (2015) [18]
F. Lang, P. J. Baker, A. A. Haghighirad, **Y. Li**, D. Prabhakaran,
R. Valentí, S. J. Blundell
Phys. Rev. B **94**, 020407 (R) (2016) [35]

In Chapter 5, we discussed the 5*d* honeycomb materials A_2IrO_3 (A = Na, Li). In these materials, the combined effect of strong spin-orbit coupling at the Ir^{4+}, crystal field, and correlation effects are both important. They can be understood as the relativistic j_{eff} =1/2 and j_{eff} = 3/2 states, which is described by the Kitaev model from the localized view, while also be described as the QMO picture from the itinerant view. Recently, the 4*d* Ru honeycomb lattice has been also proposed as a candidate of Kitaev material [25]. Due to the smaller atomic number, Ru is expected to have weaker spin-orbit coupling, however, the correlation effects in a narrow band could potentially enhance the effects of spin-orbit coupling [25, 27].

In this chapter, we will discuss the structure of α-$RuCl_3$, magnetic order, and the *ab initio* electronic-structure [18]. Further, we will also calculate the electrostatic potential in α-$RuCl_3$ for the muon spin rotation experiment [35].

7.1 Properties of α-$RuCl_3$

The Ru^{3+} ion in α-$RuCl_3$ also has a d^5 configuration but with an octahedral cage of Cl^- instead of O^{2-} in Na_2IrO_3. These octahedra are also arranged in a layered, edge-shared honeycomb network with space group that has been experimentally determined as $P3_112$ [94] or $C2/m$ [18] shown in Fig. 7.1. The α-$RuCl_3$ structure has stacking faults because of weak bonding between the honeycomb layers. The three-layer stacking periodicity with the space group of $P3_112$ was proposed in an early study [94]. The $C2/m$ structure both at room temperature and the lowest temperature measured (80 K) consists of a single layer in each unit cell. This structure was obtained from the experimentally determined space group and lattice parameters, with in DFT to relax the positions of the atoms. This constrained structural model was then checked with the intensities in the X-ray diffraction data. There are also other possibilities to have a stacking faults shown in Fig. 7.2.

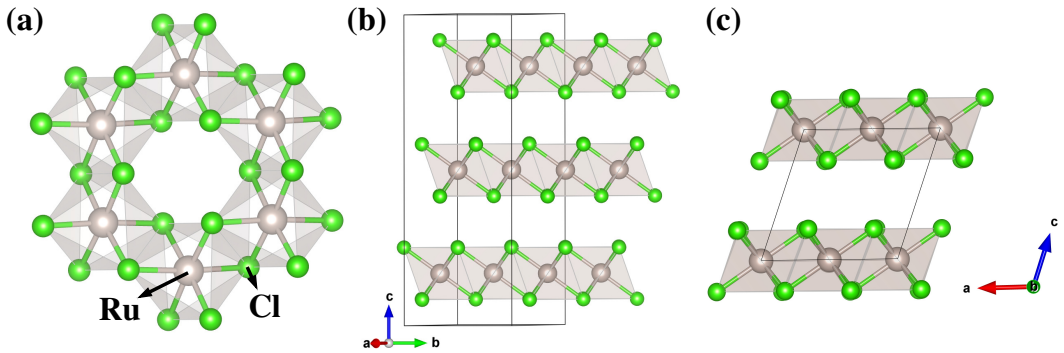

Figure 7.1: Crystal structure of α-$RuCl_3$, Ru as gray balls, and Cl as green. (a) Honeycomb layers. (b) P_3112 structure. (c) $C2/m$ structure.

Many experimental and theoretical investigations have been devoted to the magnetic properties of α-$RuCl_3$ [17, 19, 25, 96–100]. The spectroscopic studies found α-$RuCl_3$ is a Mott insulator [24, 25]. The magnetic susceptibility and specific heat indicate it to have AFM order near ~ 7 K [17, 96, 97]. Further, neutron scattering experiments [17–19] found this order is zigzag below $T_N \sim 7-14$ K, similar as Na_2IrO_3. However, α-$RuCl_3$ has a FM Weiss constant $\Theta_{iso} \sim +40$ K and the reverse susceptibility anisotropy $\chi_{ab} > \chi_c$ [17, 101], compared to Na_2IrO_3, suggesting a different character of the magnetic interactions.

Because of the similar structure as the honeycomb iridates, it is also considered to

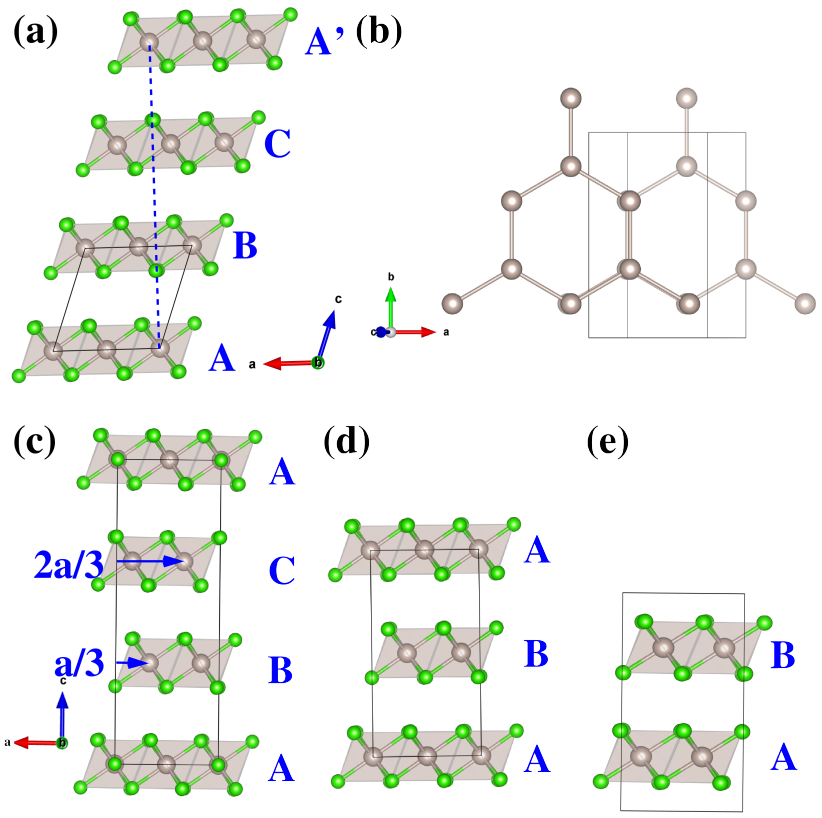

Figure 7.2: Structures and stacking orders proposed for α-$RuCl_3$. Grey and green spheres represent Ru and Cl atoms, respectively. Panel (a) shows the $C2/m$ structure with panel (b) highlighting that the A and A$'$ layers almost overlap when viewed along the c^* direction. The angle between direction AA$'$ and the a axis is 89.523°. Panel (c) presents the ABC stacking proposed in Ref. [95] (see Fig. 1 (b) there), which is almost identical to the $C2/m$ structure since $a/3 \approx -c * cos\beta$. Panel (d) shows the AB stacking proposed in Ref. [95] (see Fig. 1 (c) there) with panel (e) representing a unit cell for this AB stacking within the $C2/m$ symmetry obtained by allowing bond length differences of up to 10^{-4} .

be a candidate to display Kitaev physics. Although the SO interaction for 4d Ru^{3+} is small [98] ($\lambda_{Ru} \sim 0.15$ eV [27]), its effects can be enhanced by the electronic correlation effects [27], which introduce a splitting of the j_{eff} = 1/2 and j_{eff} = 3/2 states. The structure in the space group of $C2/m$ has a small distortion. Several theoretical investigations have been done to explain the magnetic response [19, 27, 96].

7.2 Electronic structure

7.2.1 Density of states with quasi-molecular orbitals

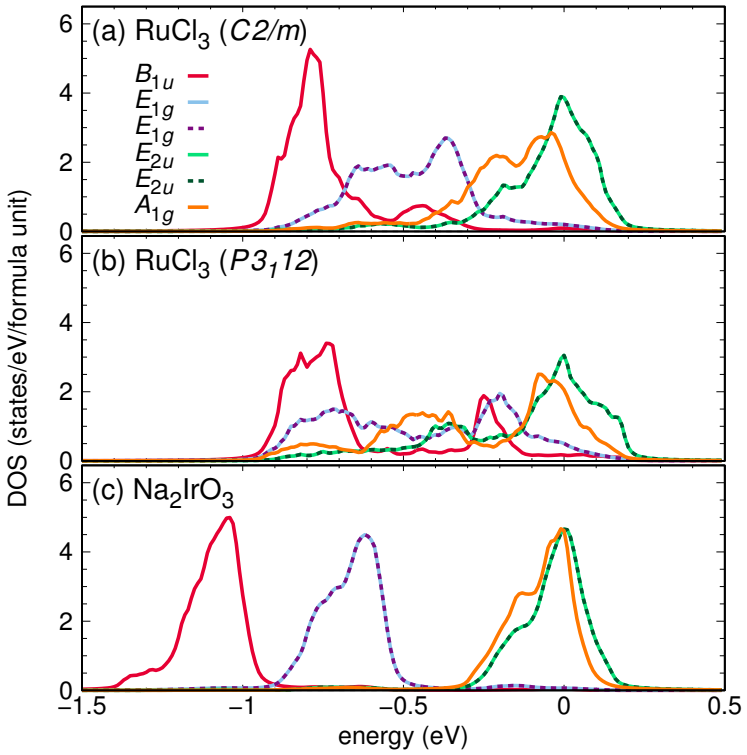

Figure 7.3: GGA density of states projected onto the quasi-molecular orbital basis of (a) α-$RuCl_3$ in the $C2/m$ structure, (b) α-$RuCl_3$ in the $P3_112$ structure and (c) Na_2IrO_3.

The electronic structure was calculated within LAPW method, the basis-size controlling parameter RK_{max} was 8 and a mesh of $8 \times 6 \times 8$ **k** points in the FBZ for the self-consistency cycle considered and a $12 \times 12 \times 12$ **k** points were used for the density of states. Structurally, the difference of the $P3_112$ [94] and $C2/m$ for one layer seems to be very small. However, the small structural differences make the electronic properties change sharply. The $P3_112$ structure has shorter Ru-Ru bonds, and less trigonal distortion. As a result, the dominant hopping for $P3_112$ is the direct metal-metal hopping $t_{1\sigma}$ while in $C2/m$ structure, the dominant hopping is the Cl p orbital assisted t_{1O} . Similar as Na_2IrO_3 [28, 29, 33], if t_{1O} is dominant, it leads to formation of quasi-molecular orbitals that consist of a linear combination of t_{2g} states of the six Ru atoms in each hexagon. We present the *nonrelativistic* density of states within GGA projected onto the QMO basis for α-$RuCl_3$ in the $C2/m$ and

$P3_112$ structures as well as for Na_2IrO_3 in Fig. 7.3. From the figure, it is clear that α-$RuCl_3$ ($C2/m$) and α-Na_2IrO_3 are nearly diagonal in the QMO basis. However, for α-$RuCl_3$ ($P3_112$), the QMO states are strongly mixed.

7.2.2 Electronic structure with GGA+SO+U

Since in this structure, the spin-orbit and correlation effects are important, we further calculated the electronic structure of α-$RuCl_3$ including the spin-orbit effects (GGA+SO) and including both spin-orbit and onsite Coulomb repulsion together (GGA+SO+U). We display the results in Fig. 7.4. For Na_2IrO_3 [28, 29], the strong spin-orbit coupling lifts the near-degeneracy of the two highest QMO, A_{1g} and E_{2u}, in order to form the relativistic $j_{\text{eff}} = 1/2$ states. In contrast, the QMOs picture is still valid in the relativistic case because of the weaker spin-orbit coupling in $4d$ Ru than $5d$ Ir (see Fig. 7.4 (b)). What's more, U has strong effect on the electronic structure, as shown in Fig. 7.4 (c). This is due to the increase of the effective spin-orbit coupling compared to the renormalized hoppings by a factor of t/U. As a result, the electronic structure including both spin-orbit coupling and Coulomb repulsion surprisingly agrees with the results for Na_2IrO_3 [28, 29, 33] of the $j_{\text{eff}} = 1/2$ and $j_{\text{eff}} = 3/2$ projection. We project the GGA+SO+U band structure for α-$RuCl_3$ into the j_{eff} basis as presented in Fig. 7.4. Although there is some mixing between the j_{eff} = 1/2 and j_{eff} = 3/2, the dominant contribution to the Fermi level is still j_{eff} = 1/2 states. Thus, we can still describe this system in the basis of j_{eff} = 1/2 orbitals, which is similar as $P3_112$ structure [27].

7.3 Electrostatic potential

F. Lang *et al.* [35] performed muon spin rotation experiments on α-$RuCl_3$ to probe the magnetic configurations. In this experiment, spin polarized muons are implanted into the sample, and decay after some time to produce positrons. In order to predict the muon stopping sites, we performed DFT calculations to compute the Electrostatic potential. We used the DFT method to plot the electrostatic Coulomb potentials of α-$RuCl_3$. In the potential map, the local maximal values give the possible positions of the muon stopping sites. We employed DFT calculations in LAPW with

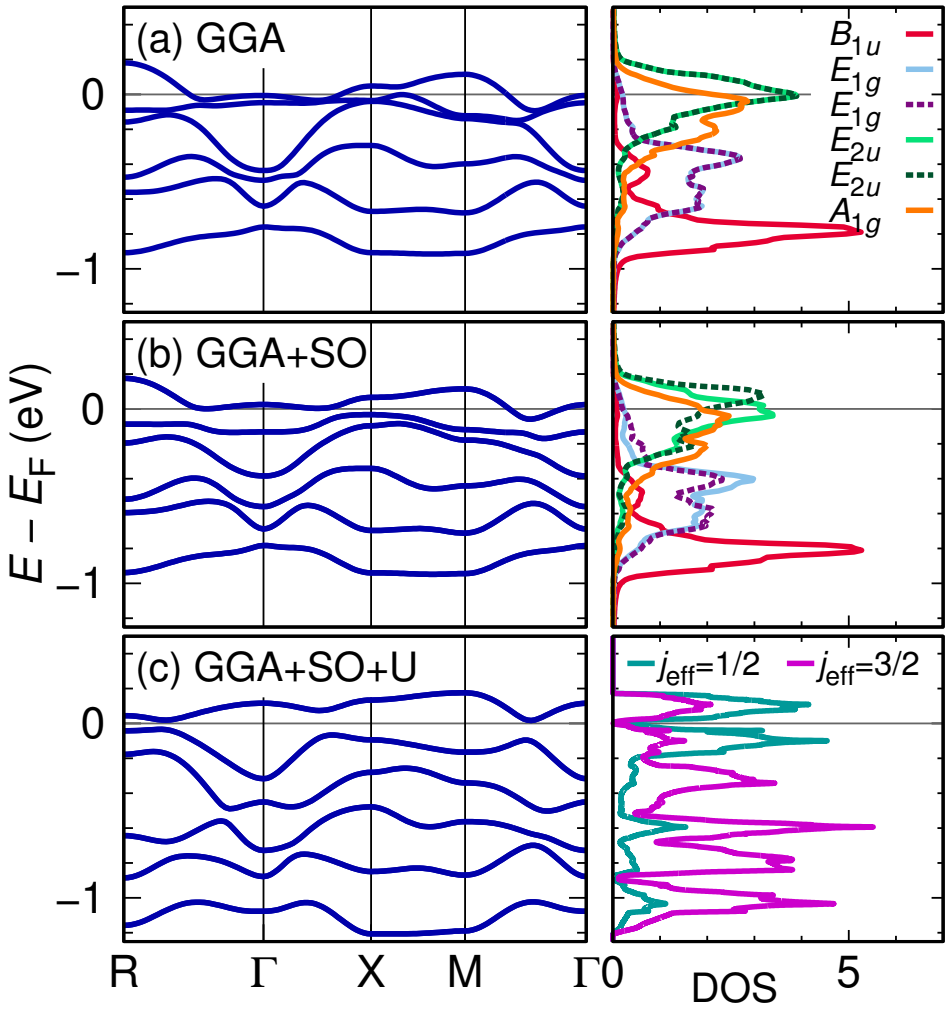

Figure 7.4: Band structure and density of states of α-$RuCl_3$ in the $C2/m$ structure obtained within (a) GGA, (b) GGA+SO, and (c) GGA+SO+U (U_{eff} = 3 eV). The right panel shows the projected nonmagnetic GGA and GGA+SO density of states onto the quasi-molecular orbital basis [28, 29] and the GGA+SO+U density of states onto the relativistic j_{eff} basis.

RK_{max} = 9 and 800 **k** points in the FBZ with GGA exchange-correlation function. From the converged electron density, the 3D electrostatic potential was computed with the combination of XCrySDen package [102] and WIEN2k, and then visualized by the VESTA software [103].

We set the maximal of the potential to zero and present the Coulomb potential map in Fig 7.5. It is possible for the muon to stop in any local maxima region. This suggests four possible muon stopping sites presented in Fig. 7.5 and Table 7.1. The site labeled Mu1 has the smallest energy cost and largest Coulomb potential 0 eV, while

the site labeled Mu4 has a potential energy lower than Mu1 by 0.4 eV. When a moun stops at such potential positions, it may also perturb its local environment, through short-ranged interactions important only for the nearest neighbour ions [104, 105]. Thus, a small displacement of Cl^- ion is also considered.

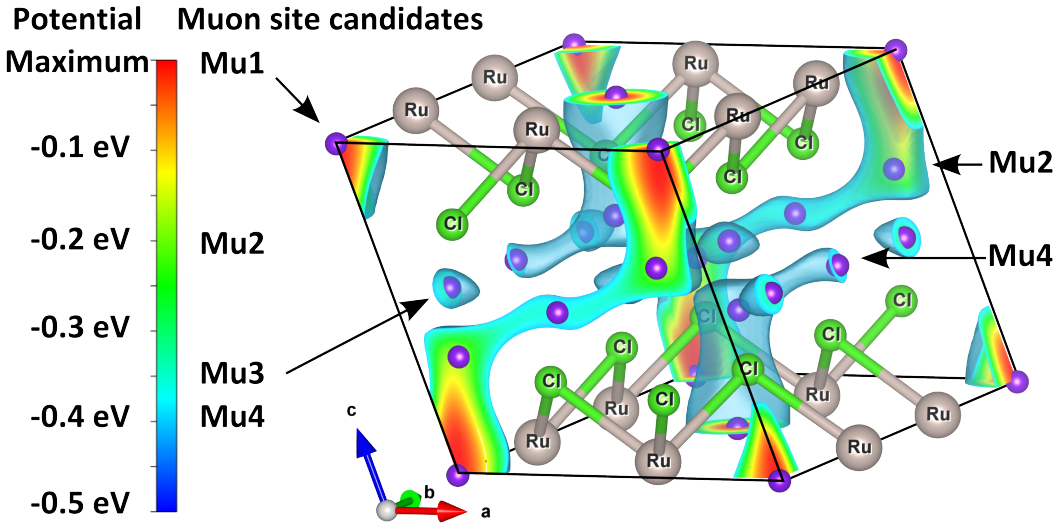

Figure 7.5: Coulomb potential of α-$RuCl_3$ calculated via DFT. The blue isosurface plotted is at -0.4 eV below the maximum. The purple spheres indicate the muon site candidates we identified. Their labels are placed next to the color scale to indicate the approximate value of the potential at the sites.

We identify, with the help of density functional theory calculations, likely muon stopping sites and combine these with dipolar field calculations to show that the two measured muon rotation frequencies are consistent with two inequivalent muon sites within a zigzag antiferromagnetic structure proposed previously.

Then the experimental group Lang *et al* [35] used muon stop positions from our DFT and combined these with dipolar field calculations to show that the two measured muon rotation frequencies are consist with two inequivalent muon sites within a zigzag antiferromagnetic structure proposed previously.

7.4 Summary

Summarizing the analysis, we investigated the different structures of α-$RuCl_3$ in $P3_112$ and $C2/m$, finding $C2/m$ have more distortion which reduces the $t_{1\sigma}$, result-

Table 7.1: Fractional coordinates of atoms and muon site candidates determined through DFT calculations. Abbreviations stand for Wyckoff position (WP) and site symmetry (SS). The fractional coordinates of α-$RuCl_3$ originate from DFT calculations and are compatible with x-ray diffraction characterization.

Atom	WP	SS	x	y	z
Ru	4g	2	0	0.33441	0
Cl	4i	m	0.73023	0	0.23895
Cl	8j	1	0.75138	0.17350	0.76619
Mu1	2a	2/m	0	0	0
Mu2	4i	m	0.14	0	0.36
Mu3	4g	2	0	0.2	0.5
Mu4	2d	2/m	0.5	0	0.5

ing in a more consistent description in terms of QMOs. More interesting, the QMOs are still effective in the relativistic calculations.

Further, we performed a GGA+SO+U calculation and analyzed the states in the relativistic basis. Finally, the electrostatic potentials were calculated in DFT to give the muon stopping position in the experiment. With the muon stop position, the magnetic configuration was investigated.

Chapter 8

Challenges in design of Kitaev materials: magnetic interactions from competing energy scales

Stephen M. Winter, **Ying Li**, Harald O. Jeschke, Roser Valentí
Phys. Rev. B **93**, 214431 (2016) [36]

In the Chapter 5 and Chapter 7, we analyzed the electronic properties of the honeycomb materials Na_2IrO_3, α-Li_2IrO_3, and α-$RuCl_3$. The purpose of this chapter is to review and refine the current understanding of magnetic interactions in these materials using both perturbative and nonperturbative methods introduced in Chapter 4, and to critically evaluate the potential for engineering the Kitaev spin liquid in real materials.

8.1 Hopping parameters for the hexagonal materials: Na_2IrO_3, α-Li_2IrO_3 and α-$RuCl_3$

For the honeycomb candidates of Na_2IrO_3, α-Li_2IrO_3, α-$RuCl_3$ we discussed in the previous two chapters, we plot the GGA bands in Figure 8.2. Further we performed the method described in Chapter 3 to calculate the hopping parameters. We use a mesh of $12 \times 12 \times 12$ **k** points in the first Brillouin zone for the energy range which

only includes the 6 t_{2g} bands. We put the onsite and nearest hopping parameters in Table 8.1, and then summarize the resulting crystal-field splitting and nearest neighbour hoppings in Table 8.2. The hopping integrals for Na_2IrO_3 agree with, but are slightly different from Ref. [29, 87] due to a finer **k**-point mesh employed in this work.

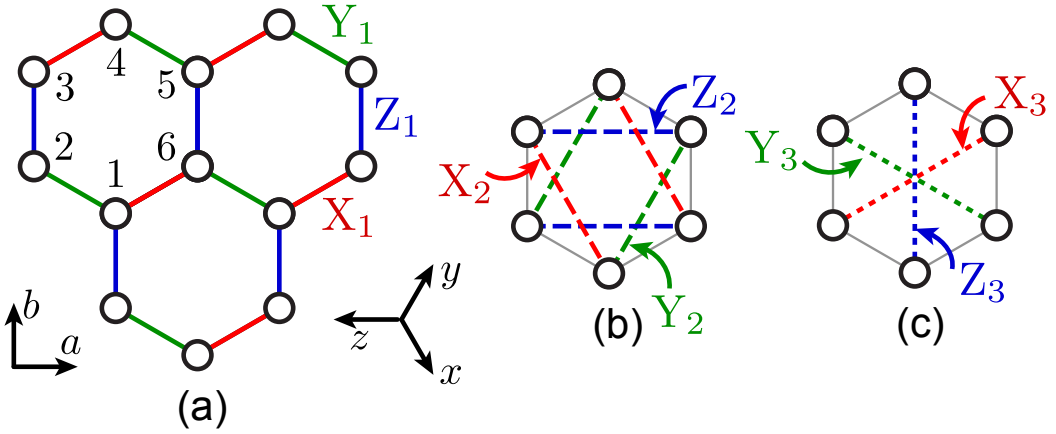

Figure 8.1: Cartoon of the honeycomb structure showing bond labels for (a) first neighbors, (b) second neighbors, and (c) third neighbors. Sites within a given hexagon are labeled $1-6$; a,b refer to the crystallographic axes, while x,y,z are the cubic axes of the local metal octahedra.

We label the hopping matrix for the nth nearest neighbour bond of $\gamma \in \{\mathrm{X}, \mathrm{Y}, \mathrm{Z}\}$ as $\mathbf{T}_n^\gamma$. The $C2/m$ symmetry gives two kinds of inequivalent nearest neighbour bonds: the Z_1 bonds, along the crystallographic b-axis, has the local C_{2h} symmetry. Following the definition in Ref. [67], we write the hopping matrix for Z_1 bond in the basis (d_{xy}, d_{xz}, d_{yz}) as:

$$\mathbf{T}_1^Z = \begin{pmatrix} t_3 & t_4 & t_4 \\ t_4 & t_1 & t_2 \\ t_4 & t_2 & t_1 \end{pmatrix}. \tag{8.1}$$

Here we used the notation from Ref. [67], which is different from the notation in previous chapters defined in Ref. [29]. The relations are shown in Table. 8.2.

While the X_1- and Y_1-bonds, in the ab-plane, have lower local C_i symmetry, and

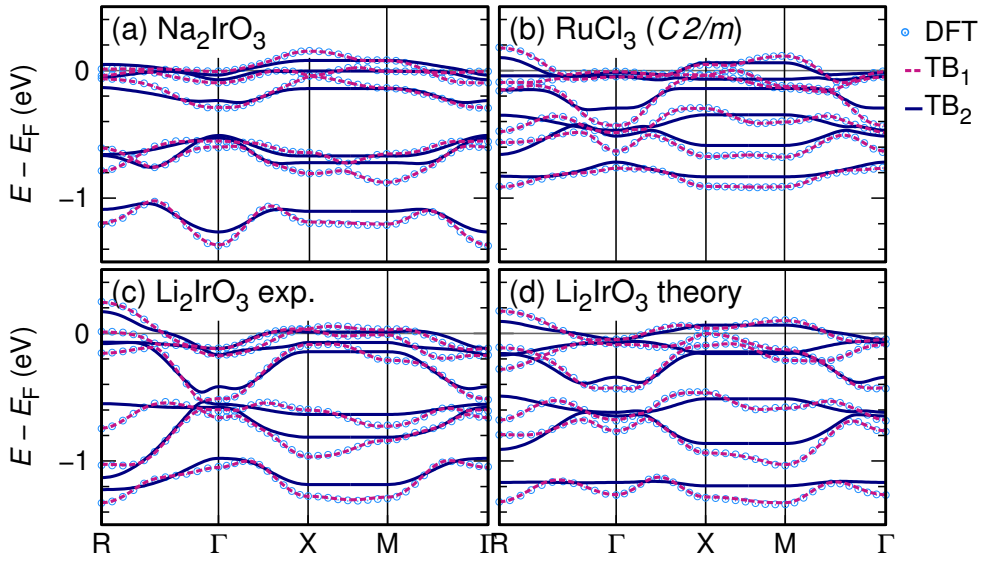

Figure 8.2: Comparison of DFT computed band structures (blue circles) and tight-binding interpolations employing hopping integrals up to 16 Å (TB_1, dashed pink line), and 3rd neighbors (TB_2, solid blue line).

hence have more unique or symmetry inequivalent hopping parameters

$$\mathbf{T}_1^X = \begin{pmatrix} t'_{1b} & t'_2 & t'_{4b} \\ t'_2 & t'_{1a} & t'_{4a} \\ t'_{4b} & t'_{4a} & t'_3 \end{pmatrix}, \; \mathbf{T}_1^Y = \begin{pmatrix} t'_{1b} & t'_{4b} & t'_2 \\ t'_{4b} & t'_3 & t'_{4a} \\ t'_2 & t'_{4a} & t'_{1a} \end{pmatrix}. \tag{8.2}$$

Without distortions, the nearly C_3 symmetry of the hopping suggests such that $t_n \approx t'_{na} \approx t'_{nb}$. However, this symmetry is not found in the real materials, causing significant differences in hopping integrals. The crystal field splitting matrix is

$$\mathbf{E}_i = \begin{pmatrix} \Delta_3 & \Delta_2 & \Delta_2 \\ \Delta_2 & 0 & \Delta_1 \\ \Delta_2 & \Delta_1 & 0 \end{pmatrix}. \tag{8.3}$$

The corresponding result for the three experimental structures is shown in Table. 8.2. In each case, CFS is small such that $\lambda \gtrsim 10\Delta_n$. For the nearest neighbour hoppings, the largest one is the oxygen assisted inter-orbital $t_2 \approx t'_2$ or direct metal-metal intra-orbital $t_3 \approx t'_3$. In the absence of distortion, the IrO_6 octahedra have 90° Ir-O-Ir bond angles. In Na_2IrO_3, the distortion of IrO_6 octahedra elongates Ir-Ir distances to $3.13 - 3.14$ Å, and Ir-O-Ir bond angles are as large as 100° [15]. The

Table 8.1: Hopping parameters for onsite and nearest neighbors (meV).

Bond		Na_2IrO_3	α-Li_2IrO_3		α-$RuCl_3$
			Exp.	Theory	$C2/m$
0	$xy \to xy$	-448.8	-477.8	-475.0	-334.1
	$xz \to xz$, $yz \to yz$	-421.5	-472.3	-469.6	-321.6
	$xy \to xz$, $xz \to yz$	-27.8	-35.0	-28.6	-17.5
	$xz \to yz$	-23.1	-37.5	-24.0	-19.8
X_1:	$xy \to xy$	47.7	72.3	75.0	45.8
	$xz \to xz$	30.0	80.2	77.1	44.9
	$xy \to xz$, $xz \to xy$	269.6	252.7	247.1	162.2
	$yz \to yz$	-20.7	-108.8	-153.1	-103.1
	$xy \to yz$, $yz \to xy$	-25.6	-1.9	-12.0	-10.9
	$xz \to yz$, $yz \to xz$	-21.4	-16.7	-9.9	-15.1
Y_1:	$xy \to xy$	47.7	72.3	75.0	45.8
	$yz \to yz$	30.0	80.2	77.1	44.9
	$yz \to xy$, $xy \to yz$	269.4	252.7	247.1	162.2
	$xz \to xz$	-20.7	-108.8	-153.1	-103.1
	$xy \to xz$, $xz \to xy$	-25.6	-1.9	-12.0	-10.9
	$yz \to xz$, $xz \to yz$	-21.4	-16.7	-9.9	-15.1
Z_1:	$xz \to xz$, $yz \to yz$	33.1	55.0	78.8	50.9
	$xz \to yz$, $yz \to xz$	264.4	219.0	230.0	158.2
	$xy \to xy$	25.4	-175.1	-178.7	-154.0
	$xz \to xy$, $xy \to xz$	-11.9	-124.5	-18.9	-20.2
	$yz \to xy$, $xy \to yz$	-11.9	-124.5	-18.9	-20.2

bond-anisotropy for Na_2IrO_3 is small, suggesting only a small bond-dependence of the magnetic interactions. The distortion does not enhance the crystal field a lot, however, it does suppress t_3 and enhance the t_2, and therefore t_2 becomes dominant ($|t_2/t_3| \sim 10$). Compared with Na^+ ion in Na_2IrO_3, for experimental structure of α-Li_2IrO_3, smaller Li^+ ion is more easily incorporated, reducing the distances of Ir-Ir to $2.98 - 2.99$, and the Ir-O-Ir bond angles becomes $\sim 94^\circ$ [22]. The lower distortion lead to larger t_3 ($|t_2/t_3| \sim 1$). The bond anisotropy in this material also becomes significant, in particular $t_4 \gg t'_{4a}, t'_{4b}$. Similarly, α-$RuCl_3$ also has similar Ru-Cl-Ru bond angles $\sim 94^\circ$ [18], introducing similar t_3, t'_3 as α-Li_2IrO_3.

We display the second nearest neighbour bonds in Figure 8.1 (b). Second neighbors linked by the X_1, Y_1 bonds are labeled as Z_2. Those bonds connected by (Y_1,

Table 8.2: Parameters for crystal field splitting and nearest neighbour hopping (meV) for experimental $C2/m$ structures of Na_2IrO_3 [15], α-Li_2IrO_3, [22] and α-$RuCl_3$ [18]. Hopping integrals are labeled according to Ref. [67]; in brackets are given the corresponding labels from Ref. [29].

Term	Na_2IrO_3	α-Li_2IrO_3	α-$RuCl_3$
Δ_1	-22.9	-37.5	-19.8
Δ_2	-27.6	-35.0	-17.5
Δ_3	-27.2	-5.5	-12.5
t_1 ($t_{\bar{1}\|\|}$)	+33.1	+55.0	+50.9
t'_{1a} ($t_{1\|\|}$)	+29.9	+80.2	+44.9
t'_{1b} ($t_{1\|\|}$)	+47.6	+72.3	+45.8
t_2 ($t_{\bar{1}\mathrm{O}}$)	+264.3	+219.0	+158.2
t'_2 ($t_{1\mathrm{O}}$)	+269.3	+252.7	+162.2
t_3 ($t_{\bar{1}\sigma}$)	+26.6	-175.1	-154.0
t'_3 ($t_{1\sigma}$)	-19.4	-108.8	-103.1
t_4 ($t_{\bar{1}\perp}$)	-11.8	-124.5	-20.2
t'_{4a} ($t_{1\perp}$)	-21.4	-16.7	-15.1
t'_{4b} ($t_{1\perp}$)	-25.4	-1.9	-10.9

Z_1) bonds and (Z_1, X_1) are X_2 and Y_2, respectively. The corresponding hoppings are in Table 8.3. The largest one, with the magnitude of $\sim 50-70$ meV, are the inter-orbital hopping sharing a label with the bond-type. Taking the X_2 bond as an example, $d_{xz} \to d_{xy}$ is the largest one. The third nearest neighbors, as shown in Figure 8.1 (c), have the same symmetry as the parallel first nearest neighbour bond, and are labeled from the corresponding first nearest neighbour bonds. The largest hopping parameters are between orbitals not sharing a label with the bond-type, e.g. $d_{yz} \to d_{yz}$ for the X_3 bond are $30 \sim 40$ meV. Both the largest second and third neighbour hoppings are from the M-L-L-M paths (M = metal, L = ligand). In all the materials, the distortions make the M-L-M angle differ from 90°, causing freedom of choice for coordinates x, y, z. We choose the same coordinates for the projectors as Ref. [29]: the local z-axis is e $\hat{z} \perp (\mathbf{a}+\mathbf{c})$, and the x, y are set to be perpendicular to z and have a 45° angle with the **b**-axis.

Table 8.3: Hopping parameters for second nearest neighbors (meV).

Bond		Na_2IrO_3	α-Li_2IrO_3		α-$RuCl_3$
			Exp.	Theory	$C2/m$
X_2:	$xz \to xz$	-0.8	-0.6	-3.7	-4.5
	$yz \to yz$	-1.6	3.6	0.2	-0.4
	$xy \to xy$	-3.6	1.2	-2.3	-3.2
	$xy \to xz$	-75.8	-56.9	-70.5	-59.1
	$xz \to xy$	-36.4	-23.8	-38.6	-24.3
	$xy \to yz$	12.7	15.2	11.0	8.3
	$yz \to xy$	-21.3	-10.4	-10.2	1.3
	$xz \to yz$	-18.4	-16.4	-11.6	-1.2
	$yz \to xz$	10.3	28.9	11.8	11.8
Y_2:	$yz \to yz$	-0.8	-0.6	-3.7	-4.5
	$xz \to xz$	-1.6	3.6	0.2	-0.4
	$xy \to xy$	-3.6	1.2	-2.3	-3.2
	$yz \to xy$	-75.8	-56.9	-70.5	-59.1
	$xy \to yz$	-36.4	-23.8	-38.6	-24.3
	$xz \to xy$	12.7	15.2	11.0	8.3
	$xy \to xz$	-21.3	-10.4	-10.2	1.3
	$xz \to yz$	-18.4	-16.4	-11.6	-1.2
	$yz \to xz$	10.3	28.9	11.8	11.8
Z_2:	$xy \to xy$	-1.5	1.0	0.6	-0.4
	$xz \to xz$	-1.6	-1.2	-2.9	-4.7
	$yz \to yz$	-1.6	-1.2	-2.9	-4.7
	$xz \to yz$	-77.0	-56.7	-73.2	-60.7
	$yz \to xz$	-30.3	-51.4	-39.6	-23.9
	$xy \to xz$, $yz \to xy$	-18.8	-12.5	-11.3	-1.7
	$xy \to yz$, $xz \to xy$	9.4	5.3	11.6	11.6

Table 8.4: Hopping parameters for third nearest neighbors (meV).

Bond		Na_2IrO_3	α-Li_2IrO_3		α-$RuCl_3$
			Exp.	Theory	$C2/m$
X_3:	$yz \to yz$	-35.3	-40.0	-33.0	-41.4
	$xy \to xy$	-8.5	-3.5	-5.8	-7.5
	$xz \to xz$	-8.2	-11.2	-6.8	-7.9
	$xy \to xz$, $xz \to xy$	-12.7	-13.0	-13.4	-7.8
	$xy \to yz$, $yz \to xy$	17.0	9.5	15.3	10.7
	$xz \to yz$, $yz \to xz$	14.9	13.1	16.3	12.7
Y_3:	$xz \to xz$	-35.3	-40.0	-33.0	-41.4
	$xy \to xy$	-8.5	-3.5	-5.8	-7.5
	$yz \to yz$	-8.2	-11.2	-6.8	-7.9
	$yz \to xy$, $xy \to yz$	-12.7	-13.0	-13.4	-7.8
	$xy \to xz$, $xz \to xy$	17.0	9.5	15.3	10.7
	$yz \to xz$, $xz \to yz$	14.9	13.1	16.3	12.7
Z_3:	$xy \to xy$	-36.8	-40.8	-33.3	-39.5
	$xz \to xz$, $yz \to yz$	-9.3	-8.1	-6.4	-8.2
	$xz \to yz$, $yz \to xz$	-13.8	-13.6	-13.5	-7.4
	$xz \to xy$, $xy \to xz$	16.6	15.8	16.6	11.7
	$yz \to xy$, $xy \to yz$	16.6	15.8	16.6	11.7

8.2 Exchange interactions for specific materials from exact diagonalization

8.2.1 Na_2IrO_3

As described in Chapter 5, this material is found to be zigzag magnetic order [14–16] with moments ordered at 45° with **a** axis in the *ac* plane [79] below $T_N = 14$ K. This order can be obtained by the nearest neighbour Heisenberg-Kitaev model with large Γ_1, Γ_1' [80], or second neighbour Kitaev coupling K_2 [69], or second and third neighbour Heisenberg couplings (J_2, J_3) [73, 75]. For the nearest neighbour parameters, a large t_2 generates the dominant ferromagnetic $K_1 < 0$ term and subdominant antiferromagnetic $J_1 > 0$. Katukuri *et al.* [81] estimated the interactions from the energy of Ir dimers by using the MRCI (MultiReference Configuration Interaction) method and suggested $J_1 = +5.0,\ K_1 = -20.5,\ \Gamma_1 = +0.5$ meV. They also found the small anisotropy between X_1 (Y_1) and Z_1 bond. Based on *ab-initio* hopping integrals, there were two calculations. From numerical second order perturbation theory (N2OPT), Yamaji *et al.* [70] found a very large $|\Gamma_1'^{xy} + \zeta_1|$ term > 8 meV for the X_1,Y_1-bonds, which can introduce the observed zigzag order. However, this result may suffer from "double-counting" the SO interaction, since they use the spin-dependent hopping integrals from relativistic DFT calculations and also include the SO coupling in the perturbation theory. In contrast, Sizyuk *et al* [69] also used perturbation theory without "double-counting" and only found the largest nearest neighbour terms $J_1 = +5.8$, $K_1 = -14.8$ meV consistent with MRCI result. Beyond nearest neighbors, they also suggested the large $J_2 = -4.4$, $K_2 = +7.9$ meV terms. The values for the third nearest neighbors are still not clear. In order to have more accurate values for the magnetic exchange parameters, it is worth to calculate the magnetic interactions with nonperturbative methods.

The resulting parameters for the first nearest neighbors are shown in Table 8.5. The $t_{2g} - e_g$ mixing is not included, which is suggested to shift the computed values ~ 2 meV [29, 70]. We compare the nearest neighbour interactions of the ED method and second order perturbation theory without and with crystal field (Ex. 2OPT) in Table 8.5. All the methods suggest a large nearest neighbour Kitaev interaction K_1 around -20 meV, with an order of magnitude smaller Heisenberg coupling J_1 and off-diagonal anisotropic exchange Γ_1, Γ_1'. For the nearest bond, the second order

perturbation theory can already give the correct result. Comparing the results of the two-site ED without and with CFS, the CFS affect the results by less than 2 meV, and seems to slightly enhance K_1 and suppress J_1, which is similar as Ref. [70]. The influence of CFS is smaller than the renormalization of the nearest neighbour terms by multi-site corrections, shown in the different results from two sites to six sites. There are only small anisotropy between X_1,Y_1, and Z_1-bonds, which was suggested to be larger in a previous study [70]. The results presented here are more in agreement with the experimental observation of near C_3 symmetry of the magnetic fluctuations above T_N [79]. In addition, the large $\Gamma_1^{\prime xy}$ or ζ_1 were proposed to accounting for the zigzag order do not appear in our calculations. All the off diagonal terms are in the magnitude of 2 meV or smaller.

From the six-site ED calculations for the clusters in Fig. 4.2 (c), we compute the second and third neighbour exchange couplings. The results are presented in Table 8.6. Different with Ref. [69], we find small second neighbour interactions, which arise from the suppression of the various second and third order hopping processes (see Fig. 4.4). Most importantly, we find the large third neighbour Heisenberg interaction $J_3 = 6.8$ meV, which is greater than the N2OPT value of 1.3 meV [70]. The high order terms beyond the second order perturbation strongly affect the results.

Based on above parameters, we suggest of Na_2IrO_3 has the minimal model for understanding the magnetic properties $J_1 \sim 0$, $J_3 > 0$, $K_1 < 0$, and $|J_3/K_1| \sim 0.4$:

$$\hat{H} = \sum_{\text{1st nn}} \left(J_1 \mathbf{S}_i \cdot \mathbf{S}_j + K_1 S_i^{\gamma} S_j^{\gamma} \right) + \sum_{\text{3rd nn}} J_3 \mathbf{S}_i \cdot \mathbf{S}_j. \tag{8.4}$$

We plot the phase diagram varying J_1 and J_3 in Figure 8.3 with K_1 = -1 meV using the method descried in Chapter 4. The experimental zigzag order appears in the large J_3/J_1 region, consistent with the predictions that J_3 is large [73, 81]. In fact, J_3 provides a large region to get the zigzag state. That means the zigzag ground state properties will not change for different choices of J_H, U, λ. The J_1-K_1-J_3 model can not determine the magnetic direction $\mathbf{n}$, which is determined by the off-diagonal interactions and bond anisotropies. We use all the calculated parameters from the real material and find the wave vector $\mathbf{q}$ parallel to Z_1-bond, and $\mathbf{n}$ is along 45° with the cubic x axis, consistent with the experiment [79] (see Fig. 8.3 (b),(c)). The Weiss temperature computed by Eq. (4.77) are same as the experiment observations [78]: $\Theta_{iso} < 0$, and $\Theta_b < \Theta_a < \Theta_c$, (i.e. $\chi_{ab} < \chi_c$). If in the nearest neighbour level, Na_2IrO_3 is close to the FM Kitaev limit, the AFM $\Theta_{iso} \sim -116$ K can only be explained by the long-range AFM term like J_3, which is similar as the explanation

Table 8.5: Nearest neighbour magnetic interactions in meV for Na_2IrO_3 obtained from various methods employing U = 1.7 eV, J_H = 0.3 eV, λ = 0.4 eV. For CFS (Crystal Field Splitting) = "no", $\Delta_n = 0$. The most accurate method theoretically is 6-site ED, highlighted in bold.

Z_1-bonds:					
Method	CFS	J_1	K_1	Γ_1	Γ'_1
exact 2OPT	no	+3.2	-20.5	+0.4	-0.9
ED (2-site)	no	+4.2	-23.7	+0.3	-1.0
ED (2-site)	full	+1.8	-25.5	-0.4	-2.8
ED (6-site)	**full**	**+1.6**	**-17.9**	**-0.1**	**-1.8**
Literature Values					
2-site MRCI [81]	approx.	+5.0	-20.5	+0.5	–
N2OPT [70]	full	+4.4	-35.1	-0.4	+1.1

X_1,Y_1-bonds:							
Method	CFS	J_1^{xy}	K_1^{xy}	ξ_1^{xy}	Γ_1^{xy}	$\Gamma_1'^{xy}$	ζ_1^{xy}
exact 2OPT	no	+0.9	-20.9	-0.1	+3.3	-1.7	-0.1
ED(2-site)	no	+1.7	-24.1	-0.2	+3.0	-2.0	-0.1
ED(2-site)	full	0.0	-23.3	+0.1	+2.0	-3.4	+0.1
ED(6-site)	**full**	**-0.1**	**-16.2**	**-0.1**	**+2.1**	**-2.3**	**+0.1**
Literature Values							
2-site MRCI [81]	approx.	+1.5	-15.2	–	+1.2	–	–
N2OPT [70]	full	+2.6	-27.9	+0.6	+1.8	-5.8	+2.7

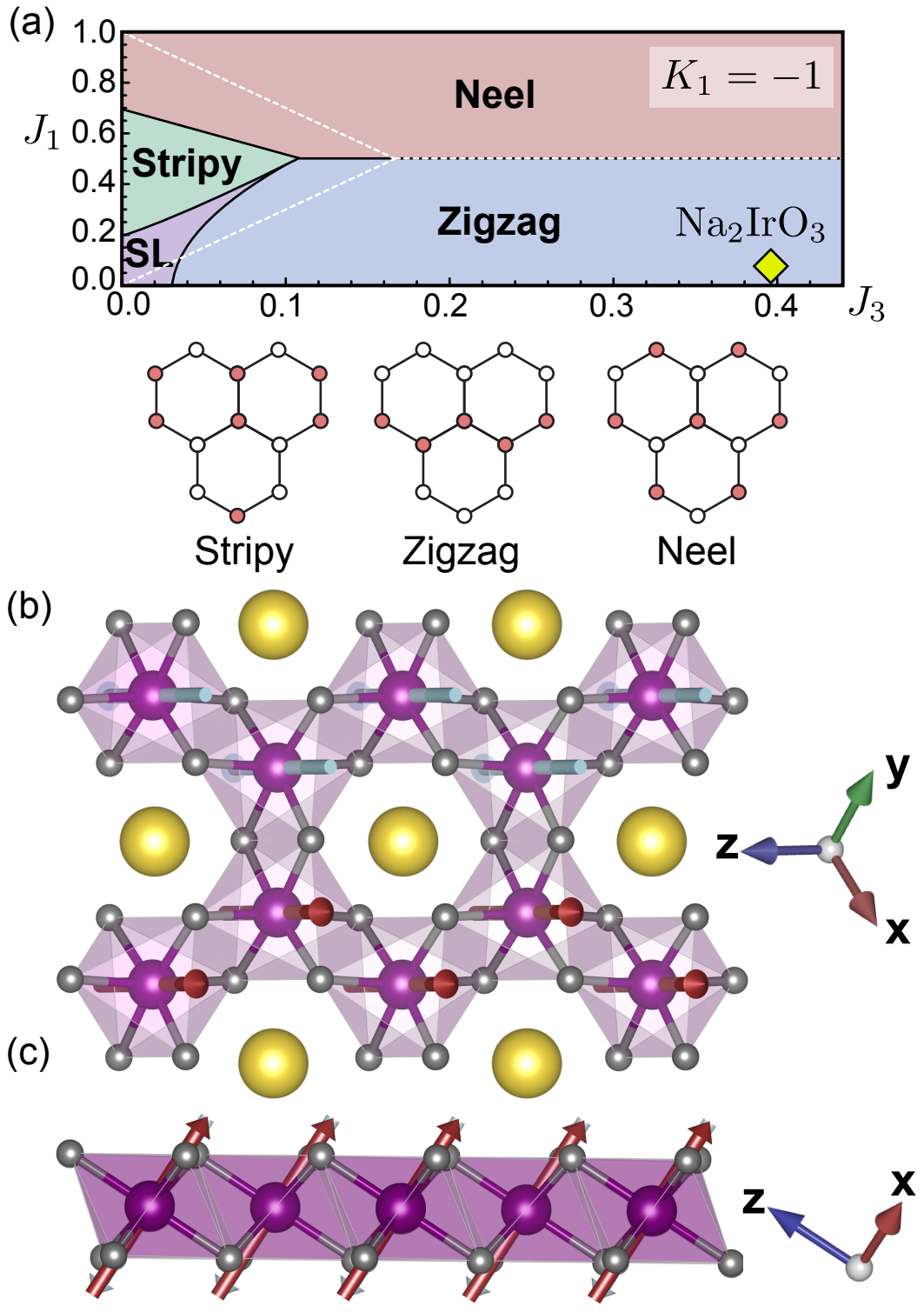

Figure 8.3: (a) Phase diagram for the minimal model of Eq. (8.4) obtained by ED on 16-site cluster in the parameter region relevant to the Na_2IrO_3; SL = Kitaev Spin Liquid. The white dashed lines indicate classical phase boundaries. (b,c) Predicted zigzag ground state and orientation of the ordered moments for Na_2IrO_3, viewed (b) along the cubic [111] direction, and (c) the cubic $[\bar{1}10]$ direction. The moments are found to be $\perp$ b-axis, nearly directly along the $\hat{x}+\hat{y}$ direction.

Table 8.6: Complete magnetic interactions in meV for Na_2IrO_3 obtained by exact diagonalization on six-site bridge and hexagon clusters employing U = 1.7 eV, J_H = 0.3 eV, λ = 0.4 eV, and full crystal field terms Δ_n. The largest terms are bolded. Site labels for $\mathbf{D}_{ij}$ refer to Fig. 8.1 (a).

Bond	J_n	K_n	ξ_n	Γ_n	Γ'_n	ζ_n
X_1, Y_1	-0.1	**-16.2**	+0.1	+2.1	-2.3	-0.1
Z_1	+1.6	**-17.9**	–	-0.1	-1.8	–
X_2, Y_2	+0.2	-1.6	-0.1	+0.9	0.0	0.0
Z_2	+0.1	-1.2	–	+0.6	-0.3	–
X_3,Y_3	**+6.7**	0.0	0.0	-0.1	0.0	-0.1
Z_3	**+6.8**	+0.3	–	-0.2	-0.1	–

Bond	Sites (i, j)	$\mathbf{D}_{ij}$
X_2	(1, 3) , (4, 6)	(-0.1, -0.5, -0.5)
Y_2	(5, 1) , (2, 4)	(-0.5, -0.1, -0.5)
Z_2	(6, 2) , (3, 5)	(-0.2, -0.2, -0.1)

of χ [73]. Therefore, the computed magnetic interactions are consistent with the known experimental properties of Na_2IrO_3.

8.2.2 α-$RuCl_3$

As described in Chapter 7, the honeycomb structure α-$RuCl_3$ (include $P3_112$ and $C2/m$) also has the zigzag order below $T_N \sim 7-14$ K [18]. Different from Na_2IrO_3, it has a FM Weiss constant $\Theta_{iso} \sim +40$ K, and a reversed susceptibility anisotropy, (i.e. $\chi_{ab} > \chi_c$), which suggests a different magnetic character [17, 101]. As shown in the previous chapter, the $C2/m$ structure has enhanced distortion of $RuCl_6$ compared with $P3_112$. The magnetic interactions of $P3_112$ structure was previously analyzed using hopping integrals from *ab initio* [27] and the second order perturbation theory formula of Ref. [67]. The authors of Ref. [27] found $J_1 \sim -12$, $K_1 \sim +17$, and $\Gamma_1 \sim +12$ meV, suggesting the material to have zigzag order. They also did the analysis for $C2/m$ structure and found the FM Kitaev coupling $K_1 < 0$. However, these calculations may have ignored Coulomb interactions between t_{2g} and

e_g orbitals, strongly modifying the results. In this section, we revisit the magnetic interactions including the long range terms for both $P3_112$ and experimental $C2/m$ structure.

Table 8.7: Complete magnetic interactions in meV for the $C2/m$ structure of α-$RuCl_3$ from Ref. [18] obtained by exact diagonalization on six-site bridge and hexagon clusters employing U = 3.0, J_H = 0.6, λ = 0.15 eV, and full crystal field terms Δ_n. The largest terms are bolded. Site labels for $\mathbf{D}_{ij}$ refer to Fig. 8.1 (a).

Bond	J_n	K_n	ξ_n	Γ_n	Γ'_n	ζ_n
X_1, Y_1	-1.4	**-7.5**	+0.2	**+5.9**	-0.8	+0.2
Z_1	-2.2	**-5.0**	–	**+8.0**	-1.0	–
X_2, Y_2	-0.1	-0.6	+0.1	+0.6	+0.6	+0.1
Z_2	+0.1	-0.9	–	+0.6	+0.3	–
X_3,Y_3	**+3.0**	-0.1	0.0	-0.1	-0.1	-0.1
Z_3	**+2.4**	+0.3	–	-0.1	-0.1	–

Bond	Sites (i, j)	$\mathbf{D}_{ij}$
X_2	(1, 3) , (4, 6)	(-0.3, -0.5, -0.5)
Y_2	(5, 1) , (2, 4)	(-0.5, -0.3, -0.5)
Z_2	(6, 2) , (3, 5)	(-0.4, -0.4, -0.1)

In $P3_112$ structure, we give the bond-averaged values $(J_1, K_1, \Gamma_1, \Gamma'_1)$ = (-5.5, +7.6, +8.4, +0.2) meV. Contrary to this, the $C2/m$ structure has bond anisotropy, and therefore we give the result of the nearest neighbour interactions for $C2/m$ structure in Table 8.7. This structure still has the FM Heisenberg coupling and AFM large Γ_1 term due to the large hopping t_1, t_3 [27, 106]. However, compared to $P3_112$ structure, the $C2/m$ structure has a smaller Heisenberg coupling and FM Kitaev term, with the bond averaged values: $(J_1, K_1, \Gamma_1, \Gamma'_1)$ = (-1.7, -6.7, +6.6, -0.9) meV. Because of the anisotropy of the structure and the hopping integrals of t_3 shown in the previous chapter, there exist the anisotropy for the magnetic interaction $K_1^{xy} < K_1^z$ and $\Gamma_1^{xy} < \Gamma_1^z$.

Like Na_2IrO_3, the second neighbour interactions are small and the third neighbour interactions are significant $J_3 \sim 2.3$ meV for $P3_112$ and ~ 2.7 for $C2/m$. These are smaller than Na_2IrO_3 because of the enhanced U in Ru. We also consider the

$C2/m$ structure of Ref. [95], where the bond has less anisotropy, but found similar interactions. Based on the above analysis, we construct the minimal model with $\Gamma_1 = -K_1$:

$$\hat{H} = \sum_{\text{1st nn}} J_1\, \mathbf{S}_i \cdot \mathbf{S}_j + K_1(S_i^\gamma S_j^\gamma - S_i^\alpha S_j^\beta - S_i^\beta S_j^\alpha) + \sum_{\text{3rd nn}} J_3\, \mathbf{S}_i \cdot \mathbf{S}_j. \tag{8.5}$$

For Z_1 bond, $\{\alpha,\beta,\gamma\}$ is the cubic axis $\{x,y,z\}$. After rotation by 45° around the local z axis, this Hamiltonian can be transformed to a Heisenberg-Kitaev formula without the off-diagonal term:

$$\hat{H} = \sum_{\text{1st nn}} A_1 \mathbf{S}_i \cdot \mathbf{S}_j + B_1 S_i^\delta S_j^\delta + \sum_{\text{3rd nn}} J_3 \mathbf{S}_i \cdot \mathbf{S}_j, \tag{8.6}$$

with $A_1 = J_1 + K_1 \sim -8.4$ meV, $B_1 = -2K_1 \sim +13.4$ meV. For different bonds, $\hat{\delta}$-axis is:

$$\hat{\delta} = \begin{cases} \frac{1}{\sqrt{2}}(0,1,1) & \text{X}_1 \text{ bond}, \\ \frac{1}{\sqrt{2}}(1,0,1) & \text{Y}_1 \text{ bond}, \\ \frac{1}{\sqrt{2}}(1,1,0) & \text{Z}_1 \text{ bond}. \end{cases} \tag{8.7}$$

For each bond, $\hat{\delta}$ is parallel to a vector joining the two bridging Cl atoms and the $\hat{\delta}$ axes are no longer 90° from each other. Therefore, even though the Hamiltonian is written in Kitaev form, it does not allow a spin liquid state. From the interactions, we calculated the Weiss constant as $\Theta_{iso} \sim -(3A_1 + B_1 + 3J_3)/4k_b > 0$, $\Theta_c < 0$ and $\Theta_a, \Theta_b > 0$, consistent with experiment [17, 101].

8.2.3 α-Li_2IrO_3

The last honeycomb material we investigate in this chapter is α-Li_2IrO_3. It also has magnetic order below $T_N = 15$ K [75], that is incommensurate with $\mathbf{q}||a$, and $|\mathbf{q}| = q \sim 0.3$ in the first Brillouin zone, as suggested by the x-ray and neutron experiments [20]. Three different models have been discussed to explain this order: (J_1, K_1, J_2, K_2) model [69, 74, 82], nearest neighbour with off-diagonal terms $(J_1, K_1, \Gamma_1, \Gamma_1')$ models [67, 72, 80], nearest neighbors with bond-anisotropy with $(J_1^z, K_1^z, \Gamma_1^z, J_1^{xy}, K_1^{xy}) \sim (-2, -10, +2, +1, -12)$ meV [83]. For the exchange parameters, calculations from a MRCI state energies on a 2-site cluster show there is

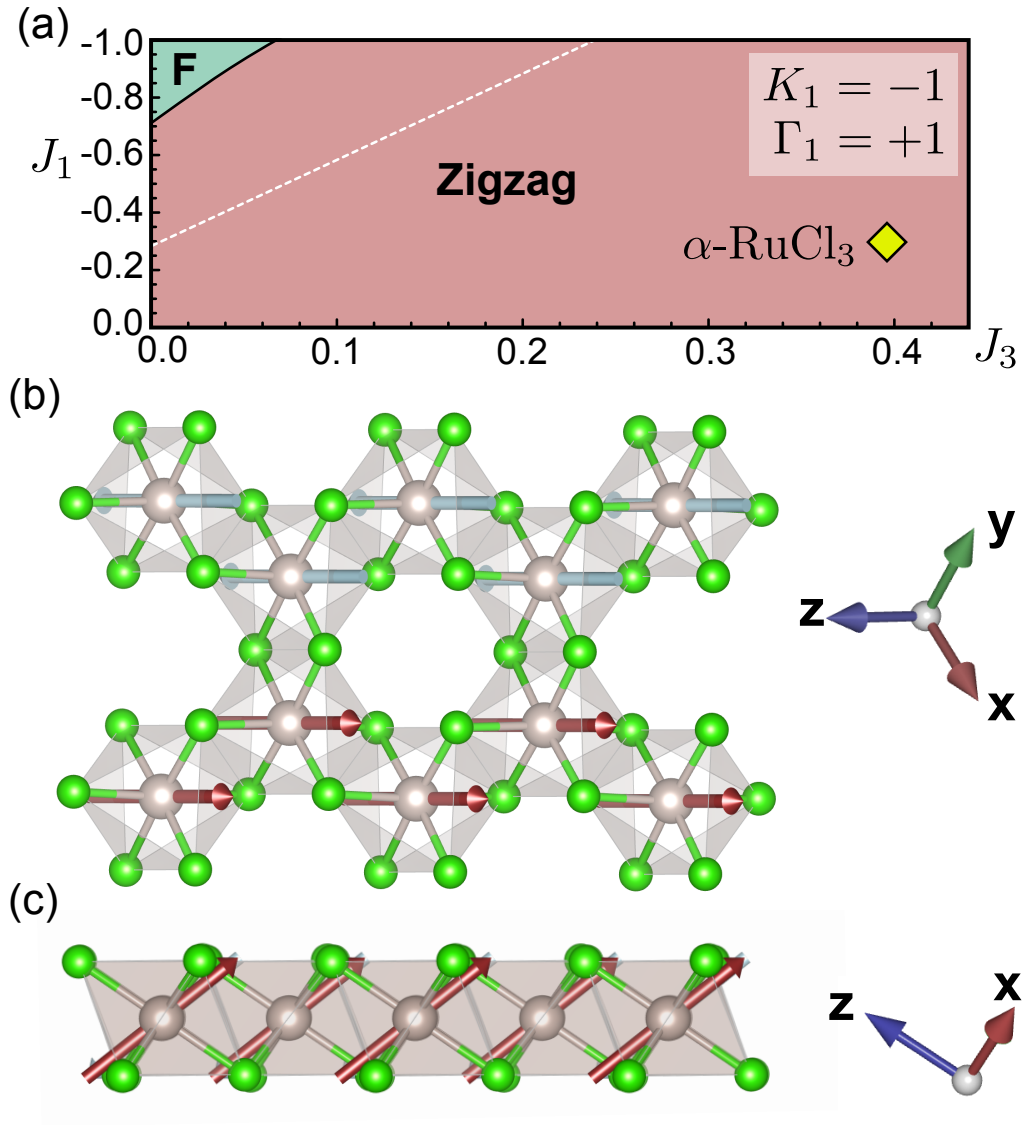

Figure 8.4: (a) Phase diagram of the minimal model of Eq. (8.5) obtained by ED on 16-site cluster in the parameter region relevant to the $C2/m$ structure of α-$RuCl_3$; F = bulk ferromagnetic order. The white dashed line indicates the classical phase boundary. (b,c) Predicted zigzag ground state and orientation of the ordered moments for the $C2/m$ structure of α-$RuCl_3$, viewed (b) along the cubic [111] direction, and (c) the cubic $[\bar{1}10]$ direction. The moments are found to be $\perp$ b-axis, nearly directly along the $\hat{x}+\hat{y}$ direction, but tilted 106° from the cubic z-axis.

large anisotropy for this structure with $(J_1^z, K_1^z) = (-19, -6)$ meV and $(J_1^{xy}, K_1^{xy}) = (+1, -12)$ meV [76]. They also show that with a large J_2, a spiral phase can be obtained. However, this suggested different phase from the spiral order identified in recent experiments [20]. Therefore, the magnetic interactions are currently unknown in α-Li_2IrO_3. In order to address the exchange parameters and magnetic configurations in this material, we performed the ED calculations for both the experimental structure [22] and relaxed one [77].

The parameters from our calculations for both structures are displayed in Table 8.8. They all show the FM Heisenberg and Kitaev nearest neighbour interactions. Consistent with Ref. [76], the experimental structure shows significant bond anisotropy. Further, the relation $K_1^z > K_1^{xy}$, $J_1^z < J_1^{xy}$, and $\Gamma_1^z > \Gamma_1^{xy}$ agree with the dipolar coupling model [83] even though Ref. [83] only include simplified interactions compared of the computed interactions. Like α-$RuCl_3$, the large direct hopping t_3 leads to the large off-diagonal $\Gamma_1^z, \Gamma_1^{xy}$ terms. In addition, the large $t_4 = -124.5$ meV for the experimental structure introduces $\Gamma_1'^z = -4.3$ meV along the Z_1 bond. Even with different anisotropy features, these two structures have similar bond-average values $J_1 \sim -3, K_1 \sim -8, \Gamma_1 \sim +9$ meV, which is consistent with the values of Ref. [80]. In contrast with the predictions in Ref. [75], with these parameters, α-Li_2IrO_3 is far away from the Kitaev limit.

For the second and third nearest neighbour interactions, we give the results in Table 8.8. Different from Na_2IrO_3 and α-$RuCl_3$, we obtain significant second neighbour interactions. Surprisingly, a significant Dzyaloshinskii-Moriya term $|\mathbf{D}_2^{xy}| > 4$ meV for the experimental structure is found. The relaxed structure also has large second neighbour terms, but both off-diagonal term and DM terms are reduced. The off-diagonal term of Γ_2^X can not be decomposed into (J_2, K_2) as considered in Ref. [69, 74], which means we need more terms for the minimal model beyond the previous simplified models. For the third nearest neighbour interaction, we find a little bit smaller values (J_3 = +4.6 and +5.9 meV) than Na_2IrO_3.

We therefore consider a minimal model that includes $(J_1, K_1, \Gamma_1, K_2, \Gamma_2, |\mathbf{D}_2|, J_3) = (-3, -8, +9, -4, +3, +3, +6)$ meV with $K_1 \approx -\Gamma_1$ and $K_2 \approx -\Gamma_2$. Similar to α-

Table 8.8: Complete magnetic interactions in meV for α-Li_2IrO_3 obtained by exact diagonalization on six-site bridge and hexagon clusters employing U = 1.7 eV, J_H = 0.3 eV, λ = 0.4 eV, and full crystal field terms Δ_n. The largest terms are bolded. Site labels for $\mathbf{D}_{ij}$ refer to Fig. 8.1 (a).

Experimental Structure						
Bond	J_n	K_n	ξ_n	Γ_n	Γ'_n	ζ_n
X_1, Y_1	**-1.0**	**-13.0**	-0.1	**+6.6**	-0.4	+0.6
Z_1	**-4.6**	**-4.2**	–	**+11.6**	**-4.3**	–
X_2, Y_2	+0.9	**-2.9**	+1.3	**+3.0**	+1.3	+0.4
Z_2	-0.9	+0.1	–	+1.5	-1.6	–
X_3,Y_3	**+4.7**	-0.2	-0.1	0.0	0.0	-0.1
Z_3	**+4.4**	+0.4	–	-0.1	-0.1	–

Bond	Sites (i, j)	$\mathbf{D}_{ij}$
X_2	(1, 3) , (4, 6)	**(-1.5, -3.2, -2.3)**
Y_2	(5, 1) , (2, 4)	**(-3.2, -1.5, -2.3)**
Z_2	(6, 2) , (3, 5)	(-0.2, -0.2, 0.0)

Relaxed Structure						
Bond	J_n	K_n	ξ_n	Γ_n	Γ'_n	ζ_n
X_1, Y_1	**-2.5**	**-9.8**	0.0	**+8.7**	-0.8	+0.1
Z_1	**-3.1**	**-6.3**	–	**+9.4**	-0.1	–
X_2, Y_2	+0.5	**-3.8**	+1.0	**+3.4**	+0.5	+0.1
Z_2	+0.2	**-3.6**	–	**+3.3**	-0.6	–
X_3,Y_3	**+6.0**	-0.1	-0.1	0.0	-0.1	-0.1
Z_3	**+5.9**	+0.2	–	-0.1	-0.1	–

Bond	Sites (i, j)	$\mathbf{D}_{ij}$
X_2	(1, 3) , (4, 6)	**(-0.3, -1.9, -1.4)**
Y_2	(5, 1) , (2, 4)	**(-1.9, -0.3, -1.4)**
Z_2	(6, 2) , (3, 5)	**(-1.2, -1.2, +0.1)**

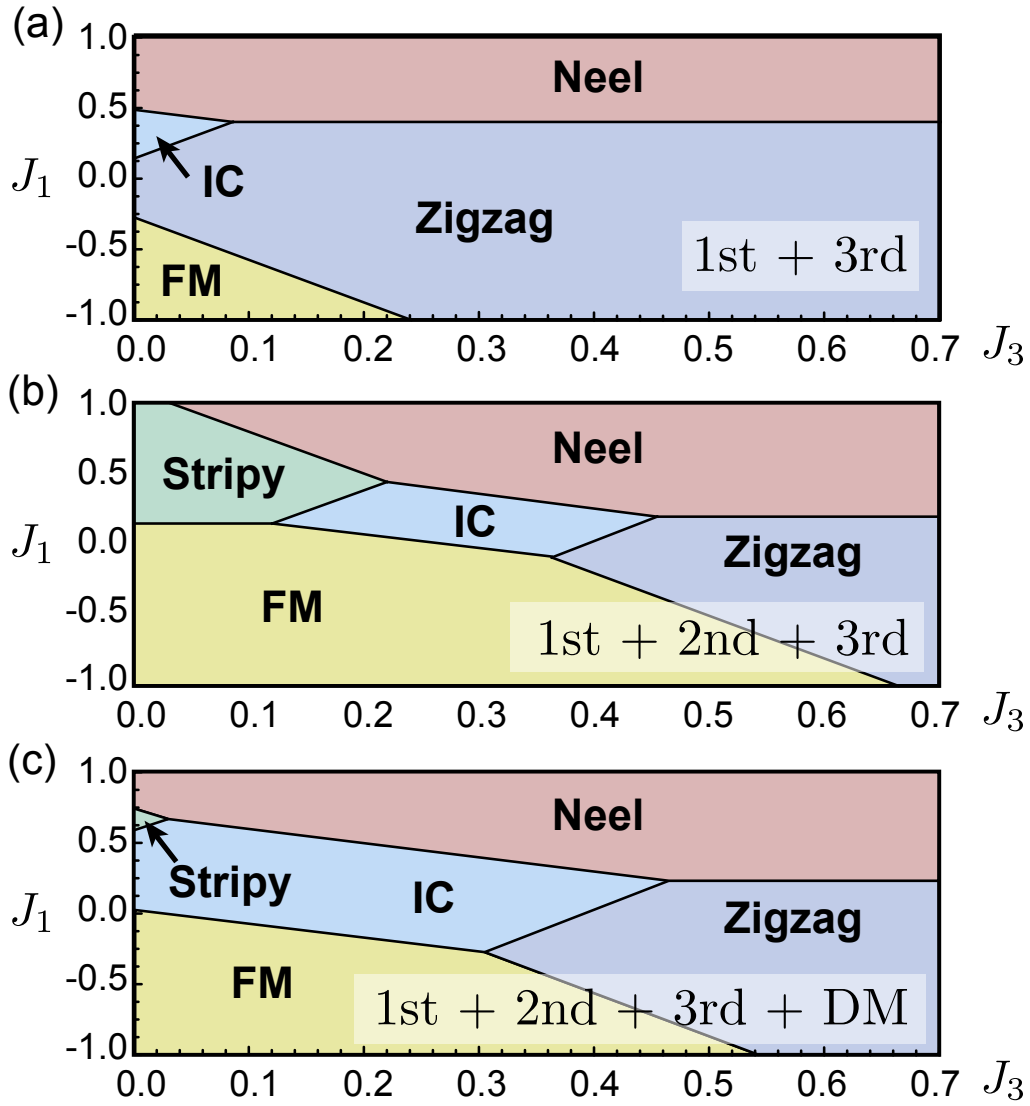

Figure 8.5: Classical phase diagrams for model Eq. (8.8) for α-Li_2IrO_3 with increasingly realistic interactions. IC = incommensurate spiral order. (a) Including only first and third neighbour interactions; $A_2 = B_2 = D = 0$, and $B_1 = +2$, i.e. $K_1 = -\Gamma_1 = -1$. (b) With $D = 0$, and with the ratio of other interactions set to reproduce the experimental q and A_a/A_{c^*}; ($B_1 = +2$, $B_2/B_1 = 0.3$, $A_2/B_2 = 0.5$). (c) With $D = 0.15$, and with the ratio of other interactions set to reproduce the experimental q and A_a/A_{c^*}; ($B_1 = +2$, $B_2/B_1 = 0.2$, $A_2/B_2 = 0.5$).

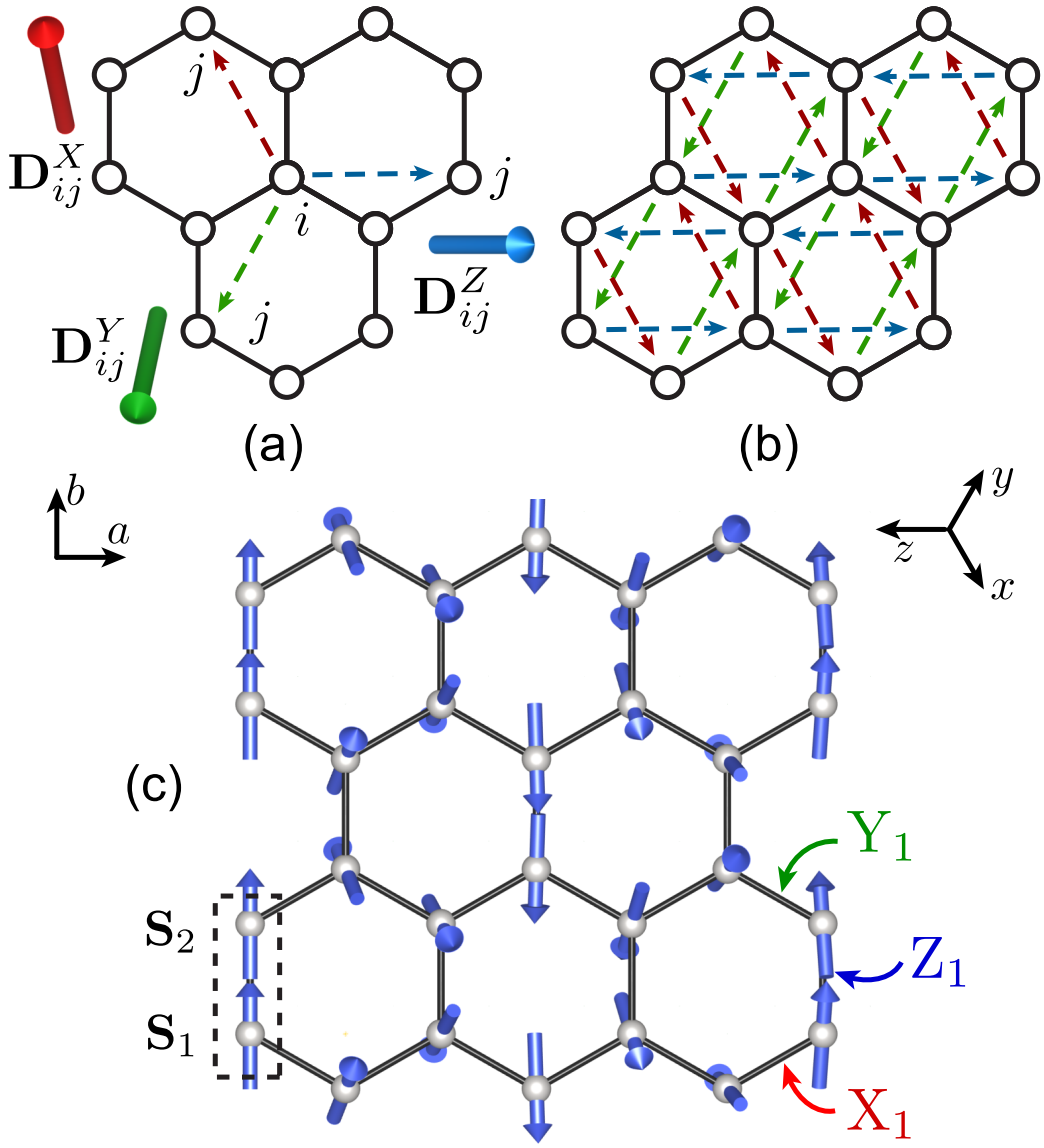

Figure 8.6: (a) Orientation of computed second neighbour DM vectors for the relaxed structure of α-Li_2IrO_3, with sense of each interaction indicated by dashed arrows. (b) Network of interactions in the full lattice. Within a given sublattice, the DM vectors are uniform, and will therefore tend to promote incommensurate states. (c) Classical ground state of the minimal model of Eq. (8.8) with $(A_1, B_1, A_2, B_2, J_3) \sim$ (-10.7, +24, -3.3,+7.0,+3.6) consistent with the experimental structure of Ref. [20].

$RuCl_3$, we rotate the direction to the following formula:

$$\hat{H} = \sum_{\text{1st nn}} A_1 \mathbf{S}_i \cdot \mathbf{S}_j + B_1 S_i^\delta S_j^\delta + \sum_{\text{3rd nn}} J_3 \mathbf{S}_i \cdot \mathbf{S}_j + \sum_{\text{2nd nn}} A_2 \mathbf{S}_i \cdot \mathbf{S}_j + B_2 S_i^\delta S_j^\delta + \mathbf{D}_{ij} \cdot \mathbf{S}_i \times \mathbf{S}_j. \tag{8.8}$$

Due to so many interactions, discussion of the magnetic order in α-Li_2IrO_3 is difficult. First, we consider the model only including first nearest neighbour couplings and J_3 in Figure 8.5 (a). Further, we add the second neighbour couplings A_2 and B_2, shifting the incommensurate(IC) region to larger J_3, shown in Figure 8.5 (b). Finally with DM vector $|\mathbf{D}_2|$, the Stripy region becomes very small, while the IC region is extended to smaller J_3 and larger J_1 region.

If there is no anisotropy of the bond, a second neighbour DM-interaction of C_3 symmetry would be $\mathbf{D}_2^X = (0,-D,-D)$, $\mathbf{D}_2^Y = (-D,0,-D)$, and $\mathbf{D}_2^Z = (-D,-D,0)$. With this, $(A_1, B_1, A_2, B_2, D, J_3)$ are (-11, +16, -3, +7, +1.5, +6) meV. The magnetic configuration can be expressed in the two-site basis (see Fig. 8.6 (c)) [20],

$$\mathbf{S}_1(\mathbf{r}) = \sum_{\mathbf{k}} (\mathbf{F}_\mathbf{k} + \mathbf{A}_\mathbf{k}) e^{-i\mathbf{k}\cdot\mathbf{r}}, \tag{8.9}$$

$$\mathbf{S}_2(\mathbf{r}) = \sum_{\mathbf{k}} (\mathbf{F}_\mathbf{k} - \mathbf{A}_\mathbf{k}) e^{-i\mathbf{k}\cdot\mathbf{r}}, \tag{8.10}$$

where the magnetic configuration is described by a single $\mathbf{q}$ vector $\mathbf{F}_\mathbf{q} = \mathbf{F}^*_{-\mathbf{q}}$, $\mathbf{A}_\mathbf{q} = \mathbf{A}^*_{-\mathbf{q}}$, and the cartesian coordinates corresponding to (a, b, c^*). Now we analyze the parameters in Eq. (8.8). For large $A_1 < 0$, $B_1 > 0$, the classical ground state is FM with $\mathbf{q} = 0$, $\mathbf{F}_\mathbf{q} = (F_a, F_b, 0)$. With $J_3 > 0$, the ground state is zigzag defined by $\mathbf{q} = (\pi, 0, 0)$ and $\mathbf{A}_\mathbf{q} = (A_a, 0, A_{c^*})$.

With the parameters $(A_1, B_1, A_2, B_2, D, J_3) \sim$ (-11, +16, -3, +7, +1.5, +6), the ground state is zigzag because of the large J_3. However, an incommensurate state appears at intermediate J_3, which has the same components as the experimental magnetic structure $\mathbf{F}_\mathbf{q} = (0, F_b, 0), \mathbf{A}_\mathbf{q} = (-iA_a, 0, -iA_{c^*})$ [20]. The experimental $\mathbf{q}$ is obtained when:

$$\frac{B_2}{B_1} \sim 0.3 - 1.3\frac{D}{B_1} \quad , \quad \frac{A_2}{B_1} \sim -0.14 + 0.5\frac{D}{B_1}. \tag{8.11}$$

Then we manipulate the parameters to find the case.

- When $D = 0$, the above condition requires $B_2 > 0, A_2 < 0$, $B_2/B_1 = 0.3$, and $A_2/B_2 = 0.5$, consistent with the bond-average value from our calcu-

lations. The ground state is shown in Fig. 8.6 (c) with $(A_1, B_1, A_2, B_2, J_3) \sim (-10.7, +24, -3.3, +7.0, +3.6)$ meV.

- The second-neighbour DM terms stabilize spiral order. Even a very small value $D/K_1 \sim 0.15$, enlarges the region of the incommensurate phase (see in Fig. 8.5 (c)). In $C2/m$ symmetry, the honeycomb lattice has two sublattices $\mathbf{S}_1$ and $\mathbf{S}_2$ related by inversion. The second neighbour interactions couple the sites in the same sublattice. Therefore, there is only one $\mathbf{D}_2$ in each sublattice (Fig. 8.6 (a,b)). Therefore, the DM-interaction gives spiral states of opposite chirality for each sublattice. Example parameters that reproduce the experimental results are $(A_1, B_1, A_2, B_2, D, J_3) \sim (-8.9, +20, -2.0, +3.9, +1.5, +3.0)$ meV.

With $(A_1, B_1, A_2, B_2, D, J_3) \sim (-8.9, +20, -2.0, +3.9, +1.5, +3.0)$ meV, the Weiss temperature is $\Theta_{iso} > 0$, different with the experimental results $\Theta_{iso} \sim -33$ K [75]. This result might be change with further refinement of the crystal structure. What's more, we predict a FM $\Theta_b \gtrsim \Theta_a > 0$, and AFM $\Theta_c < 0$, giving an inverse anisotropy of Na_2IrO_3. This could be checked in future experiments.

These results show that models with bond averaged values of $K_2, \Gamma_2, \mathbf{D}_2$ can already obtain the experimental magnetic state. Although the interactions for the real material has the bond depending parameters, especially for the experimental structure, we did not include the large number of terms because it is hard to discuss all the details of all bond-anisotropic and long-range terms.

8.3 Realization of the spin liquid in real materials

This section is aimed at discussing the realization of the Kitaev spin liquid phase in real materials. There is only a small region of parameter space from the phase diagram that exhibits this phase, as suggested by the phase diagrams in this and previous works [26, 67, 72, 75, 76, 81, 89]. In the pure Kitaev-Heisenberg model with $J_1 > 0, K_1 < 0$, the spin liquid is realized in the region $\alpha = K_1/(K_1 - 2J_1) \gtrsim 0.7 - 0.8$ [26, 89]. The long range magnetic interactions J_2 and J_3 can lift the classical degeneracy to promote order but can also frustrate the order and extended the Kitaev spin-liquid regions [75, 76, 81] (see Fig. 8.3). Without J_1, we assume that

order appears unless $|J_3/K_1| \lesssim 0.1$. The off-diagonal interactions Γ_1, Γ_1' can also drive the material away from the spin liquid, which would exist only for $\Gamma_1/K_1 \lesssim 0.1$ [67, 72]. The hopping integrals t_1, t_2, t_3 can be calculated using Slater-Koster parameters [107] from $t_{dd\sigma}, t_{dd\pi}, t_{pd\pi}$ (see Fig. 8.7) as Ref. [67]. [1]

$$\begin{aligned} t_1 &\sim \frac{1}{2}t_{dd\pi} + \frac{t_{pd\pi}^2}{\Delta_{pd}}\cos\phi, \\ t_2 &\sim -\frac{1}{2}t_{dd\pi} + \frac{t_{pd\pi}^2}{\Delta_{pd}}, \\ t_3 &\sim \frac{3}{4}t_{dd\sigma} + \frac{(t_{pd\pi} - \sqrt{3}t_{pd\sigma})^2}{8\Delta_{pd}}\cos 3\phi \\ &\quad + \frac{(\sqrt{3}t_{pd\pi} + 9t_{pd\sigma})(\sqrt{3}t_{pd\pi} + t_{pd\sigma})}{8\Delta_{pd}}\cos\phi, \end{aligned} \tag{8.12}$$

where Δ_{pd} is the charge transfer energy between the t_{2g} orbitals and the chalcogen or halogen p orbitals, and ϕ gives the angle of the metal-ligand-metal bond. In the materials A_2IrO_3, the values are obtained for

$$\begin{aligned} t_{dd\pi} \sim 0.25 f(\phi)\ \text{eV} \quad &, \quad t_{dd\sigma} \sim -0.4 f(\phi)\ \text{eV}, \\ \frac{t_{pd\pi}^2}{\Delta_{pd}} \sim 0.4\ \text{eV} \quad &, \quad \frac{t_{pd\sigma}^2}{\Delta_{pd}} \sim 0.5\ \text{eV}. \end{aligned} \tag{8.13}$$

where $f(\phi)$ is an empirical damping factor (Fig. 8.8 (a)), which can describe the decrease of the metal-metal hopping with increasing the distance of Ir-Ir bond. The metal-ligand distances are assumed to be a constant, and the p_x, p_y and p_z orbitals are roughly degenerate. Without distortion ($\phi = 90^\circ$), ligand assisted hopping only contributes to t_2, and t_1, t_3 only have the contribution from metal-metal hopping. With distortion ($\phi > 90^\circ$), the ligand assisted procedure also contributes to t_1 and t_3 but with opposite sign, which leads to nearly zero t_1 and t_3 around $\phi \sim 100^\circ$ (see Fig. 8.8 (a)). These hoppings determine the exchange parameters and magnetic interactions.

- Heisenberg coupling: The requirement for the spin liquid of $\alpha \gtrsim 0.8$ is satisfied for a wide region $95^\circ \lesssim \phi \lesssim 100^\circ$ shown in the red shaded region of Fig. 8.8 (b).

- *Off-diagonal terms:* $t_2 >> t_1, t_3, t_4$ is the region where the pure Kitaev model is realized. Off-diagonal couplings dominate the nearest neighbour magnetic

[1] Note that the expression for t_2 in the supplemental of Ref. [67] seems to have different sign notations.

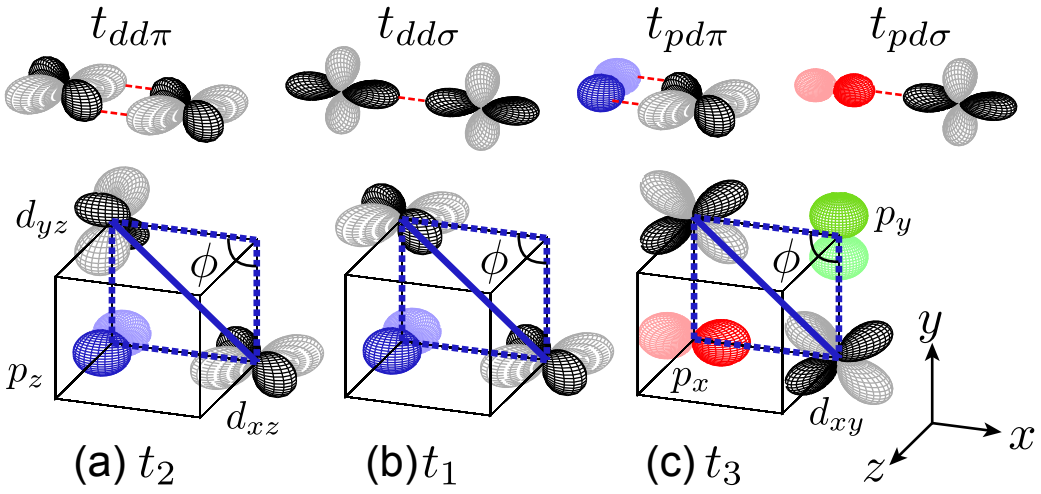

Figure 8.7: Geometry of nearest neighbour hopping integrals (a) t_2, (b) t_1, and (c) t_3 for the Z_1 bond, showing ligand mediated and direct hopping processes. These can be decomposed in terms of Slater-Koster hopping integrals $t_{dd\pi}$, $t_{dd\sigma}$, $t_{pd\pi}$, $t_{pd\sigma}$ (top) as a function of metal-ligand-metal bond angle ϕ, as in Eq. (8.12).

interactions in α-$RuCl_3$ and α-Li_2IrO_3. The condition of $|\Gamma_1/K_1| < 0.1$ for the Kitaev spin liquid can only be realized in a narrow region near $\phi \sim 100°$. Na_2IrO_3 is close to this ideal region due to larger distortion. Thus, in contrast to the initial assumptions, trigonal distortions are helpful to realize the spin-liquid. However, large distortions can introduce large t_4, which gives other large contributions to Γ_1, Γ_1' [8, 72, 80].

- Long-range interactions: Third nearest neighbour Heisenberg coupling J_3 is very robust for the d^5 honeycomb materials, which explains the zigzag order in both Na_2IrO_3 and α-$RuCl_3$. Lattice expansion could suppress J_3 in the honeycomb materials if t/U could be decreased. Some of the perturbative contributions to J_3 are absent in the 3D β-Li_2IrO_3. Thus, long-range interactions should be partially suppressed in the 3D systems.

8.4 Summary

In the C2/m honeycomb Ir^{4+} and Ru^{3+} systems, complexity arises from a combination of (i) competing Coulomb, hopping, and spin-orbit energy scales, (ii) rela-

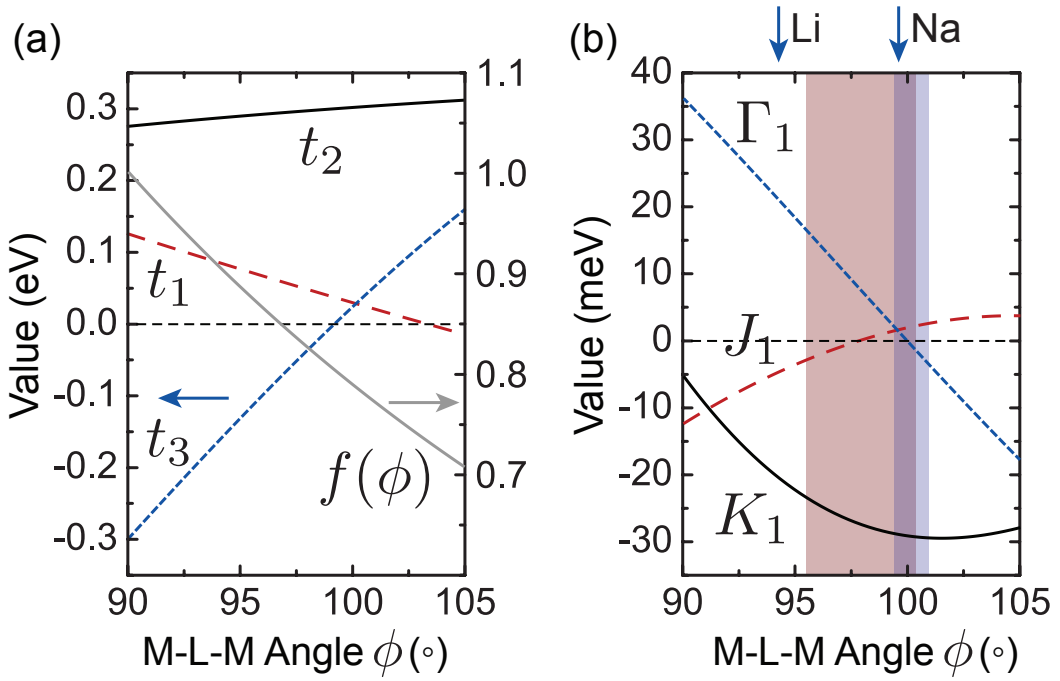

Figure 8.8: (a) Schematic dependence of hopping integrals t_{1-3} for A_2IrO_3 and empirical damping factor $f(\phi) < 1$ (grey line) on metal-ligand-metal bond angle ϕ; t_4 is assumed to be zero. (b) Resulting magnetic interactions obtained using the "Exact" 2OPT expressions. The red shaded region indicates the area where $|J_1/K_1| < 0.1$, while the blue region denotes $|\Gamma_1/K_1| < 0.1$. For α-Li_2IrO_3,$\phi \sim 95°$, while Na_2IrO_3 falls nearly in ideal region $\phi \sim 100°$.

tively low symmetry, (iii) suppression of dominant magnetic couplings, (iv) strongly anisotropic interactions, and (v) significant long-range terms. The details of the interactions in the real materials and their relationship to the experimental properties have therefore been intensively debated in the literature. In this work, we have addressed this debate by employing nonperturbative exact diagonalization methods that treat interactions at all scales on the same level, and therefore allow estimation of all parameters. The salient conclusions are as follows:

- The observed zigzag order in Na_2IrO_3 and α-$RuCl_3$ is explained naturally in terms of a large third-neighbor Heisenberg coupling J_3 that emerges as a dominant term at high orders in perturbation theory, and was therefore neglected or underestimated in most previous studies.

- Off-diagonal couplings $\Gamma_1 \sim K_1$ dominate the nearest-neighbor magnetic interactions in α-$RuCl_3$ and α-Li_2IrO_3 as a result of direct metal-metal (M-M) hopping. These terms can be suppressed by increasing the M-M bond distance, through the distortion of the local ML_6 octahedra to provide M-L-M bond angles $\phi \sim 100^\circ$. In the known materials, this ideal region is most closely approached by Na_2IrO_3, which is therefore the closest to the Kitaev limit $K_1 \gg J_1$, Γ_1 at the nearest-neighbor level. Due to the effects of direct metal-metal hopping, the ideal materials will therefore not be found with $\phi = 90^\circ$, as originally proposed.

- Although the Kitaev spin liquid is thought to be stable for a finite region of magnetic parameters, the design limitations in real materials are highly restrictive due to a large sensitivity of the interactions to structural details. This sensitivity allows for large variations in the magnitude of interactions along the different nonequivalent bonds, which typically lifts the classical degeneracy. The ideal region where the Kitaev interaction is dominant is likely confined to a small width of M-L-M bond angle $\phi \lesssim 1^\circ$, which may be difficult to satisfy in real materials simultaneously for all nonequivalent bonds.

- Given that Na_2IrO_3 was found to lie very close to the ideal region where $K_1 \gg J_1$, the most significant interaction preventing realization of the spin-liquid state in real materials is considered to be the unfrustrated long-range J_3 term. In the d^5 materials, the complementary nature of spin-orbit coupling and Coulomb repulsion in establishing the charge gap makes J_3 largely insensitive to choice of magnetic ions or other structural details. This observation seriously complicates any synthetic strategies aimed at reducing long-range couplings in edge-sharing octahedral systems.

- For α-Li_2IrO_3, the computed interactions suggest the possibility of large bond anisotropy and significant terms at first, second, and third neighbor. While several model Hamiltonians have been considered for the $\alpha-$, $\beta-$, and $\gamma-$ phase materials, the true interactions are likely considerably more complicated. We have shown, in particular, that a combination of K_2, Γ_2, and second-neighbor DM interaction D_2 may explain the observed order. The complexity of the interactions may be even greater for the lower symmetry $\beta-$ and γ-Li_2IrO_3, where Dzyaloshinskii-Moriya interactions are allowed even for cer-

tain first-neighbor bonds. It remains to be determined which models can be effectively related to the real materials, but purely nearest-neighbor models are probably unrealistic.

Given these observations, realization of the Kitaev spin liquid as a ground state in edge-sharing d^5 materials appears to represent a very significant synthetic challenge. However, given the highly complex phase diagrams, and possibility of many points of classical degeneracy within the expanded range of interactions, these systems are likely to host other exotic phases and phase transitions. Furthermore, when probed at high energies or temperatures $T > T_N$, the combined fluctuations associated with all nearby orders may give rise to novel thermodynamic or spectral properties [108–111]. Given the potential for complex interactions, future studies of such systems will benefit from comprehensive and nonperturbative ab initio estimates of all relevant interactions.

Chapter 9

Contributed work: electronic structure and spin-orbit driven novel magnetism in $d^{4.5}$ insulator $Ba_3YIr_2O_9$

S. K. Panda, S. Bhowal, **Ying Li**, S. Ganguly, Roser Valenti,
L. Nordström, and I. Dasgupta
Phys. Rev. B **92**, 180403 (R) (2015) [37]

We have studied 5*d* and 4*d* systems which all have 5 electrons in the t_{2g} orbitals. In this chapter, we will consider materials with fractional charge state $Ir^{4.5+}$ like $Ba_3YIr_2O_9$, which have 4.5 electrons in the t_{2g} orbitals. There are two structures of this material: at high-pressure (HP) and ambient pressure (AP). From the experiment, it is found that at AP, the variation of the susceptibility shows a weak anomaly around 4 K [112]. The susceptibility data [113] gives $\theta_{CW} \sim 0$ and effective moment 0.3 μ_B, while the HP structure does not order down to 2 K, and was suggested to be a gapless QSL [31]. We will show the electronic structure calculations for the AP phase using VASP, Elk, and WIEN2k. I performed the Wien2k calculations; VASP and Elk calculations were performed by S. K. Panda *et al* [37].

In Figure 9.1, we show the AP structure of $Ba_3YIr_2O_9$, which has four Ir in each unit cell forming two dimers linked by the O-Y-O paths along **c** axis in the space group $P6_3/mmc$. The Ir and O have an octahedral IrO_6 structure, but different from

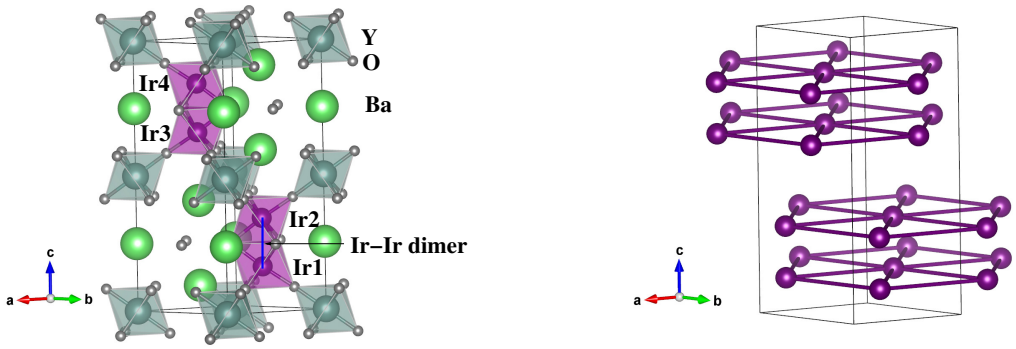

Figure 9.1: The crystal structure for the hexagonal AP phase of $Ba_3YIr_2O_9$.

the edge sharing in Na_2IrO_3. In $Ba_3YIr_2O_9$, two IrO_6 share the face, and therefore form the Ir_2O_9 bioctahedra.

9.1 Magnetic properties

We calculated the total energy for four different magnetic configurations shown in Figure 9.2.

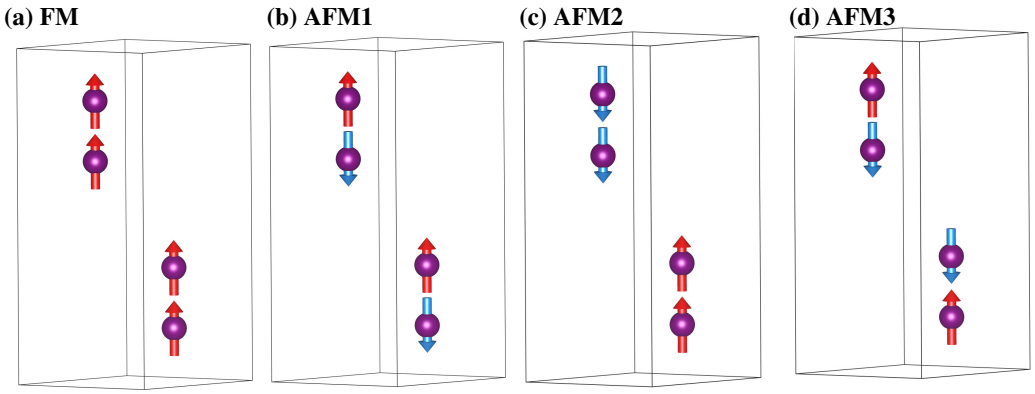

Figure 9.2: Magnetic phase of $Ba_3YIr_2O_9$.

- FM, all couplings are ferromagnetic;
- AFM1, both the intra- and inter-dimer couplings are antiferromagnetic;

- AFM2, intra-dimer coupling is ferromagnetic and inter-dimer coupling is antiferromagnetic;

- AFM3, intra-dimer coupling is antiferromagnetic and inter-dimer coupling is ferromagnetic.

The computed energy and magnetic moment using LDA+SO+U with U = 4 eV in the Elk code are displayed in Fig. 9.3. The results indicate that AFM2 is the ground

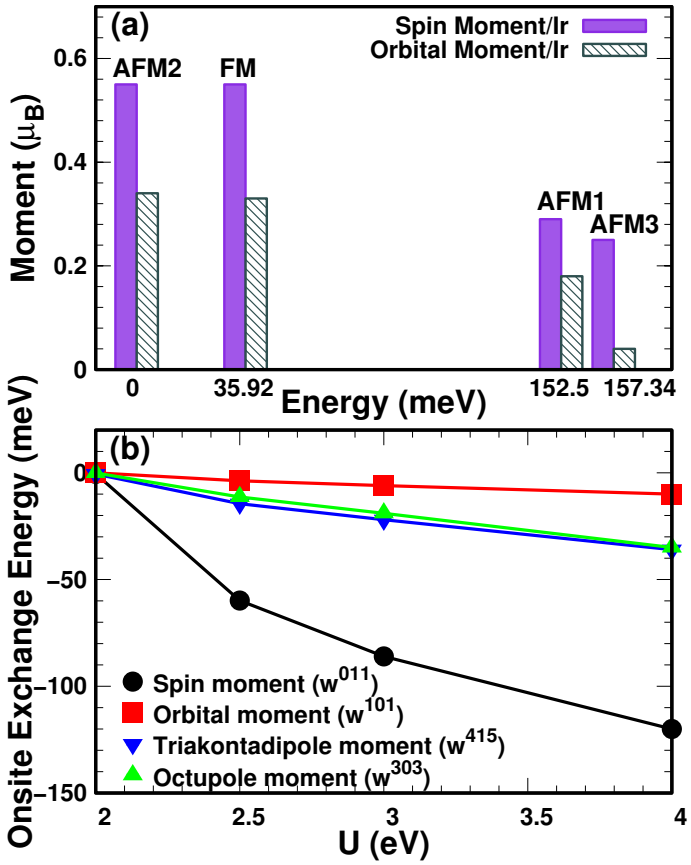

Figure 9.3: (a) The variation of spin and orbital moment at the Ir site for various magnetic configurations in the AP phase. (b) Variation of onsite exchange energy (in meV) associated with different order parameters (OP) with the variation of U in eV.

state with the spin moment on Ir site of 0.55 μ_B and the orbital moment 0.34 μ_B, which has smaller ration of $\frac{m_l}{m_s}$($\sim$0.62) than Ir^{5+} iridates like Sr_2IrO_4 [114] with $\sim$2. The AFM2 ground state (FM interaction within each dimer) implies that $Ir^{4.5+}$ iridates have strong effective Hund's coupling (J_H), which is larger than the crystal

field and spin-orbit coupling than Ir^{5+} iridates. If λ is larger than J_H, the intra-dimer will have AFM interaction such as $Ba_5AlIr_2O_{11}$ [115].

9.2 Electronic structure

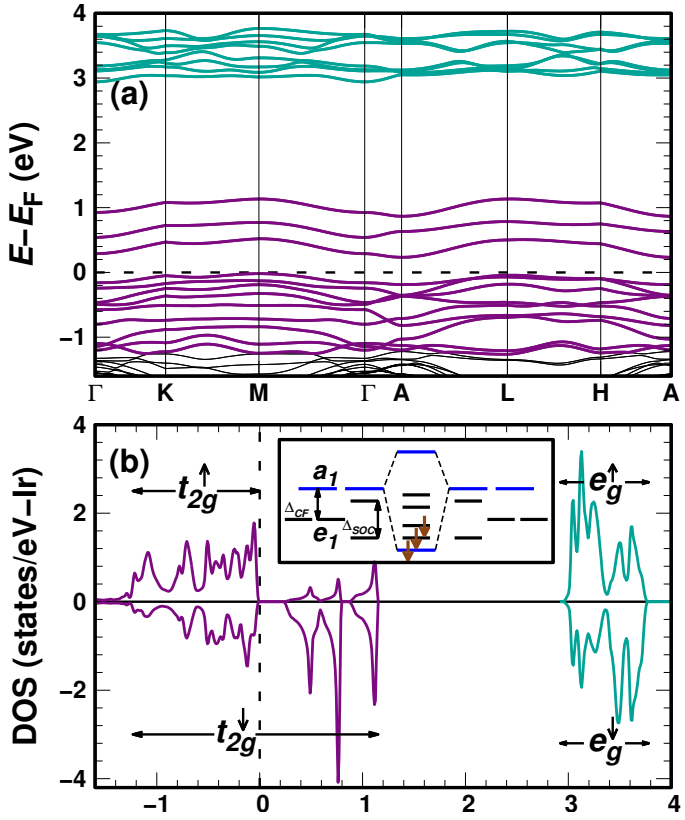

Figure 9.4: (a) Bandstructure and (b) Partial density of states (DOS) for Ir-d within LDA+U+SOC for the AP phase. The inset shows the schematic diagram to explain the insulating behavior of AP phase.

Similar to Na_2IrO_3, the electronic structure for the non magnetic phase without SO has a metallic phase and t_{2g}, e_g are split. There are twelve t_{2g} bands from the four Ir atoms around the Fermi-level. In contrast to Na_2IrO_3 (around 1.5 eV bandwidth), the bandwidth is enlarged to 2 eV in $Ba_3YIr_2O_9$. This may explain why the SO interaction becomes effectively smaller. The large bandwidth renormalizes the strength of the atomic λ. In order to reproduce the experimental insulating properties, the LDA+SO+U calculations were performed for the AFM2 configuration.

The computed DOS and bandstructure are displayed in Fig. 9.4. The insulating state with a gap of 252 meV comes from the effect of J_H, Δ_{CF}, λ and $t_{intra-dimer}$ together.

9.3 Summary

In conclusion, our detailed study of electronic and magnetic properties of $d^{4.5}$ $Ba_3YIr_2O_9$ in the AP phase suggest that a competition between J_H and SO coupling decides the magnetic properties. The J_H dominates over the SO coupling leading to FM magnetic order intra-dimer. The relatively weak value of SO coupling in the AP phase may be attributed to the large t_{2g} bandwidth in $Ba_3YIr_2O_9$.

Chapter 10

Summary and outlook

In this thesis, we performed density functional theory (DFT) calculations for several Kitaev spin-liquid candidates - 2D honeycomb Na_2IrO_3, α-Li_2IrO_3, α-$RuCl_3$, 3D γ-Li_2IrO_3, and double layer triangular $Ba_3YIr_2O_9$ to calculate the electronic properties. We also derived the microscopic models for the 2D honeycomb lattice. From the analysis of the derived models and calculations, we were able to draw important conclusions regarding the compounds, microscopic behavior and the connection between their electronic structures and experimentally observed macroscopic properties.

In the case of honeycomb lattice Na_2IrO_3, α-Li_2IrO_3, and α-$RuCl_3$, we found the quality of the Quasi-molecular orbital (QMO) picture depends on hoppings due to different trigonal distortions. Na_2IrO_3 has the largest distortions and the nonrelativistic single particle electronic structure is well described in terms of the QMO basis. However, the QMO picture is destroyed in $P3_112$ α-$RuCl_3$ as small distortion enhances metal-metal hopping. For α-Li_2IrO_3 and $C2/m$ α-$RuCl_3$, the intermediate distortion gives significantly mixed QMOs.

For the optical conductivity, we investigated the 2D Na_2IrO_3, α-Li_2IrO_3 and 3D γ-Li_2IrO_3 using both relativistic DFT method within GGA+SO+U and exact diagonalization of the full interacting Hamiltonian on finite clusters where the hopping integrals were obtained from DFT. Both methods reproduce the main peak of the in-plane component of the optical conductivity σ_c and the experimental gap. The insulating behavior can be explained by including of spin-orbit coupling and Coulomb

repulsion for d^5 filling. Using the fact that the narrow bands of Na_2IrO_3 are well described in terms of QMOs, we showed that the strength of the various interband contributions to the optical conductivity can be well described in terms of the parity of the QMOs, namely, weight suppression in like-parity transitions and weight enhancement in unlike-parity transitions. We also predict the shape of the optical conductivity for α-Li_2IrO_3. However, GGA+SO+U seems to overestimate the contribution of the $j_{1/2} \rightarrow j_{1/2}$ transition at low energies in σ_a and σ_b. The ED results, in contrast, validate the model parameters (U, J_H, λ) and suggest that the high-lying excitations seem to be well captured within a localized picure in γ-Li_2IrO_3. The comparison with the optical conductivity analysis of Na_2IrO_3 shows that the peak near 1.5 eV in both Na_2IrO_3 and γ-Li_2IrO_3 can be identified in terms of *intersite* $j_{3/2} \rightarrow j_{1/2}$ excitations. The comparison of $\sigma(\omega)$ for the various materials suggests that the relative spectral weight of the transitions may provide insight into the magnitudes of various hopping integrals, and therefore the local magnetic interactions.

All the structures show magnetic ordered ground states. Na_2IrO_3 and α-$RuCl_3$ have zigzag magnetic order, which can be reproduced by a large third-neighbor Heisenberg coupling J_3. This term comes from high orders in perturbation theory, which were neglected or underestimated in most previouis studies. α-Li_2IrO_3 has spin spiral order and can be explained by a combination of second-neighbor anisotropy interactions. With all these observations, realization of the Kitaev spin liquid as a ground state in edge-sharing d^5 materials appears to represent a very significant synthetic challenge.

As a general conclusion, all the considered materials have both large spin-orbit and strong correlation effects that need to be investigated by a combination of DFT and many body methods. The hopping integrals based on the electronic structure are used to calculate optical conductivity and magnetic interactions, which relate the electronic and magnetic properties. The exact diagonalization method on the honeycomb lattice provides a more accurate way to obtain the magnetic interactions. It can be applied to other systems. This technique is a powerful computational tool for studies of magnetic systems in strongly correlated and spin-orbit systems. On the basis of the calculations performed in this thesis, we were able to identify the main synthetic challenges for realizing a spin-liquid state in the Kitaev candidates. The methods used and developed in this thesis will no doubt help guide future work towards engineering the Kitaev spin liquid in real materials.

Appendix A

Spin-orbital coupling and relativistic basis

The behavior of $\left|d_{xy}\right\rangle$, $|d_{xz}\rangle$, $\left|d_{yz}\right\rangle$ are like the orbital $|p_z\rangle$, $\left|p_y\right\rangle$, $|p_x\rangle$. We therefore use effective $|\widetilde{p}_z\rangle$, $\left|\widetilde{p}_y\right\rangle$, $|\widetilde{p}_x\rangle$ to describe these three orbitals. With $|\widetilde{p}_z\rangle = \left|d_{xy}\right\rangle$ $\left|\widetilde{p}_y\right\rangle = |d_{xz}\rangle$ $|\widetilde{p}_x\rangle = \left|d_{yz}\right\rangle$ $l_{\text{eff}} = 1, m_{l_{\text{eff}}} = -1, 0, 1$. We define the eigenstates of $\left(\overrightarrow{L}^2, L_Z\right)$ as ϕ_{11} ϕ_{10} ϕ_{1-1}. The states of $|l, m_l\rangle$ are

$$\begin{aligned} |1,0\rangle &= |\widetilde{p}_z\rangle, \\ |1,1\rangle &= \frac{1}{\sqrt{2}}(-i\left|\widetilde{p}_y\right\rangle - |\widetilde{p}_x\rangle), \\ |1,-1\rangle &= \frac{1}{\sqrt{2}}(-i\left|\widetilde{p}_y\right\rangle + |\widetilde{p}_x\rangle). \end{aligned} \tag{A.1}$$

Here, the spin quantum number $s = \frac{1}{2}, m_s = -\frac{1}{2}, \frac{1}{2}$. Then we define the eigenstates of $\left(\overrightarrow{S}^2, S_Z\right)$ as $\chi_{\frac{1}{2}-\frac{1}{2}}$, $\chi_{\frac{1}{2}\frac{1}{2}}$. With the SO coupling, the total quantum number $j = |l+s|, |l+s-1| ... |l-s| = \frac{3}{2}, \frac{1}{2}$. $m_j = m_l + m_s = j, j-1 .... -j$. We define the state as $\varphi_{\frac{3}{2},\frac{3}{2}}$, $\varphi_{\frac{3}{2},\frac{1}{2}}$, $\varphi_{\frac{3}{2},-\frac{1}{2}}$, $\varphi_{\frac{3}{2},-\frac{3}{2}}$, $\varphi_{\frac{1}{2},\frac{1}{2}}$, $\varphi_{\frac{1}{2},-\frac{1}{2}}$. The relativistic states can be expressed as

$$\varphi_{j,m_j} = \sum_{m_l m_s} \left\langle l m_l s m_s | l s j m_j \right\rangle \phi_{l m_l} \chi_{s m_s}, \tag{A.2}$$

where $\left\langle l m_l s m_s | l s j m_j \right\rangle$ are called Clebsch-Gordan coefficients. The states are calculated as followings:

$$\begin{aligned}
\varphi_{\frac{3}{2},\frac{3}{2}} &= -\phi_{11}\chi_{\frac{1}{2}\frac{1}{2}} \\
J_-\varphi_{\frac{3}{2},\frac{3}{2}} &= -L_-\phi_{11}\chi_{\frac{1}{2}\frac{1}{2}} - S_-\phi_{11}\chi_{\frac{1}{2}\frac{1}{2}} \\
\sqrt{3}\varphi_{\frac{3}{2},\frac{1}{2}} &= -\sqrt{2}\phi_{10}\chi_{\frac{1}{2}\frac{1}{2}} - \phi_{11}\chi_{\frac{1}{2}-\frac{1}{2}} \\
\varphi_{\frac{3}{2},\frac{1}{2}} &= -\sqrt{\frac{2}{3}}\phi_{10}\chi_{\frac{1}{2}\frac{1}{2}} - \frac{1}{\sqrt{3}}\phi_{11}\chi_{\frac{1}{2}-\frac{1}{2}},
\end{aligned} \tag{A.3}$$

$$\begin{aligned}
J_-\varphi_{\frac{3}{2},\frac{1}{2}} &= -L_-\sqrt{\frac{2}{3}}\phi_{10}\chi_{\frac{1}{2}\frac{1}{2}} - S_-\phi_{10}\chi_{\frac{1}{2}\frac{1}{2}} - L_-\frac{1}{\sqrt{3}}\phi_{11}\chi_{\frac{1}{2}-\frac{1}{2}} \\
\varphi_{\frac{3}{2},-\frac{1}{2}} &= -\frac{1}{\sqrt{3}}\phi_{1-1}\chi_{\frac{1}{2}\frac{1}{2}} - \sqrt{\frac{2}{3}}\phi_{10}\chi_{\frac{1}{2}-\frac{1}{2}} \\
\varphi_{\frac{3}{2},-\frac{3}{2}} &= -\phi_{1-1}\chi_{\frac{1}{2}-\frac{1}{2}},
\end{aligned} \tag{A.4}$$

$$\begin{aligned}
\varphi^*_{\frac{1}{2},\frac{1}{2}}\varphi_{\frac{3}{2},\frac{1}{2}} &= 0 \\
\varphi_{\frac{1}{2},\frac{1}{2}} &= \frac{1}{\sqrt{3}}\phi_{10}\chi_{\frac{1}{2}\frac{1}{2}} - \sqrt{\frac{2}{3}}\phi_{11}\chi_{\frac{1}{2}-\frac{1}{2}} \\
\varphi_{\frac{1}{2},-\frac{1}{2}} &= \sqrt{\frac{2}{3}}\phi_{1-1}\chi_{\frac{1}{2}\frac{1}{2}} - \frac{1}{\sqrt{3}}\phi_{10}\chi_{\frac{1}{2}-\frac{1}{2}}.
\end{aligned} \tag{A.5}$$

Thus, the states of $\left|j,m_j\right\rangle$ are

$$\left|\frac{1}{2},\frac{1}{2}\right\rangle = \frac{1}{\sqrt{3}}\left|d_{xy}\uparrow\right\rangle + \frac{i}{\sqrt{3}}\left|d_{xz}\downarrow\right\rangle + \frac{1}{\sqrt{3}}\left|d_{yz}\downarrow\right\rangle, \tag{A.6}$$

$$\left|\frac{1}{2},-\frac{1}{2}\right\rangle = -\frac{i}{\sqrt{3}}\left|d_{xz}\uparrow\right\rangle + \frac{1}{\sqrt{3}}\left|d_{yz}\uparrow\right\rangle - \frac{1}{\sqrt{3}}\left|d_{xy}\downarrow\right\rangle, \tag{A.7}$$

$$\left|\frac{3}{2},\frac{3}{2}\right\rangle = \frac{i}{\sqrt{2}}\left|d_{xz}\uparrow\right\rangle + \frac{1}{\sqrt{2}}\left|d_{yz}\uparrow\right\rangle, \tag{A.8}$$

$$\left|\frac{3}{2},\frac{1}{2}\right\rangle = -\sqrt{\frac{2}{3}}\left|d_{xy}\uparrow\right\rangle + \frac{i}{\sqrt{6}}\left|d_{xz}\downarrow\right\rangle + \frac{1}{\sqrt{6}}\left|d_{yz}\downarrow\right\rangle, \tag{A.9}$$

$$\left|\frac{3}{2},-\frac{1}{2}\right\rangle = \frac{i}{\sqrt{6}}\left|d_{xz}\uparrow\right\rangle - \frac{1}{\sqrt{6}}\left|d_{yz}\uparrow\right\rangle - \sqrt{\frac{2}{3}}\left|d_{xy}\downarrow\right\rangle, \tag{A.10}$$

$$\left|\frac{3}{2},-\frac{3}{2}\right\rangle = \frac{i}{\sqrt{2}}\left|d_{xz}\downarrow\right\rangle - \frac{1}{\sqrt{2}}\left|d_{yz}\downarrow\right\rangle. \tag{A.11}$$

The operator

$$L_+ = L_x + iL_y \quad L_- = L_x - iL_y, \tag{A.12}$$

$$S_+ = S_x + iS_y \quad S_- = S_x - iS_y, \tag{A.13}$$

$$L_+ |l,m\rangle = \sqrt{(l+m+1)(l-m)}\,|l,m+1\rangle\,, \tag{A.14}$$

$$L_- |l,m\rangle = \sqrt{(l-m+1)(l+m)}\,|l,m-1\rangle\,, \tag{A.15}$$

$$S_+ |\uparrow\rangle = 0,\ \ S_- |\uparrow\rangle = |\downarrow\rangle\,, \quad S_z |\uparrow\rangle = \frac{1}{2}|\uparrow\rangle\,, \tag{A.16}$$

$$S_+ |\downarrow\rangle = |\uparrow\rangle\,,\ S_- |\downarrow\rangle = 0, \quad S_z |\downarrow\rangle = -\frac{1}{2}|\downarrow\rangle\,. \tag{A.17}$$

Spin-orbit coupling

$$H_{so} = \lambda(\frac{L_+S_- + L_-S_+}{2} + L_zS_z), \tag{A.18}$$

in the matrix is

$$\begin{pmatrix} 0 & 0 & 0 & 0 & \frac{i\lambda}{2} & -\frac{\lambda}{2} \\ 0 & 0 & \frac{i\lambda}{2} & -\frac{i\lambda}{2} & 0 & 0 \\ 0 & -\frac{i\lambda}{2} & 0 & \frac{\lambda}{2} & 0 & 0 \\ 0 & i\frac{\lambda}{2} & \frac{\lambda}{2} & 0 & 0 & 0 \\ -i\frac{\lambda}{2} & 0 & 0 & 0 & 0 & -\frac{i\lambda}{2} \\ -\frac{\lambda}{2} & 0 & 0 & 0 & \frac{i\lambda}{2} & 0 \end{pmatrix}, \tag{A.19}$$

which acts on the basis states $\left|d_{xy}\uparrow\right\rangle$, $|d_{xz}\uparrow\rangle$, $\left|d_{yz}\uparrow\right\rangle$, $\left|d_{xy}\downarrow\right\rangle$, $|d_{xz}\downarrow\rangle$, and $\left|d_{yz}\downarrow\right\rangle$. If we change λ as $-\lambda$, it equivalent to using d_{xy}, d_{xz}, d_{yz} as $l = 2$. The corresponding eigenvalues are $-\lambda, -\lambda, \frac{\lambda}{2}, \frac{\lambda}{2}, \frac{\lambda}{2}, \frac{\lambda}{2}$. The lower two relativistic basis are

$$\begin{aligned} \left|\widetilde{\uparrow}\right\rangle &= \frac{1}{\sqrt{3}}\left|d_{xy}\uparrow\right\rangle + \frac{i}{\sqrt{3}}|d_{xz}\downarrow\rangle + \frac{1}{\sqrt{3}}\left|d_{yz}\downarrow\right\rangle \\ &= \frac{1}{\sqrt{3}}|c\uparrow\rangle + \frac{i}{\sqrt{3}}|b\downarrow\rangle + \frac{1}{\sqrt{3}}|a\downarrow\rangle\,, \end{aligned} \tag{A.20}$$

$$\begin{aligned} \left|\widetilde{\downarrow}\right\rangle &= \frac{i}{\sqrt{3}}|d_{xz}\uparrow\rangle - \frac{1}{\sqrt{3}}\left|d_{yz}\uparrow\right\rangle + \frac{1}{\sqrt{3}}\left|d_{xy}\downarrow\right\rangle \\ &= \frac{i}{\sqrt{3}}|b\uparrow\rangle - \frac{1}{\sqrt{3}}|a\uparrow\rangle + \frac{1}{\sqrt{3}}|c\downarrow\rangle\,. \end{aligned} \tag{A.21}$$

After multiply the basis for i and j site, we obtain the basis

$$\begin{aligned}\left|\widetilde{\uparrow}_i\right\rangle\left|\widetilde{\uparrow}_j\right\rangle = &\frac{1}{3}\left|a\downarrow_i\right\rangle\left|a\downarrow_j\right\rangle - \frac{1}{3}\left|b\downarrow_i\right\rangle\left|b\downarrow_j\right\rangle + \frac{1}{3}\left|c\uparrow_i\right\rangle\left|c\uparrow_j\right\rangle \\ &+ \frac{i}{3}\left|a\downarrow_i\right\rangle\left|b\downarrow_j\right\rangle + \frac{i}{3}\left|b\downarrow_i\right\rangle\left|a\downarrow_j\right\rangle \\ &+ \frac{i}{3}\left|c\uparrow_i\right\rangle\left|b\downarrow_j\right\rangle + \frac{i}{3}\left|b\downarrow_i\right\rangle\left|c\uparrow_j\right\rangle \\ &+ \frac{1}{3}\left|c\uparrow_i\right\rangle\left|a\downarrow_j\right\rangle + \frac{1}{3}\left|a\downarrow_i\right\rangle\left|c\uparrow_j\right\rangle,\end{aligned} \tag{A.22}$$

$$\begin{aligned}\left|\widetilde{\uparrow}_i\right\rangle\left|\widetilde{\downarrow}_j\right\rangle = &-\frac{1}{3}\left|a\downarrow_i\right\rangle\left|a\uparrow_j\right\rangle - \frac{1}{3}\left|b\downarrow_i\right\rangle\left|b\uparrow_j\right\rangle + \frac{1}{3}\left|c\uparrow_i\right\rangle\left|c\downarrow_j\right\rangle \\ &+ \frac{i}{3}\left|a\downarrow_i\right\rangle\left|b\uparrow_j\right\rangle - \frac{i}{3}\left|b\downarrow_i\right\rangle\left|a\uparrow_j\right\rangle \\ &+ \frac{i}{3}\left|c\uparrow_i\right\rangle\left|b\uparrow_j\right\rangle + \frac{i}{3}\left|b\downarrow_i\right\rangle\left|c\downarrow_j\right\rangle \\ &- \frac{1}{3}\left|c\uparrow_i\right\rangle\left|a\uparrow_j\right\rangle + \frac{1}{3}\left|a\downarrow_i\right\rangle\left|c\downarrow_j\right\rangle,\end{aligned} \tag{A.23}$$

$$\begin{aligned}\left|\widetilde{\downarrow}_i\right\rangle\left|\widetilde{\uparrow}_j\right\rangle = &-\frac{1}{3}\left|a\uparrow_i\right\rangle\left|a\downarrow_j\right\rangle - \frac{1}{3}\left|b\uparrow_i\right\rangle\left|b\downarrow_j\right\rangle + \frac{1}{3}\left|c\downarrow_i\right\rangle\left|c\uparrow_j\right\rangle \\ &- \frac{i}{3}\left|a\uparrow_i\right\rangle\left|b\downarrow_j\right\rangle + \frac{i}{3}\left|b\uparrow_i\right\rangle\left|a\downarrow_j\right\rangle \\ &+ \frac{i}{3}\left|c\downarrow_i\right\rangle\left|b\downarrow_j\right\rangle + \frac{i}{3}\left|b\uparrow_i\right\rangle\left|c\uparrow_j\right\rangle \\ &+ \frac{1}{3}\left|c\downarrow_i\right\rangle\left|a\downarrow_j\right\rangle - \frac{1}{3}\left|a\uparrow_i\right\rangle\left|c\uparrow_j\right\rangle,\end{aligned} \tag{A.24}$$

$$\begin{aligned}\left|\widetilde{\downarrow}_i\right\rangle\left|\widetilde{\downarrow}_j\right\rangle = &\frac{1}{3}\left|a\uparrow_i\right\rangle\left|a\uparrow_j\right\rangle - \frac{1}{3}\left|b\uparrow_i\right\rangle\left|b\uparrow_j\right\rangle + \frac{1}{3}\left|c\downarrow_i\right\rangle\left|c\downarrow_j\right\rangle \\ &- \frac{i}{3}\left|a\uparrow_i\right\rangle\left|b\uparrow_j\right\rangle - \frac{i}{3}\left|b\uparrow_i\right\rangle\left|a\uparrow_j\right\rangle \\ &+ \frac{i}{3}\left|c\downarrow_i\right\rangle\left|b\uparrow_j\right\rangle + \frac{i}{3}\left|b\uparrow_i\right\rangle\left|c\downarrow_j\right\rangle \\ &- \frac{1}{3}\left|c\downarrow_i\right\rangle\left|a\uparrow_j\right\rangle - \frac{1}{3}\left|a\uparrow_i\right\rangle\left|c\downarrow_j\right\rangle.\end{aligned} \tag{A.25}$$

Bibliography

[1] L. Balents. Spin liquids in frustrated magnets. *Nature*, 464:199, 2010.

[2] P.W. Anderson. Resonating valence bonds: A new kind of insulator? *Materials Research Bulletin*, 8:153, 1973.

[3] P. W. Anderson. The resonating valence bond state in La_2CuO_4 and superconductivity. *Science*, 235:1196, 1987.

[4] Y. Shimizu, K. Miyagawa, K. Kanoda, M. Maesato, and G. Saito. Spin liquid state in an organic Mott insulator with a triangular lattice. *Phys. Rev. Lett.*, 91:107001, 2003.

[5] J. S. Helton, K. Matan, M. P. Shores, E. A. Nytko, B. M. Bartlett, Y. Yoshida, Y. Takano, A. Suslov, Y. Qiu, J.-H. Chung, D. G. Nocera, and Y. S. Lee. Spin dynamics of the spin-1/2 kagome lattice antiferromagnet $ZnCu_3(OH)_6Cl_2$. *Phys. Rev. Lett.*, 98:107204, 2007.

[6] A. Kitaev. Anyons in an exactly solved model and beyond. *Annals of Physics*, 321, 2006.

[7] G. Jackeli and G. Khaliullin. Mott insulators in the strong spin-orbit coupling limit: From Heisenberg to a quantum compass and Kitaev models. *Phys. Rev. Lett.*, 102:017205, 2009.

[8] G. Khaliullin. Orbital order and fluctuations in Mott insulators. *Progress of Theoretical Physics Supplement*, 160:155, 2005.

[9] A. Biffin, R. D. Johnson, S. Choi, F. Freund, S. Manni, A. Bombardi, P. Manuel, P. Gegenwart, and R. Coldea. Unconventional magnetic order on the hyperhoneycomb Kitaev lattice in β-Li_2IrO_3: Full solution via magnetic resonant x-ray diffraction. *Phys. Rev. B*, 90:205116, 2014.

[10] T. Takayama, A. Kato, R. Dinnebier, J. Nuss, H. Kono, L. S. I. Veiga, G. Fabbris, D. Haskel, and H. Takagi. Hyperhoneycomb iridate β-Li_2IrO_3 as a platform for Kitaev magnetism. *Phys. Rev. Lett.*, 114:077202, 2015.

[11] K. A. Modic, T. E. Smidt, I. Kimchi, N. P. Breznay, A. Biffin, S. Choi, R. D. Johnson, R. Coldea, P. Watkins-Curry, and G. T. McCandless. Realization of a three-dimensional spin–anisotropic harmonic honeycomb iridate. *Nat. Commun.*, 5:4203, 2014.

[12] A. Biffin, R. D. Johnson, I. Kimchi, R. Morris, A. Bombardi, J. G. Analytis, A. Vishwanath, and R. Coldea. Noncoplanar and counterrotating incommensurate magnetic order stabilized by Kitaev interactions in γ-Li_2IrO_3. *Phys. Rev. Lett.*, 113:197201, 2014.

[13] J. Chaloupka, G. Jackeli, and G. Khaliullin. Zigzag magnetic order in the iridium oxide Na_2IrO_3. *Phys. Rev. Lett.*, 110:097204, 2013.

[14] X. Liu, T. Berlijn, W.-G. Yin, W. Ku, A. Tsvelik, Y.-J. Kim, H. Gretarsson, Y. Singh, P. Gegenwart, and J. P. Hill. Long-range magnetic ordering in Na_2IrO_3. *Phys. Rev. B*, 83:220403, 2011.

[15] S. K. Choi, R. Coldea, A. N. Kolmogorov, T. Lancaster, I. I. Mazin, S. J. Blundell, P. G. Radaelli, Y. Singh, P. Gegenwart, and K. R. Choi. Spin waves and revised crystal structure of honeycomb iridate Na_2IrO_3. *Phys. Rev. Lett.*, 108:127204, 2012.

[16] F. Ye, S. Chi, H. Cao, B. C. Chakoumakos, J. A. Fernandez-Baca, R. Custelcean, T. F. Qi, O. B. Korneta, and G. Cao. Direct evidence of a zigzag spin-chain structure in the honeycomb lattice: A neutron and x-ray diffraction investigation of single-crystal Na_2IrO_3. *Phys. Rev. B*, 85:180403, 2012.

[17] J. A. Sears, M. Songvilay, K. W. Plumb, J. P. Clancy, Y. Qiu, Y. Zhao, D. Parshall, and Y.-J. Kim. Magnetic order in α-$RuCl_3$: A honeycomb-lattice quantum magnet with strong spin-orbit coupling. *Phys. Rev. B*, 91:144420, 2015.

[18] R. D. Johnson, S. C. Williams, A. A. Haghighirad, J. Singleton, V. Zapf, P. Manuel, I. I. Mazin, Y. Li, H. O. Jeschke, R. Valentí, and R. Coldea. Monoclinic crystal structure of α-$RuCl_3$ and the zigzag antiferromagnetic ground state. *Phys. Rev. B*, 92:235119, 2015.

[19] A. Banerjee, C. A. Bridges, J.-Q. Yan, A. A. Aczel, L. Li, M. B. Stone, G. E. Granroth, M. D. Lumsden, Y. Yiu, J. Knolle, S. Bhattacharjee, D. L. Kovrizhin, R. Moessner, D. A. Tennant, D. G. Mandrus, and S. E. Nagler. Proximate Kitaev quantum spin liquid behaviour in a honeycomb magnet. *Nature Materials*, nmat4604, 2016.

[20] S. C. Williams, R. D. Johnson, F. Freund, S. Choi, A. Jesche, I. Kimchi, S. Manni, A. Bombardi, P. Manuel, P. Gegenwart, and R. Coldea. Incommensurate counterrotating magnetic order stabilized by Kitaev interactions in the layered honeycomb α-Li_2IrO_3. *Phys. Rev. B*, 93:195158, 2016.

[21] R. Comin, G. Levy, B. Ludbrook, Z.-H. Zhu, C. N. Veenstra, J. A. Rosen, Y. Singh, P. Gegenwart, D. Stricker, J. N. Hancock, D. van der Marel, I. S. Elfimov, and A. Damascelli. Na_2IrO_3 as a novel relativistic Mott insulator with a 340-mev gap. *Phys. Rev. Lett.*, 109:266406, 2012.

[22] H. Gretarsson, J. P. Clancy, X. Liu, J. P. Hill, Emil Bozin, Y. Singh, S. Manni, P. Gegenwart, Jungho Kim, A. H. Said, D. Casa, T. Gog, M. H. Upton, H.-S. Kim, J. Yu, V. M. Katukuri, L. Hozoi, J. van den Brink, and Y.-J. Kim. Crystal-field splitting and correlation effect on the electronic structure of A_2IrO_3. *Phys. Rev. Lett.*, 110:076402, 2013.

[23] M. Jenderka, R. Schmidt-Grund, M. Grundmann, and M. Lorenz. Electronic excitations and structure of Li_2IrO_3 thin films grown on ZrO_2:Y (001) substrates. *Journal of Applied Physics*, 117:025304, 2015.

[24] I. Pollini. Electronic properties of the narrow-band material α-$RuCl_3$. *Phys. Rev. B*, 53:12769, 1996.

[25] K. W. Plumb, J. P. Clancy, L. J. Sandilands, V. V. Shankar, Y. F. Hu, K. S. Burch, H.-Y. Kee, and Y.-J. Kim. α-$RuCl_3$: A spin-orbit assisted Mott insulator on a honeycomb lattice. *Phys. Rev. B*, 90:041112, 2014.

[26] J. Chaloupka, G. Jackeli, and G. Khaliullin. Kitaev-Heisenberg model on a honeycomb lattice: Possible exotic phases in Iridium Oxides A_2IrO_3. *Phys. Rev. Lett.*, 105:027204, 2010.

[27] H.-S. Kim, Vijay Shankar V., A. Catuneanu, and H.-Y. Kee. Kitaev magnetism in honeycomb $RuCl_3$ with intermediate spin-orbit coupling. *Phys. Rev. B*, 91:241110, 2015.

[28] I. I. Mazin, H. O. Jeschke, K. Foyevtsova, R. Valentí, and D. I. Khomskii. Na_2IrO_3 as a molecular orbital crystal. *Phys. Rev. Lett.*, 109:197201, 2012.

[29] K. Foyevtsova, H. O. Jeschke, I. I. Mazin, D. I. Khomskii, and R. Valentí. *Ab initio* analysis of the tight-binding parameters and magnetic interactions in Na_2IrO_3. *Phys. Rev. B*, 88:035107, 2013.

[30] N. Nembrini, S. Peli, F. Banfi, G. Ferrini, Y. Singh, P. Gegenwart, R. Comin, K. Foyevtsova, A. Damascelli, A. Avella, and C. C. Giannetti. Tracking local spin-dynamics via high-energy quasi-molecular excitations in a spin-orbit Mott insulator. *arXiv: 1606.01667*, 2016.

[31] T. Dey, A. V. Mahajan, R. Kumar, B. Koteswararao, F. C. Chou, A. A. Omrani, and H. M. Ronnow. Possible spin-orbit driven spin-liquid ground state in the double perovskite phase of $Ba_3YIr_2O_9$. *Phys. Rev. B*, 88:134425, 2013.

[32] J. G. Rau, E. K.-H. Lee, and H.-Y. Kee. Spin-orbit physics giving rise to novel phases in correlated systems: Iridates and related materials. *Annual Review of Condensed Matter Physics*, 7:195, 2016.

[33] Y. Li, K. Foyevtsova, H. O. Jeschke, and R. Valentí. Analysis of the optical conductivity for A_2IrO_3(A=Na, Li) from first principles. *Phys. Rev. B*, 91:161101, 2015.

[34] Y. Li, S. M. Winter, H. O. Jeschke, and R. Valentí. Electronic excitations in γ-Li_2IrO_3. *Phys. Rev. B*, 95:045129, 2017.

[35] F. Lang, P. J. Baker, A. A. Haghighirad, Y. Li, D. Prabhakaran, R. Valentí, and S. J. Blundell. Unconventional magnetism on a honeycomb lattice in α-$RuCl_3$ studied by muon spin rotation. *Phys. Rev. B*, 94:020407, 2016.

[36] S. M. Winter, Y. Li, H. O. Jeschke, and R. Valentí. Challenges in design of Kitaev materials: Magnetic interactions from competing energy scales. *Phys. Rev. B*, 93:214431, 2016.

[37] S. K. Panda, S. Bhowal, Y. Li, S. Ganguly, R. Valentí, L. Nordström, and I. Dasgupta. Electronic structure and spin-orbit driven magnetism in $d^{4.5}$ insulator $Ba_3YIr_2O_9$. *Phys. Rev. B*, 92:180403, 2015.

[38] C. Nayak, S. H. Simon, A. Stern, M. Freedman, and S. Das Sarma. Non-abelian anyons and topological quantum computation. *Rev. Mod. Phys.*, 80:1083, 2008.

[39] G. Baskaran, S. Mandal, and R. Shankar. Exact results for spin dynamics and fractionalization in the Kitaev model. *Phys. Rev. Lett.*, 98:247201, 2007.

[40] J. Knolle, D. L. Kovrizhin, J. T. Chalker, and R. Moessner. Dynamics of a two-dimensional quantum spin liquid: Signatures of emergent majorana fermions and fluxes. *Phys. Rev. Lett.*, 112:207203, 2014.

[41] M. S. Dresselhaus. *SOLID STATE PHYSICS, PART II, Optical Properties of Solids*. 2001.

[42] R. M. Martin. *Electronic Structure - Basic Theory and Practical Methods*. 2004.

[43] P. Hohenberg and W. Kohn. Inhomogeneous electron gas. *Phys. Rev.*, 136:B864, 1964.

[44] W. Kohn and L. J. Sham. Self-consistent equations including exchange and correlation effects. *Phys. Rev.*, 140:A1133, 1965.

[45] D. M. Ceperley and B. J. Alder. Ground state of the electron gas by a stochastic method. *Phys. Rev. Lett.*, 45:566, 1980.

[46] J. P. Perdew and A. Zunger. Self-interaction correction to density-functional approximations for many-electron systems. *Phys. Rev. B*, 23:5048, 1981.

[47] J. P. Perdew and Y. Wang. Accurate and simple analytic representation of the electron-gas correlation energy. *Phys. Rev. B*, 45:13244, 1992.

[48] D. C. Langreth and M. J. Mehl. Beyond the local-density approximation in calculations of ground-state electronic properties. *Phys. Rev. B*, 28:1809, 1983.

[49] J. P. Perdew and W. Yue. Accurate and simple density functional for the electronic exchange energy: Generalized gradient approximation. *Phys. Rev. B*, 33:8800, 1986.

[50] Z. Wu and R. E. Cohen. More accurate generalized gradient approximation for solids. *Phys. Rev. B*, 73:235116, 2006.

[51] J. P. Perdew, K. Burke, and M. Ernzerhof. Generalized gradient approximation made simple. *Phys. Rev. Lett.*, 77:3865, 1996.

[52] J. P. Perdew, A. Ruzsinszky, G. I. Csonka, O. A. Vydrov, G. E. Scuseria, L. A. Constantin, X. Zhou, and K. Burke. Restoring the density-gradient expansion for exchange in solids and surfaces. *Phys. Rev. Lett.*, 100:136406, 2008.

[53] N. W. Ashcroft and N. D. Mermin. *Solid State Physics*. 1976.

[54] P. E. Blöchl. Projector augmented-wave method. *Phys. Rev. B*, 50:17953, 1994.

[55] O. K. Andersen. Linear methods in band theory. *Phys. Rev. B*, 12:3060, 1975.

[56] E. Wimmer, H. Krakauer, M. Weinert, and A. J. Freeman. Full-potential self-consistent linearized-augmented-plane-wave method for calculating the electronic structure of molecules and surfaces: O_2 molecule. *Phys. Rev. B*, 24:864, 1981.

[57] P. Blaha, K. Schwarz, G. K. H. Madsen, D. Kvasnicka, and J. Luitz. Wien2k, an augmented plane wave plus local orbitals program for calculating crystal properties (Karlheinz Schwarz, Techn. Universität Wien, Austria). 2001.

[58] D. D. Koelling and B. N. Harmon. A technique for relativistic spin-polarised calculations. *Journal of Physics C: Solid State Physics*, 10:3107, 1977.

[59] V. I. Anisimov, J. Zaanen, and O. K. Andersen. Band theory and Mott insulators: Hubbard *U* instead of stoner *I*. *Phys. Rev. B*, 44:943, 1991.

[60] V. I. Anisimov, I. V. Solovyev, M. A. Korotin, M. T. Czyżyk, and G. A. Sawatzky. Density-functional theory and NiO photoemission spectra. *Phys. Rev. B*, 48:16929, 1993.

[61] M. Aichhorn, L. Pourovskii, V. Vildosola, M. Ferrero, O. Parcollet, T. Miyake, A. Georges, and S. Biermann. Dynamical mean-field theory within an augmented plane-wave framework: Assessing electronic correlations in the iron pnictide LaFeAsO. *Phys. Rev. B*, 80:085101, 2009.

[62] G. D. Mahan. *Many-Particle Physics*. 1981.

[63] P. F. Maldague. Optical spectrum of a Hubbard chain. *Phys. Rev. B*, 16:2437, 1977.

[64] C. Ambrosch-Draxl and J. O. Sofo. Linear optical properties of solids within the full-potential linearized augmented planewave method. *Computer Physics Communications*, 175:1, 2006.

[65] J. Ferber, Y.-Z. Zhang, H. O. Jeschke, and R. Valentí. Analysis of spin-density wave conductivity spectra of iron pnictides in the framework of density functional theory. *Phys. Rev. B*, 82:165102, 2010.

[66] K. I. Kugel and D. I. Khomskii. Crystal-structure and magnetic properties of substances with orbital degeneracy. *Soviet Physics JETP*, 37:725, 1973.

[67] J. G. Rau, E. K.-H. Lee, and H.-Y. Kee. Generic spin model for the honeycomb iridates beyond the Kitaev limit. *Phys. Rev. Lett.*, 112:077204, 2014.

[68] H.-S. Kim, E. K.-H. Lee, and Y. B. Kim. Predominance of the Kitaev interaction in a three-dimensional honeycomb iridate: From ab initio to spin model. *EPL (Europhysics Letters)*, 112:67004, 2015.

[69] Y. Sizyuk, C. Price, P. Wölfle, and N. B. Perkins. Importance of anisotropic exchange interactions in honeycomb iridates: Minimal model for zigzag antiferromagnetic order in Na_2IrO_3. *Phys. Rev. B*, 90:155126, 2014.

[70] Y. Yamaji, Y. Nomura, M. Kurita, R. Arita, and M. Imada. First-principles study of the honeycomb-lattice iridates Na_2IrO_3 in the presence of strong spin-orbit interaction and electron correlations. *Phys. Rev. Lett.*, 113:107201, 2014.

[71] S. Bhattacharjee, S.-S. Lee, and Y. B. Kim. Spin-orbital locking, emergent pseudo-spin and magnetic order in honeycomb lattice iridates. *New Journal of Physics*, 14:073015, 2012.

[72] J. G. Rau and H.-Y. Kee. Trigonal distortion in the honeycomb iridates: Proximity of zigzag and spiral phases in Na_2IrO_3. *arXiv:1408.4811*, 2014.

[73] I. Kimchi and Y.-Z. You. Kitaev-Heisenberg-J_2-J_3 model for the iridates Na_2IrO_3. *Phys. Rev. B*, 84:180407, 2011.

[74] J. Reuther, R. Thomale, and S. Rachel. Spiral order in the honeycomb iridate Li_2IrO_3. *Phys. Rev. B*, 90:100405, 2014.

[75] Y. Singh, S. Manni, J. Reuther, T. Berlijn, R. Thomale, W. Ku, S. Trebst, and P. Gegenwart. Relevance of the Heisenberg-Kitaev model for the honeycomb lattice iridates A_2IrO_3. *Phys. Rev. Lett.*, 108:127203, 2012.

[76] S. Nishimoto, V. M. Katukuri, V. Yushankhai, H. Stoll, U. K. Rößler, L. Hozoi, I. Rousochatzakis, and J. van den Brink. Strongly frustrated triangular spin lattice emerging from triplet dimer formation in honeycomb Li_2IrO_3. *Nat. Commun.*, 7:10273.

[77] S. Manni, S. Choi, I. I. Mazin, R. Coldea, M. Altmeyer, H. O. Jeschke, R. Valentí, and P. Gegenwart. Effect of isoelectronic doping on the honeycomb-lattice iridate A_2IrO_3. *Phys. Rev. B*, 89:245113, 2014.

[78] Y. Singh and P. Gegenwart. Antiferromagnetic Mott insulating state in single crystals of the honeycomb lattice material Na_2IrO_3. *Phys. Rev. B*, 82:064412, 2010.

[79] S. Hwan Chun, J.-W. Kim, J. Kim, H. Zheng, C. C. Stoumpos, C. D. Malliakas, J. F. Mitchell, K. Mehlawat, Y. Singh, Y. Choi, T. Gog, A. Al-Zein, M. M. Sala, M. Krisch, J. Chaloupka, G. Jackeli, G. Khaliullin, and B. J. Kim. Direct evidence for dominant bond-directional interactions in a honeycomb lattice iridate Na_2IrO_3. *Nature Physics*, 11:462, 2015.

[80] J. Chaloupka and G. Khaliullin. Hidden symmetries of the extended Kitaev-Heisenberg model: Implications for the honeycomb-lattice iridates A_2IrO_3. *Phys. Rev. B*, 92:024413, 2015.

[81] V. M. Katukuri, S. Nishimoto, V. Yushankhai, A. Stoyanova, H. Kandpal, S. Choi, R. Coldea, I. Rousochatzakis, L. Hozoi, and J. van den Brink. Kitaev interactions between j= 1/2 moments in honeycomb Na_2IrO_3 are large and ferromagnetic: insights from *ab initio* quantum chemistry calculations. *New J. Phys.*, 16:013056, 2014.

[82] J. Reuther, R. Thomale, and S. Rachel. Magnetic ordering phenomena of interacting quantum spin Hall models. *Phys. Rev. B*, 86:155127, 2012.

[83] I. Kimchi, R. Coldea, and A. Vishwanath. Unified theory of spiral magnetism in the harmonic-honeycomb iridates α, β, and γ Li_2IrO_3. *Phys. Rev. B*, 91:245134, 2015.

[84] G. Cao, T. F. Qi, L. Li, J. Terzic, V. S. Cao, S. J. Yuan, M. Tovar, G. Murthy, and R. K. Kaul. Evolution of magnetism in the single-crystal honeycomb iridates $(Na_{1-x}Li_x)_2IrO_3$. *Phys. Rev. B*, 88:220414, 2013.

[85] C. H. Sohn, H.-S. Kim, T. F. Qi, D. W. Jeong, H. J. Park, H. K. Yoo, H. H. Kim, J.-Y. Kim, T. D. Kang, D.-Y. Cho, G. Cao, J. Yu, S. J. Moon, and T. W. Noh. Mixing between $J_{\text{eff}} = \frac{1}{2}$ and $\frac{3}{2}$ orbitals in Na_2IrO_3: A spectroscopic and density functional calculation study. *Phys. Rev. B*, 88:085125, 2013.

[86] B. H. Kim, G. Khaliullin, and B. I. Min. Electronic excitations in the edge-shared relativistic Mott insulator: Na_2IrO_3. *Phys. Rev. B*, 89:081109, 2014.

[87] I. I. Mazin, S. Manni, K. Foyevtsova, Harald O. Jeschke, P. Gegenwart, and R. Valentí. Origin of the insulating state in honeycomb iridates and rhodates. *Phys. Rev. B*, 88:035115, 2013.

[88] I. Kimchi, J. G. Analytis, and A. Vishwanath. Three-dimensional quantum spin liquids in models of harmonic-honeycomb iridates and phase diagram in an infinite-*d* approximation. *Phys. Rev. B*, 90:205126, 2014.

[89] E. K.-H. Lee, R. Schaffer, S. Bhattacharjee, and Y. B. Kim. Heisenberg-Kitaev model on the hyperhoneycomb lattice. *Phys. Rev. B*, 89:045117, 2014.

[90] E. K.-H. Lee, J. G. Rau, and Y. B. Kim. Two iridates, two models, and two approaches: A comparative study on magnetism in three-dimensional honeycomb materials. *Phys. Rev. B*, 93:184420, 2016.

[91] J. P. Hinton, S. Patankar, E. Thewalt, A. Ruiz, G. Lopez, N. Breznay, A. Vishwanath, J. Analytis, J. Orenstein, J. D. Koralek, and I. Kimchi. Photoexcited states of the harmonic honeycomb iridate γ-Li_2IrO_3. *Phys. Rev. B*, 92:115154, 2015.

[92] B. H. Kim, G. Khaliullin, and B. I. Min. Magnetic couplings, optical spectra, and spin-orbit exciton in 5*d* electron Mott insulator Sr_2IrO_4. *Phys. Rev. Lett.*, 109:167205, 2012.

[93] F. Freund, S. C. Williams, R. D. Johnson, R. Coldea, P. Gegenwart, and A. Jesche. Single crystal growth from separated educts and its application to lithium transition-metal oxides. *Scientific Reports*, 6:35362, 2016.

[94] E. Stroganov and K. and Ovchinnikov. Crystal structure of ruthenium trichloride. *Vestn. Leningrad. Univ.,Fizika, Khimiya*, 12:152, 1957.

[95] H. B. Cao, A. Banerjee, J.-Q. Yan, C. A. Bridges, M. D. Lumsden, D. G. Mandrus, D. A. Tennant, B. C. Chakoumakos, and S. E. Nagler. Low-

temperature crystal and magnetic structure of α-$RuCl_3$. *Phys. Rev. B*, 93:134423, 2016.

[96] Y. Kubota, H. Tanaka, T. Ono, Y. Narumi, and K. Kindo. Successive magnetic phase transitions in α-$RuCl_3$: XY-like frustrated magnet on the honeycomb lattice. *Phys. Rev. B*, 91:094422, 2015.

[97] M. Majumder, M. Schmidt, H. Rosner, A. A. Tsirlin, H. Yasuoka, and M. Baenitz. Anisotropic $Ru^{3+}4d^5$ magnetism in the α-$RuCl_3$ honeycomb system: Susceptibility, specific heat, and zero-field NMR. *Phys. Rev. B*, 91:180401, 2015.

[98] L. J. Sandilands, Y. Tian, A. A. Reijnders, H.-S. Kim, K. W. Plumb, Y.-J. Kim, H.-Y. Kee, and K. S. Burch. Spin-orbit excitations and electronic structure of the putative Kitaev magnet α-$RuCl_3$. *Phys. Rev. B*, 93:075144, 2016.

[99] L. J. Sandilands, Y. Tian, K. W. Plumb, Y.-J. Kim, and K. S. Burch. Scattering continuum and possible fractionalized excitations in α-$RuCl_3$. *Phys. Rev. Lett.*, 114:147201, 2015.

[100] I. Rousochatzakis, J. Reuther, R. Thomale, S. Rachel, and N. B. Perkins. Phase diagram and quantum order by disorder in the Kitaev $K_1 - K_2$ honeycomb magnet. *Phys. Rev. X*, 5:041035, 2015.

[101] Y. Kobayashi, T. Okada, K. Asai, M. Katada, H. Sano, and F. Ambe. Moessbauer spectroscopy and magnetization studies of α- and β- ruthenium trichloride. *Inorg. Chem.*, 31:4570, 1992.

[102] A. Kokalj. Xcrysden - a new program for displaying crystalline structures and electron densities. *Journal of Molecular Graphics and Modelling*, 17:176, 1999.

[103] K. Momma and F. Izumi. *VESTA*: a three-dimensional visualization system for electronic and structural analysis. *Journal of Applied Crystallography*, 41:653, 2008.

[104] J. S. Moeller, P. Bonfa, D. Ceresoli, F. Bernardini, S. J. Blundell, T. Lancaster, R De Renzi, N. Marzari, I. Watanabe, S. Sulaiman, and M. I. Mohamed-Ibrahim. Playing quantum hide-and-seek with the muon: localizing muon stopping sites. *Physica Scripta*, 88:068510, 2013.

[105] F. R. Foronda, F. Lang, J. S. Möller, T. Lancaster, A. T. Boothroyd, F. L. Pratt, S. R. Giblin, D. Prabhakaran, and S. J. Blundell. Anisotropic local modification of crystal field levels in Pr-based pyrochlores: A muon-induced effect modeled using density functional theory. *Phys. Rev. Lett.*, 114:017602, 2015.

[106] H.-S. Kim and H.-Y. Kee. Crystal structure and magnetism in α-$RuCl_3$: An *ab initio* study. *Phys. Rev. B*, 93:155143, 2016.

[107] J. C Slater and G. F. Koster. Simplified LCAO method for the periodic potential problem. *Phys. Rev.*, 94:1498, 1954.

[108] Y. Yamaji, T. Suzuki, T. Yamada, S. Suga, N. Kawashima, and M. Imada. Clues and criteria for designing a Kitaev spin liquid revealed by thermal and spin excitations of the honeycomb iridate Na_2IrO_3. *Phys. Rev. B*, 93:174425, 2016.

[109] J. Nasu, J. Knolle, D. L. Kovrizhin, Y. Motome, and R. Moessner. Fermionic response from fractionalization in an insulating two-dimensional magnet. *Nat Phys*, nphys3809, 2016.

[110] J. Yoshitake, J. Nasu, and Y. Motome. Fractional spin fluctuation as a precursor of quantum spin liquids: Majorana dynamical mean-field study for the Kitaev model. *Phys. Rev. Lett.*, 117:157203, 2016.

[111] J. Nasu, M. Udagawa, and Y. Motome. Vaporization of Kitaev spin liquids. *Phys. Rev. Lett.*, 113:197205, 2014.

[112] T. Dey, R. Kumar, A. V. Mahajan, S. D. Kaushik, and V. Siruguri. Unconventional magnetism in the spin-orbit-driven Mott insulators $Ba_3MIr_2O_9$ (M=Sc,y). *Phys. Rev. B*, 89:205101, 2014.

[113] Y. Doi and Y. Hinatsu. The structural and magnetic characterization of 6H-perovskite-type oxides $Ba_3LnIr_2O_9$ (Ln=Y, lanthanides). *Journal of Physics: Condensed Matter*, 16:2849, 2004.

[114] B. J. Kim, H. Jin, S. J. Moon, J.-Y. Kim, B.-G. Park, C. S. Leem, J. Yu, T. W. Noh, C. Kim, S.-J. Oh, J.-H. Park, V. Durairaj, G. Cao, and E. Rotenberg. Novel $J_{\text{eff}} = 1/2$ Mott state induced by relativistic spin-orbit coupling in Sr_2IrO_4. *Phys. Rev. Lett.*, 101:076402, 2008.

[115] S. V. Streltsov, G. Cao, and D. I. Khomskii. Suppression of magnetism in $Ba_5AlIr_2O_{11}$: interplay of Hund's coupling, molecular orbitals and spin-orbit interaction. *arXiv:*, 1505:00877, 2015.

Acknowledgements

During the past four years in Frankfurt, I completed this PhD thesis and learned new ways of thinking about problems with the help of many people. First of all, I'm very appreciative to my supervisor Prof. Dr. Roser Valentí who gave me the opportunity to work on my PhD projects in her group. She was very patient with me and always encouraged to slowly improve. Whenever I had problems, instead of forcing me to be fast to get results, she carefully helped me to find the way to solve the problem. With her help, I've been able to have a rich experience on DFT calculations and many-body methods, investigating interesting physics of strong spin-orbit coupling and correlated materials. I also appreciate her careful reading and correcting my English texts of this thesis.

I also would like to thank Dr. Harald Jeschke, from whom, I learned how to do DFT calculations, make nice figures and with whom I had many interesting discussions about my project. He is always very careful with details which is a nice character a scientist should have. Also, I would like to thank Dr. Stephen M. Winter. With him, I did really work on many-body methods beyond DFT, which I really enjoyed and is an important part of my thesis. He was also careful proofreading of the thesis manuscript and gave me a lot of nice suggestions and corrected my English texts. Thanks for Dr. Kateryna Foyevtsova's help, I learned how to calculate the hopping parameters and QMO from DFT. I also thank my former colleague Dr. Juan Shen. She is also Chinese and helped me a lot when I just came to Germany.

It has been a pleasure to work in a friendly atmosphere of our research group. I would like to thank my colleagues Kira Riedl, Michaela Altmeyer, Daniel Guterding, Dr. Francesc Salvat-Pujol, Steffen Backes, Dr. Vladislav Borisov, Aaram J. Kim, Milan Tomic, Ryui Kaneko, and other colleagues for all help and discussions and our secretary Frau Maripola Kolokotsa and Frau Anne Metz. Thanks to Kira

Riedl for german translating of the abstract. I would like to thank Prof. Dr. Peter Kopietz for taking over the role of the second referee of my thesis.

Finally, I thank my husband Ge Xu for his support and discussion during my PhD work. I gratefully acknowledge the China Scholarship Council for financial support.